

**Eco-friendly halogen-free solvent processed  
efficient polymer solar cell fabrication and  
morphology engineering**

by

**Guler Kocak**

B.Sc., M.Sc.

*Thesis submitted to Flinders University*

*for the degree of*

**Doctor of Philosophy**

College of Science and Engineering

Institute for Nanoscale Science & Technology

20.03.2023

---

*Dedicated to selfless people with perseverance having compassion for others like my mother,  
and to my father... your soul will always be with me no matter where I  
am.*

*“Nothing in life is to be feared, it is only to be understood. Now is the time to understand more, so that we may fear less.”*

*- Marie Salomea Skłodowska Curie*

# Table of Contents

<b>Table of Contents</b> .....	iii
<b>Abstract</b> .....	vii
<b>Declaration</b> .....	ix
<b>Acknowledgements</b> .....	x
<b>List of figures</b> .....	xi
<b>List of tables</b> .....	xvii
<b>Abbreviations and acronyms</b> .....	xxii
<b>Chapter 1: Introduction</b> .....	<b>1</b>
1.1 Climate change impact on energy trends.....	2
1.1.1 Current energy solutions.....	3
1.2 Conjugated polymers.....	5
1.3 Inorganic and organic photovoltaics (OPV).....	5
1.4 Polymer solar cells (PSCs).....	6
1.5 Working principle of organic solar cells.....	7
1.6 Advantages and challenges of OPV.....	8
1.7 Device structure of OPVs.....	8
1.7.1 Single layer OSCs.....	9
1.7.2 Bi-layer planar heterojunction OSCs.....	9
1.7.3 Bulk heterojunction OSCs.....	9
1.7.4 Ternary blend OSCs.....	10
1.7.5 Conventional and inverted device architectures.....	10
1.8 Photoactive layer.....	10
1.9 Band gap.....	11
1.10 Solubility and molecular weight.....	11
1.11 Eco-friendly solvent processing.....	12
1.12 Small molecules.....	13
1.13 Organic evaporated molecules in OSC.....	13
1.14 Fullerene polymer solar cells.....	14
1.15 Donors and fullerene acceptors.....	15
1.16 Non-fullerene acceptors (NFAs).....	16
1.17 Molecular stacking.....	19
1.18 Donor-Acceptor copolymers and Non-fullerene polymer solar cells (NF PSCs).....	20
1.19 Stability of NF PSCs.....	20
1.20 Morphology.....	21
1.21 Treatments for better cell performances.....	22

1.21.1	Solvent vapor annealing.....	23
1.21.2	Thermal annealing.....	23
1.21.3	Solvent additives.....	24
1.21.4	Washing.....	24
1.21.5	High Vacuum drying.....	25
1.22	Other types of photovoltaic solar cells.....	25
1.22.1	Perovskite solar cells.....	25
1.22.2	Dye-sensitized solar cells (DSSCs).....	26
1.23	Printing polymer solar cells.....	27
1.23.1	Doctor Blading.....	27
1.23.2	Ink-Jet Printing (Non-contact printing).....	28
1.23.3	Slot-die coating.....	28
1.23.4	Mini-roll coater.....	29
1.24	Aim.....	31
1.25	References.....	32
<b>Chapter 2: Research Methodology.....</b>		<b>38</b>
2.1	Introduction.....	39
2.2	Materials, principles and instruments.....	39
2.2.1.	Materials.....	39
2.2.2.	Photovoltaic effect.....	40
2.2.3.	Photoelectric effect.....	41
2.2.4.	Comparison of bandgap of metals, semiconductors, and insulators.....	42
2.3	Device fabrication.....	45
2.3.1	Glove box system.....	45
2.3.2	Cleaning substrates.....	46
2.3.3	Spin-coating and slot-die coating of thin-film layers.....	46
2.3.4	Thermal evaporation of electrodes.....	47
2.4	Device characterization.....	48
2.4.1	Diode characteristics (I-V) curve.....	48
2.4.2	IPCE Characteristics.....	50
2.5	Neutral impact collision ion scattering spectroscopy (NICISS).....	51
2.6	X-ray photoelectron spectroscopy (XPS).....	52
2.7	Single-crystal X-ray diffraction (XRD) and X-ray powder diffraction (PXRD).....	53
2.8	Atomic force microscopy (AFM).....	55
2.9	High temperature gel-permeation chromatography (HT-GPC).....	57
2.10	Profilometry.....	57
2.11	Thermal stability measurements.....	58
2.11.1	Dynamic mechanical thermal analysis (DMTA).....	58

2.11.2 TGA-DSC Simultaneous thermal analyzer (STA).....	59
2.12 References.....	60

**Chapter 3: Effect of process parameters and additives on PTB7-Th:ITIC BHJ polymer solar cells.....62**

3.1 Introduction.....	63
3.1.1 D-A copolymers and NF acceptors.....	63
3.1.2 PTB7 and PTB7-Th copolymers.....	65
3.2 Methodology, device fabrication, and characterization.....	67
3.2.1 Materials.....	67
3.2.2 PTB7, PTB7-Th, ITIC and DIO.....	68
3.2.3 NF OPV device fabrication and characterization.....	70
3.3 AFM morphology characterization.....	79
3.3.1 AFM roughness measurements.....	81
3.4 XPS and NICISS analysis.....	83
3.5 Thermal studies.....	93
3.5.1 STA studies.....	93
3.5.1.1 STA experiments of PTB7-Th with and w/o DIO.....	94
3.5.2 DMA studies.....	100
3.6 XRD and P-XRD studies of PTB7-Th:ITIC (1:1.3) thin films.....	103
3.6.1 STA of ITIC crystals formed via slow crystallization in the presence of DIO.....	104
3.7 Conclusion.....	106
3.8 Contributions.....	108
3.9 References.....	109

**Chapter 4: Optimizing polymer solar cells using non-halogenated solvent blends.....112**

4.1 Introduction.....	113
4.2 Methodology.....	118
4.2.1 Materials.....	118
4.2.2 Substrate preparation.....	118
4.2.3 Device fabrication.....	119
4.2.4 Photo-physical properties.....	120
4.2.5 Film thickness and topography.....	120
4.3 Results and discussion.....	120
4.3.1 Solvent and solvent additives.....	120
4.3.2 Photovoltaic properties.....	125
4.3.3 Photoluminescence (PL).....	132
4.3.4 Surface topography.....	133
4.4 Conclusion.....	136

4.5 Contributions.....	137
4.6 References.....	138
<b>Chapter 5: Printing eco-friendly polymer solar cells, the effect of molecular weight on efficiency, and morphology characterization.....</b>	<b>142</b>
5.1 Introduction.....	143
5.2 Methodology.....	147
5.2.1 Mini roll coater (MRC) – components and operation.....	151
5.2.2 ZnO NP and BHJ preparation.....	154
5.3 Slot-die coating defects, adjustments, and printed OPV degradation.....	156
5.3.1 Chatter defects.....	157
5.3.2 Ribbing defects.....	158
5.3.3 Neck-in defects.....	159
5.3.4 Edge defects.....	160
5.3.5 Streak defects.....	161
5.3.6 Bubble defects.....	162
5.4 Discussion and results.....	163
5.4.1 Effect of molecular weight of PTNT polymer on photovoltaic properties of selection of printed PSCs.....	163
5.4.2 Device fabrication.....	164
5.5 Photovoltaic properties of PTNT:PC <sub>71</sub> BM and PTNT:ITIC (MJ-A159 batch) devices using different solvent additives.....	173
5.6 Printed Device Performances for PTNT:PC <sub>71</sub> BM(2:3) processed from non-toxic solvent systems.....	178
5.6.1 PTNT Printed device photovoltaic properties.....	180
5.6.2 PTNT Printed device morphology studies.....	188
5.7 Conclusion.....	195
5.8 Contributions.....	196
5.9 References.....	197
<b>Chapter 6: Summary.....</b>	<b>199</b>
<b>6.1 General Summary and conclusions.....</b>	<b>199</b>
<b>6.2 Future Work.....</b>	<b>202</b>
<b>Appendix.....</b>	<b>205</b>
A.1 J-V graph of PTB7-Th devices.....	205
B.1 STA of PTB7-Th blends.....	211
C.1 DMA of PTB7-Th blends.....	213

## Abstract

Increasing energy demand and diminishing non-renewable energy resources have resulted in facing our biggest challenges for the last decades, and these are indications for more alarming problems such as global warming and pollution. The motivation for this research is based on the state-of-the-art actions to take in order to solve these problems and propose that eco-friendly organic photovoltaics can play a vital role.

The most abundant and clean energy is solar, and it needs to be utilized with cost-effective and eco-friendlier techniques in the future. Existing solar panels that are commonly used are fabricated in a costlier manner and they require materials that can negatively impact the environment. Whereas, organic photovoltaics (OPV) offer both lightweight architecture and eco-friendliness, and their efficiencies are approaching to 20% with ongoing research which are exceptionally promising.

Yet, the most important challenges for OPVs are their large-scale applicability and environmental effect for future industrial production. In order to fabricate large-scale and also flexible devices, it is preferable to be able to experiment with materials that are processable in air without using toxic chemicals in a cost-effective way.

Therefore, this thesis focuses on both optimization of photo-active layers of OPVs with non-halogenated processing solvents and fabrication of these eco-friendlier solar cells via slot-die coating printing technique. The donor-acceptor (D-A) groups of organic materials are selected initially to be evaluated in inverted devices and different post-treatments were methodically analysed. The successful solvent systems that gave the best performing devices for polymer-fullerene and polymer-non fullerene D-A pairs were specifically tested and characterized for their applicability in printed devices.

In Chapter 3, a highly popular donor polymer PTB7-Th and non-fullerene acceptor (NFA) ITIC pair was tested in devices made using eco-friendly solvent systems with spin-coating process. The existing solvent systems and fabrication ways for the formation of the organic thin film layer for the same polymer and fullerene systems were also used for comparison. The best performing device efficiency with NFA system was found to be greater than that of reported in the literature and our experiments gave a PCE of 8.5% even when we use our eco-friendly fabrication method.

Also, techniques for efficient and proper removal of toxic solvent additives for the same D-A pairs were investigated. In order to support this research besides the device performances, surface and thermal characterizations were further carried out.

In Chapter 4, the motivation was solely on the eco-friendly fabrication and optimization of photo-active layers of solar cells. High performing devices using less harmful solvent systems were found for PTNT polymer and fullerene materials, and they are tested later in Chapter 5 for their applicability for printing techniques.

In Chapter 5, materials that were extensively studied in previous chapters were also evaluated for flexible device fabrication with eco-friendly methods and post-treatments such as PTNT polymer and fullerene acceptors. PTNT polymer gave high efficiencies (~5%) with this flexible device processing using green solvents, and supported our proposal of new fabrication techniques and use of non-halogenated solvent systems in many more OSC materials commonly tested in literature. The device photovoltaic properties and the microscopy images of the thin film layers were always reported to complement each other and supported our arguments when different treatments were applied. The morphology controllability using pre-and post- treatments of active layers were investigated in detail, especially in Chapter 3 and 5.

In summary, the inverted polymer solar cells were fabricated with novel green and cost-effective techniques and examined for other comparable polymer-acceptor systems for the best efficiency and eco-friendliness. They were also tested in flexible cell architecture appropriateness and proved their importance for future use in large-scale green solar cell applications with good efficiencies.

**Keywords:** polymer solar cells, eco-friendly, solvent additive, OSC, NFA, non-fullerene acceptor, slot-die coating, mini-roll coater, printed solar cell, spin-coating, environmentally friendly, annealing, vacuum drying.

## **Declaration**

“I certify that this thesis: 1. does not incorporate without acknowledgment any material previously submitted for a degree or diploma in any university 2. and the research within will not be submitted for any other future degree or diploma without the permission of Flinders University; and 3. to the best of my knowledge and belief, does not contain any material previously published or written by another person except where due reference is made in the text.”.

Signed:

Date: 15.08.2022

## Acknowledgements

From the very excitement of my first day as I was visiting the campus, the laboratories, and admiring the nature surrounded me to the very last days of completion of my thesis; my PhD journey has been life-changing and initiated an enormous personal growth with many learnings and challenges in becoming a researcher. I had the opportunity to be out of my comfort zone once again living and learning abroad by myself, as well as, finding friends and colleagues that supported me in this valuable experience.

I would like to thank to my Supervisor Prof. Mats Andersson in believing me for this journey and supporting me in every challenge that came along the way. I have been inspired by his scientific work for years, and by his kindness, which made me never give up and let myself learn from my mistakes.

Even tough kindness makes one vulnerable, I am grateful that it also helps me always look forward to chasing my dreams and be hopeful for the future.

I would also like to thank to my colleagues, Dr. Desta Gedefaw, Dr. Yanting Yin, Dr. Caroline Pan, Bradley Kirk, Anand Kumar for their help in the lab with organic synthesis, surface characterization, device fabrication and many more.

My best friend Dr. Carolin Reichherzer has been always with me and supported me in the worst times during my PhD. Most importantly, she helped me cope and continue to heal throughout the pandemic when I also had the pain of sudden loss of my father.

Finally, I would like to thank to my family for their ongoing support and love during this long journey, and to my dearest partner for his love, endless support and being my driving force behind all that I do. I am forever grateful to have you all in my life.

## List of figures

Figure 1.1: CO <sub>2</sub> levels over the years.....	2
Figure 1.2: IPCC, 2021 Average temperature rise prediction.....	3
Figure 1.3: Global energy potential diagram.....	4
Figure 1.4 Sunlight and solar energy potential in Australia.....	6
Figure 1.5: Structures of common fullerene acceptors.....	14
Figure 1.6: The structures of NF acceptor ITIC derivatives and IDIC.....	17
Figure 1.7: UV-Vis spectra of thin film cast from chloroform for ITIC derivatives.....	18
Figure 1.8: Structures of Y6 NFA.....	18
Figure 1.9: Charge transport and dissociation in BHJ OSC.....	19
Figure 1.10: Flexible organic solar cell construction.....	27
Figure 1.11: Doctor blade and ink-jet printing concepts.....	28
Figure 1.12: Strips of organic solar cells via slot-die coating.....	30
Figure 2.1 Photoelectric effect.....	41
Figure 2.2 Band diagrams of different materials.....	42
Figure 2.3 Band diagram of semiconductor material.....	43
Figure 2.4: Band gap of conjugated polymers and effect of conjugation length.....	44
Figure 2.5: I-V characteristics of a solar cell.....	48
Figure 2.6: I-V Measurement of a flexible solar cell.....	49
Figure 2.7: EQE efficiency curve depiction of a solar cell.....	50
Figure 2.8: IPCE Measurement setup of a solar cell.....	51
Figure 2.9: X-ray photoelectron spectroscopy working principle.....	53
Figure 2.10: Schematic diagram of X-ray powder diffraction method.....	54
Figure 2.11: XRD spectrum representation (Intensity versus diffraction angle 2theta).....	55

Figure 2.12: AFM working principle scheme.....	56
Figure 3.1: PTB7 and PTB7-Th structures.....	66
Figure 3.2: PC <sub>71</sub> BM vs ITIC for PTB7-Th devices.....	67
Figure 3.3: Structures of main solvent and solvent additives used in PSC studies.....	68
Figure 3.4: PSC device architecture with BHJ of PTB7-Th:ITIC.....	69
Figure 3.5: Device photo of PSC from PTB7-Th:ITIC (1:1.3) (19.5 mg/mL) (2500 rpm) processed with o-xylene with 0.6% DIO additive.....	74
Figure 3.6: J-V graph of PSCs from PTB7-Th:ITIC (1:1.3) (19.5 mg/mL) processed with o-xylene for AA additive and drying optimization.....	77
Figure 3.7: AFM Height images of thin films processed from CB main solvent and 0.6% DIO additive(top) versus processed from o-xylene main solvent + 2% AA (bottom) (Scales are 200 nm and 1µm for both solvent systems).....	79
Figure 3.8: AFM Height images of devices – CB main solvent + 2% DIO (top) / 2%DIO annealed (middle) / 4% DIO annealed (bottom). (Scales are 200 nm and 1µm for all 3 solvent systems).....	80
Figure 3.9: XPS Spectra of thin films processed with o-xylene + DIO, CB + DIO.....	86
Figure 3.10: XPS Spectra of thin films of o-xylene and CB at Iodine B.E. region.....	86
Figure 3.11: XPS Spectra and Concentration analysis of thin films processed with CB + 4% DIO.....	87
Figure 3.12: S vs N and F elemental composition analysis with thin films of CB, CB + DIO and CB + DIO annealed.....	88
Figure 3.13: S vs N and F elemental composition analysis with thin films of o-xylene and o-xylene + DIO.....	89
Figure 3.14: NCISS Spectrum for Iodine elemental comparison at as cast and annealed samples.....	91

Figure 3.15: NCISS Depth profile spectra.....	92
Figure 3.16: STA of pure ITIC and DIO.....	95
Figure 3.17: STA of ITIC + 10% PTB7-Th with and w/o DIO.....	95
Figure 3.18: STA of PTB7-Th processed from CB with and w/o DIO.....	96
Figure 3.19: STA of of ITIC + 10% PTB7-Th processed from CB w/o DIO.....	96
Figure 3.20: TGA of ITIC + 10% PTB7-Th processed from CN, PN, DPE and DIO.....	97
Figure 3.21: STA mass percentage comparison of blends of PTB7-Th: ITIC (1:1.3) processed from CB in different drying conditions.....	98
Figure 3.22: STA mass percentage comparison of blends of PTB7-Th: ITIC (1:1.3) processed from CB + 0.6% DIO in different drying conditions.....	98
Figure 3.23: STA of PTB7-Th: ITIC (1:1.3) o-xylene + 2% AA vacuum dried.....	100
Figure 3.24: DMA storage modulus analysis of PTB7-Th:ITIC (1:1.3) processed from CB with and w/o DIO.....	101
Figure 3.25: DMA of PTB7-Th:ITIC (1:1.3) processed from CB with and w/o DIO in high vacuum.....	102
Figure 3.26: DMA of PTB7-Th:ITIC (1:1.3) processed from o-xylene with 2% AA.....	103
Figure 3.27: STA of ITIC crystal in the presence of DIO developed by slow crystallization.....	104
Figure 4.1: Chemical structures of PTNT, o-xylene, and solvent additives used in BHJ blends.....	117
Figure 4.2: Illustration of the steps in the spin-coating of BHJ thin films processed by the solvent additive system.....	122
Figure 4.3: Representation of the effect of solvent additives (DIO) on PSCs.....	122
Figure 4.4: Polymer solar cell architecture used in this study.....	125
Figure 4.5: Energy level diagram of the constructed polymer solar cell.....	126

Figure 4.6: J-V characteristics of devices optimized using MN and PN additives in different donor-acceptor ratios.....	128
Figure 4.7: J-V characteristics of devices optimized using MN and PN additives in different film thicknesses.....	129
Figure 4.8: Photovoltaic devices with and without solvent additives: (a) Representative current density-voltage curves; (b) EQE versus wavelength.....	131
Figure 4.9: Normalized PL emission spectra of active layers from PTNT:PC <sub>71</sub> BM blends using different solvent additives (corrected and normalized to film thickness).....	133
Figure 4.10: AFM images (5 μm x 5 μm) showing the surface topography of PTNT:PC <sub>71</sub> BM (2:3) blend from o-xylene with different solvent additives at RT. The scale bar is 500 nm...	134
Figure 5.1: Slot-die coating (R2R coating).....	148
Figure 5.2: Mini-roll coater (FOM Technologies).....	149
Figure 5.3: Flexible PSC device architecture.....	150
Figure 5.4: Mini roll coater (MRC) FOM Technologies and the main control units.....	151
Figure 5.5: Schematic diagram of the meniscus formed during the slot-die coating process and MRC slot-die coating head (13 mm).....	153
Figure 5.6: MRC Programmable syringe pump and process of film coating.....	153
Figure 5.7: Printed PTNT:PC <sub>71</sub> BM device geometry schematic and complete device photo.....	155
Figure 5.8: Strips of slot-die coated thin films and the complete device solar simulation characterization under light.....	156
Figure 5.9: Appearance of chatter defects during slot-die coating.....	157
Figure 5.10: Appearance of ribbing defects during slot-die coating.....	158
Figure 5.11: Appearance of neck-in defects during slot-die coating.....	159
Figure 5.12: Slot-die head adjustable components for defect free coating process.....	160

Figure 5.13: Appearance of edge defects during slot-die coating.....	161
Figure 5.14: Appearance of streak defects during slot-die coating.....	162
Figure 5.15: Appearance of bubble defects during slot-die coating.....	162
Figure 5.16: FOM Mini-roll coater used for printing of polymer solar cells.....	179
Figure 5.17: PTNT structure and the printed strips of photoactive layer using MRC.....	180
Figure 5.18: Printed complete polymer solar cell device.....	180
Figure 5.19: AFM Topography height images of printed solar cell device (o-xy + 2% AA).....	189
Figure 5.20: AFM height images of printed solar cell device (o-xy + 2% MN).....	190
Figure 5.21: AFM height images of printed solar cell device (o-xy + 0.5% MN).....	190
Figure 5.22: AFM height images of printed solar cell device (o-xy + 4% AA).....	191
Figure 5.23: AFM height images of printed solar cell device (Fast print).....	192
Figure 5.24: AFM height images of printed solar cell device (Slow print).....	193
Figure A.1: J-V graph of devices annealed vs as-cast.....	205
Figure A.2: J-V graphs of devices -thickness optimization.....	205
Figure A.3: J-V graphs of devices – DIO concentration optimization.....	206
Figure A.4: J-V graphs of devices – PN performance and concentration optimization.....	206
Figure A.5: J-V graphs of devices - DIO performance after drying under high vacuum overnight.....	207
Figure A.6: J-V graphs of devices – DIO comparison using eco-friendly main solvent o-xylene.....	207
Figure A.7: J-V graphs of devices – MN additive comparison using CB main solvent.....	208
Figure A.8: J-V graphs of devices 0.3% DIO and MN additive comparison using o-xylene.....	209
Figure A.9: J-V graphs of devices – CB main solvent + 2% AA additive comparison.....	210

Figure A.10: J-V graphs of devices – CB main solvent + 2% AA high vacuum drying treatment comparison.....	210
Figure B.1: STA of PTB7-Th: ITIC (1:1.3) CB + 0.6% DIO – 130 °C annealed.....	211
Figure B.2: STA of PTB7-Th: ITIC (1:1.3) CB + 0.6% DIO – vacuum oven dried.....	211
Figure B.3: STA of PTB7-Th: ITIC (1:1.3) CB + 0.6% DIO – high vacuum dried.....	212
Figure C.1: DMA of PTB7-Th: ITIC (1:1.3) CB vacuum oven dried.....	213
Figure C.2: DMA of PTB7-Th: ITIC (1:1.3) CB high vacuum dried.....	213
Figure C.3: DMA of PTB7-Th: ITIC (1:1.3) CB annealed.....	214
Figure C.4: DMA of PTB7-Th: ITIC (1:1.3) CB +0.6% DIO vacuum oven dried.....	214
Figure C.5: DMA of PTB7-Th: ITIC (1:1.3) CB +0.6% DIO high vacuum dried.....	215
Figure C.6: DMA of PTB7-Th: ITIC (1:1.3) CB +0.6% DIO annealed.....	215
Figure C.7: DMA Comparison for CB and CB+DIO samples-vacuum oven.....	216
Figure C.8: DMA Comparison for CB and CB+DIO samples - annealed.....	216

## List of tables

Table 1.1: Chemwatch hazard ratings of o-xylene and various solvent additives.....	12
Table 3.1 Main solvents used in PSC fabrication.....	67
Table 3.2: Photovoltaic properties of PSCs from PTB7-Th:ITIC (1:1.3) (23 mg/mL) with annealed vs as-cast & from PTB7-Th:ITIC (1:1.3) (19.5 mg/mL) with thickness optimization.....	72
Table 3.3: Photovoltaic properties of PSCs from PTB7-Th:ITIC (1:1.3) (23 mg/mL) with PN additive.....	73
Table 3.4: Photovoltaic properties of PSCs from PTB7-Th:ITIC (1:1.3) (23 mg/mL) (2500 rpm) with and w/o DIO additive.....	73
Table 3.5: Photovoltaic properties of PSCs from PTB7-Th:ITIC (1:1.3) (19.5 mg/mL) (2500 rpm) processed with o-xylene with and w/o DIO additive.....	74
Table 3.6: Photovoltaic properties of PSCs from PTB7-Th:ITIC (1:1.3) (23 mg/mL) processed with CB for MN additive optimization via thickness.....	75
Table 3.7: Photovoltaic properties of PSCs from PTB7-Th:ITIC (1:1.3) (19.5 mg/mL) processed with o-xylene for MN additive and 0.3% DIO optimization.....	76
Table 3.8: Photovoltaic properties of PSCs from PTB7-Th:ITIC (1:1.3) (19.5 mg/mL) processed with o-xylene for AA additive and drying optimization.....	77
Table 3.9: Photovoltaic properties of PSCs from PTB7-Th:ITIC (1:1.3) (23 mg/mL) processed with CB for AA additive and drying optimization.....	78
Table 3.10: Photovoltaic properties of PSCs from PTB7-Th:ITIC (1:1.3) (23 mg/mL) processed with CB and DIO additive for drying and thickness optimization.....	78
Table 3.11: Roughness Measurements of devices processed from CB and o-xylene.....	81

Table 3.12: Roughness Measurements of devices processed from CB solvent + DIO additive.....	82
Table 4.1: Various physical properties of solvents and solvent additives used in this study.....	123
Table 4.2: Hazard identification and classifications of the solvents.....	124
Table 4.3: Summary of the photovoltaic performance properties of optimized PTNT:PC <sub>71</sub> BM (2:3) solar cells with mean values and standard deviation from six devices.....	130
Table 4.4: The integrated currents from EQE (IPCE) compared to the Jsc from I-V measurement of corresponding devices.....	132
Table 4.5: Root mean square (rms) value of BHJ films treated by various solvent additives.....	135
Table 5.1: Photovoltaic properties for MJ-A159 (P1) PTNT:PC <sub>71</sub> BM (1:2) 30 mg/mL in o-xylene + 1% MN.....	165
Table 5.2: Photovoltaic properties for MJ-B55 (P2) PTNT:PC <sub>71</sub> BM (1:2) 30 mg/mL in o-xylene + 1% MN.....	166
Table 5.3: Photovoltaic properties for MJ-B67 (P3) PTNT:PC <sub>71</sub> BM (1:2) 30 mg/mL in o-xylene + 1% MN.....	166
Table 5.4: Photovoltaic properties summarized for 3 batches of PTNT.....	167
Table 5.5: Photovoltaic properties for MJ-A159 (P1) PTNT:PC <sub>71</sub> BM (2:3) 25 mg/mL in o-xylene + 2% MN.....	168
Table 5.6: Photovoltaic properties for MJ-A159 (P1) PTNT:PC <sub>71</sub> BM (2:3) 25 mg/mL in o-xylene + 2% MLN.....	168
Table 5.7: Photovoltaic properties for MJ-A159 (P1) PTNT:PC <sub>71</sub> BM (2:3) 25 mg/mL in o-xylene + 3% DIO.....	168

Table 5.8: Photovoltaic properties for MJ-B55 (P2) PTNT:PC <sub>71</sub> BM (2:3) 25 mg/mL in o-xylene + 2% MN.....	169
Table 5.9: Photovoltaic properties for MJ-B55 (P2) PTNT:PC <sub>71</sub> BM (2:3) 25 mg/mL in o-xylene + 2% MLN.....	169
Table 5.10: Photovoltaic properties for MJ-B55 (P2) PTNT:PC <sub>71</sub> BM (2:3) 25 mg/mL in o-xylene + 3% DIO.....	170
Table 5.11: Photovoltaic properties summarized for 2 batches of PTNT with MN, MLN and DIO additives compared (MJ-A159 vs MJ-B55).....	170
Table 5.12: Photovoltaic properties for PTNT:ITIC (2:3) (25 mg/mL) in o-xylene + 3% DIO.....	174
Table 5.13: Photovoltaic properties for PTNT:PC <sub>71</sub> BM 25 mg/mL, o-xylene + 2% MN.....	174
Table 5.14: Photovoltaic properties for PTNT:PC <sub>71</sub> BM 25 mg/mL, o-xylene + 2% AA.....	174
Table 5.15: Photovoltaic properties for PTNT:PC <sub>71</sub> BM 25 mg/mL, o-xylene + 2% MLN...	175
Table 5.16: Photovoltaic properties for PTNT:PC <sub>71</sub> BM 25 mg/mL, o-xylene + 2% AA.....	176
Table 5.17: Photovoltaic properties for PTNT:ITIC:PC <sub>71</sub> BM (1:0.3:1.2) (25 mg/mL) in o-xylene + 3% DIO.....	176
Table 5.18: Photovoltaic properties for PTNT:ITIC (2:3) (25 mg/mL) in o-xylene + 3% DIO.....	177
Table 5.19: Photovoltaic properties summarized for PTNT with MLN, MN, DIO and AA additives compared (MJ-A159).....	177
Table 5.20: Photovoltaic properties summarized for PTNT:PC <sub>71</sub> BM processed from o-xylene and 2% AA additive solvent system in vacuum dried conditions.....	181
Table 5.21: Photovoltaic properties summarized for PTNT:PC <sub>71</sub> BM processed from o-xylene and 2% AA additive solvent system without vacuum drying.....	181
Table 5.22: Photovoltaic properties summarized for PTNT:PC <sub>71</sub> BM processed from o-xylene	

and 0.5% AA additive solvent system with vacuum drying.....	182
Table 5.23: Photovoltaic properties summarized for PTNT:PC <sub>71</sub> BM processed from o-xylene and 2% AA additive solvent system with vacuum drying (in the same experiment batch to compare the results to 2% MN additive performance).....	183
Table 5.24: Photovoltaic properties summarized for PTNT:PC <sub>71</sub> BM processed from o-xylene and 2% MN additive solvent system with vacuum drying (in the same experiment batch to compare the results to 2% AA additive performance).....	183
Table 5.25: Photovoltaic properties summarized for PTNT:PC <sub>71</sub> BM processed from o-xylene and 2% AA additive solvent system with annealing (in the same experiment batch to compare the results to annealed 2% MN additive performance).....	184
Table 5.26: Photovoltaic properties summarized for PTNT:PC <sub>71</sub> BM processed from o-xylene and 2% MN additive solvent system with annealing (in the same experiment batch to compare the results to annealed 2% AA additive performance).....	184
Table 5.27: Photovoltaic properties summarized for PTNT:PC <sub>71</sub> BM processed from o-xylene and 2% AA additive solvent system with annealing (in the same experiment batch to compare the results to annealed 4% AA additive performance).....	185
Table 5.28: Photovoltaic properties summarized for PTNT:PC <sub>71</sub> BM processed from o-xylene and 4% AA additive solvent system with annealing (in the same experiment batch to compare the results to annealed 2% AA additive performance).....	185
Table 5.29: Photovoltaic properties summarized for PTNT:PC <sub>71</sub> BM processed from o-xylene and 2% AA additive solvent system with vacuum drying (lower slot-die head).....	186
Table 5.30: Photovoltaic properties summarized for PTNT:PC <sub>71</sub> BM (25mg/mL) processed from o-xylene and 2% AA additive solvent system with vacuum drying (in the same experiment batch to compare the results to PC <sub>61</sub> BM performance).....	186
Table 5.31: Photovoltaic properties summarized for PTNT:PC <sub>61</sub> BM (30mg/mL) processed	

from o-xylene and 2% AA additive solvent system with vacuum drying (in the same experiment batch to compare the results to PC <sub>71</sub> BM performance).....	187
Table 5.32: Photovoltaic properties summarized for PTNT:PC <sub>71</sub> BM processed from o-xylene and 2% AA additive solvent system with vacuum drying (in the same experiment batch to compare the results to 0.5% MN additive).....	187
Table 5.33: Photovoltaic properties summarized for PTNT:PC <sub>71</sub> BM processed from o-xylene and 0.5% MN additive solvent system with vacuum drying (in the same experiment batch to compare the results to 2% AA additive).....	188
Table 5.34: Roughness measurements of printed devices using different solvent additives and ratios (o-xy + 2% AA).....	188
Table 5.35: Roughness measurements of printed devices using different solvent additives and ratios (o-xy + 2% MN).....	189
Table 5.36: Roughness measurements of printed devices using different solvent additives and ratios (o-xy + 0.5% MN).....	190
Table 5.37: Roughness measurements of printed devices using different solvent additives and ratios (o-xy + 4%AA).....	191
Table 5.38: Roughness measurements of printed devices using different coating speeds (Fast Print).....	192
Table 5.39: Roughness measurements of printed devices using different coating speeds (Slow Print).....	193

## Abbreviations and acronyms

AA	<i>p</i> -anisaldehyde
AFM	Atomic force microscopy
AM 1.5	Air mass 1.5
BE	Binding energy
BHJ	Bulk heterojunction
CB	Chlorobenzene
CN	1-Chloronaphthalene
CT	Charge transfer
D-A	Donor Acceptor
DIO	1,8-diiodooctane
DMTA	Dynamic mechanical thermal analysis
DSC	Differential scanning calorimetry
E <sub>g</sub>	Band gap
ETL	Electron transport layer
EQE	External quantum efficiency
eV	Electron volt
FF	Fill factor
GPC	Gel permeation chromatography
HOMO	Highest occupied molecular orbital
HTL	Hole transport layer
ITO	Indium tin oxide
IPCE	Incident photon to current efficiency
IQE	Internal quantum efficiency
J <sub>sc</sub>	Current density
LUMO	Lowest unoccupied molecular orbital
LiF	Lithium fluoride
MeOH	Methanol
M <sub>n</sub>	Number average molecular weight
M <sub>w</sub>	Weight average molecular weight
MRC	Mini-roll coater
NDI	Naphthalene diimide
NFA	Non-fullerene acceptors
NICISS	Neutral Impact Collision Ion Scattering Spectroscopy
NMR	Nuclear magnetic resonance spectroscopy

OLED	Organic light emitting diode
NP	Nano-particle
OPV	Organic photovoltaic
OSC	Organic solar cell
<i>o</i> -DCB	1,2-dichlorobenzene
PA	Poly(acetylene)
PCE	Power conversion efficiency
PEDOT:PSS	Poly(3,4-ethylenedioxythiophene):poly(styrenesulfonic acid)
P3HT	Poly(3-hexylthiophene)
PC <sub>61</sub> BM	[6,6]-Phenyl-C <sub>61</sub> -butyric acid methyl ester
PC <sub>71</sub> BM	[6,6]-Phenyl-C <sub>71</sub> -butyric acid methyl ester
PL	Photoluminescence
PSC	Polymer solar cell
PV	Photovoltaic
R <sub>s</sub>	Series resistance
R <sub>2R</sub>	Roll-to-roll
R <sub>sh</sub>	Shunt resistance
SC	Spin-coating
STA	Simultaneous thermal analysis
TA	Thermal annealing
TGA	Thermal gravimetric analysis
UV-Vis-NIR	Ultraviolet-visible-near infrared
VA	Vapor annealing
VB	Valence band
V <sub>oc</sub>	Open-circuit voltage
XPS	X-Ray photoelectron spectroscopy
ZnO	ZnO



# **CHAPTER 1**

## **Introduction**

This chapter presents an introduction to the various research conducted in the thesis, and the motivations based on literature and previous experiments.

## 1.1 Climate change impact on energy trends:

Our world is facing the biggest threat yet in the next decades with climate change consequences and environmental harm due to growing human activity which are unavoidable parts of our regular life everywhere in the world.

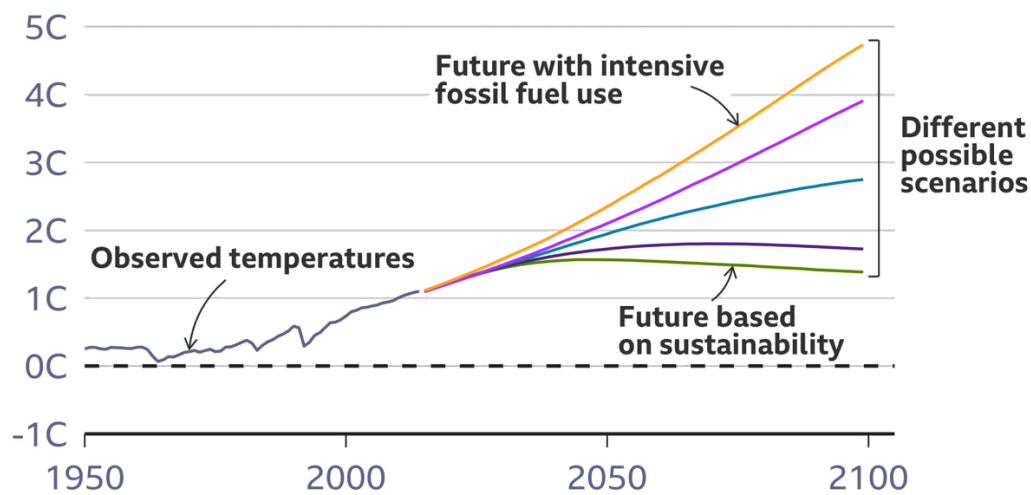
Below are the CO<sub>2</sub> levels that are reported in record levels, and it is about to be too late if we maintain the practice of burning fossil-fuel burning energy resources. If the use of fossil fuel continues at this degree, and humanity expends the reserves over the next few centuries, CO<sub>2</sub> will continue to rise to levels of order of 1500 ppm. The atmosphere would then not return to pre-industrial levels even after tens of thousands of years into the future as given in Figure 1.1.<sup>1</sup>

“This image has been removed due to copyright restriction. Available online from [https://climate.nasa.gov/climate\\_resources/24/graphic-the-relentless-rise-of-carbon-dioxide/](https://climate.nasa.gov/climate_resources/24/graphic-the-relentless-rise-of-carbon-dioxide/)” and credited as Luthi, D., et al. 2008; Etheridge, D.M., et al. 2010; Vostok ice core data/J.R. Petit et al.; NOAA Mauna Loa CO<sub>2</sub> record. Some description adapted from the Scripps CO<sub>2</sub> Program website, Keeling Curve Lessons.

**Figure 1.1:** CO<sub>2</sub> levels over the years.<sup>1</sup>

Understanding the impacts of these recent dramatic increases is important to distinguish and alleviate the causes behind them. The global warming is also on the rise, it will probably reach or exceed 1.5 degrees of warming within just two decades and the last decade on Earth

has been the warmest reported by the recent IPCC climate change assessment.<sup>2</sup> The change in average global temperatures relative to 1850-1900 is shown in Figure 1.2 below with observed temperatures and future simulations.<sup>3</sup>



Note: Each line shows the average temperature rise for a scenario

**Figure 1.2:** IPCC, 2021 Average temperature rise prediction<sup>3</sup>

### 1.1.1 Current energy solutions:

Existing energy resources to avoid climate problems are solar, wind, hydro, and bio energies mainly. Although, they are all very advantageous compared to fossil fuels, there are also some drawbacks to resolve using more advanced and novel energy technologies. The ultimate goal should be to use the cleanest, cheapest and most flexible and versatile energy resource.

For the renewable wind energy, the principle is that the wind power turns the blades of a turbine to generate energy, yet the area needed is much bigger, the portability of energy source is not viable and the manufacturing is expensive. The hydro renewable energy resource is another solution, and it needs flowing water which moves downhill through turbines which

rotate and generate energy. However, the need for water resources and the limited space applicable limits this energy solution, as well. Bioenergy is using natural materials like agricultural waste, algae to produce energy and it is a good source to convert waste and side bio-products into energy. It needs material harvesting and processing facilities and unfortunately it is not sufficient enough yet. <sup>4</sup>

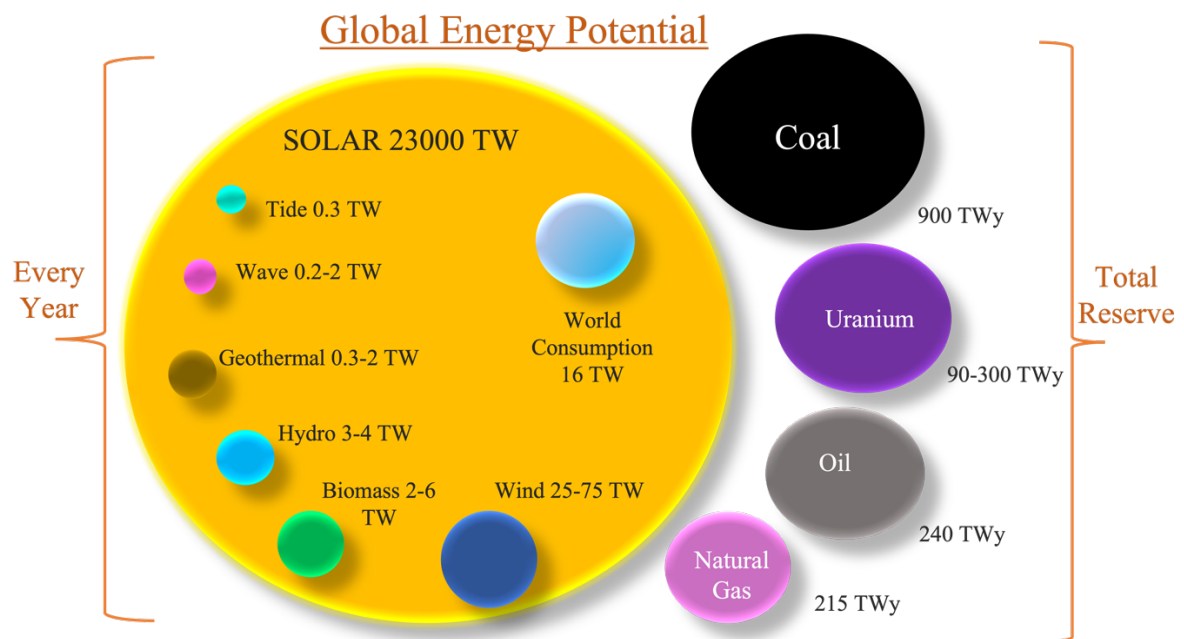


**Figure 1.3:** Global energy potential diagram <sup>5</sup>

Lastly, solar energy is by far the largest energy resource and has been used and harvested as the cleanest energy and has found an extensive usage in industrial and household applications. Above is the global energy potential analyzed where world energy consumption is  $10^4$  less than solar energy absorbed by earth. <sup>5</sup> The applicability of an individual energy resource depends on its cost, weight, efficiency and energy payback time. In the present work, solar energy technologies are investigated through photovoltaics research.

## **1.2 Conjugated polymers:**

Alan J. Heeger, Alan MacDiarmid and Hideki Shirakawa discovered that polyacetylene can conduct electricity after doping with iodine and received Nobel prize in Chemistry. <sup>6</sup> Their research has become the basis of organic photovoltaics using semi-conducting polymers. The delocalization of pi-electrons along the backbone of conjugated polymers with alternating single and double bonds provide semi-conducting materials and the fabrication of organic solar devices began. These polymer structures offer unique potential for modifications.

## **1.3 Inorganic and organic photovoltaics (OPVs):**

Light from the sun is harvested as energy and converted it to electricity through solar panels. The current inorganic silicon based solar panels have installation and transportation costs that are very high due to weight and expensive processing. Their energy payback time is also much longer than that of organic solar cells. <sup>7</sup>

When we look back to the history, the first silicon cells quickly found practice in satellite technologies as it is easier to put lightweight energy devices in space. The cost of the cells also dramatically decreased in 1960s when cheaper Si sources were utilized.

Organic photovoltaics later became the key to solve the existing drawbacks of these inorganic Si solar devices providing unique applications with ongoing promising research. They are distinctive in terms of their simple, cost effective and potential innovative designs as well as being the possible best candidate for the future energy resource.

In Australia, climate change action is also very critical, and the usage of renewable energy goals must increase rapidly in the near future. The renewable energy potential goals are set to

be doubled by 2030. <sup>8</sup> The solar energy potential of Australia is another advantage as given in Figure 1.4, and the rooftop solar panels are already providing good evidence in terms of their extensive use and benefits. <sup>9</sup>

“This image has been removed due to copyright restriction. Available online from <https://reneweconomy.com.au/north-australias-electrifying-future-powering-asia-with-renewables-80382/>”

**Figure 1.4** Sunlight and solar energy potential in Australia. <sup>9</sup>

#### **1.4 Polymer solar cells (PSCs):**

Polymers have been found to provide solution processable semi-conductive materials and became a popular research topic for the most novel solar energy technologies. Their semi-conductivity characteristics and wide range of light absorption are vital to convert energy. The adjustable energy levels also provide a large range of potential materials to be synthesized and engineered both for donor and acceptor polymers. In particular, copolymers having an electron rich and electron deficient unit, became very popular for OSC research and through side chain engineering and fluorination strategies they have the effect of intra-molecular push-pull

electronics which make them capable for solar energy harvesting and conversion into electricity. The optimal molecular configuration, molecular stacking, crystallinity, the band gap parameters, and their eco-friendly solvent processability and lightweight will potentially make polymer solar cells globally the most self-sustainable energy resource in future.<sup>10</sup>

## **1.5 Working principle of organic solar cells:**

A solar cell converts light into electricity. For instance, using ITO coated glass substrate as anode meets the demand of having a transmissive electrode to permit for light to pass through to the photo-active layer. In brief, the energy conversion process has four essential steps in the frequently accepted mechanism. First of all, the absorption of photons takes place, and the light is absorbed by the active layer resulting in the formation of excitons, secondly the generated excitons migrate to the interface of the donor and acceptor for the charge separation, thirdly, as they reach the interface, the excitons dissociate into free charges, and finally the charges are transported to the correct electrodes and collected. In the active layer, the donor is normally an organic semiconductor material, and the acceptor could be a polymer, small molecule or a fullerene derivative.<sup>11</sup> As the active layer in the solar cell absorbs a photon, the electron in the HOMO of the donor is excited to the LUMO which holds the negative charge, and the hole is formed in the HOMO due to the absence of the electron. This electron-hole pair is bound to each other by coulomb attraction forces and called exciton. Through the active layer, it reaches the donor-acceptor interface. Additionally, at the donor-acceptor interface, the difference in LUMO levels of the donor and the acceptor needs to be bigger than the exciton binding energy for an efficient exciton dissociation. Once the free charges are collected at the corresponding electrodes, electricity is achieved.<sup>12</sup>

## **1.6 Advantages and challenges of OPV:**

In organic photovoltaics, organic materials such as polymers and small molecules are used in order to convert solar energy into electricity. Compared to conventional inorganic solar cells, they are not yet used to a large extent, mainly because of their comparatively lower efficiency. Yet, they have more important advantages, which are particularly promising for their future use. There is a substantial number of organic materials readily available and their processable capabilities in various methods make them advantageous in terms of low-cost and environmentally friendly manufacturing. Their processability is also cost-efficient for large scale production. They can be used as such thin layers as ~100 nm whereas silicon solar cells are much thicker. This is indeed an important advantage over silicon as typical Si wafers must be 100-300  $\mu\text{m}$  thick to achieve efficient light absorption.<sup>13</sup> Organic solar cells are compatible both with glass and plastic substrates, as well. In addition, most importantly, they are environmentally friendly to use in the roll-to-roll manufacturing unlike expensive silicon counterparts. Such printing techniques have been much improved lately in order to achieve optimal morphology, good interfacial adhesion and longer device lifetimes.

## **1.7 Device structure of OPVs:**

The versatile processability of organic photo-active layers provide different architecture for OPV device fabrications. The basic architecture includes a transparent substrate for light transmittance, a transparent conductive anode, interfacial thin film layer for better charge mobility, a thin photo-active semi-conducting organic layer and a conductive cathode. The organic layer can be designed as single layer, bi-layer or bulk-heterojunction (BHJ) as given below:

### **1.7.1 Single layer OSCs:**

In single layer SCs, the design was simple and homojunction. They have a one layer of light absorbing film sandwiched between electrodes. Since they do not have sufficient charge dissociation throughout the cell, the efficiencies were lower than their counterparts.<sup>14</sup> Hence, more light absorbing layers that can increase charge transport and mobility compared to single layer OSCs are preferable.

### **1.7.2 Bi-layer planar heterojunction OSCs:**

These solar cells have two different semiconducting layers on top of each other. After dissociation of the excitons formed, the free charges travel towards different electrodes and so the recombination is minimized. Yet, they have a limitation in regard to efficiency since they have an insufficient interfacial area of donor and acceptor species where the exciton dissociates and allows charge separation.<sup>15</sup>

### **1.7.3 Bulk heterojunction (BHJ) OSCs:**

In a publication from Heeger et al, the BHJ structure for polymer-fullerene blends was introduced. Later, it was recognized that the domain sizes of donor and acceptor could be further optimized using additives to alter the morphology. They have a large interface provided that the morphology is optimal. Thereby, the BHJ structure has become the dominant architecture for organic solar cells.<sup>16-19</sup>

#### **1.7.4 Ternary blend OSCs:**

These solar cells have more than two materials forming layers for absorbing photons and charge generation which are blended homogeneously in a BHJ structure. The unique combinations and different parameters of ternary blends present opportunities to increase the existing BHJ solar cells' efficiencies with additional charge generation and morphology optimizations.

#### **1.7.5 Conventional and inverted device architectures:**

The main differences between these structures are that in conventional device structures the cathode is on the top, while in inverted structures the cathode is on the substrate. Thus, inverted structure leads to improved stability if the substrate is made of glass and stable cathode materials are used. Conventional devices start to degrade from the top electrode and cause a rapid reduction of the short circuit current density,  $J_{sc}$ . Low work function electrodes like calcium, aluminum used as cathodes are prone to oxidation with oxygen and moisture. Whereas, in an inverted structure, these materials are normally replaced with transparent oxides like Zinc oxide (ZnO) and the rapid degradation of the cell is prevented. Upon exposure to moisture, inverted devices have a tendency to lower the open circuit voltage,  $V_{oc}$ , due to the decrease in the work function of anodic buffer layer (e.g. MoOx).

#### **1.8 Photoactive layer:**

The photo-active layer is the thin layer made of the BHJ blend that absorbs the photons, and where charge dissociation and transfer occur. The device architecture using BHJ design

offers the most beneficial mixing and active layer formation for OPVs and the charge separation upon light exposure is the most significant process which affects the overall performance of solar cell efficiencies.

## **1.9 Band gap:**

The energy band gap ( $E_g$ ) is influenced by many parameters of the polymers such as the pi-electron delocalization, bond length, molecular weight, sidechains and other intra and intermolecular interactions. There are many strategies to achieve the desired band gap for optimal number of photons. Utilising donor and acceptor units, push-pull approach, changing the substitutes, and improving the co-planarity of molecular backbone are among them.<sup>20</sup>

## **1.10 Solubility and molecular weight:**

Solubility of the OPV materials is very important for the device preparation as they are processed from solutions. Insoluble materials cannot be used and may cause defects if they are present in thin active layers. Molecular weight of polymers also needs to be carefully optimized for the best device performance as their effect on solubility and photon absorption can influence the photovoltaic properties.

The common solvents used so far in OPV studies were mainly toxic halogenated ones. Yet, recently the eco-friendly solvents are also becoming good candidates with new studies and optimizations. These solvents along with solvent additives will be discussed in this thesis, as well. The host solvents are the main solvents that the organic materials are dissolved from, and the additives have selective solubilities towards donor or acceptor materials of the active layer. The differences in solubility and boiling points of these solvents present many different options

to obtain the best active layer with stable solar cell performance. There can be trade-offs between efficiency and stabilities, and in this thesis, we are also focusing on the stabilities as even with high efficiencies if a solar cell degrades in long term by the remaining solvents in active layer, the stability of these devices will not be achieved. <sup>21</sup>

## 1.11 Eco-friendly solvent processing:

The eco-friendly and water/alcohol-based solvents have been investigated on many different conjugated polymers and materials for the best stability and efficiency. The discovery of optimal solvent system in OPV devices will also help them to be scalable for large-scale applications. They also provide future self-sustainable energy resources that will eventually solve the climate change problems to a great degree. <sup>22</sup> The Chemwatch hazardous rating of the most popular solvent additives and the non-halogenated *o*-xylene used for the deposition of the active layers are listed below in Table 1.1:

**Table 1.1:** Chemwatch hazard ratings of *o*-xylene and various solvent additives <sup>23</sup>

Solvent	Flammability	Toxicity	Body Contact	Reactivity	Chronic	Hazard Alert Code
<i>o</i> -xylene	2	2	2	1	0	2
1-methoxynaphthalene (MN)	1	1	1	1	2	2
1-phenylnaphthalene (PN)	1	2	1	1	0	2
<i>p</i> -anisaldehyde (AA)	1	2	2	1	0	2
1-chloronaphthalene (CN)	1	2	2	1	0	2
1,8-diiodooctane (DIO)	1	2	2	1	0	2
1-methylnaphthalene (MLN)	1	2	2	1	2	2

\*(0= Minimum 1=Low 2=Moderate 3=High 4=Extreme), Globally Harmonized System of Classification and Labelling of Chemicals (GHS), 2021.

## 1.12 Small molecules:

Organic solar cells also use small molecules as photoactive materials, and their properties differ greatly from polymers. Unlike polymers, small molecules' distinct structures do not provide different molecular weight.

## 1.13 Organic evaporated molecules in OSC:

Another approach for preparing thin films is by evaporating small organic molecules using vacuum thermal evaporation (VTE) at low temperatures. This is one of the methods for the vacuum evaporation technology as it does not need high temperatures up to  $>1000$  °C, like the traditional thermal deposition. Mostly small molecules are suitable to form thin films with the use of physical vapor deposition (PVD). Since organic molecules are particularly sensitive to heat, it is more critical to adjust deposition rate and increment in temperature. The biggest advantage of this method is the controllability of deposition, studies with concentration gradient films are an example. In a study with organic solar cells based on a heterojunction layer involving a low bandgap oligothiophene as the donor and fullerene C<sub>60</sub> as the acceptor, the organic layers were deposited by thermal evaporation in an ultra-high vacuum (UHV) multichambered system with a typical pressure of  $10^{-7}$  mbar. These small molecule OSCs gave PCE of around 3.5%.<sup>24</sup> Another advantage in terms of controllability is its ability to form very thin layers less than 30 nm, however, the quality of films is not sufficient for large area devices and also for slot-die coated devices. With an easily adjustable coating speed, slot-die coating can ensure good control over film thickness.<sup>25</sup> However, these methods are not proper for ultrathin film deposition as the ultra-thin film can disintegrate during liquid transfer from the flowing solution or form unevenly on the substrate. Initial studies using evaporated organic

molecules started in 1980s and later tested more through characterizations of additional parameters such as substrates, surface area, crystallinity of thin film, and electrical characterization.<sup>26</sup> Also, C<sub>60</sub> and C<sub>70</sub> fullerenes are used in bi-layer OPVs with a hybrid approach where evaporation is used for the acceptor deposition, and spin-coating or other solvent processing techniques are used for the donors. A study showed how specifically evaporated molecules have advantage over spin-casted ones as they provided better thermal stability and vertical phase separation.<sup>27</sup> Yet; the costly steps in evaporating acceptors are still disadvantageous compared to solvent processing.

### 1.14 Fullerene polymer solar cells:

Fullerenes have been extensively used as acceptor materials in photo-active layers in polymer solar cells, where the name of these molecules stem from the structure of buckminsterfullerene. The discovery of fullerenes was done by Sir. Harold W. Kroto, Richard E. Smalley, and Robert F. Curl, Jr., and they were awarded the Nobel Prize in 1996.<sup>28</sup>

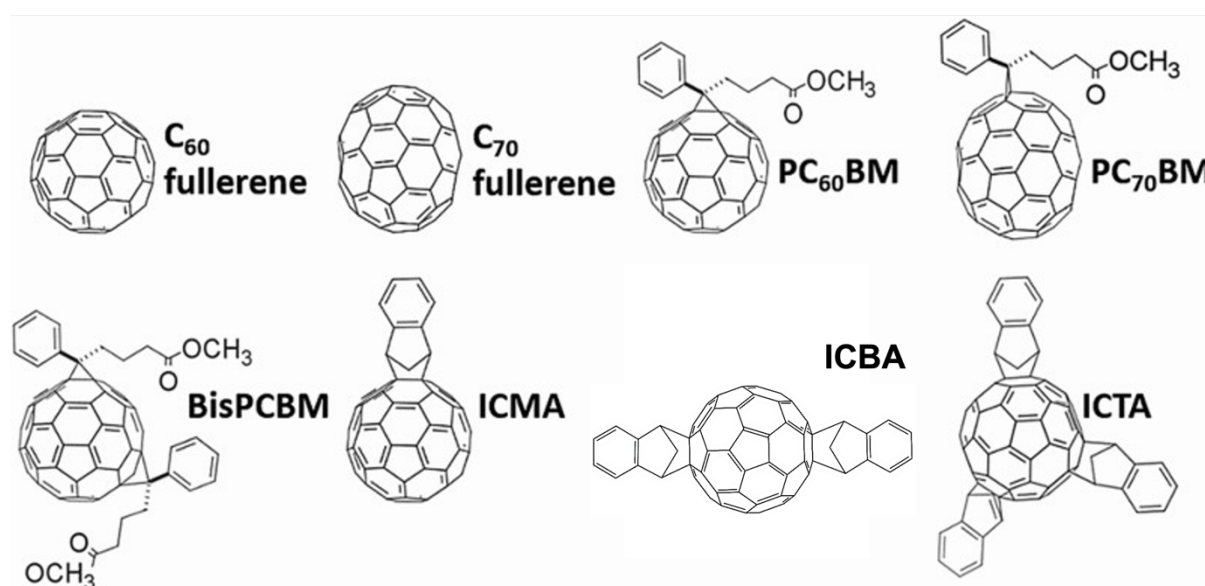


**Figure 1.5:** Structures of common fullerene acceptors.<sup>29</sup>

The most popular derivatives of these compounds are PC<sub>61</sub>BM and PC<sub>71</sub>BM. The others are C<sub>60</sub>, C<sub>70</sub>, bisPC<sub>61</sub>BM, ICMA, and ICBA. The structures of these are given in Figure 1.5.

They provided high electron affinity, ultrafast charge transfer capability and good stability. The disadvantages are their high cost, high lying LUMO levels and the low optical absorption. The unwanted phase segregation due to high crystallization with elevated temperatures is also a negative parameter that affects device stability of PSCs.

### **1.15 Donors and fullerene acceptors:**

The nanostructure of BHJ layer is comprised of donor and acceptor materials. The BHJ blends using donor polymers and fullerene acceptors have been the most common formula for efficient photovoltaic performance in the earlier stage. The control and stability of these nanostructures are very challenging; thus, careful material selection and combinations, and morphology optimizations are needed for good charge transport and high performing devices. The history of photon absorbing and charge generating donors started from the discovery of the conjugated polymers and then spanned to an immense number of derivatives with increasing conjugation and different structures of side-groups. P3HT (poly(3-hexylthiophene)) became the 2<sup>nd</sup> generation of donor polymers and extensive research were conducted using P3HT and fullerenes in BHJs.<sup>30</sup> The increasing efficiencies lead to breakthroughs achieved with high performing polymers. The D-A copolymer derivatives' improved pi-pi stacking, stronger and wider absorption, good solubility, increasing thermal stability and suitable crystallinity with PC<sub>71</sub>BM, and have achieved higher efficiencies in a very short time.<sup>31</sup>

## 1.16 Non-fullerene acceptors (NFAs):

Although fullerenes have been used in PSCs by many studies, the challenges in terms of better performance, stability and large-scale commercialization required acceptor materials with better molecular packing, electron mobility, light absorption, and so on. NF acceptors have become solutions to some of these challenges. Since one of the most important electronic properties for photovoltaic device materials is the absorption, especially in the visible region, NFAs compared to fullerene acceptors also provide superiority in terms of light harvesting. The absorption spectra of fullerenes range only from 380-500 nm even for the strong absorbing PC<sub>71</sub>BM. Whereas, different derivatives of ITIC, which are the most commonly used non-fullerene acceptor in many studies, show absorption wavelength range of 500-800 nm<sup>32,33</sup> as given in Figure 1.7. Other NFAs also have differing wide absorption ranges making them very versatile in achieving higher performance with increased photocurrent generation. Moreover, as in the example of ITIC derivatives, using easily tunable electronic properties such as adding substituents on the end-groups and modifying the crystallinity and morphology of NFAs, better cell performances are being achieved.<sup>34</sup> The  $\pi$ -electron rich core and  $\pi$ -electron deficient end capping units are both readily flexible for modification and have the most impact on photovoltaic performance as explained more in detail in Chapter 3.

The modifications of different core and end-capping group led to promising candidates from ITIC families such as IDIC NFAs as shown in Figure 1.6. These structural modifications will continue in the future and support the novel combinations in emergent photovoltaic research.

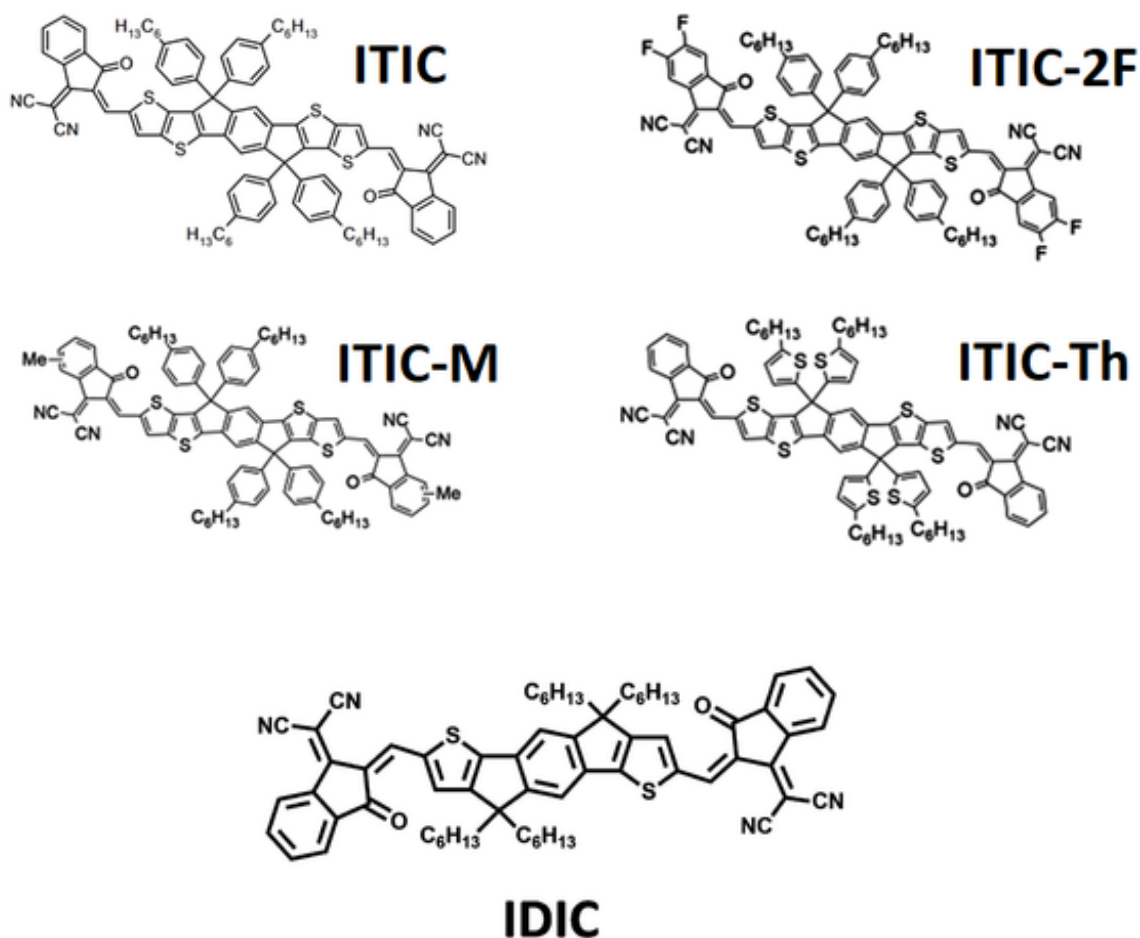


**Figure 1.6:** The structures of NF acceptor ITIC derivatives and IDIC. <sup>34</sup>

NFAs have broader ranges of light absorption and with high specific absorption coefficients the thin films formed with NFAs provide good performing devices in terms of active layer thickness variation with increased packing and uniformity. <sup>33</sup> Even though halogenated derivatives of ITIC has increased absorbance compared to ITIC (Figure 1.7), the extra synthesis steps to increase the materials' costs are not favorable for the large-scale commercial use of OPVs with NFAs. <sup>35</sup>

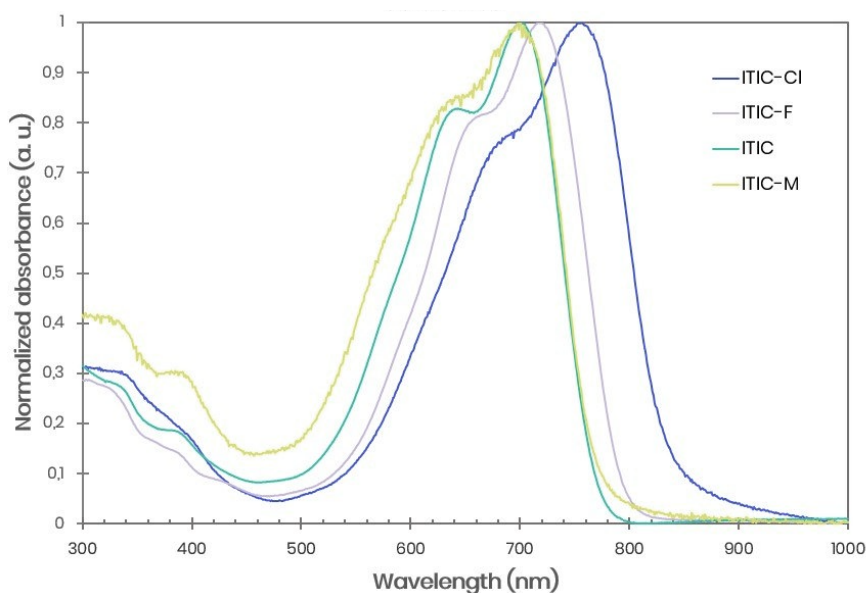


**Figure 1.7:** UV-Vis spectra of thin film cast from chloroform for ITIC derivatives. <sup>32</sup>

Due to the aforementioned properties of ITIC, the photovoltaic studies using ITIC as NFA has also been investigated in detail (Chapter 3) in this thesis.

“This image has been removed due to copyright restriction. Available online from <https://doi.org/10.1016/j.joule.2019.01.004>.”

**Figure 1.8:** Structure of Y6 NFA. <sup>36</sup>

Currently, the most widely studied NFA is Y6, due to its high photovoltaic performances with a few different donor polymers. Y6 is a BTP-4F classed acceptor where the electron deficient benzothiadiazole (BT) core is centered in the molecular structure as shown in Figure 1.8. <sup>36</sup> It is one of the newest NIR absorbing NFAs that was first developed in 2019 and used with a high performing polymer, PM6. This enhancement in harvesting more solar light led to

the era of using low bandgap NF acceptors in PSC studies, boosting efficiencies from 13% to around 18%.<sup>37</sup>

### 1.17 Molecular stacking:

The molecular stacking and aggregation due to intermolecular interactions affecting the crystallinity need to be studied to achieve good performance of polymer solar cells. The cells comprise many different materials where phases need to separate in a well-matched manner to provide crucial charge transport. The aggregation in these materials and non-covalent interactions eventually affect molecular crystallinity. Thus, blend films need to be homogenous in macro-scale and have phase separation in nano-scale for the optimum molecular morphology as depicted in the scheme in Figure 1.9. Ultimately, the crystallinity provides large planar  $\pi$  system and more stable conformation of molecules for efficient charge transport in organic thin films. In the case of low crystallinity, the blends in the thin films have many amorphous regions causing weak aggregation in the system that might result in low charge mobility.

Thus, solvent additives play a key role in altering the molecular aggregation dynamics by changing the acceptor domain size and promoting formation of closely packed fullerene aggregates in fullerene-based devices.<sup>38-40</sup>

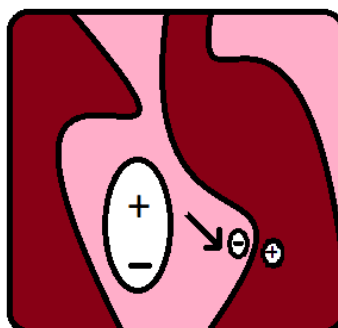


**Figure 1.9:** Charge transport and dissociation in BHJ OSC.

## **1.18 Donor-Acceptor Copolymers and Non-fullerene polymer solar cells (NF PSCs):**

Conjugated polymers being the core of OSC research started the developments of many donor-acceptor (D-A) copolymers and have been used in numerous combinations with fullerene and non-fullerene acceptors. As OSCs are competing with inorganic material based solar cells, particularly in terms of high efficiencies, the latest achievements using the D-A copolymers have become significant. The criteria for these copolymers to perform well are the low band gap, wide light absorption  $\lambda$  range and adjustable energy level and high photon absorption. The donor part is designated as the electron rich unit, and the acceptor part as the electron deficient unit. This opposite charged interactions (intra-molecular push-pull electronic effects), side chain engineering, and fluorination strategies make the D-A copolymer perform well in OSC thin film. <sup>40,41</sup>

## **1.19 Stability of NF PSCs:**

As discussed before, after discovering the well-matched combinations of D-A pairs, the critical parameter to achieve next is the stability. In NFAs such as ITIC molecule, the molecular ordering affect the microstructure of BHJ blends and eventually has an impact on  $J_{sc}$  of the device. Hence, it is very important to shift to non-fullerene PSCs if high efficiencies are aimed. <sup>42</sup> For instance, the 3 derivatives used in a study to test the optimal crystal packing of NFAs and stable morphologies presented IDTT-C6-TIC, IDTT-C8-TIC and IDTT-C10-TIC (9.6%, 13.7% and 12.5%). When the  $\pi$ - $\pi$  stacking decreased, the non-radiative recombination is also reduced below 0.15 V. <sup>39</sup>

Consequently, after a thorough investigation of stability of NF donors and acceptors, it is realized that they can be very good candidates if the crystallinity of the blend films is

controlled. This control could be explained for the blends from the polymer donor perspective with 3 methods.

- Polymer molecular structure
- Post-processing conditions
- Compatibility b/w donor and acceptor.

## 1.20 Morphology:

The methods discussed for controlling crystallinity also affects the blend morphology. Different molecular structures are used to increase the conjugated planar core with side chain engineering and halogenation strategies. The increased conjugation provides more enlarged  $\pi$  electron cloud and wider delocalized  $\pi$  orbitals like PE series of copolymers.<sup>43</sup> Side-chains can improve the solubility and modifies the packing disorder, and halogenation is also critical in increasing the electronegativity in molecules and lowering the energy levels which results in proper molecular aggregation and suitable crystallinity. The crystallinity is therefore a key parameter for describing the good morphology. Crystallization results in over-lapping of  $\pi$ -electron orbitals between molecules. This process also increases the delocalization range of  $\pi$  electrons.

The crystalline properties can be investigated by thermal studies for PSC thin film blends as done in this thesis in next sections in Chapter 3. Using side-chain engineering, thermal properties of polymers can be altered, such as melting point and glass transition behaviour. The  $T_g$  (glass-transition temperature) is also the most crucial parameter for the polymer thermal properties. An example of good thermal stability is ITIC where the growth of nanometer sized acceptor crystals and highly metastable nanostructures offer diffusion-limited crystallization below  $T_g$ , limiting the growth of the large crystals for high performing devices.<sup>44,45</sup>

## 1.21 Treatments for better cell performances:

Other methods to obtain better morphology and suitable crystallinity for blends of PSCs are solvent annealing, thermal annealing, using solvent additives, washing and vacuum drying. Among them, using solvent additives is very popular, and DIO has become a commonly used solvent additive. Most studies have been conducted using DIO that has high boiling point of 167°C and low vapor pressure of 0.04 Pa (25°C) owing to its different solubilities of donor and acceptor materials.<sup>46</sup> Thus, the morphology can be changed greatly. Other alkanedihalide solvent additives are DCIO and DBrO. In a study using PTB7:PC<sub>71</sub>BM and these three solvent additives, the device efficiencies were compared to that of the devices without using solvent additives. Only DBrO and DIO devices worked and gave PCEs of 3.05% and 5.32%, respectively. The reference device's efficiency (without additive) was 1.99%. This study also showed how DIO improved the structural order of the donor in the blend, facilitated PC<sub>71</sub>BM into polymer network, and thus resulted in a finely interpenetrated BHJ morphology<sup>47,48</sup> As the toxic solvents like DIO was later found to be concerning for large-size devices and other applications, environmentally friendly solvent systems have become preferable and will be the key for future high performing OSCs together with NFAs. In this thesis, DIO and its effects on many different devices and alternative green solvents were investigated and other combinations were proposed for large area printed devices in air.

### **1.21.1 Solvent vapor annealing:**

The treatments using solvent vapors are favorable in increasing efficiencies via morphology modification by swelling and re-organizing the blends in the active layer. Solvent vapor annealing is a method for the post-deposition step and is also utilized for NF based OPV. The disadvantages such as reproducibility and scalability however make this treatment not popular among researchers as morphology control is already very difficult to manage. Some studies showed how the crystallinity and phase separation can be altered through solvent vapor annealing to achieve a good photovoltaic performance. The parameters such as duration, temperature and amount of solvent also makes solvent vapor annealing method to be very difficult to standardize.<sup>49</sup> This method is also advantageous for the OSCs that uses spray coating technique for the active layer in both fullerene and non-fullerene systems.<sup>50</sup>

### **1.21.2 Thermal annealing:**

A widely used method for morphology modification is thermal annealing. The optimum temperature for the best performance is critical and depends on the donor-acceptor materials and combinations. Prior to device characterizations, the thermal characterizations can give a good indication of the temperature where the crystallization occurs and how that can affect the OPV performance. The degradation of the device in post-deposition step also makes the method difficult to reproduce without sufficient testing at elevated temperatures for longer durations.<sup>51,52</sup> Studies including materials processed by high-boiling point solvent system can also get benefited from this treatment as the remaining solvents and solvent additives can be removed more efficiently.

### **1.21.3 Solvent additives:**

One of the most popular methods modifying morphology is using solvent additives. Due to the increasing use of environmentally friendly and non-harmful solvents, the use and benefit of solvent additives will grow more in OSC technology in the future, especially in developing and up-scaling printed devices for large area applications and commercialization.<sup>53</sup> In our research, we also focused on using and testing various eco-friendly additives for fullerene and non-fullerene systems in both rigid and flexible solar cells. However, many studies with DIO led to problems such as residual DIO in the film and causing degradation due to photostability issues.<sup>54,55</sup> Low vapor-pressure solvent additives can also act as swelling agents to improve efficiency and the post-treatment effects are solely on the degree of swelling for well-mixed morphologies rather than enhanced selective solubilities.<sup>56</sup>

### **1.21.4 Washing:**

In developing the best performing PSCs, the most crucial challenge is stability. PSCs processed from low-volatile solvents such as DIO have this challenge. Residual solvents and/or solvent additives can be trapped in the photoactive layer and cause degradation over time. Some methods to remove the remaining solvents are drying, annealing and washing with alcohols. Methanol washing for example has been shown to remove these residues to a great extent although more efficient methods are needed for the best stability. In a study that compares different alcohol washing treatments, PTB7:PC<sub>71</sub>BM system has been investigated and all different washing experiments had a positive outcome and improved the device performance.<sup>57</sup>

### **1.21.5 High Vacuum drying:**

As stated before, high vacuum drying is another method to enhance stability of PSCs via removing excess solvent trapped in the device and optimizing the morphology. Phase separations with finer structures are reported in the studies using vacuum drying technique. In this thesis, it is also investigated systematically for the fabrication of PSCs with both non-halogenated and halogenated solvent systems, and is further extended to the printed devices. The usage of high vacuum initiates the re-arrangement of structures without using extra materials or high annealing temperatures and in some cases, it greatly improves photovoltaic performance and stability.<sup>58,59</sup> Hence, it is proposed to be widely used for future stable PSC fabrication.

## **1.22 Other types of photovoltaic solar cells:**

The emerging photovoltaic technologies have numerous advantages that have been discovered rapidly with different types of solar cells, and besides polymer solar cells, the other most popular types are perovskite and dye-sensitized solar cells. The demand for global energy and increasing interest in state-of-the-art technologies will establish a competitive market for all 3 types and their applications.<sup>60</sup>

### **1.22.1 Perovskite solar cells:**

Perovskite materials originally stem from calcium titanium oxide mineral  $\text{CaTiO}_3$  which was discovered in 1839. Later, more materials showed a similar crystallographic arrangement, and the formula of perovskite is simplified as  $\text{ABX}_3$ .<sup>60</sup> A and B are cations of

different sizes and X is anion that links to both. Differing from conventional Si-based solar cells, perovskite solar cells also adapt the thin-film technologies with compatible layers where the photon absorber (perovskite) layer converts energy and transfers charges to electron-hole transport layers. Perovskite solar cells were originally developed from dye-sensitized solar cells. In 2009, Kojima et al. used perovskite as a sensitizer in liquid-based TiO<sub>2</sub> DSSCs and achieved a PCE of 3.2% and 3.8% for devices sensitized with (CH<sub>3</sub>NH<sub>3</sub>)PbBr<sub>3</sub> and (CH<sub>3</sub>NH<sub>3</sub>)PbI<sub>3</sub>, respectively.<sup>62</sup> Device architectures advanced to planar structures where the perovskite material is sandwiched between electron- and hole-transporting layers. Having more components and arrangements, perovskite solar cells need control of many factors. TiO<sub>2</sub> is used in these solar cells as electron transport layer and possess high transparency and suitable band gap. However, in order to obtain the desired phase of TiO<sub>2</sub>, the fabrication process involves very high temperatures which increases the cost and hinders practical production of perovskite solar cells. Studies to replace TiO<sub>2</sub> have been various, and one of the materials are ZnO nanoparticles.<sup>63</sup> Still, these recent studies have challenges for lower device stability and efficiency compared to TiO<sub>2</sub> based devices. Most importantly, perovskite solar cells use environmentally dangerous lead (Pb) which contributes to good optoelectronic properties. These materials therefore make them disadvantageous compared to highly efficient organic solar cells, specifically in flexible large-size solar cell technologies.<sup>64,65</sup>

### **1.22.2 Dye-sensitized solar cells (DSSCs):**

As mentioned, since DSSCs are evolved to be more stable with the development of perovskite solar cell type, the focus of researchers in the field has shifted from DSSCs. Still, they have potential for future development in case the stability issues for commercialization can be overcome. The solid-state electrolyte contributes to the increased stability for DSSCs,

but results in decreased solar cell efficiency. <sup>66</sup> Hence, the tradeoff of these parameters needs to be further investigated, and eco-friendly and cost-effective options may be found to compete with organic solar cells.

### 1.23 Printing polymer solar cells:

Printed photovoltaics is the next sustainable and the most significant trailblazer technology. Until now, electronic devices have been mainly fabricated on substrates like silicon and glass that are rigid and heavy. But with printing technology, we will be able to make thinner, ultra-light weight electronic devices that can be rolled, bended and folded without breaking. In Figure 1.10, the basic architecture of a printed OPV is illustrated.

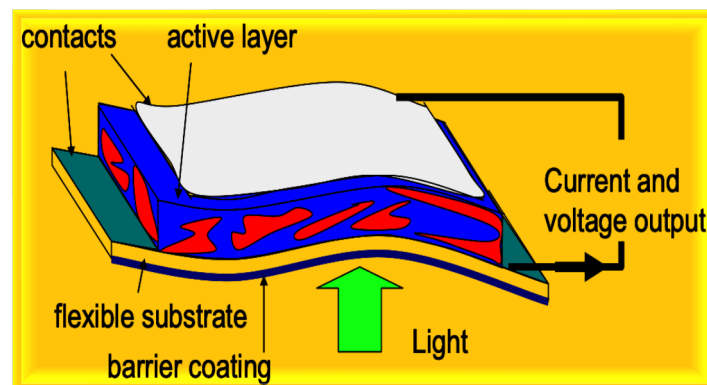


**Figure 1.10:** Flexible organic solar cell construction.

#### 1.23.1 Doctor Blading:

With doctor blading, low amount of solution is used during the formation of films. The solution is placed in front of a blade which is moved across the substrate with a certain and adjustable speed and height in order to form a thin wet film of a desired thickness. This film

can be heated to dry efficiently. PEDOT:PSS layers can be formed using this technique as they are not generally coated in oxygen and moisture free environment. <sup>67</sup>

### 1.23.2 Ink-jet Printing (Non-contact printing):

Ink-jet printing is another relatively new printing method. It is generally preferred in industries owing to its high resolution and film quality. It is applicable to laboratory scale with more compact models. The inks are generally mixtures of several materials in order to achieve the best performance. There are some losses of solution during the film formation due to dripping at the edges, however it is possible to recycle the lost amount of solution. The upscaling of this method for OPV fabrication has also currently been investigated. <sup>68</sup> Schemes of ink-jet printing concept with doctor-blade is given for comparison in Figure 1.11. <sup>69</sup>

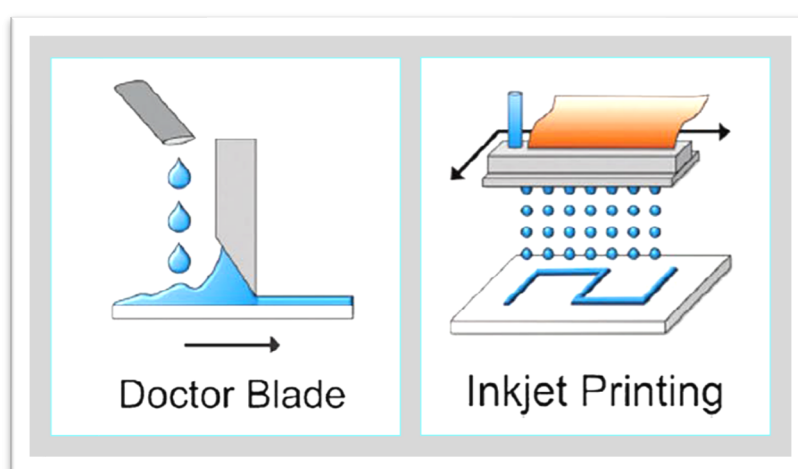


**Figure 1.11:** Doctor blade and ink-jet printing concepts. <sup>69</sup>

### 1.23.3 Slot-die Coating:

Slot-die coating is a non-contact large area processing technique for the deposition of homogeneous wet films. This is a roll-to-roll coating system where many layers can be coated

on top of each other for their use in organic solar cells. It is easy to construct stripes of organic solar cells from a tiny amount of solution. It has many advantages over spin-coating in terms of saving material and time and also layer controllability. This technique provides readily formed layers of thin films which are dried quickly. It is crucial to optimize the speed of the cylinder that holds the plastic substrate in the slot-die system, along with the amount of the solution given to the system through a proper tubing apparatus. One drawback of the system is that they are not as compact as spin-coaters and thus is difficult to place in oxygen and moisture free environment. This technique works very well for viscous solutions at high speeds as well. In previous studies, this technique is used for the coating of ZnO, active layers, PEDOT:PSS, and metal contacts.<sup>70,71</sup> In Chapter 5, this technique is used and tested for eco-friendly solvent systems and final optimization of the devices.

#### **1.23.4 Mini Roll Coater:**

The Mini Roll Coater is a compact slot-die coater and flexographic printing unit for flexible substrates. It is capable of coating without the operator having to touch the coated layers, while mimicking roll-to-roll coating conditions; in the present study, it was used for the printing of polymer solar cells. The mini roll coater also provides easy formation of many thin layers with a proper thickness adjustment and use of small amounts of ink. The instrument forms a meniscus between the slot-die head and the substrate on the cylinder and stripes of the different layers are coated as the cylinders rotates.<sup>72</sup>

The easy handling of these strips and sheets are also very advantageous as they can be cut into different area of solar cells in required shapes. The strips of polymer thin films can be characterized individually via nano-imaging and the post-treatments of the films can be carried

out accordingly. A photo of the printed polymer thin film strips coated using mini roll coater is shown in Figure 1.12.

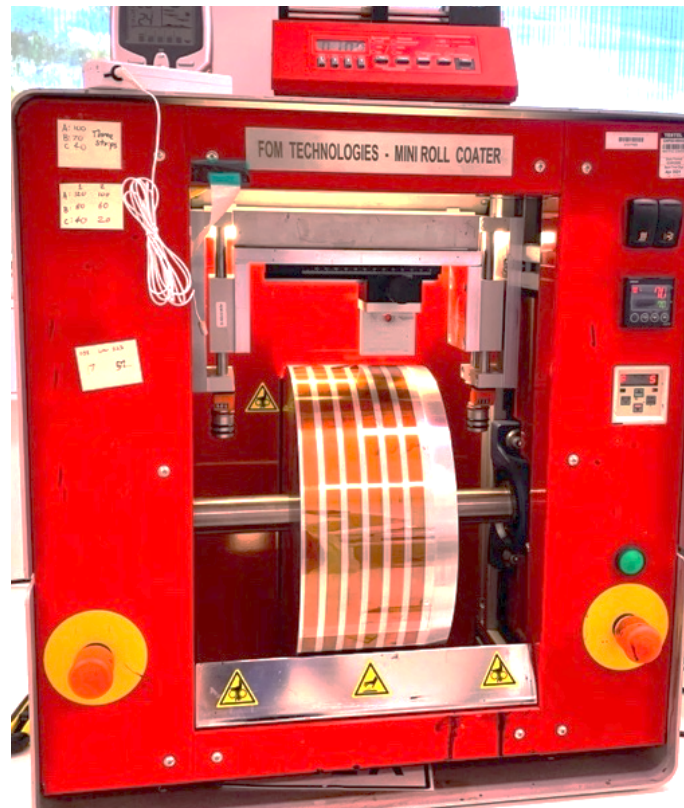


**Figure 1.12:** Strips of organic solar cells via slot-die coating.

## 1.24 Aim:

The main aim of this thesis is to investigate the optimization of eco-friendly polymer solar cells (PSCs) through systematic selection of the processing solvent systems, post-treatments and overcoming stability challenges in order to achieve the best solar cell performance. For this purpose, the polymer solar cell fabrication and characterization have been performed initially using the most conventional materials, and then using their eco-friendly and higher performing alternates. All the methods and processes used are given in Chapter 2 and other methodological processes are given in each research chapter. In Chapter 4, the fullerene-based PSCs have been tested using the novel solvent systems and later for higher stability, cost-effectiveness, and efficiency. NF PSCs have also been studied by carefully avoiding the existing degradation factors reported in the literature and to provide a valuable knowledge for future OSC technology as given in Chapter 3. The photovoltaic properties were analyzed for each factor impacting the solar cell efficiency and stability, furthermore morphology characterizations were carried out on each OPV system investigated. These outcomes give insights into the control of morphology, the selections of the donor-acceptor combination, and significance of using non-halogenated solvent systems, in particular for printed OSCs.

In Chapter 5, for the study of printing PSCs, mini-roll coating method was selected to better understand the basics of morphology variations using BHJ systems with flexible substrates and their interface layer interactions. Some factors are further tested using eco-friendly approach in this method. Through all device fabrication experiments, photo-active layers that are examined in this thesis mostly comprise well-known polymer donor and acceptor materials and will benefit future studies on similar materials and processes.

## 1.25 References:

1. Luthi, D., et al. 2008; Etheridge, D.M., et al. 2010; Vostok ice core data/J.R. Petit et al.; NOAA Mauna Loa CO<sub>2</sub> record. Some description adapted from the Scripps CO<sub>2</sub> Program website, "Keeling Curve Lessons."
2. IPCC, 2018: Summary for Policymakers. In: Global Warming of 1.5°C. An IPCC Special Report on the impacts of global warming of 1.5°C above pre-industrial levels and related global greenhouse gas emission pathways, in the context of strengthening the global response to the threat of climate change, sustainable development, and efforts to eradicate poverty [Masson-Delmotte, V., P. Zhai, H.-O. Pörtner, D. Roberts, J. Skea, P.R. Shukla, A. Pirani, W. Moufouma-Okia, C. Péan, R. Pidcock, S. Connors, J.B.R. Matthews, Y. Chen, X. Zhou, M.I. Gomis, E. Lonnoy, T. Maycock, M. Tignor, and T. Waterfield (eds.)]. World Meteorological Organization, Geneva, Switzerland, 32 pp.
3. IPCC, 2021: Climate Change 2021: The Physical Science Basis. Contribution of Working Group I to the Sixth Assessment Report of the Intergovernmental Panel on Climate Change [Masson-Delmotte, V., P. Zhai, A. Pirani, S.L. Connors, C. Péan, S. Berger, N. Caud, Y. Chen, L. Goldfarb, M.I. Gomis, M. Huang, K. Leitzell, E. Lonnoy, J.B.R. Matthews, T.K. Maycock, T. Waterfield, O. Yelekçi, R. Yu, and B. Zhou (eds.)]. Cambridge University Press.
4. Sayed, E. T., Wilberforce, T., Elsaid, K., Rabaia, M. K. H., Abdelkareem, M. A., Chae, K. J., & Olabi, A. G. (2021). "A critical review on environmental impacts of renewable energy systems and mitigation strategies: Wind, hydro, biomass and geothermal." *Sci Total Environ*, 766, 144505.
5. A fundamental look at energy reserves for the planet, R. Perez, M. Perez, The IEA SHC Newsletter Solar Update, Vol. 62, Nov 2015.
6. Shirakawa, H; Louis, Edwin J.; MacDiarmid, A. G.; Chiang, C. K.; Heeger, A. J. (1977). "Synthesis of electrically conducting organic polymers: Halogen derivatives of polyacetylene, (CH) x". *Journal of the Chemical Society, Chemical Communications* (16): 578.
7. Fraunhofer ISE: Photovoltaics Report, updated: 27 July 2021.
8. Australia's 2030 Emissions Reduction Target, Commonwealth of Australia, 2015.
9. Australia solar energy potential, Andrew Blakers, Australian National University.
10. Hou, W., Y. Xiao, G. Han and J. Y. Lin (2019). "The Applications of Polymers in Solar Cells: A Review." *Polymers* (Basel) 11(1).
11. Chen, L. X. (2019). "Organic Solar Cells: Recent Progress and Challenges." *ACS Energy Letters* 4(10): 2537-2539.

12. Rita Narayan, M. and J. Singh (2013). "Study of the mechanism and rate of exciton dissociation at the donor-acceptor interface in bulk-heterojunction organic solar cells." *Journal of Applied Physics* 114(7).
13. Riede, M., D. Spoltore and K. Leo (2020). "Organic Solar Cells—The Path to Commercial Success." *Advanced Energy Materials* 11(1).
14. Kolesov, V. A., C. Fuentes-Hernandez, W. F. Chou, N. Aizawa, F. A. Larrain, M. Wang, A. Perrotta, S. Choi, S. Graham, G. C. Bazan, T. Q. Nguyen, S. R. Marder and B. Kippelen (2017). "Solution-based electrical doping of semiconducting polymer films over a limited depth." *Nat Mater* 16(4): 474-480.
15. Huang, L., P. Jiang, Y. Zhang, L. Zhang, Z. Yu, Q. He, W. Zhou, L. Tan and Y. Chen (2019). "Unraveling the Morphology in Solution-Processed Pseudo-Bilayer Planar Heterojunction Organic Solar Cells." *ACS Appl Mater Interfaces* 11(29): 26213-26221.
16. Rafique, S., S. M. Abdullah, K. Sulaiman and M. Iwamoto (2018). "Fundamentals of bulk heterojunction organic solar cells: An overview of stability/degradation issues and strategies for improvement." *Renewable and Sustainable Energy Reviews* 84: 43-53.
17. Scharber, M. C. and N. S. Sariciftci (2013). "Efficiency of bulk-heterojunction organic solar cells." *Prog Polym Sci* 38(12): 1929-1940.
18. Huang, Y., E. J. Kramer, A. J. Heeger and G. C. Bazan (2014). "Bulk heterojunction solar cells: morphology and performance relationships." *Chem Rev* 114(14): 7006-7043.
19. Zhang, H., Y. Li, X. Zhang, Y. Zhang and H. Zhou (2020). "Role of interface properties in organic solar cells: from substrate engineering to bulk-heterojunction interfacial morphology." *Materials Chemistry Frontiers* 4(10): 2863-2880.
20. Jiang, Y., C. Cabanetos, M. Allain, P. Liu and J. Roncali (2015). "Manipulation of the band gap and efficiency of a minimalist push-pull molecular donor for organic solar cells." *Journal of Materials Chemistry C* 3(20): 5145-5151.
21. He, Q., W. Sheng, M. Zhang, G. Xu, P. Zhu, H. Zhang, Z. Yao, F. Gao, F. Liu, X. Liao and Y. Chen (2021). "Revealing Morphology Evolution in Highly Efficient Bulk Heterojunction and Pseudo-Planar Heterojunction Solar Cells by Additives Treatment." *Advanced Energy Materials* 11(7).
22. Li, J., Wang, Y., Liang, Z., Qin, J., Ren, M., Tong, J., Xia, Y. (2020). "Non-toxic green food additive enables efficient polymer solar cells through adjusting the phase composition distribution and boosting charge transport." *Journal of Materials Chemistry C*, 8(7), 2483-2490.
23. Chemwatch material safety sheets and hazard ratings (2021).
24. Schulze, K., Uhrich, C., Schüppel, R., Leo, K., Pfeiffer, M., Brier, E., Bäuerle, P. (2006). "Efficient Vacuum-Deposited Organic Solar Cells Based on a New Low-Bandgap Oligothiophene and Fullerene C<sub>60</sub>." *Advanced Materials*, 18(21), 2872-2875.

25. Kyaw, A. K., Lay, L. S., Peng, G. W., Changyun, J., & Jie, Z. (2016). "A nanogroove-guided slot-die coating technique for highly ordered polymer films and high-mobility transistors." *Chem Commun (Camb)*, 52(2), 358-361.
26. Mo, Z.; Lee, K. B.; Moon, Y. B.; Kobayashi, M.; Heeger, A. J.; Wudl, F. (1985). *Macromolecules*, 18, (10), 1972-1977.
27. Faure, M. D. M., & Lessard, B. H. (2021). "Layer-by-layer fabrication of organic photovoltaic devices: material selection and processing conditions." *Journal of Materials Chemistry C*, 9(1), 14-40.
28. Kroto, H., Heath, J., O'Brien, S. et al. (1985). "C<sub>60</sub>: Buckminsterfullerene." *Nature* 318, 162–163.
29. Speller, E. M., (2017). "The significance of fullerene electron acceptors in organic solar cell photo-oxidation", *Materials Science and Technology*, 33:8, 924-933.
30. Zhang, F., Zhuo, Z., Zhang, J., Wang, X., Xu, X., Wang, Z., Wang, Y. (2012). "Influence of PC<sub>60</sub>BM or PC<sub>70</sub>BM as electron acceptor on the performance of polymer solar cells." *Solar Energy Materials and Solar Cells*, 97, 71-77.
31. Fan, R., Huai, Z., Sun, Y., Li, X., Fu, G., Huang, S., Yang, S. (2017). "Enhanced performance of polymer solar cells based on PTB7-Th:PC<sub>71</sub>BM by doping with 1-bromo-4-nitrobenzene." *Journal of Materials Chemistry C*, 5(42), 10985-10990.
32. He, Y., & Li, Y. (2011). "Fullerene derivative acceptors for high performance polymer solar cells." *Phys Chem Chem Phys*, 13(6), 1970-1983.
33. Hou, J., Inganäs, O., Friend, R. H., & Gao, F. (2018). "Organic solar cells based on non-fullerene acceptors." *Nat Mater*, 17(2), 119-128.
34. Cui, Y., Yao, H., Zhang, J., Zhang, T., Wang, Y., Hong, L., Hou, J. (2019). "Over 16% efficiency organic photovoltaic cells enabled by a chlorinated acceptor with increased open-circuit voltages." *Nat Commun*, 10(1), 2515.
35. Du, X., Heumueller, T., Gruber, W., Classen, A., Unruh, T., Li, N., & Brabec, C. J. (2019). "Efficient Polymer Solar Cells Based on Non-fullerene Acceptors with Potential Device Lifetime Approaching 10 Years." *Joule*, 3(1), 215-226.
36. Yuan, J., Zhang, Y., Zhou, L., Zhang, G., Yip, H.-L., Lau, T.-K., Zou, Y. (2019). "Single-Junction Organic Solar Cell with over 15% Efficiency Using Fused-Ring Acceptor with Electron-Deficient Core." *Joule*, 3(4), 1140-1151.
37. Li, C., Zhou, J., Song, J. *et al.* (2021). "Non-fullerene acceptors with branched side chains and improved molecular packing to exceed 18% efficiency in organic solar cells." *Nat Energy* 6, 605–613.

38. Ware, W., Wright, T., Mao, Y., Han, S., Guffie, J., Danilov, E. O., Gautam, B. (2020). "Aggregation Controlled Charge Generation in Fullerene Based Bulk Heterojunction Polymer Solar Cells: Effect of Additive." *Polymers (Basel)*, 13(1).
39. Ye, L., Weng, K., Xu, J., Du, X., Chandrabose, S., Chen, K., Sun, Y. (2020). "Unraveling the influence of non-fullerene acceptor molecular packing on photovoltaic performance of organic solar cells." *Nat Commun*, 11(1), 6005.
40. Qiu, D., Adil, M. A., Lu, K., & Wei, Z. (2020). "The Crystallinity Control of Polymer Donor Materials for High-Performance Organic Solar Cells." *Front Chem*, 8, 603134.
41. Bronstein, H., Nielsen, C.B., Schroeder, B.C. *et al.* (2020) "The role of chemical design in the performance of organic semiconductors." *Nat Rev Chem* 4, 66–77.
42. Zhang, Q., Yuan, X., Feng, Y., Larson, B. W., Su, G. M., Maung Maung, Y., Ma, W. (2020). "Understanding the Interplay of Transport-Morphology-Performance in PBDB-T-Based Polymer Solar Cells." *Solar RRL*, 4(4).
43. Song, J., Hu, Q., Zhang, Q., Xiong, S., Zhao, Z., Ali, J., Liu, F. (2021). "Manipulating the Crystallization Kinetics by Additive Engineering toward High-Efficient Photovoltaic Performance." *Advanced Functional Materials*, 31(14).
44. Yin, J., Zhou, W., Zhang, L., Xie, Y., Yu, Z., Shao, J., Chen, Y. (2017). "Improved Glass Transition Temperature towards Thermal Stability via Thiols Solvent Additive versus DIO in Polymer Solar Cells." *Macromol Rapid Commun*, 38(20).
45. Rahaman, A. B., Giri, D., Sarkar, A., Patra, S. K., & Banerjee, D. (2019). "Effect of thermodynamic glass transition on charge transport properties in a benzodithieno-imidazole  $\pi$ -conjugated polymer: fullerene blend." *Materials Research Express*, 6(11).
46. Wang, Z., Zhang, F., Li, L., An, Q., Wang, J., & Zhang, J. (2014). "The underlying reason of DIO additive on the improvement polymer solar cells performance." *Applied Surface Science*, 305, 221-226.
47. Zhang, Y., Li, X., Xu, D., Meng, F., Hu, R., & Zhao, J. (2019). "Alkanedihalides additives for morphology control of PTB7:PC<sub>71</sub>BM-based polymer solar cells." *Surface and Coatings Technology*, 358, 481-486.
48. Huang, D., Li, Y., Xu, Z., Zhao, S., Zhao, L., & Zhao, J. (2015). "Enhanced performance and morphological evolution of PTB7:PC<sub>71</sub>BM polymer solar cells by using solvent mixtures with different additives." *Phys Chem Chem Phys*, 17(12), 8053-8060.
49. Zomerman, D., Kong, J., McAfee, S. M., Welch, G. C., & Kelly, T. L. (2018). "Control and Characterization of Organic Solar Cell Morphology Through Variable-Pressure Solvent Vapor Annealing." *ACS Applied Energy Materials*. 1(10), 5663–5674.
50. Zhao, H., Wang, L., Wang, Y., Su, W., Lin, D., Cai, W., Hou, L. (2021). "Solvent-Vapor-Annealing-Induced Interfacial Self-Assembly for Simplified One-Step Spraying Organic Solar Cells." *ACS Applied Energy Materials*, 4(7), 7316-7326.

51. Cui, C., & Li, Y. (2021). "Morphology optimization of photoactive layers in organic solar cells." *Aggregate*, 2(2).
52. Zhang, W., Hu, R., Zeng, X., Su, X., Chen, Z., Zou, X., Yartsev, A. (2019). "Effect of Post-Thermal Annealing on the Performance and Charge Photogeneration Dynamics of PffBT4T-2OD/PC<sub>71</sub>BM Solar Cells." *Polymers (Basel)*, 11(3).
53. Li, P., Zhang, Y., Yu, T., Zhang, Q., Masse, J.-P., Yang, Y., Ma, D. (2020). "Unveiling Photovoltaic Performance Enhancement Mechanism of Polymer Solar Cells via Synergistic Effect of Binary Solvent Additives." *Solar RRL*, 4(10).
54. Azeez, A., & Narayan, K. S. (2021). "Dominant Effect of UV-Light-Induced "Burn-in" Degradation in Non-Fullerene Acceptor Based Organic Solar Cells." *The Journal of Physical Chemistry C*, 125(23), 12531-12540.
55. Pearson, A. J., Hopkinson, P. E., Couderc, E., Domanski, K., Abdi-Jalebi, M., & Greenham, N. C. (2016). "Critical light instability in CB/DIO processed PBDTTT-EFT:PC<sub>71</sub>BM organic photovoltaic devices." *Organic Electronics*, 30, 225-236.
56. Fontana, M. T., Kang, H., Yee, P. Y., Fan, Z., Hawks, S. A., Schelhas, L. T., Schwartz, B. J. (2018). "Low-Vapor-Pressure Solvent Additives Function as Polymer Swelling Agents in Bulk Heterojunction Organic Photovoltaics." *The Journal of Physical Chemistry C*, 122(29), 16574-16588.
57. Guo, S., Cao, B., Wang, W., Moulin, J. F., & Muller-Buschbaum, P. (2015). "Effect of alcohol treatment on the performance of PTB7:PC<sub>71</sub>BM bulk heterojunction solar cells." *ACS Appl Mater Interfaces*, 7(8), 4641-4649.
58. Yan, Y., Li, W., Cai, F., Cai, J., Huang, Z., Gurney, R. S., Wang, T. (2018). "Correlating Nanoscale Morphology with Device Performance in Conventional and Inverted PffBT4T-2OD:PC<sub>71</sub>BM Polymer Solar Cells." *ACS Applied Energy Materials*, 1(7), 3505-3512.
59. e, L., Jing, Y., Guo, X., Sun, H., Zhang, S., Zhang, M., . . . Hou, J. (2013). "Remove the Residual Additives toward Enhanced Efficiency with Higher Reproducibility in Polymer Solar Cells." *The Journal of Physical Chemistry C*, 117(29), 14920-14928.
60. Giannouli, M., & Sudhakar, K. (2021). "Current Status of Emerging PV Technologies: A Comparative Study of Dye-Sensitized, Organic, and Perovskite Solar Cells." *International Journal of Photoenergy*, 2021, 1-19.
61. Bhatt, V., Kumar, M., Yadav, P., Kumar, M., & Yun, J.-H. (2018). "Low cost and solution processible sandwiched CH<sub>3</sub>NH<sub>3</sub>PbI<sub>3</sub>-xCl<sub>x</sub> based photodetector." *Materials Research Bulletin*, 99, 79-85.
62. Park, N.-G. (2015). "Perovskite solar cells: an emerging photovoltaic technology." *Materials Today*, 18(2), 65-72.

63. Zhang, P., Wu, J., Zhang, T., Wang, Y., Liu, D., Chen, H., .Li, S. (2018). "Perovskite Solar Cells with ZnO Electron-Transporting Materials." *Adv Mater*, 30(3).
64. Zhang, Q., Hao, F., Li, J., Zhou, Y., Wei, Y., & Lin, H. (2018). "Perovskite solar cells: must lead be replaced - and can it be done?" *Sci Technol Adv Mater*, 19(1), 425-442.
65. Koo, D., Jung, S., Seo, J., Jeong, G., Choi, Y., Lee, J., . . . Park, H. (2020). "Flexible Organic Solar Cells Over 15% Efficiency with Polyimide-Integrated Graphene Electrodes." *Joule*, 4(5), 1021-1034.
66. Kumar, M., & Kumar, S. (2016). "Liquid crystals in photovoltaics: a new generation of organic photovoltaics." *Polymer Journal*, 49(1), 85-111.
67. Schneider, S. A., Gu, K. L., Yan, H., Abdelsamie, M., Bao, Z., & Toney, M. F. (2021). "Controlling Polymer Morphology in Blade-Coated All-Polymer Solar Cells." *Chemistry of Materials*, 33(15), 5951-5961.
68. Bihar, E., Corzo, D., Hidalgo, T. C., Rosas-Villalva, D., Salama, K. N., Inal, S., & Baran, D. (2020). "Fully Inkjet-Printed, Ultrathin and Conformable Organic Photovoltaics as Power Source Based on Cross-Linked PEDOT:PSS Electrodes." *Advanced Materials Technologies*, 5(8).
69. Chilvery, A., Das, S., Guggilla, P., Brantley, C., & Sunda-Meya, A. (2016). "A perspective on the recent progress in solution-processed methods for highly efficient perovskite solar cells." *Sci Technol Adv Mater*, 17(1), 650-658.
70. Andersson, L. M. (2015). "Fully Slot-Die-Coated All-Organic Solar Cells." *Energy Technology*, 3(4), 437-442.
71. Chaturvedi, N., Gasparini, N., Corzo, D., Bertrandie, J., Wehbe, N., Troughton, J., & Baran, D. (2021). "All Slot-Die Coated Non-Fullerene Organic Solar Cells with PCE 11%." *Advanced Functional Materials*, 31(14).
72. Angmo, D., Dam, H. F., Andersen, T. R., Zawacka, N. K., Madsen, M. V., Stubager, J., Krebs, F. C. (2014). "All-Solution-Processed, Ambient Method for ITO-Free, Roll-Coated Tandem Polymer Solar Cells using Solution-Processed Metal Films." *Energy Technology*, 2(7), 651-659.

# **CHAPTER 2**

## **Principles and Research Methodology**

This chapter presents the major technical principles that were applied in experiments and the characterizations, the research methodology used in answering thesis research questions was also given, from fabrication ways to instrument principles.

## 2.1 Introduction:

Major techniques used in this thesis were presented in this chapter, prioritizing the greener methods of polymer solar cell fabrication and focusing on parameters that matters the most for the environmental impact of solar energy generation. The methods are given with the solar cell materials used throughout the experiments carried out. The structures of main polymers were also summarized. Finally, the device preparation and characterization were explained in detail and other characterisations used were examined.

## 2.2 Materials, principles and instruments:

### 2.2.1 Materials:

[6,6]-phenyl-C<sub>61</sub>-butyric acid methyl ester (PC<sub>61</sub>BM) (purity > 99%) and [6,6]-phenyl-C<sub>71</sub>-butyric acid methyl ester (PC<sub>71</sub>BM) (purity > 99%) were purchased from Solenne BV. Poly(2,5-thiophene-alt-4,9-bis(2-hexyldecyl)-4,9-dihydrodithieno[3,2-c:3',2'-h][1,5]naphthyridine-5,10-dione) (PTNT) was synthesized as described in a previous publication.<sup>1</sup> The molecular weight of PTNT was Mn = 55.7 kg/mol and Mw = 163.2 kg/mol relative to polystyrene standards, using an Agilent PL-GPC 220 Integrated High Temperature GPC System with refractive index detectors using 3 × PL gel 10 μm MIXED-B LS, 300 × 7.5 mm<sup>2</sup> columns with 1,2,4-trichlorobenzene at 150 °C as eluent. Other PTNT batches were also synthesized in a similar manner. The molecular weights of all are given in Chapter 5 methodology. The PTNT polymer was blended with PC<sub>71</sub>BM in 2:3 weight ratio in the optimal devices. The solvents CB, *o*-DCB, *o*-xylene, DIO, MN, MLN, PN, CN and AA were all purchased from Sigma Aldrich Co. LLC. and used without further purification. Zinc acetate

dihydrate (99.9%), ethanolamine (99.5%) and 2-methoxyethanol (99.8%) were also purchased from Sigma Aldrich. PTB7-Th ( $M_w > 50000$  (GPC)) and ITIC (>98%) were purchased from Lumtec (Luminescence Technology Corp.) Aluminium (Al), Silver (Ag) and Molybdenum oxide ( $MoO_x$ ) were also purchased from Sigma Aldrich Co. LLC. Patterned ITO (indium tin oxide) glass substrates purchased from Xin Yan Technology Ltd. ( $10 \Omega/sq.$ ) For printed devices, the ZnO NP dispersion was prepared as described in a previously published study.<sup>2</sup> ITO-PET sheets were purchased from Dongguan Hongdian Technology Co. ( $50 \text{ ohm sq}^{-1}$ ) and used via a mini-roll coater (FOM technologies). The ZnO NP layer (35 nm) was deposited using  $0.1 \text{ mL min}^{-1}$  flow-rate, a drum speed of  $1.0 \text{ m min}^{-1}$  and drum temperature at  $70 \text{ }^\circ\text{C}$  to achieve a strip width of around 13 mm. After reaching to stable temperature, the BHJ layer (150–250 nm) was deposited swiftly with an ink of total volume 1 mL with adjustable drum speed and a distinct flow rate (for optimum thickness) at a drum temperature at  $70 \text{ }^\circ\text{C}$  to obtain a strip width of around 13 mm.

### **2.2.2 Photovoltaic effect:**

Alexander Edmond Becquerel found the photovoltaic effect in 1839 where he created the world's first photovoltaic cell. Silver chloride was placed in an acidic solution, and it was illuminated while connected to platinum electrodes, generating voltage and current, hence this effect is also called becquerel effect. Antoine Henri Becquerel also received the Nobel prize in 1903 for this discovery that forms the basis of photovoltaic effect.<sup>3</sup>

While the photoelectric effect includes photons pushing the electrons out of a material completely, in the photovoltaic effect, photons from a light source push electrons only out of their atomic orbitals but keep them in the material; this permits them to flow freely through the material.<sup>4</sup>

### 2.2.3 Photoelectric effect:

In 1887, H. Hertz discovered when light shines on metal, electrons are expelled. Later, A. Einstein received Nobel prize in 1921 for detailed explanation of this phenomenon. The electrons are emitted to open space whereas in photovoltaic effect, the electrons enter a different material. <sup>5</sup>

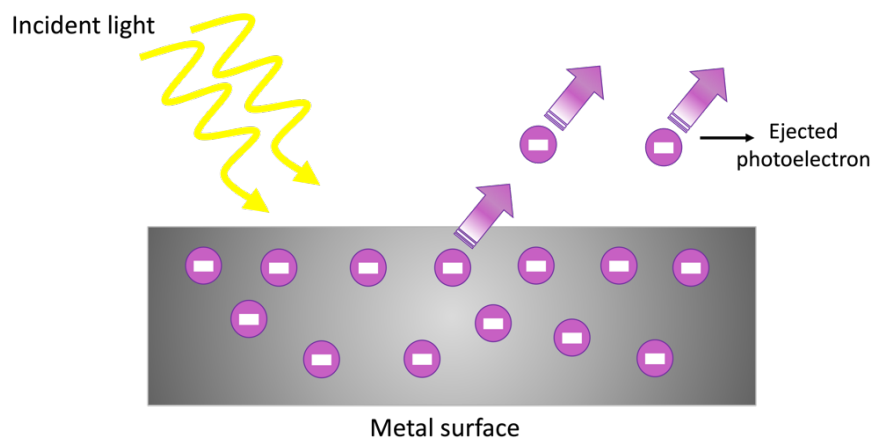


**Figure 2.1** Photoelectric effect.

It has been determined experimentally that when light (photon energy) strikes a metal plate, electrons will be ejected from the metal as depicted in Figure 2.1. The energy does work to remove electrons from metal. The work energy is converted into kinetic energy of the ejected electrons. <sup>6</sup>

### 2.2.4 Comparison of bandgap of metals, semiconductors and insulators:

The difference between conductors, insulators and semiconductors is the accessible energies for electrons in the materials. Instead of having discrete energies as in the case of free

atoms, the available energy states form bands. The conduction process is determined if there are electrons in this conduction band. In insulators the electrons in the valence band are separated by a large gap from the conduction band, in conductors like metals the valence band overlaps the conduction band, and in semiconductors there is a small enough gap between the valence and conduction bands that thermal or other excitations can bridge the gap as shown in Figure 2.2. With such a small gap, the presence of a small percentage of a doping material can increase conductivity dramatically.<sup>7</sup>

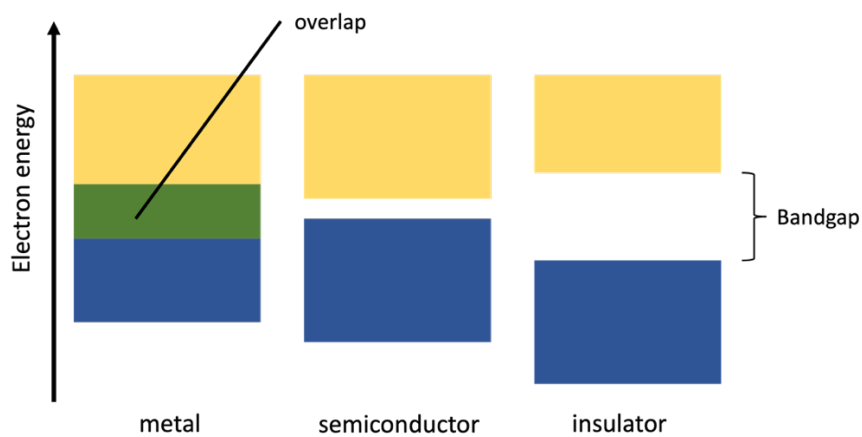


**Figure 2.2** Band diagrams of different materials.

An important parameter in the band theory is the Fermi level, the top of the available electron energy levels at low temperatures. The position of the Fermi level with the relation to the conduction band is a crucial factor in determining electrical properties.<sup>6</sup>

In metals there are certain energy levels for the electron to escape, the energy is in the form of work function.

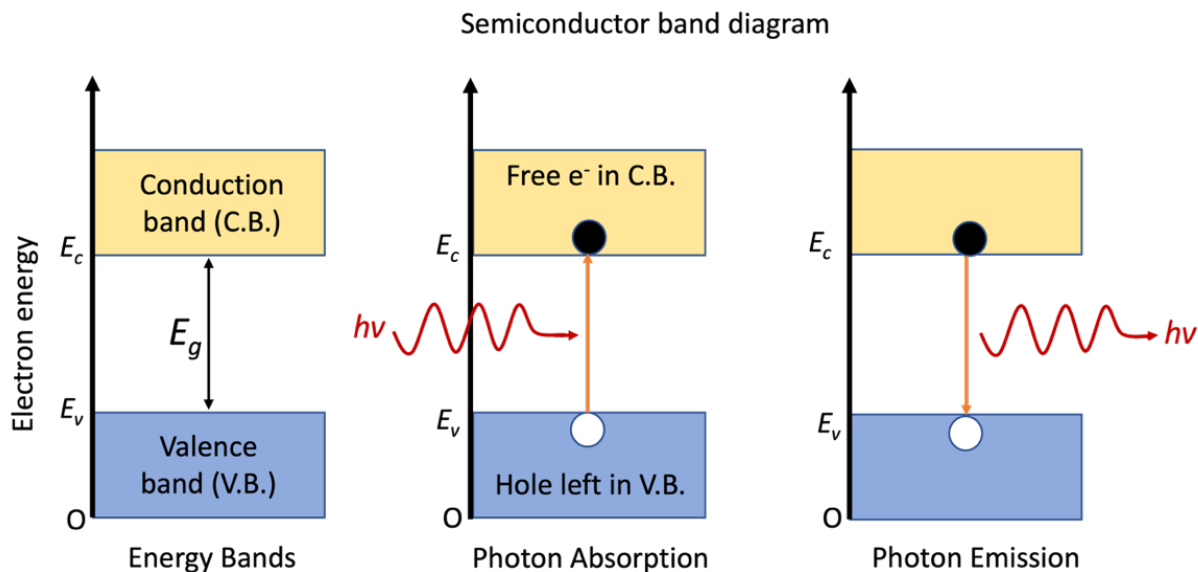


**Figure 2.3** Band diagram of semiconductor material.

In semiconductors like silicon that is used in solar cells, there is a small gap between vacuum and valence band where positive and negative charges are present and through photovoltaic effect principles, they can be used to conduct electricity. The different band diagrams are depicted in Figure 2.3. The parameter for the efficiency of this photovoltaic process is photovoltaic efficiency.

In conjugated polymers, the conductivity is determined by the band gap which is the difference between HOMO and LUMO energy levels. The band structure of the conjugated polymer is through the interaction of the  $\pi$ - orbitals of the repeating units along the polymer chain. An illustration of how this interaction and the conjugation length determines the band gap is given in Figure 2.4:

“This image has been removed due to copyright restriction. Available online from [https://doi.org/10.1016/0038-1098\(79\)91043-3](https://doi.org/10.1016/0038-1098(79)91043-3)”

**Figure 2.4:** Band gap of conjugated polymers and effect of conjugation length. <sup>9</sup>

The increasing  $\pi$ -system (the conjugation length) leads to a decrease for the distance between the energy levels, hence a decrease of the bandgap. It also means as the number of repeating units increase, the HOMO-LUMO bandgap decreases. The HOMO and LUMO energy levels form where the former means, the highest occupied molecular orbital, and the latter is the lowest unoccupied molecular orbital.

Therefore, the parameters that affect the bandgap of a  $\pi$ -conjugated polymer are numerous. Some of them are; molecular weight (Mw), intermolecular interactions, substituents to the main backbone, coplanarity of polymers, dihedral angle, aromatic resonance energy and bond length alternation. <sup>10</sup> For the conjugation length effect, there is a threshold value where aromatic rings are more than 6-10, after that there is a limited decrease of bandgap via Mw. Also, the substituents attached to the main polymer backbone increases Mw.

As mentioned, the parameter for the solar cell performance is the photovoltaic efficiency and there are 2 methods to measure, the first one is power conversion efficiency (PCE) and the other one is incident to photon conversion efficiency (IPCE) or external quantum efficiency (EQE).

## **2.3 Device Fabrication:**

The consistent and methodological fabrication of devices have been applied throughout the thesis and any changes made were noted. As the cell fabrication has many steps that can be affected with minor changes and contamination, several devices were constructed and tested to average the measurements and to remove any mistakes due to human or instrument errors.

Organic solar cells have the challenge of being moisture and O<sub>2</sub> sensitive, also their active layers are sensitive to dust and other particles in air. Therefore, closed and controllable fabrication spaces are required. Glovebox is an enclosed and sealed environment with an inert atmosphere that provides a proper working station for the fabrication of organic solar cells.

### **2.3.1 Glove Box System:**

It consists of several chambers that can be under vacuum or vented easily. A HEPA filter system is used for the capture of contaminants, especially toxic highly volatile solvents. It is very important to seal and dry the chemicals before bringing them into glovebox. Nitrogen and argon can be used to provide an inert atmosphere inside. Trapping and filtering fine particles, dust, fumes, bacteria, and aerosols. Any materials that are transferred into the glovebox are previously dried for several hours and placed in antechambers under vacuum. During fabrication of active layers, the dusts and any other contamination can cause defects in the thin film and can drastically affect the complete device performance.

Therefore, the regular maintenance and disciplined usage of this system is very significant in organic solar cell fabrication. Inert technologies glove box system components also include sensors for pressure, H<sub>2</sub>O and O<sub>2</sub> that needs to be checked to be below 0.1 ppm prior to every experiment and cleaned or replaced when regular maintenance is conducted.

### **2.3.2 Cleaning Substrates:**

The substrates of ITO-glass and ITO-PET were cleaned using suitable solvents and later using UV-light to remove the organic small impurities. This is the most important step of the device fabrication as contaminants could cause defects in thin films and eventually short devices with poor morphology.

### **2.3.3 Spin-coating and Slot-die coating of thin film layers:**

The spin coating for the formation of the thin film layers on ITO-glass substrates were carried out in the glove box for BHJ layers and in ambient atmosphere for ZnO interface layers. Specialty Coating Systems G3P-8 model spin coater was used. The speeds and the amount of material were always adjusted step-by-step for the optimization of uniform films with better morphology. It is very significant to be consistent in spin-coating parameters as the ink amount and the dispersion across the circular path is disadvantageous over slot-die coating system. For some materials, PTFE filters were used to avoid defects in the film. The drying process can also be done via last part of high-speed spin coating and later with other drying techniques. After usage, the chuck and the surroundings of the instrument need to be thoroughly cleaned to avoid contamination and formation of good films.

In slot-die coating experiments, mini-roll coater from FOM Technologies was used. The substrates are ITO-PET as it is the most widely used flexible conductive plastic. It also has heat stability for BHJ formation and drying of the films and very cost-effective. The amount of ink used in this technique is minimum compared to the spin-coating technique as the ink flows from a tubing that has a certain diameter, and the ink flow is controlled via pumping controller. The drum speed and temperature could also be adjusted easily with the right

positions and knobs. The rotation of the drum can be changed with the control panel. The substrate mounting is very easy where high temperature resistant tapes are used for stabilizing the substrate in drum-roll. The most important step is the adjustment of the slot-die head and the height as it has immense effect on film formation as discussed in Chapter 5 of this thesis. Strips of thin film layers can be formed easily with this technique layer by layer in a more controlled way than spin coating and the flexible polymer solar cells are fabricated less effortlessly. The parameters for the final films were explained later in detail as well in flexible device experimentation further in the thesis. The cleaning of the slot-die head and the tubings and other compartments need to be done regularly and quickly in multiple sets of experiments. Later strips were cut into pieces that will fit to the mask of the metal evaporation for the completion of the final solar cell device.

### **2.3.4 Thermal evaporation of electrodes:**

The coating and metal deposition systems can be in glovebox systems as well. They are paired with vacuum and turbo pumps. In evacuation chamber, the vacuum pressure can go down up to  $10^{-7}$  mbar depending on the duration of the pumping and instrument properties. The evaporator chamber includes different compartments for different materials to be deposited and assigned corresponding sensors and wirings. The thermal evaporation is done using increasing electrical current with Angstrom system and Inficon deposition controller.

## 2.4 Device Characterization:

### 2.4.1 Diode characteristics (I-V curve):

“This image has been removed due to copyright restriction. Available online from <https://www.pveducation.org/pvcdrom/solar-cell-operation/iv-curve>”

**Figure 2.5:** I-V characteristics of a solar cell. <sup>11</sup>

Power is plotted as a function of current and voltage where the maximum power is determined when the solar cell is operated to give the maximum power output. The short-circuit current ( $I_{sc}$ ), the open-circuit voltage ( $V_{oc}$ ), the fill factor (FF) and the efficiency are all parameters determined from the IV curve as plotted in Figure 2.5.  $I_{sc}$  is the maximum current from a solar cell and occurs when the voltage across the device is zero.  $V_{oc}$  is the maximum voltage from a solar cell and occurs when the net current through the device is zero.

So the formula for power conversion efficiency (PCE):  $PCE = \eta = P_{MP}/P_{in}$

$P_{MP}$  = Output max power  $P_{in}$  = Reference lamp (Incoming power  $E$ :  $1000\text{W}/\text{m}^2$  sun energy (AM1.5G standard)).

$$PCE = I_{sc} \times V_{oc} \times FF / P_{in}$$

Also, in the I-V curve, the point  $J_{max}$  and  $V_{max}$  shows the maximum power and as the curve becomes more rectangular, the power gets higher. Thus, the ratio of the  $V_{oc} \times I_{sc}$  and  $V_{max} \times I_{max}$  defines the squareness the efficiency of the solar cell. This squareness is defined as Fill Factor (FF). It can have a maximum value of 1 in the most theoretical case when the shunt resistance ( $R_{sh}$ ) of the device is high and the series resistance ( $R_s$ ) of the device is zero.  $R_s$  increases when there are traps to decrease the amount of charge carriers. <sup>12</sup> In summary, fill

factor is determined by diode characteristic and series resistance, short circuit current increases as the bandgap decreases, and determined by absorption, reflection and recombination of charges, finally open-circuit voltage increases as the bandgap increases and it is determined by recombination for a given material bandgap. In organic solar cells,  $V_{oc}$  mainly depends on the energy gap between HOMO level of the donor component and LUMO level of the acceptor component of the BHJ.  $V_{oc}$  also depends on the mobility of free charge carriers, electrode work functions, light intensity and energy traps in the active area causing poor charge transport (the amount of energetic disorder).<sup>13</sup> The open circuit voltage can be affected by the fabrication process since the lifetime of the charge carriers decrease with an increasing amount of defects and contaminations, something which can easily occur in the production step. The thickness of the active layer is also one of the parameters that affect the device performance through altering the Fill Factor. As the thickness of the layer drops severely, the thin layer results in shorting and inefficient device performance. The optimum thickness needs to provide high  $J_{sc}$  which means the mobility of the charges needs to be high for efficient charge transfer.<sup>14</sup> As shown in Figure 2.6, The I-V characterization of each solar cell was carried out using a light source of Xenon lamp and a Keithley power source, then the data were averaged from multiple solar cell measurements in experiments. Dark I-V data were also taken for each experiment.

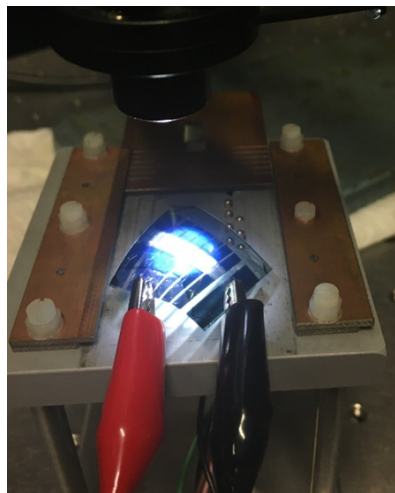


**Figure 2.6:** I-V Measurement of a flexible solar cell.

## 2.4.2 IPCE Characteristics:

In IPCE measurements, the incident photon to current ratio is determined for best performing cells and EQE curve is plotted. The same light source used together with a monochromator in a dark room. The experimental IPCE data was compared with the current from the corresponding I-V data for accuracy, our experiment setup is given in Figure 2.8.

“This image has been removed due to copyright restriction. Available online from <https://www.ijser.org/onlineResearchPaperViewer.aspx?Computer-Simulation-and-Characterization-of-Solar-Energy-and-Photovoltaic-Cells.pdf>”

**Figure 2.7:** EQE efficiency curve depiction of a solar cell. <sup>15</sup>

The external quantum efficiency (EQE) is the current obtained outside the device per incoming photon in the IPCE measurements. EQE is mainly the ratio between the number of collected carriers and the amount of all incident photons shined on the device active area at a given wavelength. The EQE efficiency spectrum is given in Figure 2.7 across wavelength as the external quantum efficiency depends on both the absorption of light and the collection of charges. Therefore, the bandgap and absorbance of material is directly related to IPCE.

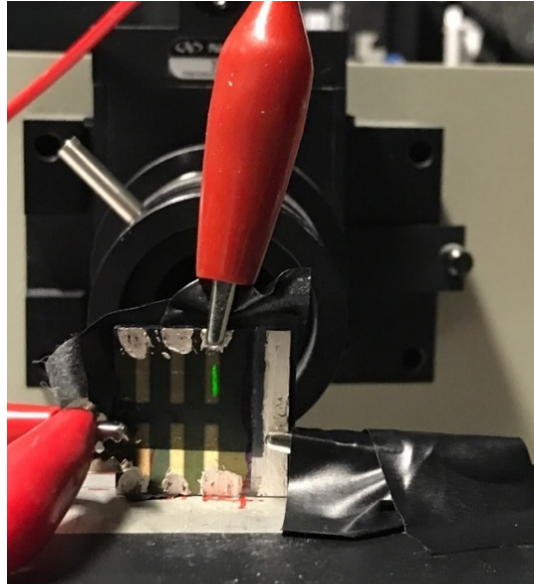


**Figure 2.8:** IPCE Measurement setup of a solar cell.

## **2.5 Neutral Impact Collision Ion Scattering Spectroscopy (NICISS):**

Ion scattering spectroscopy (ISS) is a surface characterization technique to obtain structural and compositional characteristics about the near-surface region of matter. NICISS obtains this information from the interaction of projectiles with the target such as charge transfer process, elastic and inelastic kinetic energy transfer, backscattering from target atoms, sputtering of atoms.<sup>16</sup> Since the development of ISS by Smith in 1967, numerous ion scattering techniques were developed with their advantages and disadvantages relevant to the choice of investigation. Few of those ion scattering techniques currently in use to explore crystalline and non-crystalline matter are; Low energy ion scattering spectroscopy (LEISS), Impact collision ion scattering spectroscopy (ICISS), Rutherford backscattering spectroscopy (RBS) & Neutral impact collision ion scattering spectroscopy (NICISS). Niehus and Comsa developed Neutral impact collision ion scattering spectroscopy (NICISS), and later Andersson and Morgner modified it to study soft matters. Our NICISS is custom built in collaboration with SPECS.

NICISS technique obtain concentration depth profile information for soft matters (liquid surfaces, polymers, foam films) and crystalline surfaces. It is advantageous in characterizing lighter elements and specifying certain elements with average thickness of around 30 nm at depth resolution of few Angstrom ( $\text{\AA}$ ).<sup>17</sup>

The NICISS data is represented as a spectrum peaks and steps corresponding to the different elements in the matter. This spectrum is a combination of the following main constituents, photon peak appears as ion beam first where  $\text{He}^+$  interactions occur at the sample surface, which becomes the starting point for the spectrum. Elemental steps are the backscattered projectiles of an element present and revealed at the TOF detector specific to the individual elements. NICISS spectrum is converted into a depth scale from the TOF scale, which is non-linearly related to energy loss. As a result, the elements can be analysed at the near surface and composition of surface can also be determined depending on the goal of the experiment.<sup>18</sup>

## **2.6 X-ray photoelectron spectroscopy (XPS):**

X-rays are highly energetic compared to optical light and they can breach through solid materials. Some X-rays do not breach due to the interaction with the material and thus causes an absorption contrast. This depends on the electron density and the electron energy levels that are available. Low energy X-rays excite core electrons to HOMO levels or higher states. These states are specific to the molecules' absorption profile, this method can be used to characterize thin films of OPV materials. As the ordered molecules in OPVs depend on the crystallinity features of thin films, the X-ray studies not only helps to make compositional maps but also to investigate the packing and charge transport analysis. In the end, it could be used to support device photovoltaic characterizations.<sup>19</sup>

The working principle is also shown below in Figure 2.9 where how from basic photoelectric effect the technology is developed and made use of in measuring different regions on the surface of the matter.

The XPS setup used in our experiments are also custom built in collaboration with SPECS.

“This image has been removed due to copyright restriction. Available online from <https://www.novami.com/nova-technology/x-ray-photospectroscopy-xps/>”

**Figure 2.9:** X-ray photoelectron spectroscopy working principle. <sup>20</sup>

## **2.7 Single-crystal X-ray diffraction (XRD) and X-ray powder diffraction (PXRD):**

X-ray diffraction is based on constructive interference of monochromatic x-rays and a crystalline sample. The interaction of incident rays with the sample produces constructive interference where Bragg's law is satisfied. <sup>21</sup>

In OPV studies, materials are semi-crystalline and amorphous in general, thus the thin film of organic layers are difficult to use for crystalline property detection which is also a limitation for this technique. Therefore, in order to gain better understanding of the crystalline features, X-ray powder diffraction can be used for materials that are unable or difficult to be grown as single crystals of appropriate size and quality. Although this method is very challenging to use for the determination of structure, especially for organic materials; in the present thesis, it gives

an insight for the determination of different interaction of molecules with crystalline features. There are also theoretical comparison methods for powder XRD to determine the structure of organic materials called direct-space strategy where trial structures are generated in direct space, independently of experimental powder XRD data. Indeed, the crystal structures of several oligopeptides have been determined from powder XRD data using the direct-space strategy for structure solution as studied by Tedesco et al.<sup>22</sup> A comparison of experimental schemes of single-crystal X-Ray diffraction and Powder X-ray diffraction are illustrated below in Figure 2.10:

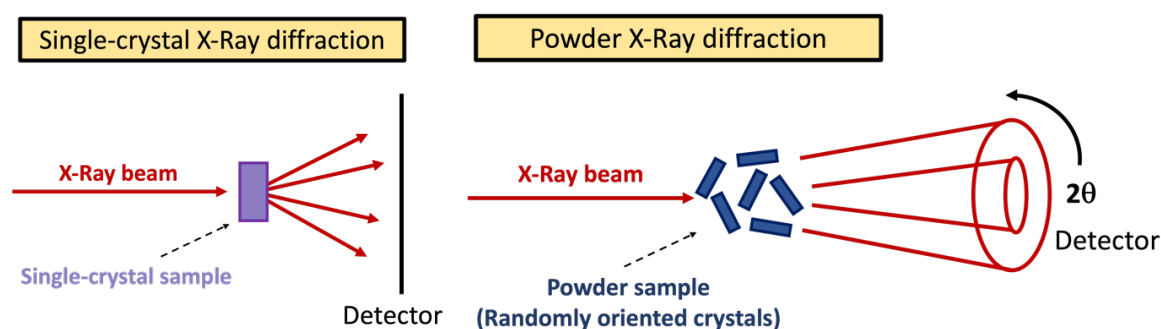


**Figure 2.10:** Schematic diagram of X-ray powder diffraction method.

In order to keep the X-ray beam focused, the crystalline sample rotates, the detector moves in a circle around the sample, and its position is recorded as the angle is  $2\theta$ . The detector then records the number of X-rays observed at each angle  $2\theta$ .<sup>23</sup> The diffraction data in the case of the powder XRD measurement gives a one dimension overlapped XRD data, whereas single-crystal XRD diffraction data is three-dimensional and easier to analyze. The overlapped X-ray intensity is recorded as counts as shown in a powder XRD spectra and an example spectra with XRD peaks for individual elemental determination is given in Figure 2.11.

“This image has been removed due to copyright restriction. Available online from <https://www.wiley.com/enus/X+Ray+Diffraction+Procedures%3A+For+Polycrystalline+and+Amorphous+Materials%2C+2nd+Edition-p-9780471493693>”

**Figure 2.11:** XRD spectrum representation (Intensity versus diffraction angle  $2\theta$ ).<sup>24</sup>

The powder is constituted by large collection of crystallites with arbitrary scattering of crystallite orientations giving a peak overlap in 1-dimension. The density of peaks increases at higher  $2\theta$  values as intensity decreases.<sup>25</sup> In the present thesis, Bruker D8 Advance Powder X-Ray diffractometer was used and the experimental grazing incidence diffraction data from the thin film samples of organic material are analyzed qualitatively and compared to the reference patterns to determine what phases are present. The reference patterns were shown with lines, and the position and intensity of these lines were matched for the identification of unknown materials by searching existing databases. Minor mismatch in peak positions and intensities were ignored as experimental error.

## **2.8 Atomic Force Microscopy (AFM):**

AFM instruments operate with the principle of surface sensing using an extremely sharp tip on a micromachined silicon probe. This tip is used to image samples by scanning across the surface line by line, and this process of scanning can vary depending on different operating modes. These modes are contact mode and tapping mode. The fundamental principle of AFM stems from the nanoscale tip attaching to the small cantilever which forms a spring. As this tip contacts to the surface, the cantilever bends and this bending is detected using a laser diode

and a photodetector. <sup>26</sup> Thus, tip-sample interaction is determined using the characteristics of the bending.

In contact mode, the tip is pressed into the surface and the interaction force is screened through electronic feedback loop in order to keep the deflection constant during the scanning. In the tapping mode, the contact between tip and sample is omitted and they are both protected from possible damage. The cantilever is vibrated near its resonance frequency and the tip subsequently moves up and down with a sinusoidal motion. This motion is affected by the sample surface properties and with the attractive and repulsive interactions, and by keeping the amplitude of the tapping mode constant (the energy applied to the cantilever), the topography of the sample is scanned line by line. <sup>27</sup> A Bruker AFM instrument in tapping mode was used for the topography measurements of thin films of solar cells and the image analysis is done via Nanoscope software for the comparison of performance of solar cells. A working principle diagram of these measurement processes are given below in Figure 2.12.

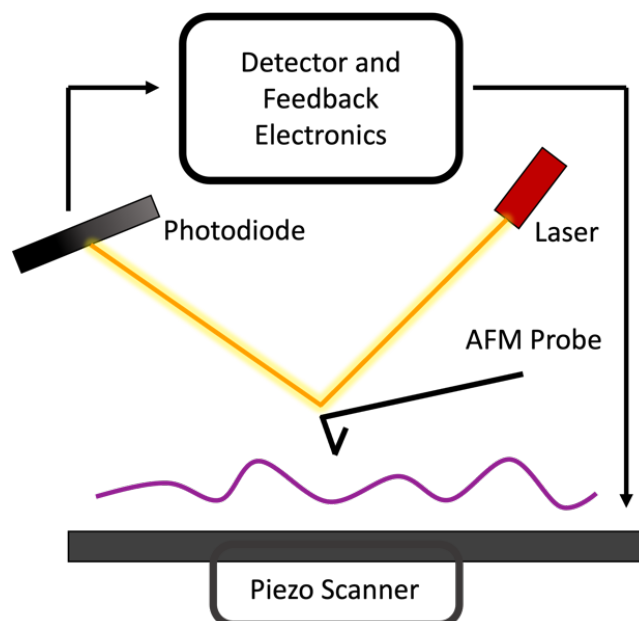


**Figure 2.12:** AFM working principle scheme.

## **2.9 High Temperature Gel Permeation Chromatography (HT-GPC):**

As polymers are composed of repeating units of monomers in a regular and certain number, the molecular weight differs from each batch of conjugated polymers, as well. The GPC measurements were carried out for determining the molecular weight and the distribution of polymer chain molecular weight (PDI).<sup>28</sup> In the present thesis, 1260 Infinity II Model GPC instrument is used at 150°C with 1,2,4-trichlorobenzene. The size and the travel time speeds of the particles that are traveling through an HPLC column (3xPLgel Mixed-B LS, 7.5x300 mm, 10µm) give specific data as compared to that of a reference polystyrene (PS) standard with a known molecular weight and elution time. Mn (number average Mw), Mw (weight average Mw) and the polydispersity index (PDI) were all determined in the end.

## **2.10 Profilometry:**

This method is used for the determination of surface profile, thicknesses of thin film layers of OSCs and film roughness. It is very critical to measure the thickness and apart from the AFM technique, profilometry gives a thorough analysis by tracing the topography of a surface with a probe that is in contact with the sample. The measurements were analysed in a surface step height analysis system; therefore, scratches were used in the active layers to form a difference in heights. The surfaces must be clean for accuracy of the contact profilometry. Measurements were also averaged for minimizing the experimental errors. Veeco Wyko NT9100 optical profilometer model was used in our measurements.

## **2.11 Thermal stability Measurements:**

The thermal properties of the conjugated polymers used in PSCs are very crucial for the performance of the cells.

There are 2 distinct types of states, amorphous and glassy states that determines the thermal properties of materials. In the former, the distribution of polymer chains in the matrix is entirely arbitrary, and at temperatures below the melting point, the molecular motions begin. As this motion increases, the material transforms from a glass state through a rubber-like state till it melts completely. In the glassy state, the material is rigid and brittle as the flow of units of the chains are stationary in a still position.

### **2.11.1 Dynamic mechanical thermal analysis (DMTA):**

In this thesis, DMTA method is used for the thermal characteristics of the polymer materials. Non-destructive methods are appropriate for the determination of thermal physical properties of polymers. It is important to determine these in order to achieve good morphology for the BHJ active layers of cells. The determination of glass transition temperature ( $T_g$ ) can be done in this latest method. The measurement gives many parameters to analyse such as dynamic modulus, storage modulus, loss modulus and  $\tan \delta$ .<sup>29</sup> The sample preparation needs to be done very carefully to form a uniform film with sufficient thickness of material coated on a glass fibre substrate. The polymer solution is drop-casted onto the substrate consecutively and gets dried in air. The fibre needs to have 45° angle strands to achieve good DMTA signal without clamps causing the fibre stretched asymmetrically. The uniform polymer coating is achieved with these multiple steps of coating and the thermal transitions and properties were determined readily.<sup>30</sup> In this thesis, DMTA measurements were done on TA Q800 DMA in strain-controlled mode. The data was interpreted to study thermomechanical properties.

### **2.11.2 TGA-DSC Simultaneous Thermal Analyzer (STA):**

For the investigation of efficient polymer solar cells, the active layers need to show good thermal stabilities, and for this purpose, thermal gravimetric analysis (TGA) and differential scanning calorimetry (DSC) techniques are used.

It is conducted through measurement of the material's response to stress by DSC simultaneously with mass changes in response to the temperature and time with TGA.<sup>31</sup> The two methods are able to work compatibly because of the test conditions' similarity for both techniques. Simultaneous analysers are useful for the analysis of polymeric materials and melting and crystallization processes could be analysed from the mutual data as presented in Chapter 3 of this thesis. The simultaneous thermal analysis (STA) measurements were carried out on Perkin Elmer Thermal Analyzer 8000 Instrument.

## 2.12 References:

1. Kroon, R., Diaz de Zerio Mendaza, A., Himmelberger, S., Bergqvist, J., Bäcke, O., Faria, G. C., Andersson, M. R. (2014) "A New Tetracyclic Lactam Building Block for Thick, Broad-Bandgap Photovoltaics" *Journal of the American Chemical Society*, 136(33), 11578-11581.
2. Krebs, F. C. (2008) "Air stable polymer photovoltaics based on a process free from vacuum steps and fullerenes" *Solar Energy Materials and Solar Cells*, 92(7), 715-726.
3. E. Becquerel (1839). "Mémoire sur les effets électriques produits sous l'influence des rayons solaires". *Comptes Rendus*. 9: 561–567.
4. Hertz, Heinrich (1887). "Ueber einen Einfluss des ultravioletten Lichtes auf die electrische Entladung" *Annalen der Physik*. 267 (8): 983–1000.
5. Hybertsen, M. S. and Louie, S. G. (1986). "Electron correlation in semiconductors and insulators: Band gaps and quasiparticle energies." *Physical Review B*, 34(8), 5390-5413.
6. Patricia Spieth Ramsay (2013). "Heinrich Hertz, the Father of Frequency", *The Neurodiagnostic Journal*, 53:1, 3-26.
7. Klassen, S. (2009). "The Photoelectric Effect: Reconstructing the Story for the Physics Classroom. *Science & Education*", 20(7-8), 719-731.
8. Kahn, A. (2016). "Fermi level, work function and vacuum level. *Materials Horizons*", 3(1), 7-10.
9. P.M. Grant and I.P. Batra (1979), "Band structure of polyacetylene, (CH)<sub>x</sub>", *Solid State Communications*, 29(3), 225-229.
10. Colladet, K., Fourier, S., Cleij, T.J., Lutsen, L., Gelan, J., and Vanderzande, D., (2007) "Low Band Gap Donor-Acceptor Conjugated Polymers toward Organic Solar Cells Applications", *Macromolecules*, 40, 65-72.
11. Solar Cell Operation, IV Curve, (2022), Retrieved from <https://www.pveducation.org/pvcdrom/solar-cell-operation/iv-curve>
12. Riedel, I. and Dyakonov, V. (2004), "Influence of electronic transport properties of polymer-fullerene blends on the performance of bulk heterojunction photovoltaic devices." *Phys. Stat. Sol. (A)*, 201: 1332-1341.
13. Tress, W., Leo, K., & Riede, M. (2012), "Optimum mobility, contact properties, and open-circuit voltage of organic solar cells: A drift-diffusion simulation study." *Physical Review B*, 85(15), 155201.
14. Vandewal, K., Gadisa, A., Oosterbaan, W.D., Bertho, S., Banishoeib, F., Van Severen, I., Lutsen, L., Cleij, T.J., Vanderzande, D. and Manca, J.V. (2008), "The Relation Between Open-Circuit Voltage and the Onset of Photocurrent Generation by Charge-Transfer Absorption in Polymer : Fullerene Bulk Heterojunction Solar Cells." *Adv. Funct. Mater.*, 18: 2064-2070.
15. Diab A., El-Ghanam S.M., Kamh S.A., Soliman F.A.S., (2016), "Computer Simulation and Characterization of Solar Energy and Photovoltaic Cells" *International Journal of Scientific & Engineering Research*, 7(2), 188.

16. Andersson, G., Morgner, H.; Pohl, H., (2008), "Energy-loss straggling of helium projectiles at low kinetic energies: Deconvolution of concentration depth profiles of inorganic salt solute in aqueous solutions." *Phys. Rev. A*, 78 (3), 032904.
17. Andersson, G., Morgner, H., (1998) "Impact collision ion scattering spectroscopy (ICISS) and neutral impact collision ion scattering spectroscopy (NICISS) at surfaces of organic liquids." *Surface Science*, 405 (1), 138-151.
18. Andersson, G., Morgner, H., (1999), "Determining the stopping power of low energy helium in alkanethiolates with Neutral Impact Collision Ion Scattering Spectroscopy (NICISS)." *Nuclear Instruments and Methods in Physics Research Section B: Beam Interactions with Materials and Atoms*, 155 (4), 357-368.
19. Stevie, F. A., & Donley, C. L. (2020). "Introduction to x-ray photoelectron spectroscopy." *Journal of Vacuum Science & Technology A*, 38(6).
20. X-Ray Photoelectron Spectroscopy (XPS), 2022, Retrieved from <https://www.novami.com/nova-technology/x-ray-photospectroscopy-xps/>.
21. Epp, J., (2016), "4 - X-ray diffraction (XRD) techniques for materials characterization", *Materials Characterization Using Nondestructive Evaluation (NDE) Methods*, Woodhead Publishing, 81-124.
22. Tedesco, E., Turner, G.W., Harris, K.D.M., Johnston, R.L., Kariuki, B.M., (2000), "Structure determination of an oligopeptide directly from powder diffraction data." *Angew Chemie Int. Ed.* 39, 4488–4491.
23. Vaia, R.A. and Liu, W. (2002), "X-ray powder diffraction of polymer/layered silicate nanocomposites", *Model and practice. J. Polym. Sci. B Polym. Phys.*, 40: 1590-1600.
24. Klug, H. P., and L. E. Alexander. 1974. *X-ray diffraction procedures for polycrystalline and amorphous materials*. 2nd ed. Wiley, New York.
25. Iwashita N., (2016), "X-ray Powder Diffraction", *Materials Science and Engineering of Carbon*, Butterworth-Heinemann, 7-25.
26. Ando, T. (2022). *Principle of AFM*. In: *High-Speed Atomic Force Microscopy in Biology. NanoScience and Technology*. Springer, Berlin, Heidelberg.
27. Atamny, F., Baiker, A., (1995), "Direct imaging of the tip shape by AFM", *Surface Science*, 323(3), L314-L318.
28. Williams, T. (1970), "Gel permeation chromatography: A review.", *J Mater Sci* 5, 811–820.
29. Sha H., Zhang, X., Harrison, I. R., (1991) "A dynamic mechanical thermal analysis (DMTA) study of polyethylenes", *Thermochimica Acta*, 192, 233-242.
30. Costa, C. S. M. F., Fonseca A. C., Serra A. C. & Coelho J. F. J. (2016) "Dynamic Mechanical Thermal Analysis of Polymer Composites Reinforced with Natural Fibers", *Polymer Reviews*, 56:2, 362-383.
31. Golebiewski, J., Galeski A., (2007) "Thermal stability of nanoclay polypropylene composites by simultaneous DSC and TGA", *Composites Science and Technology*, 67, 3442–3447.

# CHAPTER 3

## **Effect of process parameters and additives on PTB7-Th:ITIC BHJ polymer solar cells**

This chapter presents the study of polymer solar cells produced by non-fullerene acceptors and their performance with different treatments for the purpose of tuning the morphology. PTB7-Th as the donor polymer and ITIC NF acceptor were chosen primarily for this reason. Several solvent systems were studied and found to show different characteristics and proved the significance of effective solvent removal as a post-device treatment. An alternative non-harmful solvent system was found to be more advantageous and showed better device performance. Making it a future promising solvent candidate for the fabrication of similar polymer and NF acceptor systems.

## **3.1 Introduction:**

### **3.1.1 D-A copolymers and NF acceptors:**

As mentioned in Chapter 1, the PSCs using donor-acceptor (D-A) copolymer donors and NF acceptors recently showed to be reaching record efficiencies. The beginning of the discovery and further studies towards these developments are very important. D-A copolymers can be varied using different building blocks and using side-chain engineering.

PTB7-Th is one of the most commonly used and well performing BDT-T unit-based polymer and in 2013, using a fullerene derivative of PC<sub>71</sub>BM, the researchers achieved 7.64% cell efficiency.<sup>1</sup> Later, pairing with non-fullerene (NF) acceptors, it gave much higher efficiencies; PTB7-Th:ITIC and PTB7-Th:IHIC, 6.80% and 9.77% respectively. Also, using  $\alpha$ -substituted (PDI) derivatives and DPE doping, high device current densities were achieved attributed to the increased contact between the active layer and the interfacial area of the electrode.<sup>2,3</sup> The fact that D-A copolymers present perpetual alternatives for such combinations and high efficiencies opened a new period for NF PSCs. PTB7-Th donor copolymer was also used with polymer acceptors which led to more research on its derivatives. These were done by side chain engineering, halogenation, and thiophene bridging leading to record device efficiencies.

In the thesis study, PTB7-Th is also chosen for better co-planarity of molecular backbone, better pi-pi stacking and optimal crystallinity. These features were tested with ITIC acceptor where a specific diffusion-limited crystallization is offered as also mentioned in this Chapter. Moreover, the good compatibility of PTB7-Th with ITIC can be an example for other high-performing donor polymers such as PM6, D18 where they pair with NF acceptors such as Y6 for NFA OPVs.

PTB7 having less conjugation but more stability photo-oxidatively has been also another motivation to experiment on PTB7-Th in order to improve such drawbacks, and offer better and eco-friendly solvent systems without impairing the stability of PTB7-Th:ITIC pair.

The fluorination on the donor polymers also assisted for higher extinction coefficient, stronger crystallinity, small RMS roughness which eventually provided smooth surface and uniform bulk morphology, and efficiency of 11.1%.<sup>4</sup>

Later by adding more conjugation to D-A copolymers; D- $\pi$ -A copolymers with thiophene  $\pi$  - bridge, specifically polymers with stronger absorption and longer conjugated planes were synthesized achieving more stable molecular conformation. The donor unit of BDT-T and acceptor units of BDD and BTz are among them. The combination based on BDT-T and BDD units resulted in the D- $\pi$ -A copolymer of PBDB-T.<sup>5</sup>

Using fullerenes and NF acceptors such as ITIC; PBDB-T also gave high cell efficiencies, from 6.67% in the case of fullerene to 11.21% with NF acceptor.<sup>6</sup> Especially with ITIC acceptor, the co-planarity provided better film morphology and phase separation.

PM6 polymer (BDT-T and BDD units) has recently become a very high performing copolymer for PSC research and has been extensively investigated.

Using PM6 with PC<sub>71</sub>BM, highest efficiencies were achieved with a fullerene acceptor, yet since  $\pi$ - $\pi$  stacking in this system is disrupted with the fullerene, the focus on the latest research was on NF PSCs where charge transfer is increased greatly. As explained in molecular stacking it is crucial to have the right crystallinity on polymer solar devices and copolymers like PM6 used to experiment on discovering the acceptor that will give the best molecular packing.<sup>7</sup> Later Y6 (BTP-4F) is discovered to achieve record efficiency of 15.6% when used with PM6. Therefore, having the superior molecular packing and co-planarity, PM6:Y6 acquired a very low energetic offset and disorder which contributes to a good morphology and

low voltage loss. This resulted in a high device performance showing elevated FF and Jsc values. Y6-Cl (BTP-4Cl) is also investigated and gave a PCE of 16.5%.<sup>8</sup>

Other copolymers based on D- $\pi$ -A structure can be synthesized based on BDT-T and BTz units. Btz provided an additional alkyl chain on the backbone and hence increased the solubility. This combination led to copolymer group of J series which gave high efficiencies and used also for all polymer solar cells (i.e. J50, J51).<sup>9,10</sup>

Using thiophenes and BTz, a group of FTAZ polymers were also investigated. When fullerenes were used as the acceptors, due to poor molecular packing, FTAZ:PC<sub>61</sub>BM gave 5.99%, however, later using NFAs such as IDIC, the crystallinity of the BHJ layer was increased and the dominant face-on orientation provided high device efficiencies (12.14%).<sup>11</sup> Later a record efficiency of 18.22% was achieved using D18 which is another D- $\pi$ -A copolymer.<sup>12</sup> When paired with the well performing Y6 acceptor, molecular stacking improved and led to further PSC studies using D18.

These examples show how significant the morphology of the polymer solar cells is for device performance but also shows us how to engineer the thin film blend using different D-A pairs in terms of their structure for better molecular packing, favorable energy order, high absorbance and stability.

### **3.1.2 PTB7 and PTB7-Th copolymers:**

One of the D-A copolymer that has been very popular in NF PSC research is PTB7-Th as mentioned.<sup>1</sup> It is essentially derived from D-A polymer called PTB7 which is BDT based and through a D- $\pi$ -A type modification, PTB7-Th is synthesized (Figure 3.1). Former has an alkoxy side chain, and the latter has alkyl thiophene. The advantages of this modification are, improved co-planarity of molecular backbone with elongated effective conjugation plane,

broad and stronger absorption with 25 nm onset red shift, and better  $\pi$ - $\pi$  stacking and shorter  $\pi$ - $\pi$  stacking distance.<sup>13</sup>

Although they are both well compatible with most acceptors, in particular, with NFAs hence providing strong crystallinity, PTB7 shows better photostability than PTB7-Th. In conjugated polymers, the conjugation bonds are very strong and the larger side chain of alkyl thiophene causes faster photo-oxidative degradation since it is the weakest in the polymer structure, so they break easily under external excitation such as light. Some comparative studies also included effects of different types of acceptors (Fullerene vs NFAs) and solvent additives on the photostability<sup>14</sup>, the structures of PC<sub>71</sub>BM and ITIC were also given in Figure 3.2.

PC<sub>71</sub>BM is also more stable than ITIC which shows the complex compromise of factors for stability of polymer solar cells.<sup>15</sup> Therefore, it is important to analyse each donor polymer for their stability performance in PSCs individually for both fullerene and NF acceptors via different degradation pathways.<sup>22</sup>

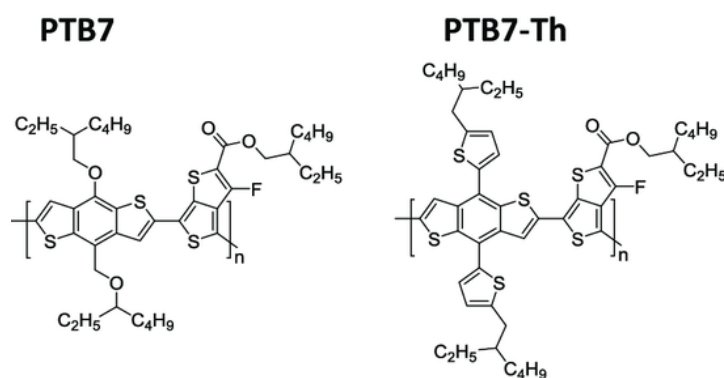


**Figure 3.1:** PTB7 and PTB7-Th structures.

Even though PTB7-Th is less photostable since side-chains also have role in molecular packing, solubility and electron affinity, it gives higher solar cell performance than PTB7.

Other factors for the difference in the stabilities of different types of acceptors are the crystallization dynamics and thermal properties.<sup>17</sup> PTB7-Th forms optimum nano-scale crystals with NF acceptor ITIC as its crystallization occurs at much higher temperature than

that of PC<sub>71</sub>BM, it also offers good device performance when printed.<sup>16</sup> Larger molecules also have less diffusion (mobility) and provides solid-state like firmness in the molecule which helps stability. Thus, it will also provide higher thermal stability.

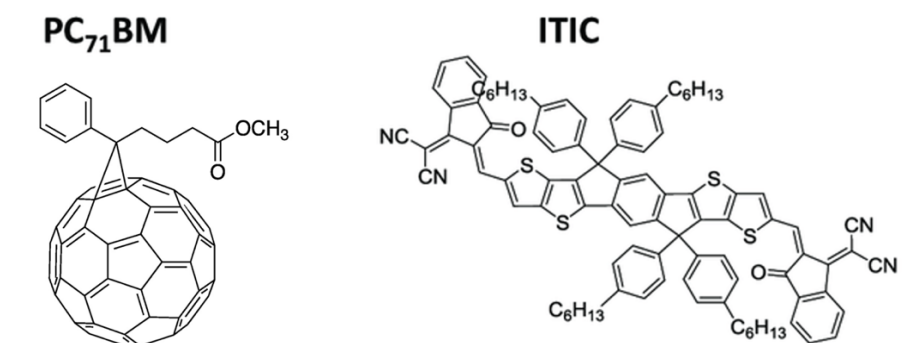


**Figure 3.2:** PC<sub>71</sub>BM vs ITIC for PTB7-Th devices.

Furthermore, ITIC has unique thermal properties which is due to its ability to form a polymorph at low T as it goes into a diffusion limited crystallization below its T<sub>g</sub> ~ 180°C which contributes to higher device performance with NF PSCs.<sup>17</sup> Other factors for the good morphology compatibility of NFAs over fullerenes are the preferred face-on orientation, as this results in high device performance, as well.

## 3.2 Methodology, Device Fabrication and Characterization:

### 3.2.1 Materials:

**Table 3.1** Main solvents used in PSC fabrication.

Solvent	Molecular Formula	Boiling Point (°C)
Chlorobenzene (CB)	C <sub>6</sub> H <sub>5</sub> Cl	132
<i>o</i> -xylene	C <sub>8</sub> H <sub>10</sub>	144
1-Methoxynaphthalene (MN)	C <sub>11</sub> H <sub>10</sub> O	270
1-Phenylnaphthalene (PN)	C <sub>16</sub> H <sub>12</sub>	324
1,8-Diiodooctane (DIO)	C <sub>8</sub> H <sub>16</sub> I <sub>2</sub>	333
<i>p</i> -anisaldehyde (AA)	C <sub>8</sub> H <sub>8</sub> O <sub>2</sub>	248

Main solvents and solvent additives used in this study to deposit photoactive layers are listed above and their boiling points were given in Table 3.1.<sup>18</sup> Among them CB and DIO are harmful and toxic solvents as stated in Chapter 2. Their structures are given below in Figure 3.3:

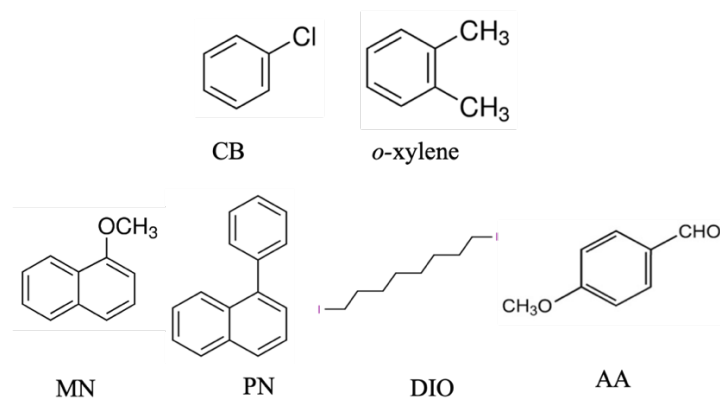


**Figure 3.3:** Structures of main solvent and solvent additives used in PSC studies.

### 3.2.2 PTB7, PTB7-Th, ITIC and DIO:

Bulk heterojunction solar cells using non-fullerene acceptors in their active layers have surpassed power conversion efficiencies up to 18% by tailoring their nano-morphology for overcoming the problematic energy loss.<sup>12</sup> These new efficiencies are getting closer to the solar cells using inorganic silicon and shows the potential of organic photovoltaics in improving the renewable energy market in future. The low cost of production and extensive research and industry investment will make OPVs the cheapest clean energy resources with various interdisciplinary applications. The NF acceptor materials having a good energy alignment (HOMO of donor and LUMO of acceptor) with the wide bandgap donor in the active layer enhances the charge carrier dynamic through careful treatments that change the surface topography, phase separation, crystallinity.<sup>19</sup>

In this study we investigated how effective solvent additives are in terms of their effect on changing nanoscale morphology without severely affecting the stability of the devices. The

presence of non-fullerene acceptors enabled the advantage of lower energy loss compared to the fullerene acceptors. Moreover, increased molecular packing and stability along with eco-friendly solvent processing eased the fullerene acceptor limitations.<sup>13</sup> As the future goal is to make the devices printable and upscale them, it is crucial to use non-toxic solvents as the priority consideration before focusing on increasing the efficiencies with different treatments. 1,8-diodioctane (DIO) solvent additive has been very popular in many bulk-heterojunction (BHJ) solar cell systems, many researchers got benefited from its high boiling point and effectivity in making both fullerene and non-fullerene devices much more stable and efficient.<sup>20</sup> In the system of PTB7-Th:ITIC non-fullerene solar cell system, DIO has been also used extensively and proved to not only enhance the charge transport but also help to have more photostable and heat stable solar devices.<sup>21</sup> In a study where DIO is used in PTB7-Th:PC<sub>71</sub>BM system; the solvent additive is said to enhance the device efficiency and long-term stability, whereas other recent studies claim that DIO stays in the active layer as residue and decreases the device stability in the longer term. Especially for photostability, the contradictory results have become our motivation to investigate the real effects caused by DIO.<sup>22,23</sup>

Later, we worked on a solvent system that is non-toxic and eco-friendly which offered higher efficiencies than DIO in PTB7-Th:ITIC system as discussed in our results and shown using a device diagram in Figure 3.4 where BHJ is PTB7-Th:ITIC processed from o-xylene and AA additive:

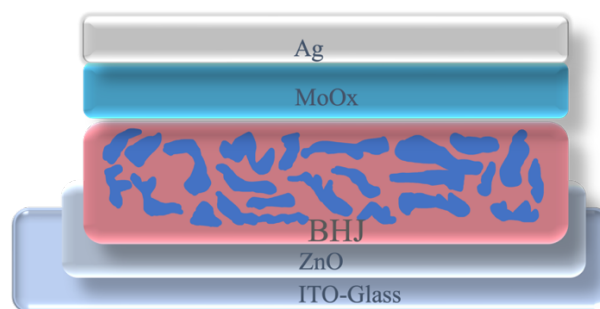


**Figure 3.4:** PSC device architecture with BHJ of PTB7-Th:ITIC.

It has been found that DIO stays in the thin film and treatments for removing it are not found to be effective due to its disruption with temperature and actual device conditions, which means DIO can mostly be removed at elevated temperatures and conditions where a solar cell cannot perform and last well.

For instance, a study suggests that high annealing temperatures like 175°C and vacuum drying at  $10^{-8}$  mbar are both effective in removing the solvent additive of DIO from the active layer.<sup>24</sup> This annealing temperature is not suitable for solar cell performance and the vacuum drying is an additional fabrication step where the thermal evaporation chambers of pressure already help to remove the solvents during evaporation of electrodes.

Yet, DIO still has extensive use in OPV fabrication as high boiling point solvent additives have different solubilities towards donor and acceptor in the active layer and during the film formation. This mostly leads to a well separated domain where charges can be transported and dissociate for the best device efficiency.

ITIC has also been extensively investigated as it is found to expedite the high  $J_{sc}$  current densities, the stacking of ITIC molecules in the device architecture is improved using DIO when paired with PTB7-Th polymer.<sup>25, 26</sup>

### **3.2.3 NF OPV Device Fabrication and Discussion:**

The inverted solar cell devices constructed with PTB7-Th:ITIC donor-acceptor system have been studied with and without DIO using host solvent CB, other halogenated and non-halogenated solvent systems. The results showed that using appropriate treatment to remove DIO the efficiencies increased slightly although a more environmentally friendly solvent system gave a better performance which is o-xylene and AA (p-anisaldehyde). The study where

they also used the same solvent system with the acceptor PC<sub>71</sub>BM showed that AA solvent additive also improves the nano-morphology and gives very stable device performances.

As our aim was to discover the most stable design and fabrication method for PTB7-Th polymer solar cells, the devices were done using ITIC in an inverted device architecture. Our results showed better device efficiencies and have become better alternatives compared to the devices with active layers processed from toxic solvent systems containing DIO.

Firstly, the solar cells with CB host solvent were fabricated and tested before and after an annealing treatment. The addition of DIO slightly increased the performance of the devices. We examined the presence of DIO in these devices and suspected that a small amount (0.6%v/v) of DIO staying in the thin films of devices make them degradable over time. The next step was to use drying techniques of annealing and vacuum drying to remove DIO. The efficiencies for these devices are given below in Table 3.2.

Device fabrications were done using inverted solar cell structure of ITO/ZnO/PTB7-Th:ITIC(1:1.3)/MoO<sub>x</sub>/Ag. As chlorobenzene (CB) is used commonly with DIO in the device fabrication of PTB7-Th based PSCs, in the first set of optimization experiments, the active layer film was processed from the solution prepared with CB + 0.6% DIO (23 mg/mL). The solution was stirred at 70°C overnight and spin-coated with various spin speeds for 60 s and tested both as cast and using annealing treatment (at 130°C for 15 min and drying under vacuum overnight). All devices are also averaged from 6 total cells.

**Table 3.2:** Photovoltaic properties of PSCs from PTB7-Th:ITIC (1:1.3) (23 mg/mL) with annealed vs as-cast and from PTB7-Th:ITIC (1:1.3) (19.5 mg/mL) with thickness optimization.

Device	$J_{sc}$ (mA/cm <sup>2</sup> )	$V_{oc}$ (V)	FF (%)	PCE (%)
CB + 0.6% DIO 23 mg/mL; 2000 rpm, 45s annealed	16.29 (16.30 ± 0.08)	0.82 (0.82 ± 0.01)	57 (56 ± 1)	7.68 (7.52 ± 0.12)
CB + 0.6% DIO 23 mg/mL; 2000 rpm, 45s as-cast	17.00 (16.73 ± 0.14)	0.82 (0.82 ± 0.01)	54 (54 ± 1)	7.55 (7.38 ± 0.10)
CB + 2% DIO 19.5 mg/mL; 2750 rpm	13.23 (12.89 ± 0.34)	0.83 (0.83 ± 0.01)	51 (50 ± 1)	5.59 (5.37 ± 0.18)
CB + 2% DIO 19.5 mg/mL; 2500 rpm	13.27 (13.14 ± 0.19)	0.82 (0.82 ± 0.01)	50 (50 ± 1)	5.44 (5.31 ± 0.12)
CB + 2% DIO 19.5 mg/mL; 2000 rpm	12.37 (12.09 ± 0.18)	0.81 (0.81 ± 0.01)	47 (46 ± 1)	4.77 (4.59 ± 0.11)
CB + 2% DIO 19.5 mg/mL; 2000 rpm post-annealed	9.86 (9.67 ± 0.13)	0.75 (0.74 ± 0.03)	44 (43 ± 1)	3.21 (3.07 ± 0.13)

The concentration of DIO was also increased to see the effect and found to decrease the device efficiency and cause increased instability in PSCs. The removal of high boiling point additive with 2% DIO had also become more challenging. We tried various thicknesses for optimization and even though high spin speed assisted in fast drying of the BHJ thin film and increased the efficiencies, devices fabricated from 2750 rpm spin speed still gave poor performance compared to 0.6% DIO devices. Then, we decided to test a less harmful solvent system and started from PN as eco-friendly additive; the device photovoltaic characterization is given below in Table 3.3.

**Table 3.3:** Photovoltaic properties of PSCs from PTB7-Th:ITIC (1:1.3) (23 mg/mL) with PN additive.

Device	J <sub>sc</sub> (mA/cm <sup>2</sup> )	V <sub>oc</sub> (V)	FF (%)	PCE (%)
CB + 0.6% PN	15.67 (15.62 ± 0.20)	0.78 (0.78 ± 0.01)	53 (53 ± 1)	6.50 (6.43 ± 0.10)
CB + 2% PN	9.51 (9.13 ± 0.25)	0.65 (0.64 ± 0.01)	43 (40 ± 1)	2.66 (2.35 ± 0.19)

Later with a different set of devices, the active layer film was processed from the solution prepared with CB and with CB + 0.6% DIO, the solution was stirred at 70°C overnight and spin-coated with 2500 rpm for 60 s and annealed at 130°C for 15 min after drying under vacuum overnight. The reference device without solvent additive and the best device from 0.6% DIO additive concentration were fabricated and tested in the same batch of experiments for better optimisation and accuracy.

**Table 3.4:** Photovoltaic properties of PSCs from PTB7-Th:ITIC (1:1.3) (23 mg/mL) (2500 rpm) with and w/o DIO additive.

Device	J <sub>sc</sub> (mA/cm <sup>2</sup> )	V <sub>oc</sub> (V)	FF (%)	PCE (%)
CB	17.07 (16.90 ± 0.17)	0.82 (0.82 ± 0.01)	56 (56 ± 0)	7.84 (7.76 ± 0.07)
CB + 0.6% DIO	16.69 (16.33 ± 0.24)	0.82 (0.82 ± 0.01)	59 (59 ± 1)	7.98 (7.83 ± 0.10)

These solvent additive treatments such as annealing and drying under vacuum were found to differ slightly but significant as it can be critical to have even a small amount of high boiling point DIO solvent remained after device completion.

In order to solve the remaining solvent residue problem and to follow eco-friendlier device fabrications for such NF-PSC system; next o-xylene as the main solvent was experimented and optimized, the device photovoltaic properties is given in Table 3.5.

**Table 3.5:** Photovoltaic properties of PSCs from PTB7-Th:ITIC (1:1.3) (19.5 mg/mL) (2500 rpm) processed with o-xylene with and w/o DIO additive.

Device	J <sub>sc</sub> (mA/cm <sup>2</sup> )	V <sub>oc</sub> (V)	FF (%)	PCE (%)
o-xylene, 2000 rpm	15.68 (15.55 ± 0.16)	0.81 (0.81 ± 0.01)	56 (56 ± 1)	7.17 (7.03 ± 0.13)
o-xylene + 0.6% DIO, 2000 rpm	15.09 (15.30 ± 0.25)	0.82 (0.81 ± 0.01)	53 (54 ± 1)	7.14 (6.68 ± 0.24)

The main solvent o-xylene showed reasonable performance, however the device using o-xylene and 0.6% DIO additive caused haziness as shown below in Figure 3.5:

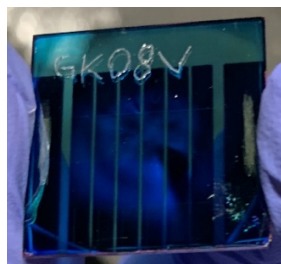


**Figure 3.5:** Device photo of PSC from PTB7-Th:ITIC (1:1.3) (19.5 mg/mL) (2500 rpm) processed with o-xylene with 0.6% DIO additive.

DIO additive with o-xylene additive hence found to be unstable because of the poor morphology and efficiency.

Another eco-friendly non-harmful solvent additive MN was also initially tested with CB in order to see its potential use. The active layer film was processed from the solution prepared with CB and 1% MN (23mg/mL); the solution was stirred at 75°C overnight and spin-coated with 2500 rpm for 60 s as-cast and 3000/2500 rpm/2000 rpm speeds for 60 s and annealed at 130°C for 15 min after drying under vacuum overnight.

Devices from CB and MN additive gave better performance when processed as-cast but still much lower than DIO. The efficiency increased with decreasing thickness when annealed as shown in Table 3.6.

**Table 3.6:** Photovoltaic properties of PSCs from PTB7-Th:ITIC (1:1.3) (23 mg/mL) processed with CB for MN additive optimization via thickness.

Device	J <sub>sc</sub> (mA/cm <sup>2</sup> )	V <sub>oc</sub> (V)	FF (%)	PCE (%)
CB + 1% MN, 2500 rpm, as-cast	16.22 (16.21 ± 0.06)	0.81 (0.81 ± 0.02)	55 (54 ± 1)	7.20 (7.06 ± 0.09)
CB + 1% MN, 2000 rpm, annealed	16.22 (16.23 ± 0.14)	0.80 (0.80 ± 0.01)	51 (50 ± 1)	6.58 (6.49 ± 0.06)
CB + 1% MN, 2500 rpm, annealed	16.77 (16.40 ± 0.21)	0.80 (0.80 ± 0.01)	52 (52 ± 1)	6.97 (6.84 ± 0.10)
CB + 1% MN, 3000 rpm, annealed	16.36 (16.22 ± 0.12)	0.80 (0.80 ± 0.01)	53 (53 ± 1)	7.0 (6.84 ± 0.10)

After comparing PN, MN and CB and o-xylene experiments, it was decided to follow the eco-friendly approach with o-xylene main solvent and to study whether additives could be removed efficiently. Consequently, inverted device structure was used again, and the active layer film was processed from the solution prepared with o-xylene and 0.3% DIO (19.5 mg/mL); the solution was stirred at 75°C overnight and spin-coated with 2500 rpm&2000 rpm for 60 s as-cast and 2500 rpm and 2000 rpm for 60 s annealed at 130°C for 15 min after drying under vacuum overnight. The o-xylene and 0.3% DIO devices did not have haziness this time and had homogeneous good films. Whereas the annealed devices had poor efficiency and were not stable. In another set, the active layer film was processed from the solution prepared with o-xylene and 1% MN (19.5 mg/mL); the solution was stirred at 75°C overnight and spin-coated with 2500 rpm and 2000 rpm for 60 s annealed at 130°C for 15 min after drying under vacuum overnight. All device performance using o-xylene and 0.3% DIO, and MN additive is given in Table 3.7.

**Table 3.7:** Photovoltaic properties of PSCs from PTB7-Th:ITIC (1:1.3) (19.5 mg/mL) processed with o-xylene for MN additive and 0.3% DIO optimization.

Device	J <sub>sc</sub> (mA/cm <sup>2</sup> )	V <sub>oc</sub> (V)	FF (%)	PCE (%)
o-xylene + 0.3% DIO 2500 rpm, as-cast	17.09 (17.02 ± 0.17)	0.82 (0.82 ± 0.01)	56 (54 ± 1)	7.80 (7.45 ± 0.20)
o-xylene + 0.3% DIO 2000 rpm, as-cast	17.16 (16.99 ± 0.17)	0.82 (0.82 ± 0.01)	51 (49 ± 1)	7.12 (6.82 ± 0.18)
o-xylene + 1% MN 2500 rpm, annealed	16.41 (16.18 ± 0.15)	0.81 (0.81 ± 0.01)	55 (54 ± 1)	7.28 (7.08 ± 0.13)
o-xylene + 1% MN 2000 rpm, annealed	16.56 (16.19 ± 0.19)	0.81 (0.81 ± 0.01)	53 (53 ± 1)	7.11 (6.91 ± 0.23)

Main solvent of o-xylene was discovered to be working for this system as reported in the literature as well for PTB7-Th donor polymer PSC systems, thus we continued to test o-xylene systems to further analyse the best non-harmful solvent system for this NF-PSC. CB-DIO solvent system is also continued to be analysed for the same system to study if harmful DIO could be removed. These experiments with DIO removal focus are also given in Chapter 3.

Another non-harmful and eco-friendly solvent additive p-anisaldehyde (AA) was tested with further using treatments such as annealing, high-vacuum drying and washing; the performance of solar cells was aimed to be increased greatly.

#### **Devices processed from o-xylene + AA solvent system:**

The structure of devices are ITO/PTB7-Th:ITIC (19.5mg/mL)(1:1.3)/MoO<sub>x</sub>/Ag where BHJ was processed from o-xylene and 2% AA additive, stirred at 75°C overnight and analysed when as-cast after drying under vacuum overnight/vacuum dried. Solutions were 1 mL in total

as usual. All films were dried in the Glove Box first and dried in the evaporation chamber up to  $10^{-7}$  mbar for 1 hour before the evaporation for the as-cast devices. Annealed devices were heated at  $130^{\circ}\text{C}$  for 15 min. The devices were stable, and the best performing was with annealed; 1200 rpm device. This is the old batch of PTB7-Th with  $M_n = 80\,000$ . The device photovoltaic properties are given in Table 3.8.

**Table 3.8:** Photovoltaic properties of PSCs from PTB7-Th:ITIC (1:1.3) (19.5 mg/mL) processed with o-xylene for AA additive and drying optimization.

Device	$J_{sc}$ (mA/cm <sup>2</sup> )	$V_{oc}$ (V)	FF (%)	PCE (%)
o-xylene + 2% AA 2500 rpm, annealed	15.39 (15.50 ± 0.12)	0.80 (0.80 ± 0.01)	58 (57 ± 1)	7.22 (7.13 ± 0.20)
o-xylene + 2% AA 2500 rpm, high vacuum dried	16.47 (15.50 ± 0.18)	0.81 (0.80 ± 0.01)	63 (57 ± 1)	8.49 (8.20 ± 0.21)

In this first set of treatment comparison, annealed devices showed significantly lower performance compared to high vacuum drying, the J-V plot is also shown in Figure 3.6. The best performing device was found using o-xylene main solvent and 2% AA additive which is higher than that of the DIO processed devices. The high vacuum drying was also found to be very effective in increasing the device performance whereas annealing was disadvantageous.

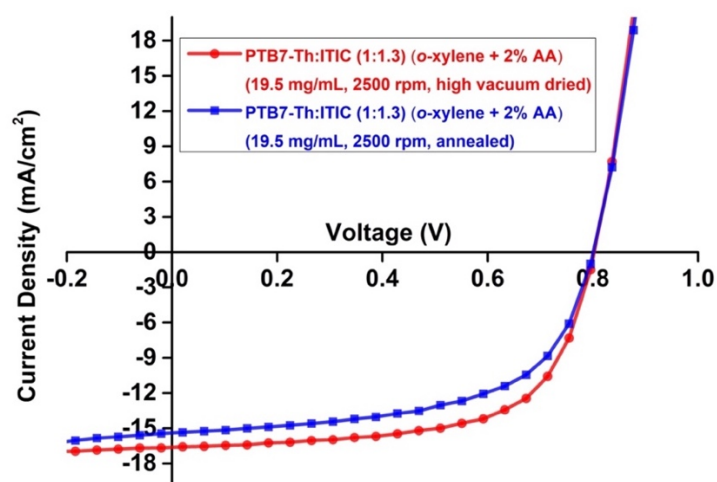


**Figure 3.6:** J-V graph of PSCs from PTB7-Th:ITIC (1:1.3) (19.5 mg/mL) processed with o-xylene for AA additive and drying optimization.

After discovering its effective performance, AA additive was also experimented using CB main solvent for comparison, and the device performance is given below:

**Table 3.9:** Photovoltaic properties of PSCs from PTB7-Th:ITIC (1:1.3) (23 mg/mL) processed with CB for AA additive and drying optimization.

Device	$J_{sc}$ (mA/cm <sup>2</sup> )	$V_{oc}$ (V)	FF (%)	PCE (%)
CB + 2% AA 2500 rpm, annealed	16.06 (15.69 ± 0.23)	0.80 (0.80 ± 0.01)	56 (54 ± 1)	7.22 (6.85 ± 0.23)
CB+ 2% AA 2500 rpm, high vacuum dried	16.90 (16.60 ± 0.23)	0.80 (0.80 ± 0.01)	59 (59 ± 1)	8.04 (7.84 ± 0.14)

Later DIO devices using as-cast systems were also tested to be able to see clearly if high vacuum drying is an effective method and much better than annealing as reported in literature, and device summaries are given below in Table 3.10.

**Table 3.10:** Photovoltaic properties of PSCs from PTB7-Th:ITIC (1:1.3) (23 mg/mL) processed with CB and DIO additive for drying and thickness optimization.

Device	$J_{sc}$ (mA/cm <sup>2</sup> )	$V_{oc}$ (V)	FF (%)	PCE (%)
CB + 0.6% DIO 2500 rpm, as-cast	15.78 (15.42 ± 0.18)	0.81 (0.81 ± 0.01)	57 (57 ± 1)	7.30 (7.08 ± 0.11)
CB+ 0.6% DIO 2500 rpm,high vacuum dried	16.35 (16.05 ± 0.17)	0.82 (0.82 ± 0.01)	60 (58 ± 1)	7.98 (7.66 ± 0.18)
CB + 0.6% DIO 2000 rpm, as-cast	16.27 (15.68 ± 0.36)	0.82 (0.81 ± 0.01)	56 (56 ± 1)	7.50 (7.18 ± 0.26)

The devices showed good efficiency as expected and showed us the effective use of high vacuum drying again. We also tested 4% DIO even though the thin films were poor due to the excess residual solvent additive and observed very poor film characteristics and device performance hence discontinued for further testing for increased DIO concentration.

### 3.3 AFM Morphology Characterization:

The device efficiencies were also supported by examining the topographical properties via AFM.

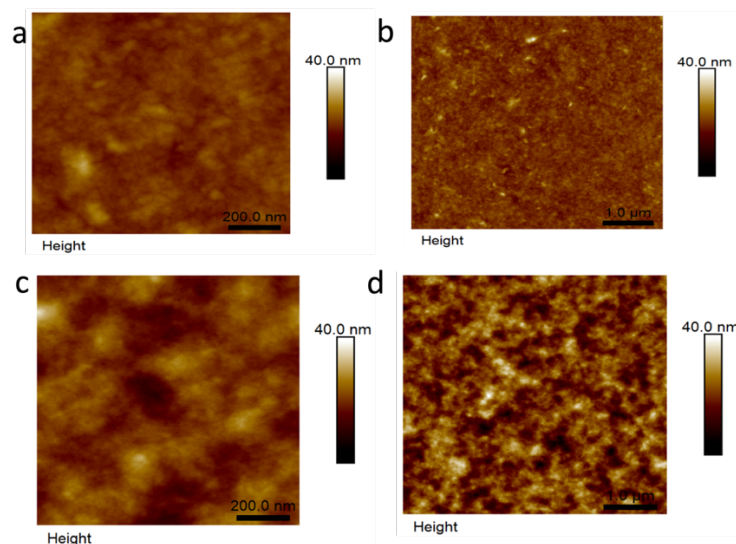


**Figure 3.7:** AFM Height images of thin films processed from CB main solvent and 0.6% DIO additive (top) (a and b) versus processed from o-xylene main solvent + 2% AA (bottom) (c and d) (Scales are 200 nm and 1 μm for both solvent systems)

The PTB7-Th:ITIC active layer using CB and 0.6% DIO were compared to o-xylene and 2% AA as shown in Figure 3.7. In general solvent additives enable polymers to provide better packing resulting in increased performance. However, too much phase separation may decrease charge transport and mobility, thus, causing low FF and device efficiencies. This effect of excess phase separation can be seen in the AFM sample with 2% DIO in Figure 3.8 (top). Hence, the best nano-scale morphology was achieved using 0.6% DIO among DIO processed devices as it also gives the best device efficiency among them, the AFM height images summarized in Figure 3.8.

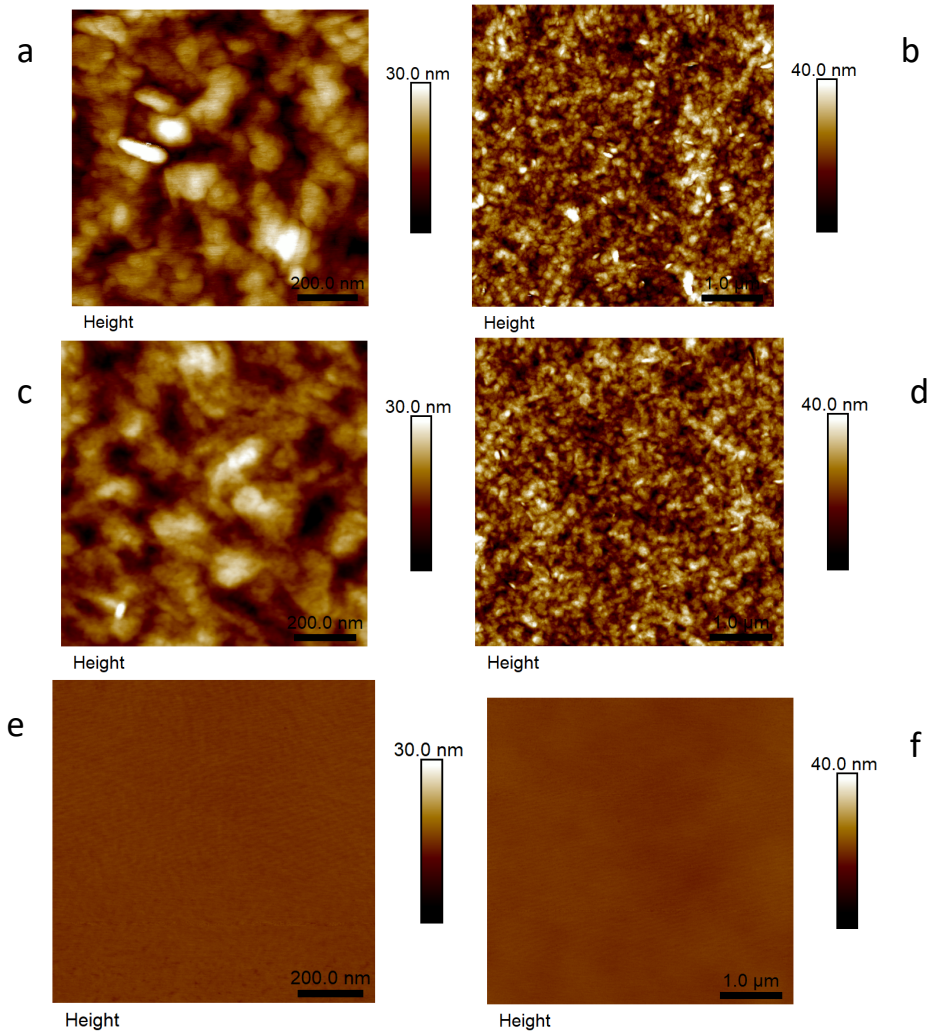


**Figure 3.8:** AFM Height images of devices – CB main solvent + 2% DIO (top) (a and b) / 2%DIO annealed (middle) ( c and d) / 4% DIO annealed (bottom) (e and f). (Scales are 200 nm and 1 $\mu$ m for all 3 solvent systems)

The phase separation in BHJ blend vanishes once 4% DIO is used, and the surface is flat. Even though the devices were annealed, they became unable to completely dry due to the high amount of DIO, and AFM technique was not appropriate to analyse the surface. The roughness data for all films was also examined to be able to detect the differences in similar topographies.

### 3.3.1 AFM Roughness Measurements:

**Table 3.11:** Roughness Measurements of devices processed from CB and o-xylene.

<b>Sample 1: PTB7-Th:ITIC (1:1.3) (CB+0.6% DIO)</b>				
<b>Scale</b>	1 $\mu\text{m}$ x 1 $\mu\text{m}$		5 $\mu\text{m}$ x 5 $\mu\text{m}$	
<b>Scan</b>	Rq (nm)	Ra (nm)	Rq (nm)	Ra (nm)
<b>1</b>	2.15	1.58	2.72	1.74
<b>2</b>	1.62	1.26	2.12	1.59
<b>3</b>	1.61	1.25	2.43	1.69
<b>4</b>	1.73	1.3	2.11	1.51
<b>5</b>	1.64	1.24	1.8	1.36
<b>Average</b>	1.75	1.33	2.24	1.58
<b>STDev</b>	0.23	0.14	0.35	0.15

<b>Sample 2: PTB7-Th:ITIC (1:1.3) (o-xy+2% AA)</b>				
<b>Scale</b>	1 $\mu\text{m}$ x 1 $\mu\text{m}$		5 $\mu\text{m}$ x 5 $\mu\text{m}$	
<b>Scan</b>	Rq (nm)	Ra (nm)	Rq (nm)	Ra (nm)
<b>1</b>	3.60	2.83	4.66	3.72
<b>2</b>	3.09	2.43	5.35	4.25
<b>3</b>	3.39	2.63	4.88	3.88
<b>4</b>	3.56	2.78	5.305	3.90
<b>5</b>	3.16	2.49	4.68	3.73
<b>Average</b>	3.36	2.63	4.98	3.90
<b>STDev</b>	0.23	0.17	0.33	0.21

The best devices from CB and o-xylene systems have lower roughness compared to that of devices with higher DIO concentration except 4% DIO as more amount of additive stayed in the film. The roughness of the 2% DIO device is also much higher than that of 0.6% showing the decrease in charge mobility as can also be seen in device performance with low  $J_{sc}$  and FF. This can also be due to the sensitivity of the thin films towards roughness, they can easily cause shorts in devices and create current leakages.

**Table 3.12:** Roughness Measurements of devices processed from CB solvent + DIO additive.

Scan	PTB7-Th:ITIC / CB + 2% DIO							
	1 um x 1 um				5 um x 5 um			
	Rq (nm)		Ra (nm)		Rq (nm)		Ra (nm)	
<b>1</b>	4.43		3.46		5.97		4.76	
<b>2</b>	4.41		3.49		5.79		4.61	
<b>3</b>	4.85		3.88		6.35		4.9	
<b>4</b>	4.75		3.84		5.89		4.65	
<b>5</b>	5.32		4.34		6.49		4.95	
<b>Average</b>	4.75	± 0.33	3.80	± 0.32	6.10	± 0.27	4.77	± 0.13
Scan	PTB7-Th:ITIC / CB + 2% DIO Annealed							
	1 um x 1 um				5 um x 5 um			
	Rq (nm)		Ra (nm)		Rq (nm)		Ra (nm)	
<b>1</b>	5.12		4.03		6.76		5.23	
<b>2</b>	5.68		4.37		6.64		5.17	
<b>3</b>	5.65		4.31		6.69		5.17	
<b>4</b>	5.88		4.65		7.02		5.53	
<b>5</b>	5.52		4.17		6.71		5.22	
<b>Average</b>	5.57	± 0.25	4.31	± 0.21	6.76	± 0.13	5.26	± 0.14
Scan	PTB7-Th:ITIC / CB + 4% DIO Annealed							
	1 um x 1 um				5 um x 5 um			
	Rq (nm)		Ra (nm)		Rq (nm)		Ra (nm)	
<b>1</b>	0.248		0.194		0.384		0.298	
<b>2</b>	0.256		0.202		0.341		0.265	
<b>3</b>	0.427		0.331		0.399		0.308	
<b>4</b>	0.276		0.215		0.425		0.334	
<b>5</b>	0.306		0.242		0.49		0.39	
<b>Average</b>	0.30	± 0.07	0.24	± 0.05	0.41	± 0.05	0.32	± 0.04

In summary, this topography and roughness analysis showed us the effectiveness of removing solvent additives through vacuum drying, and it is also further studied via thermal and surface characterization to demonstrate how it is better than annealing especially in BHJ films using ITIC.

### 3.4 XPS and NCISS Analysis:

OPV studies that have been carried out by researchers mostly showed the effects of solvent additive 1,8- diiodooctane (DIO) on various polymer solar cell systems and discussed that these effects were different and in some cases contradictory.<sup>27,28</sup> The reasons for these disagreeing results are mainly due to the ability of DIO to improve the BHJ active layer nano-morphology and its disadvantageous effects on solar cell degradation. DIO solvent has a very high boiling point and a low vapor pressure (332.5 °C at 760 mm Hg , 0.0375 Pa at 25 °C), thus the active layers processed with DIO have residues remaining in BHJ films that can expedite many degradation processes with different mechanisms including photoinduced degradation.<sup>29,30</sup>

Some studies suggest that the remaining DIO can be fully removed via high vacuum and annealing treatment or washing with a swelling agent, while some studies suggest that it is not possible to remove DIO completely from the films unless applying harsh treatments, so it has only a negative effect on solar cell stability in the long term.<sup>31</sup>

Some of these studies focused on the donor polymer PTB7-Th and fullerene acceptors, however PTB7-Th with non-fullerene acceptor ITIC blend system has not been fully studied in terms of degradation mechanisms caused by DIO and how DIO stays in the film and also performance of methods to remove DIO efficiently.

In this thesis, we partially agree with the studies suggesting DIO permanently stays in PTB7-Th:ITIC active layer films although sometimes can be removed to a great extent using extreme treatments such as annealing at very high temperatures which are less applicable during a device fabrication.

We also suggested a non-halogenated eco-friendly solvent additive p-anisaldehyde (AA) as a great alternative to DIO for this system. Previous studies' device efficiencies using

AA in the active layers of PTB7-Th:PC<sub>71</sub>BM has been also been surpassed by our photovoltaic device analysis with more stable solar cells using AA additive.

First of all, for the removal of DIO, the PTB7-Th:ITIC blend films that were dried in different conditions (vacuum & high vacuum & annealing) prior to the device fabrication were analyzed via X-ray Photoelectron Spectroscopy (XPS) and Neutral Impact Collision Ion Spectroscopy (NICISS).

DIO is a very commonly used solvent additive to improve the phase separation of donor and acceptor in photo-active layers of both fullerene and non-fullerene solar cells due to solvent evaporation dynamics. Google Scholar presents many articles almost each year where DIO was used for OSC as a solvent additive compatibilizer. However, it cannot be considered as a compatibilizer as it causes permanent instability in BHJ solar cells.<sup>32</sup> Moreover, in some recent studies it is reported that DIO dissociates readily into iodoctane and iodine radicals extracting H atom of the side alkyl chain in PTB7-Th.<sup>33</sup> In the presence of oxygen, chain reaction will result in chemical degradation of donor materials. Therefore, we decided to identify the residual DIO to study its negative effects particularly in PTB7-Th:ITIC BHJs.

The first set of XPS experiments were conducted in a similar manner of previous studies done with OPV devices.<sup>16</sup> XPS spectra were acquired using an ultrahigh vacuum apparatus built by SPECS (Berlin, Germany) with a base pressure of a few  $10^{-10}$  mbar. During the elemental analysis, the specific interests were C1, N1, O1, S1 and finally I. High resolution scans were recorded for I species to be able to identify it efficiently.

The chemical composition and ratios were examined for each sample and individual curve fittings of elements of interests were done. Since the amount of DIO used on the formation of BHJ (PTB7-Th:ITIC) solar cells is very low 0.6% (v/v) relative to chlorobenzene (CB) main solvent, several adjustments during measurements were carried out. First, each sample was measured individually with minimal exposure to O<sub>2</sub> and moisture and initial X-ray

irradiation. The XPS sample chamber was needed to be under high vacuum before the measurement, so the samples were quickly measured by mounting them one by one in the sample chamber. This avoided the immediate removal of DIO in the XPS chamber prior to the measurements to a certain degree as high vacuum ( $10^{-7}$  mbar) conditions are also present prior and during the electrode deposition of solar cell fabrication. PTB7-Th:ITIC (1:1.3 w/w%) blends were prepared precisely in the same way as OPV devices. The donor-acceptor blends were dissolved in CB and DIO solvent mixture where the latter is only 0.6% (v/v). The solutions were then spin-coated on clean ITO-glass substrates and organic thin films were dried in 3 different conditions similar to that of device fabrication in order to compare the presence of DIO solvent remaining in the corresponding BHJ thin films.

Several experiments were conducted for this purpose whereas the challenges of ultra-high vacuum sample chamber of XPS and irradiation effects on DIO degradation were present as they might influence the interpretation of XPS data. Later, NICISS experiments were successfully conducted in order to distinctly study the presence of DIO in the BHJ films using a novel approach as NICISS is more sensitive than XPS with the detection of heavier elements such as Iodine and due to higher cross section for back scattering. As interpreted from the experiments, the  $3d_{5/2}$  binding energy  $I_2$  is shown at 620 eV where it is in iodide form (C-I) as given in the XPS spectra below in Figure 3.9.

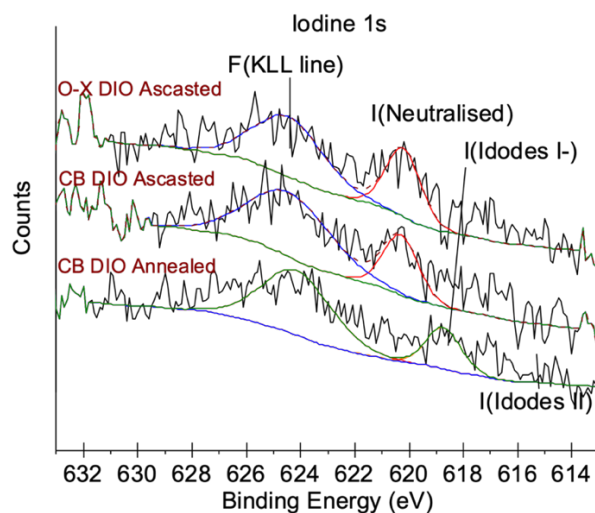


**Figure 3.9:** XPS Spectra of thin films processed with o-xylene + DIO, CB + DIO.

The spectra corresponding to the Iodine region without presence of DIO was also given as a reference in Figure 3.10.

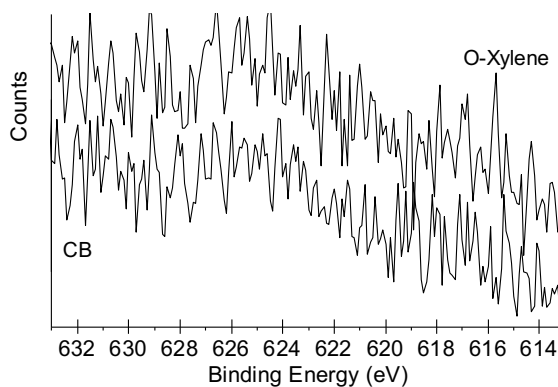


**Figure 3.10:** XPS Spectra of thin films of o-xylene and CB at Iodine B.E. region.

For the DIO containing thin films, the samples are scanned for I spectra at least 50 times during these measurements for the clear detection due to the very small percentage of DIO compared to CB solvent that the BHJ processed from. When annealed, the C-I peak is not seen any more which can be due to the removal of DIO from the top surface as shown in Figure 3.9. The F (KLL) line is from auger line which cannot be assigned to C-I species. Furthermore, the

experiment with higher DIO concentration (4% DIO) helped us immensely to identify the distinct Iodine peak positions in XPS as seen in Figure 3.11. Generally, software is used for the concentration calibration as the XPS peaks are used to quantitate particular groups besides the identification of elements. Here, relevant amounts are interpreted from area under the curve for the quantification of XPS spectra.

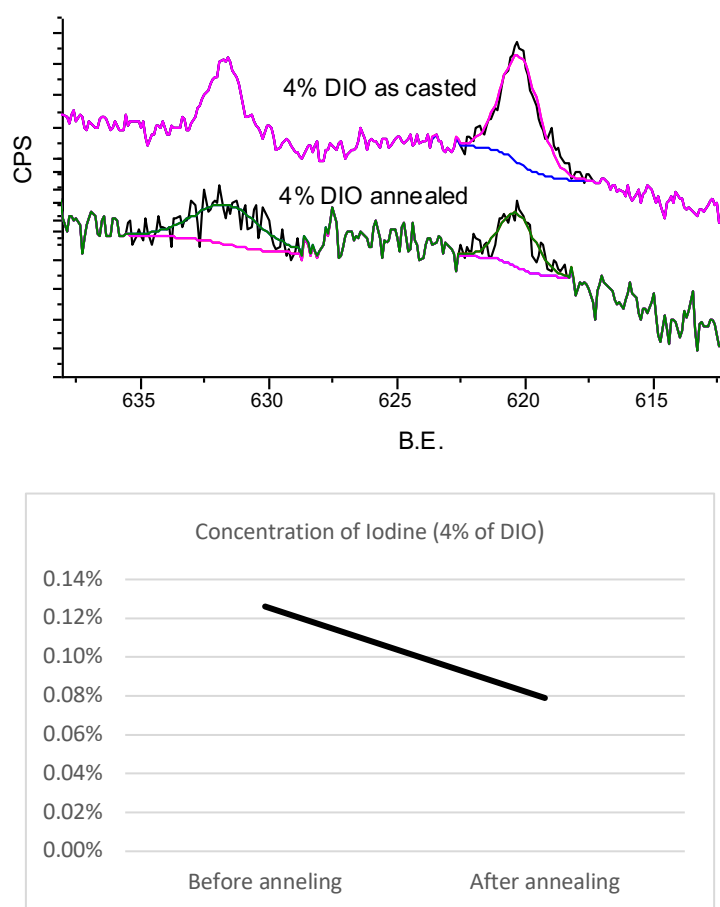


**Figure 3.11:** XPS Spectra and Concentration analysis of thin films processed with CB + 4% DIO

These CB+ 4% (v/v) DIO samples had the same peaks observed at 620 eV and the relative intensity of DIO dropped when the sample is annealed. In this case, DIO on surface was not completely removed even though we had high vacuum conditions from XPS and annealing. This is also suggesting DIO in the presence of ITIC is not possible to be removed completely even with excess drying treatments. Although DIO improves the ITIC packing and

enables good morphology for better cell performance and is still used as a popular additive in many organic solar cell research worldwide, in terms of stability of devices, we show that is indisputably unfavourable.

Therefore, it is very important to replace DIO additive for PTB7-Th polymer and ITIC acceptor systems to achieve stable OSCs with much better alternatives such as eco-friendly additive AA as we previously discussed in this study with photovoltaic characterizations.

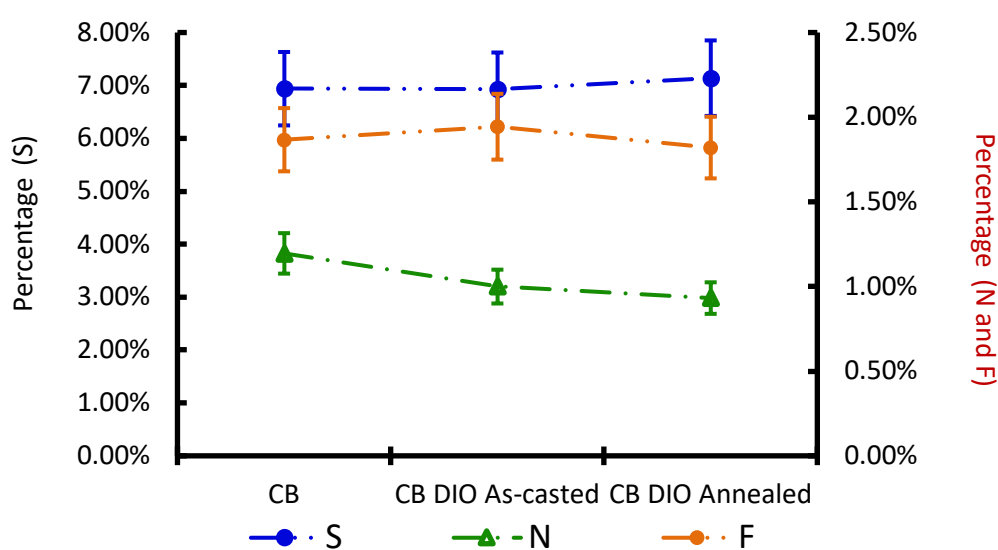


**Figure 3.12:** S vs N and F elemental composition analysis with thin films of CB, CB + DIO and CB + DIO annealed.

In Figure 3.12, N containing components are only coming from ITIC and F containing ones are coming from PTB7-Th. Thus, the XPS showing the relative concentration of these elements in samples with DIO amount can tell us about how ITIC migrates and get affected by DIO amount and possible co-crystallization. In a previous study <sup>34</sup>, they used XPS measurements for the same interpretation yet solubility and XPS studies cannot be enough to clarify this phenomenon without a depth profile study of NICISS or clear detection of I in surface and bulk of BHJ layer. In that study, they proposed ITIC migrates to surface as the amount of DIO increases with several characterizations. In our case, the polymer-acceptor is

the same but the technique for the film formation is only spin-coating. This vertical distribution of ITIC and PTB7-Th can be affected by fast and slow drying kinetics and DIO addition. The impractical removal of DIO from active layer due to its interaction with ITIC, possibly forming co-crystals, can also be deduced using XPS and NCISS in addition to STA and DMA studies. Although fast evaporation of DIO during spin-coating can reduce the possibility of formation of crystals, still the decreasing N on top surface as suggested by XPS can be the indication of how it is not released and stays in the bottom of the film with ITIC, agreeing with the NCISS analysis clarifying slower evaporation of DIO in the bulk of the BHJ film which to be discussed below. Thus, the favourable crystallinity is always hard to achieve using DIO additive unlike other solvent additives. The same trend can also be seen in the sample using o-xylene main solvent instead of CB as shown in Figure 3.13.

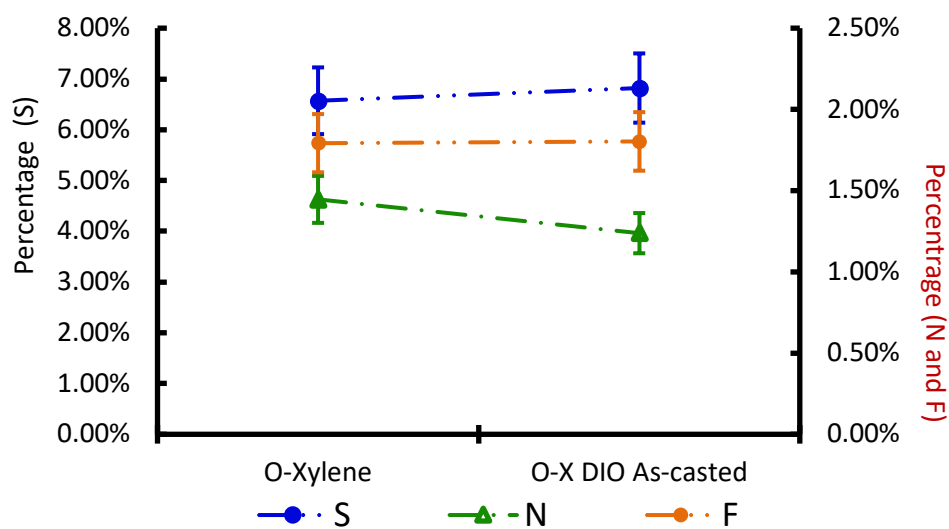


**Figure 3.13:** S vs N and F elemental composition analysis with thin films of o-xylene and o-xylene + DIO

NICISS, is used to determine the concentration depth profiles of the elements at soft-matter surfaces up to a depth of 20 nm. In this thesis, the Iodine (I) from DIO was determined and experimental conditions were modified specifically for the most accurate measurement. During NICISS measurements, the tests were performed at low temperatures (2-8°C) in order to avoid the excess removal of DIO from the organic thin films due to NICISS sample chamber's ultra-high vacuum conditions ( $1 \times 10^{-7}$  mbar). There was no set duration for cooling the NICISS sample chamber as the purpose was only to reduce excess vaporisation of DIO during measurement. The samples were prepared as same as they were used in device fabrication; thin films of PTB7-Th:ITIC blends (~100 nm) processed from CB:DIO (0.6% v/v) solvent mixture were spin-coated on ITO-glass substrates. For each sample, there were 5 scans every 20-30 minutes at the same spot of the thin film sample. The surface of the films was homogeneous in terms of the DIO distribution. For the reference sample from a previous experiment, the scan was done only at one location for longer time (~1.5 hours). The reason for this setup was firstly to avoid the risk of surface damage and excess solvent removal when we focused on one spot longer, and secondly, we needed to be clear if/how much DIO is getting removed by NICISS high vacuum conditions and how the spectra is changing over time. In NICISS measurement, it only penetrates on the surface within 10 nm in 2 hours with constant depth, so surface damage is not present in our samples.

Accordingly, the elements of interest, elemental ratios and depth profiles were investigated from the surface of the BHJ layer as well as its bulk properties.

Neutralized iodine from DIO can never be detected by XPS because it is immediately removed with ultra-high vacuum, yet C-I detection is aimed to be achieved even though we have very low concentration of DIO. The NICISS spectrum shows the elemental step or peak of I element, the backscattered projectiles of the element present in the target cause an energy loss which forms a step being specific to each element. As seen in Figure 3.14 below, iodine is

successfully found to be present both in as cast and annealed sample; the iodine step starts at 3.75 nm at calculated TOF when the I distribution is normalized.

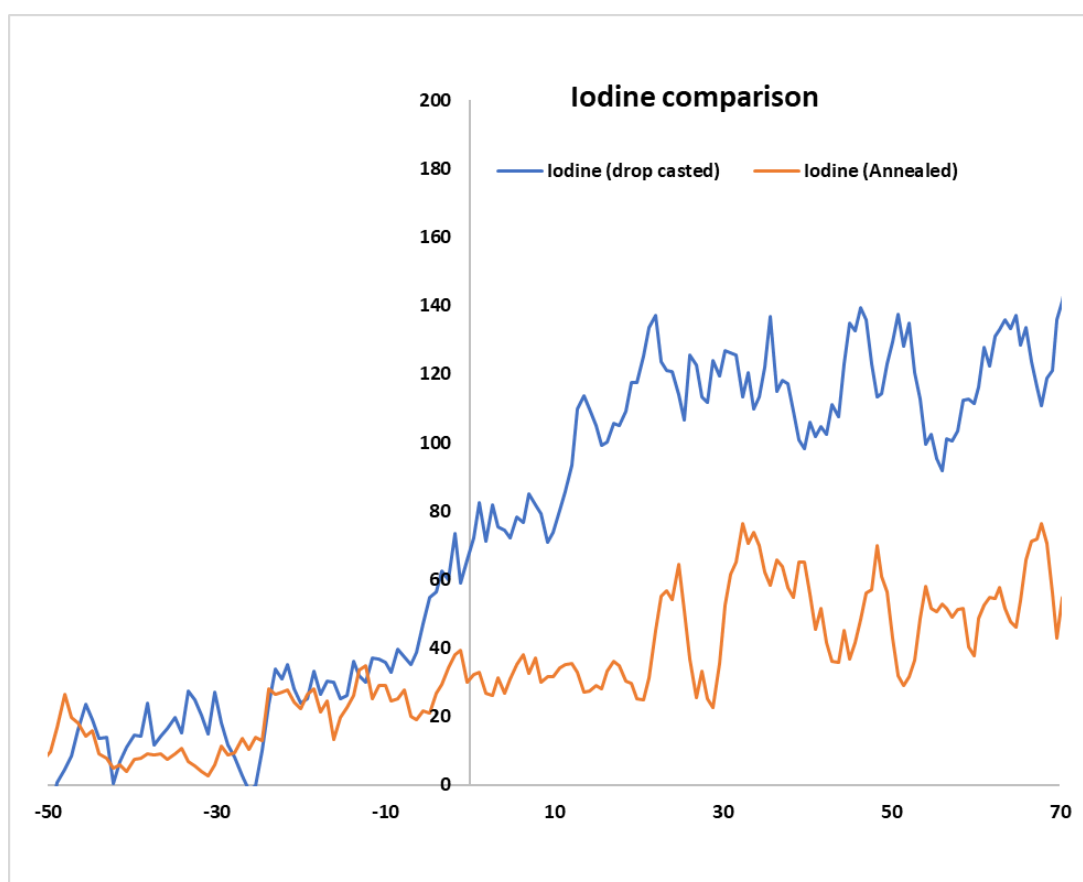


**Figure 3.14:** NICISS Spectrum for Iodine elemental comparison at as cast and annealed samples

There is a clear difference between reference CB and DIO as cast and annealed. But there is no difference in the depth composition. Before annealing, iodine sits on the sample surface and also distributing at least 7 nm layer in bulk. After annealing, the sharp decrease of the concentration of iodine is observed. There is still iodine left but mainly observed inside the bulk, which means the surface iodine is easily coming out. This suggests that at first DIO is getting removed from sample everywhere, however, surface iodine (top 2-3 nm) migrates at a quicker rate than that of the bulk (7nm) and leaves the surface which is also in agreement with our XPS measurements. Our interpretation for vertical distribution of ITIC is different than the

study done by L. Hou et. al <sup>16</sup> which eventually can be explained by the difference in sample preparation with a slower evaporation of DIO, hence more removal of DIO.

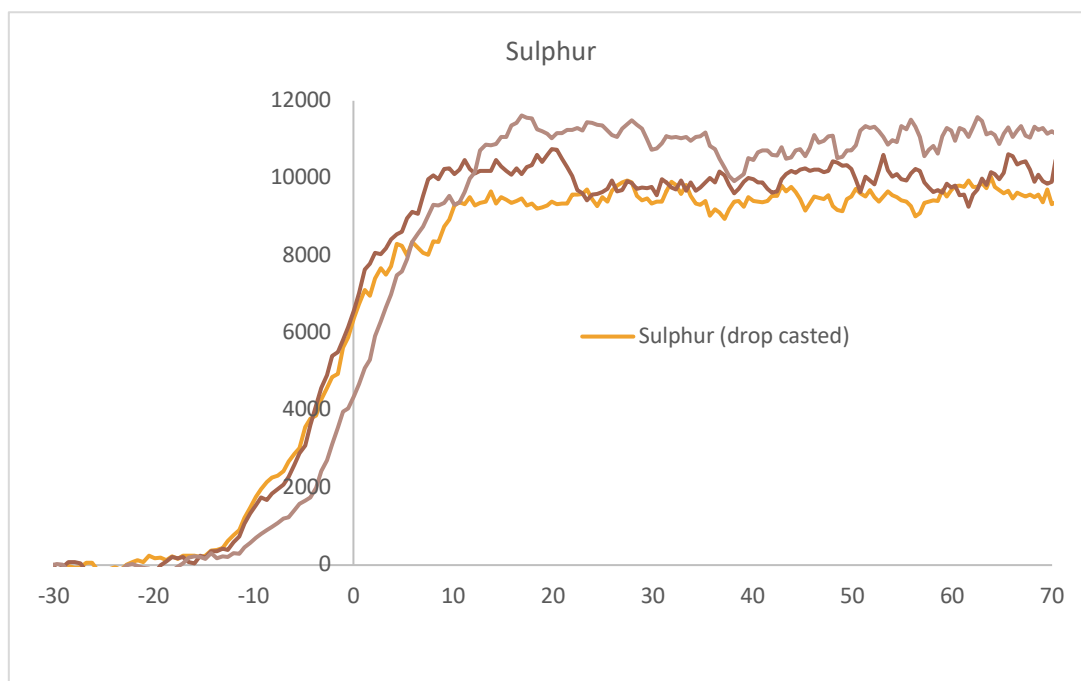


**Figure 3.15:** NICISS Depth profile spectra

The diffusion of Iodine in and out of the BHJ film was observed with NICISS, yet there were interesting results, and they are discussed later in combination with thermal studies.

The experiments suggest that remaining DIO removed immediately, forming more C-I species within the top PTB7-Th rich phase which readily evaporates; and C-I within ITIC rich bulk phase. This outcome agrees with XPS results and also DMA and STA thermal studies where it is reported that ITIC forms small crystals and DIO is only released after a recrystallization process which may be attributed to the trapped DIO in these crystals.

The C depth profile of pure polymer, BHJ blend as cast and annealed were also carried out where the conversion of elemental step from TOF range to concentration depth profile was also analysed as shown in Figure 3.15. A difference in carbon content or depth position for all samples is not observed.

Hence, For N and F elemental depth profiles could be useful, yet we need to run experiments for a much longer time and detect the elements from different spots to see the difference of chemical compositions on surface and bulk. The current experiments cannot detect it as N and F cross section is very close to S species for our BHJ blend. It can however be done as an accompanying experiment for future work.

### **3.5 Thermal Studies:**

Thermal stability and determination of crystalline features of these active layers were then studied to see the effect of DIO on ITIC as to further support XPS and NICISS results. Our previous findings suggested a possible interaction between DIO and ITIC.

The iodine from DIO were proved to be present and it also showed us how it can affect the arrangement of donor and acceptor molecules within the device with different surface treatments. A DIO removal study in which XRF is used to identify iodine also agrees with our results.<sup>49</sup> On top of identifying DIO in the active layer films, we suspected the interaction with ITIC and examined the crystallinity of different compositions. The findings from thermal studies showed us, with ITIC, significant weight loss ~ at 200-210 °C is present, and DIO is only released greatly after crystallization of ITIC suggesting that DIO always stays in the film among ITIC crystals during its “*polymorph I*” phase.<sup>17</sup> These experiments for STA and DMA are explained in detail below:

#### **3.5.1 STA studies:**

For efficient solar cell performance, besides the device efficiency and morphology optimization, long-term stability is also key, hence we also investigated thermal stability of

BHJ and analysed the effect of solvent additive and the thermal annealing. There are several degradation pathways, and in inverted OPVs, the major ways can be divided into those that stem from the kinetics of thin film drying during deposition of BHJ and also surface treatments to control initial morphology. The solvent additives enable the selective solvation of fullerenes /acceptor components and may decrease OPV performance due to the deteriorating blend morphology and disruption of optimum crystallinity. As mentioned in Chapter 2, two main techniques have been used in this study of the thesis which are STA and DMA also to discuss the possible DIO residual in the films. STA, combines TGA (thermal gravimetric analysis) where we determine the weight loss simultaneously with a DSC (differential scanning calorimetry) to detect the thermal transitions.

#### **3.5.1.1 STA experiments of PTB7-Th with and w/o DIO:**

The samples with excess ITIC were dried in glove-box antechamber overnight, they were cut into small pieces for STA measurement, each sample has ~3.5 mg. First, STA experiments were carried out and donor and acceptor were analysed separately in order to see the effect of DIO individually (Figure 3.24). Based on our STA results, it was suspected that DIO co-crystallise with ITIC and cannot be easily removed regardless of drying conditions. DIO is therefore stays in the film as concluded from these preliminary results and further investigated for the blends. It can also be deducted that DIO only releases after ITIC crystallization. The sample prepared with 0.6% DIO was only dried in the vacuum oven at rt. overnight.

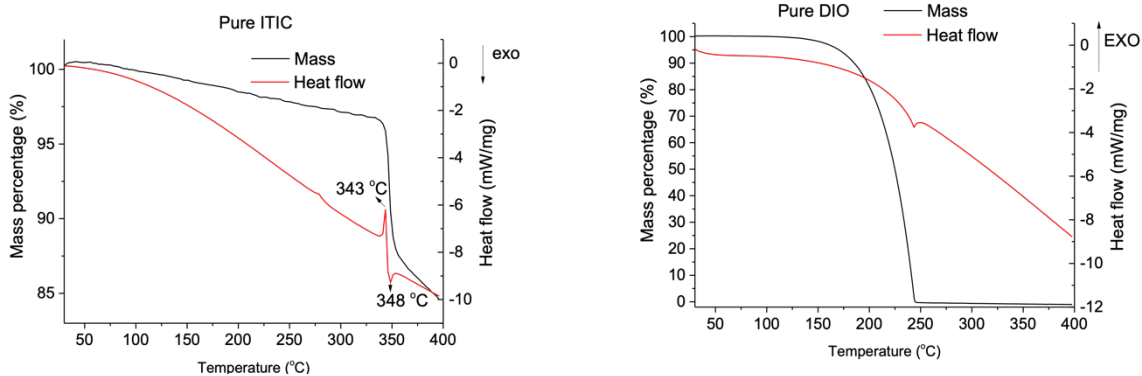


**Figure 3.16:** STA of pure ITIC and DIO.

As seen in Figure 3.16, the pure ITIC did not experience any significant weight loss below  $\sim 340$  °C, and an endothermic peak is found at 343 °C that is attributed to the melting of ITIC crystals, followed by an exothermic process at 348 °C that is a result from thermal degradation. We also measure the pure DIO sample and found it to completely evaporate below  $\sim 250$  °C as evidenced by the weight loss.

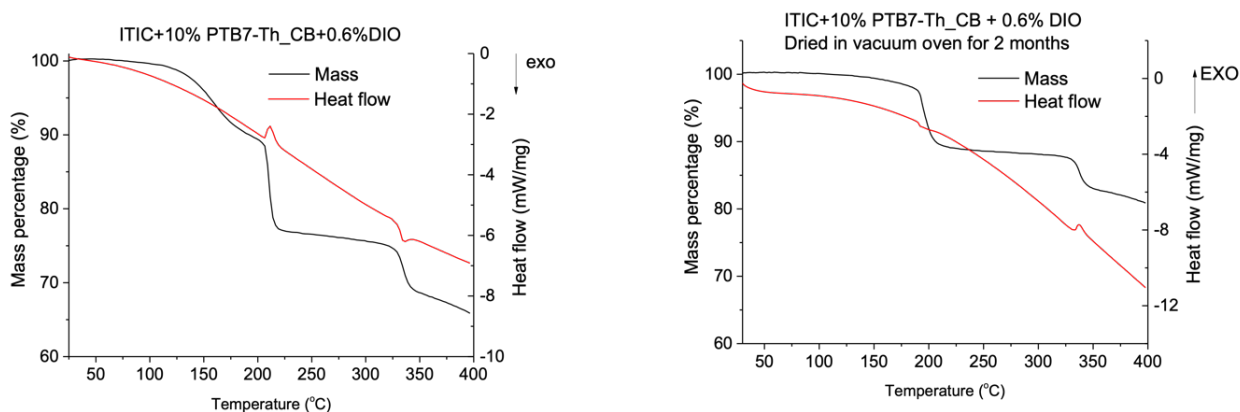


**Figure 3.17:** STA of ITIC + 10% PTB7-Th with and w/o DIO.

The ITIC + 10% PTB7-Th sample processed from CB with 0.6% DIO was then examined after drying in the vacuum oven at rt. overnight. STA analysis was given in Figure 3.17. An initial weight drop is found between 120 and 200 °C, which might be the residual CB in the sample. The most interesting feature is the big weight loss (10%) at  $\sim 200$  °C

accompanied by a clear endothermic peak, which we assume to be the removal of DIO from ITIC-DIO co-crystals. To eliminate the interference from residual CB and to test if DIO can be further removed by extended drying durations, an ITIC + 10% PTB7-Th sample was kept under vacuum over two months prior to the STA measurements. As expected, the initial weight loss below 200 °C is absent, however, the 200 °C weight loss still remained. We now can draw our preliminary conclusion that DIO remained in the film in the presence of ITIC.

This is further confirmed by examining the STA of PTB7-Th sample processed with DIO additive, where no weight loss was found before its thermal degradation (above 350 °C) given in Figure 3.18.

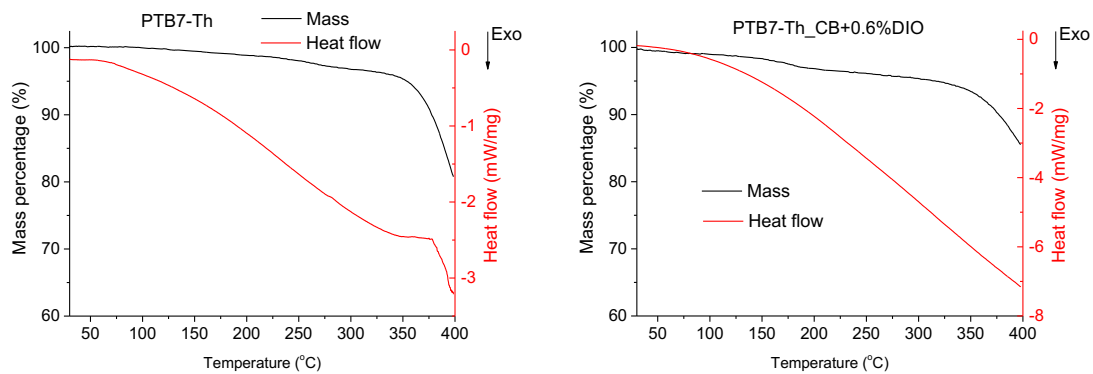


**Figure 3.18:** STA of PTB7-Th processed from CB with and w/o DIO.

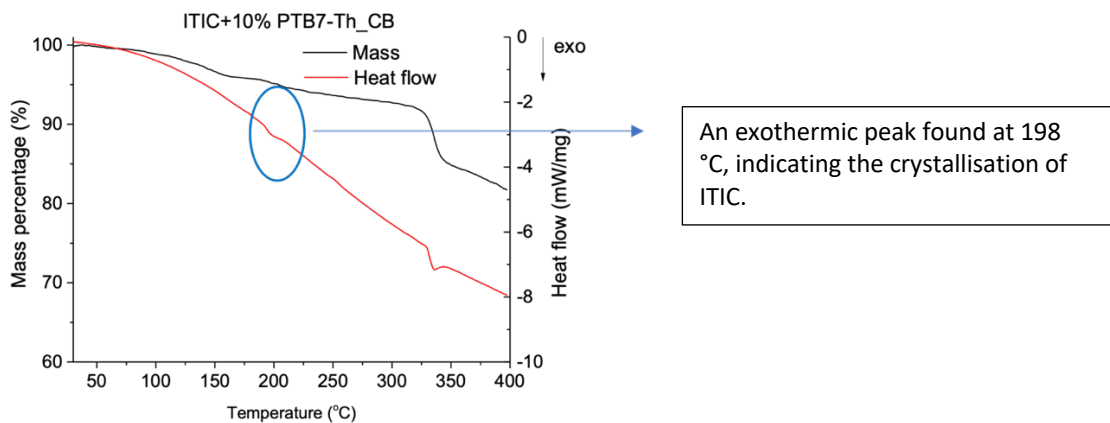


**Figure 3.19:** STA of ITIC + 10% PTB7-Th processed from CB w/o DIO.

Another ITIC + 10% PTB7-Th sample was prepared using only CB (Figure 3.19). In this case, no clear weight loss at 200 °C was found. But an exothermic peak was observed at ~200 °C, which we believe is the cold crystallisation of ITIC. Hence, another conclusion we can draw from here is that the release of DIO only occurred after the crystallisation of pure ITIC.

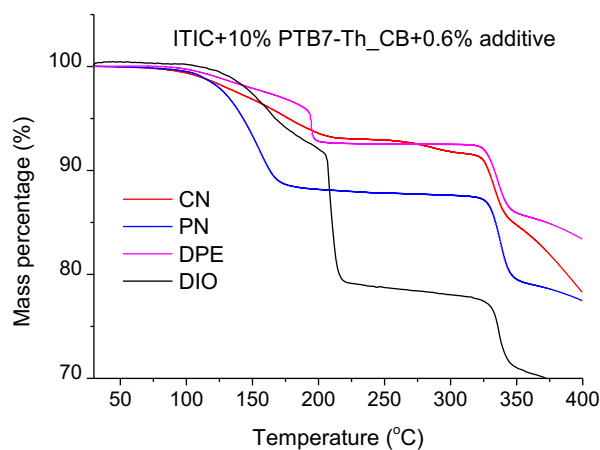


**Figure 3.20:** TGA of ITIC + 10% PTB7-Th processed from CN, PN, DPE and DIO.

To understand if other solvent additives behave similar to DIO; CN, PN, and DPE samples were examined using TGA and summarized in Figure 3.20. The bigger weight loss was found to be with DIO and hence investigated further, and an alternative eco-friendly solvent and solvent additive system was proposed and tested (o-xylene + AA). For 3 different drying conditions using only CB main solvent, STA was carried out and a comparison of mass percentages were given in Figure 3.21.

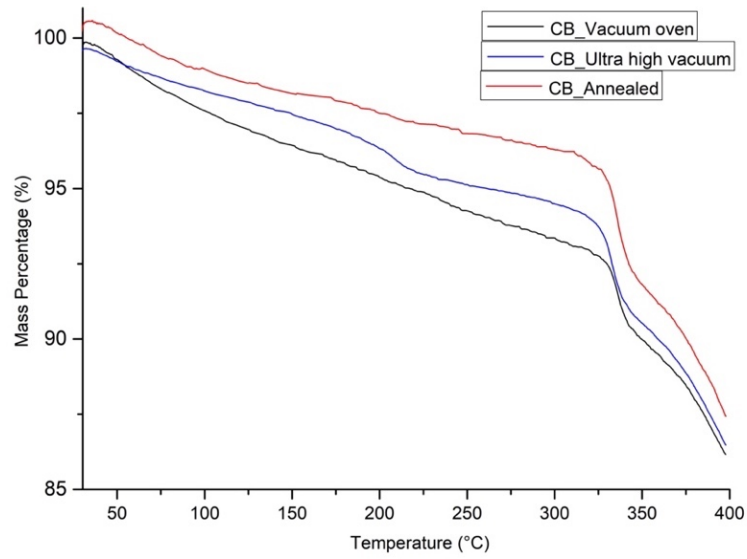


**Figure 3.21:** STA mass percentage comparison of blends of PTB7-Th: ITIC (1:1.3) processed from CB in different drying conditions.

Next the BHJ treated with CB and 0.6% DIO solvent additive samples were tested and mass percentage comparison was summarized below in Figure 3.22:

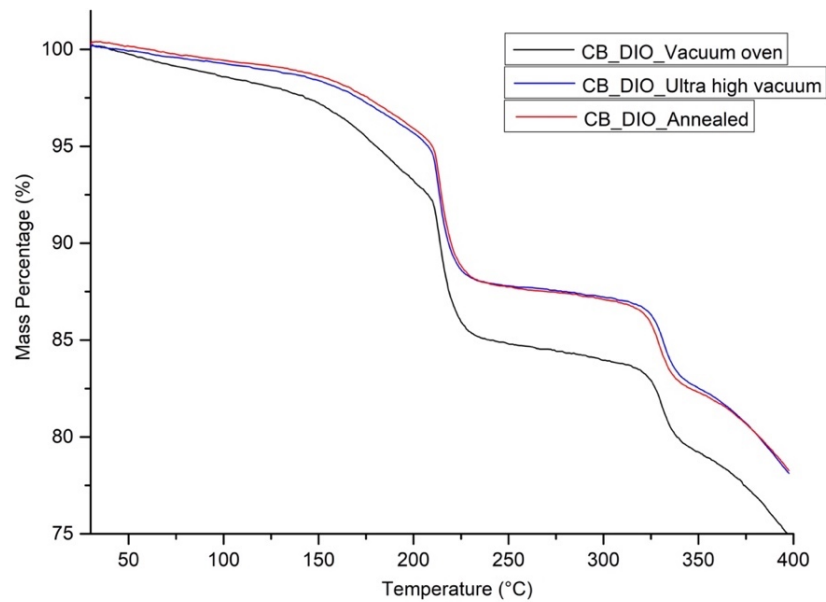


**Figure 3.22:** STA mass percentage comparison of blends of PTB7-Th: ITIC (1:1.3) processed from CB + 0.6% DIO in different drying conditions.

When we compare the weight losses in Figure 3.21 and 3.22, overall, there is still a significant amount of weight loss showing the evaporation of DIO from the sample. Also, we need to take into account that the biggest difference of sample preparation of STA and DMA samples compared to the OPV device fabrication is the thickness. It is almost a factor 10 thicker due to the difference between drop casting and spin coating techniques. As discussed earlier; in the NICISS measurements we cannot see the DIO, suggesting that we can remove the DIO from thin films similarly to the BHJ layer in the solar cell devices. The only condition we certainly see DIO in NICISS measurements ( $10^{-8}$  mbar) is when we cool down the sample holder with liquid  $N_2$  and it was easier to detect. Previously, it was harder to detect in XPS measurements, as well.

From these results, it is clear that when ITIC was processed from DIO containing solutions, the decrease in the weight loss is the most. As investigated through other methods, this interaction is very critical and even though it is difficult to determine whether it is physical or chemical, we showed the potential of using more complex techniques for exact determination of this interaction that degrades the OPVs processed in the presence of DIO. There are some studies suggesting use of NMR, FTIR and XRF of which we also conducted several experiments. The relevant results were given in Appendix for these additional experiments for potential future work. There are also photo-induced degradations due to DIO that furthers makes this system unfavourable for efficiency improvement of organic solar cells. The photodegradation studies were also carried out for discovering potential pathways of degradations and summarized followingly.

As our optimum devices are processed using eco-friendly solvent systems and proved to have the best performance; the thermal analysis studies were also performed on samples prepared using o-xylene and AA solvent additive and STA analysis is given below in Figure 3.23.

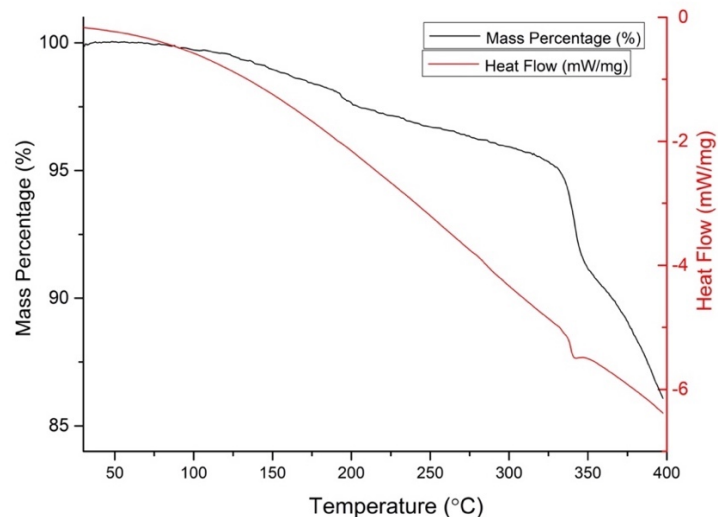


**Figure 3.23:** STA of PTB7-Th: ITIC (1:1.3) o-xylene + 2% AA vacuum dried.

It clearly shows that AA solvent additive was not remaining in the sample, and the mass percentage loss is negligible compared to that of the DIO containing samples.

### 3.5.2 DMA Studies:

DMA analysis was also carried out for both samples of PTB7-Th:ITIC (1:1.3) blends processed from CB main solvent (with and w/o DIO) for all 3 drying conditions. Compared to samples prepared using CB, the samples prepared from CB and DIO showed much higher  $E'$  and multiple crystallizations around 200 °C, suggested by the  $E'$  increase and peaks of  $E''$  (Figure 3.24).

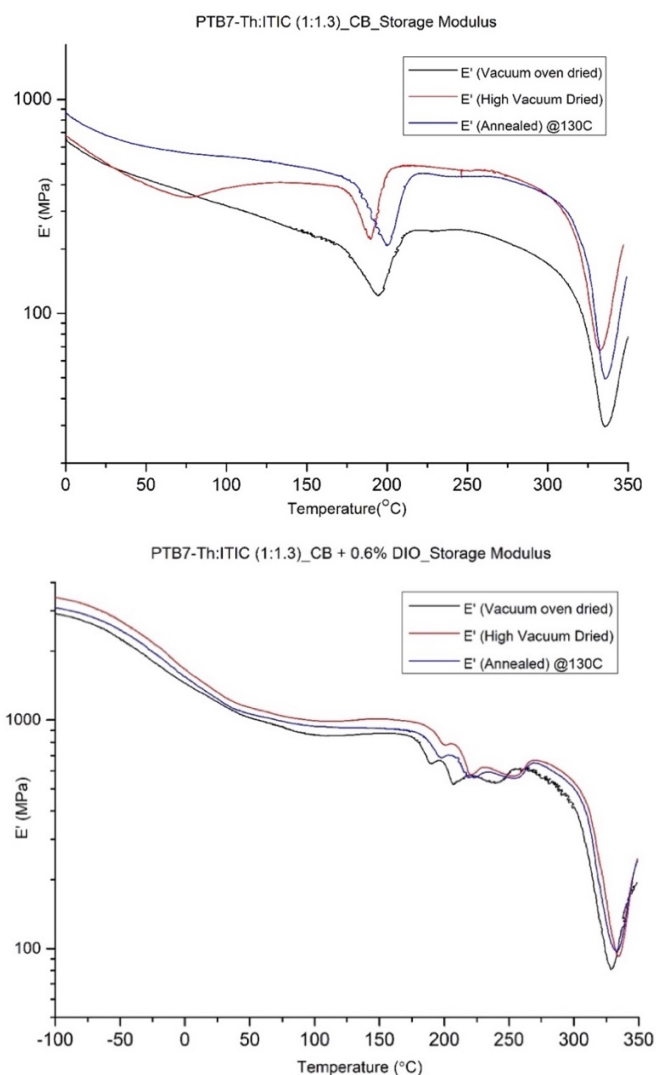


**Figure 3.24:** DMA storage modulus analysis of PTB7-Th:ITIC (1:1.3) processed from CB with and w/o DIO.

Order of  $E'$  in 3 drying condition when DIO present:  $E'$  high vac. ( $10^{-7}$  mbar) >  $E'$  An (130 °C) >  $E'$  vac. Oven ( $\sim 10^{-1}$ )

Among the different drying conditions with DIO, highest  $E'$  is with the high vacuum dried sample. This could indicate better stiffness and regulation of crystallinity. The PTB7-Th:ITIC samples prepared using DIO showed two clear sub-Tg transitions, which is not found in the CB processed ones (only a broad sub-Tg peak was found). The two sub-Tgs could be originated from the side-chain relaxation of PTB7-Th and ITIC, respectively, indicating that DIO induced higher degree of phase separation compared to CB.

The cold crystallization (195°C) is more significant in the case of samples prepared using just CB compared to the samples prepared using CB with DIO. This could be a result from the pre-formed crystals between ITIC and DIO, thus, less crystals can be formed during the heating process in the DMA measurements.

Comparisons of both blends in 3 drying conditions (CB & CB+DIO) samples were also done, as high vacuum is also the best condition for device fabrication from CB, the comparison in high vacuum is given below in Figure 3.25.

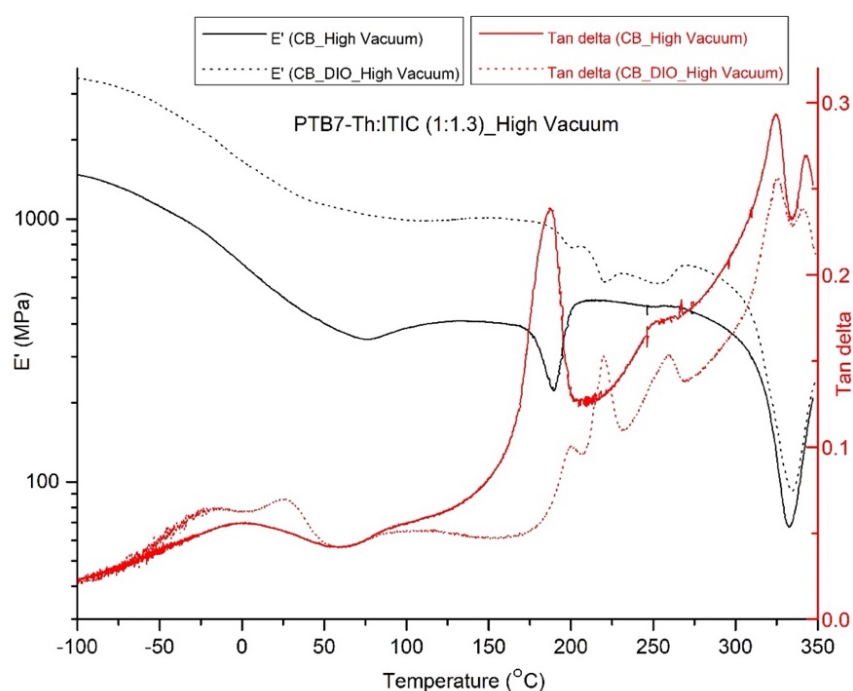


**Figure 3.25:** DMA of PTB7-Th:ITIC (1:1.3) processed from CB with and w/o DIO in high vacuum.

The DIO containing sample showed high  $E'$ , suggesting higher stiffness, which could also be caused by the pre-formed crystals.

Lastly, o-xylene and 2% AA additive system was also analysed as it gives the best performance using eco-friendly solvent system. As AA solvent additive showed to be not present in the film and not interacting with ITIC, the samples were dried in vacuum and tested afterwards. Even without further drying, there is no weight loss indicating residual AA additive which support our device analysis as seen in DMA analysis in Figure 3.26.

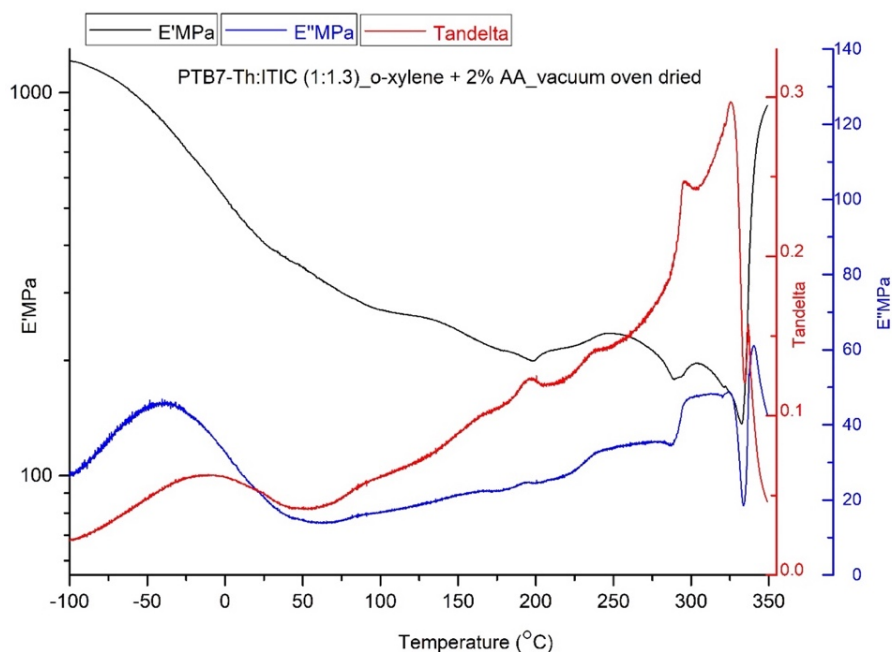


**Figure 3.26:** DMA of PTB7-Th:ITIC (1:1.3) processed from o-xylene with 2% AA.

### 3.6 XRD and P-XRD Studies of PTB7-Th:ITIC (1:1.3) thin films:

XRD studies were carried also out in order to identify the interactions between ITIC and DIO additive, later P-XRD studies were found to be more compatible as they can be done using thin films of our blends, P-XRD images were obtained to compare the effect and additions of DIO. The results need further processing with more enhanced database because the iodine from our samples were not individually identified from the present XRD instrument. Several similar structures were compared and showed to support our results indirectly.

### 3.6.1 STA of ITIC crystals formed via slow crystallization in the presence of DIO:

We also carried out an experiment where ITIC was used with the presence of DIO for its slow crystallization and without any treatments for DIO removal, these crystals were examined using STA. The XRD studies of the crystals did not give a conclusive result and can be further studied using advanced instruments. As shown in Figure 3.27, the slowly formed ITIC crystals do not contain DIO, and an endothermic peak at 281°C indicates the melt of crystals. Further XRD studies can also be carried out using these ITIC crystals for our future studies for comparison.

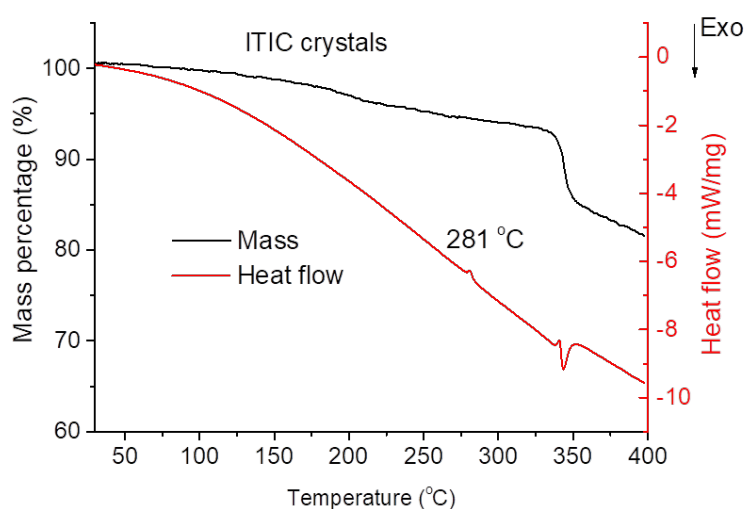


**Figure 3.27:** STA of ITIC crystal in the presence of DIO developed by slow crystallization.

The slow crystallization process for the interaction of ITIC and DIO has different drying kinetics however in nanoscale the same interaction was identified with thermal and surface characterization techniques. In future more characterizations can be carried out on this topic. It is proposed that ITIC prevents PTB7-Th to be photodegraded with an orderly packing and increases the efficiency, and DIO actually contributes to this stability even more to the point where it also causes degradation by staying in the active layer. The exact type of this

interaction can be studied furthermore in the future via SEM-EDX. NMR studies can also be done to detect the individual changes and interaction of ITIC and DIO.

### 3.7 Conclusion:

In Chapter 3, PTB7-Th donor polymer and ITIC non-fullerene acceptor blend was extensively studied in presence of several solvent systems. DIO solvent additive was among these solvents as a high boiling point and toxic additive which is popular in PSC fabrication for their well-tuning of morphology. However, due to the toxicity and difficulty of DIO to remove its residues from BHJ thin films, we first decided to identify the drawbacks of using DIO in this BHJ blend and then offered a better and eco-friendly method for better performing polymer solar cells.

The first preliminary experiments confirmed the increasing efficiencies in PTB7-Th:ITIC based PSCs using DIO additive, so we systematically optimized the concentration and other solvent systems for better performance and eco-friendliness. The o-xylene main solvent and AA additive performed the best in many device batches compared to DIO, and other solvent additives. The best device gave a maximum power conversion efficiency of 8.5% from o-xylene + 2% AA additive. In literature, this combination has been mostly used for fullerene acceptors paired with PTB7-Th, so it was significant to show the effectiveness of AA additive in non-fullerene PSC fabrication. Topography analysis via AFM supported our results along with roughness measurements of several blends as well as optimizing the best devices with XPS, NISS, STA, and DMA characterizations.

In this research, most importantly, we focused on the remaining DIO in the active layer, the reasons behind this residue occurrence, particularly when interacted with ITIC acceptor. XPS and NISS surface analysis showed us the residual iodine from DIO. XPS spectra of samples with higher DIO gave higher signals in the corresponding iodine elemental region detecting its presence. As the signals were not high enough due to the concentration of I in the sample, to be certain we further examined the samples processed in the presence of DIO and

without DIO, using NICISS, STA and DMA studies. NICISS analysis was found to be effective when the sample chamber was cooled down to avoid evaporation of DIO, and Iodine was identified in DIO containing sample.

After these findings, in order to effectively remove the DIO additive, 3 drying techniques were also compared through each characterization. High vacuum drying found to be the most effective compared to annealing and vacuum drying in all our characterizations which also supported our solar cell photovoltaic properties. These complimentary findings are crucial for future studies in terms of fabrication of polymer solar cells, eco-friendly solvent processing, extensive usage in large-scale and printable applications.

### **3.8 Contributions:**

*Dr. Yanting Yin: Performed XPS measurements and data interpretation.*

*Dr. Caroline Pan: Assisted with measurement and data interpretation of STA and DMA.*

*Anand Kumar: Assisted with NICISS measurement and data interpretation.*

*Bradley Kirk: Performed AFM measurements of active layers.*

*Alex Sibley: Assisted with PXRD measurements and data interpretation.*

*Prof. Mats Andersson: Assisted with experiment design and the interpretation of device data.*

### 3.9 References:

1. Liao, S. H., Jhuo, H. J., Cheng, Y. S., and Chen, S. A. (2013). "Fullerene derivative doped zinc oxide nanofilm as the cathode of inverted polymer solar cells with low-bandgap polymer (PTB7-Th) for high performance" *Adv. Mater.* 25, 4766–4771.
2. Lin, Y., Wang, J., Zhang, Z. G., Bai, H., Li, Y., Zhu, D., et al. (2015). "An electron acceptor challenging fullerene for efficient polymer solar cells" *Adv. Mater.* 27, 1170–1174.
3. Wang, W., Yan, C., Lau, T. K., Wang, J., Liu, K., Fan, Y., et al. (2017). "Fused hexacyclic nonfullerene acceptor with strong near-infrared absorption for semitransparent organic solar cells with 9.77% efficiency" *Adv. Mater.* 29, 1701308.
4. Su, W., Fan, Q., Guo, X., Wu, J., Zhang, M., and Li, Y. (2019) "Efficient as-cast semi-transparent organic solar cells with efficiency over 9% and a high average visible transmittance of 27.6" *Phys. Chem. Chem. Phys.* 21, 10660–10666.
5. Qian, D., Ye, L., Zhang, M., Liang, Y., Li, L., and Huang, Y., et al. (2012) "Design, application, and morphology study of a new photovoltaic polymer with strong aggregation in solution state." *Macromolecules* 45, 9611–9617.
6. Zhao, W., Qian, D., Zhang, S., Li, S., Inganas, O., Gao, F., et al. (2016) "Fullerene free polymer solar cells with over 11% efficiency and excellent thermal stability" *Adv. Mater.* 28, 4734–4739.
7. Zhang, M., Guo, X., Ma, W., Ade, H., and Hou, J. (2015) "A Large bandgap conjugated polymer for versatile photovoltaic applications with high performance" *Adv. Mater.* 27, 4655–4660.
8. Cui, Y., Yao, H., Zhang, J., Zhang, T., Wang, Y., Hong, L., et al. (2019) "Over 16% efficiency organic photovoltaic cells enabled by a chlorinated acceptor with increased open-circuit voltages" *Nat. Commun.* 10:2515.
9. Gao, L., Zhang, Z. G., Bin, H., Xue, L., Yang, Y., Wang, C., et al. (2016a) "High efficiency nonfullerene polymer solar cells with medium bandgap polymer donor and narrow bandgap organic semiconductor acceptor" *Adv. Mater.* 28, 8288–8295.
10. Gao, L., Zhang, Z. G., Xue, L., Min, J., Zhang, J., Wei, Z., et al. (2016b) "All-polymer solar cells based on absorption-complementary polymer donor and acceptor with high power conversion efficiency of 8.27%" *Adv. Mater.* 28, 1884–1890.
11. Lin, Y., Zhao, F., Prasad, S. K. K., Chen, J. D., Cai, W., Zhang, Q., et al. (2018) "Balanced partnership between donor and acceptor components in nonfullerene organic solar cells with >12% efficiency" *Adv. Mater.* 30:1706363.
12. Liu, Q., Jiang, Y., Jin, K., Qin, J., Xu, J., Li, W., et al. (2020) "18% efficiency organic solar cells." *Sci. Bull.* 65, 272–275.
13. Qiu D, Adil MA, Lu K and Wei Z (2020) "The Crystallinity Control of Polymer Donor Materials for High-Performance Organic Solar Cells" *Front. Chem.* 8:603134.

14. Doumon, N. Y., Dryzhov, M. V., Houard, F. V., Le Corre, V. M., Rahimi Chatri, A., Christodoulis, P., and Koster, L. J. A. (2019) "Photostability of Fullerene and Non-Fullerene Polymer Solar Cells: The Role of the Acceptor." *ACS Applied Materials & Interfaces*, 11(8), 8310-8318.
15. Park, S., & Son, H. J. (2019) "Intrinsic photo-degradation and mechanism of polymer solar cells: the crucial role of non-fullerene acceptors" *Journal of Materials Chemistry A*, 7(45), 25830-25837.
16. Lin, Y., Jin, Y., Dong, S., Zheng, W., Yang, J., Liu, A., Hou, L. (2018) "Printed Nonfullerene Organic Solar Cells with the Highest Efficiency of 9.5%" *Advanced Energy Materials*, 8(13), 1701942.
17. Yu, L., Qian, D., Marina, S., Nugroho, F. A. A., Sharma, A., Hultmark, S., Müller, C. (2019). "Diffusion-Limited Crystallization: A Rationale for the Thermal Stability of Non-Fullerene Solar Cells" *ACS Applied Materials & Interfaces*, 11(24), 21766-21774.
18. Smallwood, I. M. (1996). Toulene. In I. M. Smallwood (Ed.), *Handbook of Organic Solvent Properties*. Oxford: Butterworth-Heinemann.
19. Ye, L., Weng, K., Xu, J., Du, X., Chandrabose, S., Chen, K., Sun, Y. (2020) "Unraveling the influence of non-fullerene acceptor molecular packing on photovoltaic performance of organic solar cells" *Nature Communications*, 11(1), 6005.
20. Zusan, A., Giesecking, B., Zerson, M., Dyakonov, V., Magerle, R., and Deibel, C. (2015) "The Effect of Diiodooctane on the Charge Carrier Generation in Organic Solar Cells Based on the Copolymer PBDTTT-C" *Scientific Reports*, 5(1), 8286.
21. Song, X., Gasparini, N., and Baran, D. (2018) "The Influence of Solvent Additive on Polymer Solar Cells Employing Fullerene and Non-Fullerene Acceptors" *Advanced Electronic Materials*, 4(10), 1700358.
22. Wang, C., Gann, E., Chesman, A. S. R., and McNeill, C. R. (2019) "Residual solvent additive enables the nanostructuring of PTB7-Th:PC<sub>71</sub>BM solar cells via soft lithography" *AIP Advances*, 9(6), 065024.
23. Zhao, L., Zhao, S., Xu, Z., Qiao, B., Huang, D., & Xu, X. (2016) "Two effects of 1,8-diiodooctane on PTB7-Th:PC<sub>71</sub>BM polymer solar cells" *Organic Electronics*, 34, 188-192.
24. Tremolet de Villers, B. J., O'Hara, K. A., Ostrowski, D. P., Biddle, P. H., Shaheen, S. E., Chabynyc, M. L., Kopidakis, N. (2016) "Removal of Residual Diiodooctane Improves Photostability of High-Performance Organic Solar Cell Polymers" *Chemistry of Materials*, 28(3), 876-884.
25. Mica, N. A., Thomson, S. A. J., & Samuel, I. D. W. (2018). Electron mobility of non-fullerene acceptors using a time of flight method. *Organic Electronics*, 63, 415-420.
26. Vijayan, R., Azeez, A., and Narayan, K. S. (2020) "Toward reliable high performing organic solar cells: Molecules, processing, and monitoring" *APL Materials*, 8(4), 040908.

27. Holliday, S., and Luscombe, C. K. (2018) "Low Boiling Point Solvent Additives for Improved Photooxidative Stability in Organic Photovoltaics" *Advanced Electronic Materials*, 4(10), 1700416.
28. Doumon, N. Y., Wang, G., Qiu, X., Minnaard, A. J., Chiechi, R. C., and Koster, L. J. A. (2019) "1,8-diiodooctane acts as a photo-acid in organic solar cells" *Scientific Reports*, 9(1), 4350.
29. Jacobs, I. E., Wang, F., Bedolla Valdez, Z. I., Ayala Oviedo, A. N., Bilsky, D. J., and Moulé, A. J. (2018). "Photoinduced degradation from trace 1,8-diiodooctane in organic photovoltaics" *Journal of Materials Chemistry C*, 6(2), 219-225.
30. Xie, Y., Hu, X., Yin, J., Zhang, L., Meng, X., Xu, G., Chen, Y. (2017) "Butanedithiol Solvent Additive Extracting Fullerenes from Donor Phase To Improve Performance and Photostability in Polymer Solar Cells" *ACS Applied Materials & Interfaces*, 9(11), 9918-9925.
31. Yan, Y., Li, W., Cai, F., Cai, J., Huang, Z., Gurney, R. S., Wang, T. (2018) "Correlating Nanoscale Morphology with Device Performance in Conventional and Inverted PffBT4T-2OD:PC<sub>71</sub>BM Polymer Solar Cells" *ACS Applied Energy Materials*, 1(7), 3505-3512.
32. Fontana, M. T., Kang, H., Yee, P. Y., Fan, Z., Hawks, S. A., Schelhas, L. T., Schwartz, B. J. (2018) "Low-Vapor-Pressure Solvent Additives Function as Polymer Swelling Agents in Bulk Heterojunction Organic Photovoltaics" *The Journal of Physical Chemistry C*, 122(29), 16574-16588.
33. Zhao, X., Zhao, J., Wu, R., Liu, D., Wang, G., Li, P., Song, Q. (2017) "Impact of additive residue on the photodegradation of high performance polymer solar cells" *Organic Electronics*, 49, 226-233.
34. Jiang, X., Kim, H., Deimel, P. S., Chen, W., Cao, W., Yang, D., Müller-Buschbaum, P. (2020) "Internal nanoscale architecture and charge carrier dynamics of wide bandgap non-fullerene bulk heterojunction active layers in organic solar cells" *Journal of Materials Chemistry A*, 8(44), 23628-23636.

# CHAPTER 4

## **Optimizing polymer solar cells using non-halogenated solvent blends**

This chapter is a modified version of the published article *Optimizing Polymer Solar Cells Using Non-Halogenated Solvent Blends*. *Polymers*, 2019, 11, 544. with additional information and measurements added. These include the preliminary photovoltaic characterizations for experiments of solar cells with different active layer thicknesses and donor-acceptor blend ratios.

## 4.1 Introduction:

For over a decade, the advancements of organic solar cells (OSCs) have made an exceptionally great impact among the researchers working on solar energy technologies. The high-performance solar cells have been vastly studied and optimized where record power conversion efficiencies (PCEs) of up to 18% was achieved recently which make these cells as effective as their inorganic counterparts.<sup>1</sup> The popularity of organic solar cells is not only for their increasing efficiencies but also due to their versatility for fabricating cost-efficient, eco-friendly, thin, flexible and light-weight devices.<sup>2-3</sup>

Nonetheless, there are still some challenges present to be eliminated for the production of the best organic solar cell devices. The first challenge is to create efficient charge transport in the organic photoactive layer in which the absorption of photons creates the electrons and holes to travel throughout the device. The device architecture design helps for this challenge with a bulk heterojunction (BHJ) system to achieve a well-mixed donor-acceptor blend processed from a common solvent.<sup>4</sup> Another challenge is the short exciton diffusion distance (~10 nm) which limits the solar cell architecture for achieving exciton dissociation on the interface of donor-acceptor materials that absorb light for the photocurrent generation. The BHJ system and morphology optimization are also helpful for the exciton diffusion.<sup>5-6</sup> The solvents used for the formation of the active layer have also been one of biggest challenges for the best performing solar cells. The most commonly used traditional solvents are halogenated and toxic, and therefore not preferable for large scale industrial manufacturing as it is mostly an ambient atmosphere process.<sup>7</sup> These solvents are also accompanied by popular solvent additives for better active layer morphology. However, these additives are mostly not eco-friendly, too. On the contrary, using less-toxic non-halogenated solvents have led the way to the eco-friendly fabrication methods and increased their significance crucially in OSC fabrication.<sup>8-10</sup>

Therefore, in this study, we aimed to show the effects of using solvent additives on polymer solar cell performance and to create novel environmentally friendly small-scale prototype devices to be used in large-scale manufacturing and roll-to-roll processing. The best green solvent to be employed ultimately is the water and it is indeed possible to process solar cells with water in the case of devices using active layers formed by polymer nanoparticles (PNPs).<sup>11-12</sup> Alcohols are also considered as potential well-known green solvent alternatives for the upscaling.<sup>13</sup>

Yet, the most frequently used solvents for the organic solar cells are not green solvents like water or alcohol; they are mostly chlorinated and toxic such as chloroform, chlorobenzene (CB) and *o*-dichlorobenzene (*o*-DCB); in addition, the two widespread toxic solvent additives used are 1-chloronaphthalene (CN) and 1,8-diiodooctane (DIO).<sup>14-15</sup> These additives have been studied extensively and they have been very advantageous on the increased performance of OSCs.<sup>16-17</sup> Whereas, the alternative solvent system selected for this study has a non-toxic main solvent *o*-xylene in combination with various less-harmful solvent additives. These different solvent systems dissolve the donor polymer and fullerene acceptor blends to be deposited as a thin photo-active layer of OSC devices.

Earlier, PTNT donor polymer was already found to show good device performance when processed from a toxic solvent system, but the device structure being conventional resulted in poor device stability and a lack of environmental friendliness has been a drawback.<sup>18</sup>

PTNT is also moderately soluble in many halogenated and non-halogenated common solvents and its ability to form a relatively thick photoactive layer makes it a good candidate for large area and flexible polymer solar cell manufacturing.<sup>19</sup> The acceptor chosen in this study was PC<sub>71</sub>BM which has higher photon absorption capacity than PC<sub>61</sub>BM. In addition, it has a well-matched energy alignment with the donor polymer facilitating good active layer morphology and efficient charge transport for a stable solar cell device performance.<sup>15, 20</sup>

Several other optimizations for improved morphology have also been another challenging part of the fabrication of organic solar cells. The surface treatment techniques to achieve better active layer morphologies require the formation of good phase separation between homogeneously well-mixed donor-acceptor species in the photo-active layer of the device. As a result; greater charge separation, good charge transport properties and high stability are achieved. <sup>4, 21</sup>

One of the most commonly used treatments is the ‘annealing’ of the active layer in order to modify the nanoscale morphology. <sup>22-23</sup> As annealing is also a fast-drying technique, the two critical parameters to be considered are the temperature and the duration of the heating of the active layer. Thus, this treatment dramatically changes the degree of the crystallinity which should not be severely increased either in BHJ blends. Other treatments are ‘solvent vapor annealing’ and use of ‘solvent additives’ both of which may cause different effects on the morphology than that of the annealing technique. <sup>24-25</sup> It is better to first gain insight about the dynamics of these effects as they differ depending on the donor-acceptor blend system and on the technique of the coating of the thin film layer.

In solvent additive morphology treatment, the additives usually have much higher boiling points (BPs) than that of the main solvents and they dissolve the individual components of the blends in different durations and with different degrees of solubility. <sup>26</sup> Thus, the well intermixed blends provide better and smoother nanoscale morphology. They can also facilitate a superior phase separation than halogenated toxic solvents. <sup>27</sup>

After overcoming these challenges, prior to the device fabrication step, a surface characterization technique such as Atomic Force Microscopy (AFM) is also used to examine the fine tuning of the nanoscale morphology. In this current study, AFM analysis of the photo-active thin layers allowed us to compare the effects of different additives in terms of optimized nanostructure, photophysical properties and film thickness and how to improve them

practically. Accordingly, the ultimate purpose was the optimization of these active layers for the best eco-friendly and efficient device to be used in the flexible polymer solar cell applications and large-scale processing for the upcoming future research.

There are many studies that focus on the cost-efficient way of manufacturing these types of solar cells, as well.<sup>28</sup> Thus, we also aim to prevent material waste by carefully planning each step of the fabrication and using other possible ways to achieve non-harmful solar cell devices unlike the previous studies. So far, for the PTNT:PC<sub>71</sub>BM bulk heterojunction solar cell structure, the best cell efficiency using halogenated solvents are found to be around 5% in an initial OPV study.<sup>18</sup> The ongoing studies using more additional materials in the active layer or solvents make them less cost efficient and unlikely to upscale, too. The state-of-the-art polymer solar cells need to be fabricated using the simplest, cheapest and eco-friendliest techniques for their potential to have wide usage and applicability in large-scale manufacturing.

Hence, in this chapter, we focused on the use and optimization of eco-friendly fabrication techniques without compromising from other advantageous properties and achieving higher efficiencies using non-toxic solvent systems. These systems for depositing the photo-active layer are made of non-toxic *o*-xylene and several additives that are both toxic and non-toxic to compare their performance. The 1-methoxynaphthlene (1-MN) and 1-phenylnaphthalene (1-PN) additives gave average power conversion efficiencies (PCEs) of 6.0 % and 5.2% which are better than that of the halogenated ones and these eco-friendly devices also showed stable performance. Consequently, they were proved to be much more suitable for the large-scale production and flexible devices without giving any harm to the environment and health. The halogenated devices processed with 1,8-diiodooctane (DIO) and 1-chloronaphthalene (CN) solvent additives were also tested with *o*-xylene main solvent and they showed average efficiencies of 4.9% and 3.7%. The photophysical studies also showed the extent of the well-mixing by using different solvent systems. The photoluminescence

quenching when using MN and PN additives became the evidence for the extensive energy transfer which are also compatible with the corresponding device performances. In summary, 1-1-methoxynaphthalene (MN) is both a non-harmful and novel solvent additive for the upscaling of efficient eco-friendly flexible polymer solar cells. It has not been used before as a processing solvent additive for the enhancement of polymer solar cell morphology to the extent of our knowledge and furthermore found to be the best performing solvent additive in this study.

The materials and their structures used for this study are given below in Figure 4.1.

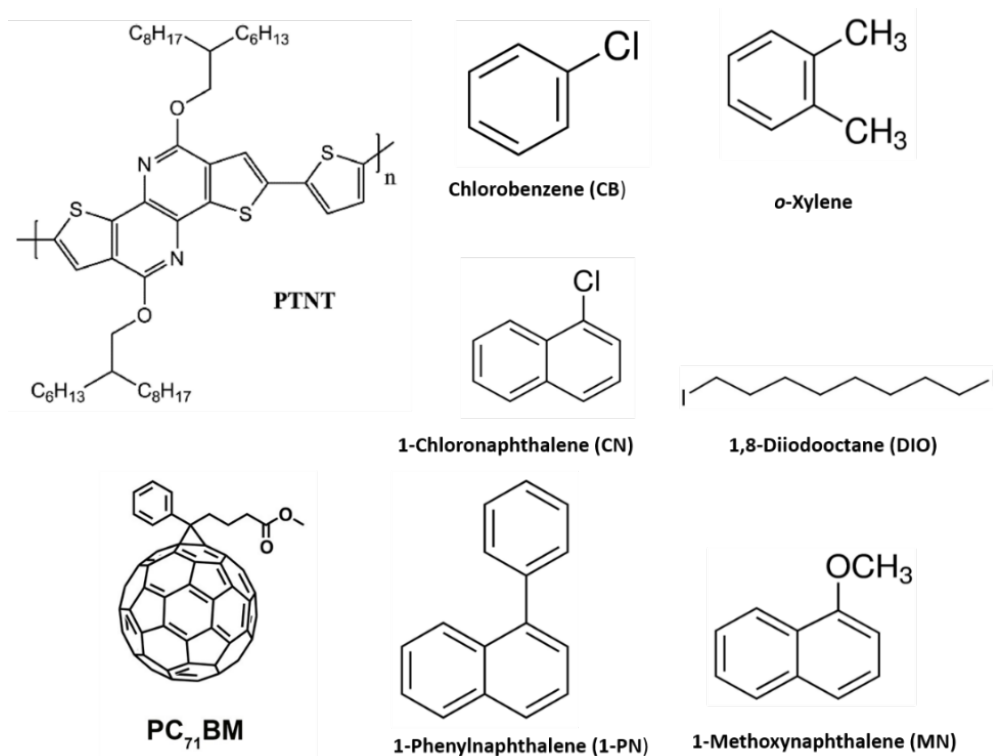


**Figure 4.1:** Chemical structures of PTNT, o-xylene, and solvent additives used in BHJ blends.

## 4.2 Methodology:

### 4.2.1 Materials:

[6,6]-phenyl- $C_{71}$ -butyric acid methyl ester (PC<sub>71</sub>BM) (purity > 99%) was purchased from Solenne BV. Poly(2,5-thiophene-alt-4,9-bis(2-hexyldecyl)-4,9-dihydrodithieno[3,2-c:3',2'-h][1,5]naphthyridine-5,10-dione) (PTNT) was synthesized as described in a previous publication<sup>18</sup>. The molecular weight of PTNT was  $M_n = 55.7$  kg/mol and  $M_w = 163.2$  kg/mol relative to polystyrene standards, using an Agilent PL-GPC 220 Integrated High Temperature GPC System with refractive index detectors using  $3 \times$  PL gel 10  $\mu$ m MIXED-B LS,  $300 \times 7.5$  mm<sup>2</sup> columns with 1,2,4-trichlorobenzene at 150 °C as eluent. The polymer was blended with PC<sub>71</sub>BM in 2:3 weight ratio. The solvents *o*-xylene, DIO, MN, PN and CN were purchased from Sigma Aldrich Co. LLC. and used without further purification as well as zinc acetate dihydrate (99.9%), ethanolamine (99.5%) and 2-methoxyethanol (99.8%). Silver (Ag) and Molybdenum oxide (MoO<sub>x</sub>) were also purchased from Sigma Aldrich Co. LLC.

### 4.2.2 Substrate Preparation:

Patterned ITO (indium tin oxide) glass substrates purchased from Xin Yan Technology Ltd. (10  $\Omega$ /sq.) were firstly cleaned with 5% detergent solution (Pyroneg) at 90 °C for 20 min. The ITO-glass substrates were then washed in deionized (DI) water and consecutively ultrasonicated in DI water, acetone, and isopropanol for 10 minutes each. Next, they were exposed to UV-ozone irradiation for 20 minutes to remove the organic impurities and contaminants from the surface. ZnO interface layer (25 nm) was spin-coated from a zinc oxide sol-gel precursor, which is prepared as described in previously published studies.<sup>29</sup> Zinc acetate dihydrate (0.5 g) was dissolved in 2-methoxyethanol (5 mL) and ethanolamine (150  $\mu$ L) solution under vigorous stirring overnight. The ZnO solution was then filtered through a PTFE syringe filter (0.45  $\mu$ m) to be spin-coated (3000 rpm, 60 seconds) on pre-cleaned ITO-glass

substrates. Lastly, the ZnO films were annealed at 280 °C in air inside a pre-heated furnace for 10 minutes.

### 4.2.3 Device Fabrication:

Previously prepared ITO coated glass substrates coated with ZnO in an ambient atmosphere were transferred to a glovebox (Innovative Technologies Pure Lab <sup>HE</sup>) with an oxygen and moisture free inert atmosphere (N<sub>2</sub>). All BHJ blend solutions were prepared in the glovebox for the active layer formation using a spin-coater (Specialty Coating Systems, G3P-8). The polymer solar cells were fabricated in an inverted device configuration; ITO-glass/ZnO/PTNT:PC<sub>71</sub>BM /MoO<sub>x</sub>/Ag. Firstly, the blends were prepared by dissolving the polymer:acceptor mixture (2:3 w/w%) in a solvent system of *o*-xylene and the corresponding solvent additive (v/v%) at 85°C under stirring for overnight. The final concentration of the solution was 25 mg/mL. The warm solutions then spin-coated with a spin speed of 1000 rpm for 60 seconds and dried with 3000 rpm for 30 seconds. Finally, the photo-active films were allowed to dry for 3 hours under vacuum in the evaporator chamber (<10<sup>-6</sup> mbar) prior to the electrode deposition. The hole transport layer of MoO<sub>x</sub> (12 nm) and the metallic Ag (80 nm) electrode were thermally deposited using a shadow mask in the evaporation chamber (< 1x10<sup>-6</sup> mbar) (Covap system supplied by Angstrom Engineering). The active areas of individual cells were determined by the mask as 0.10 cm<sup>2</sup> for the testing. The completed solar devices were tested in an ambient atmosphere for their photovoltaic properties using a Keithley 2400 Source Meter and Oriel solar simulator having a Newport 150 W Xenon lamp under AM 1.5G illumination giving a light intensity output of 100mW/cm<sup>2</sup>. The dark and illuminated current-voltage (J-V) data were recorded and the best devices were also tested with comparison to a Silicon detector for their Incident Photon to Current Efficiency (IPCE). The integrated currents from the IPCE measurement were also compared to the current density J<sub>sc</sub> from J-V data of the corresponding devices.

#### **4.2.4 Photo-physical properties:**

The thin-film photoluminescence characterization was carried out using a Cary Eclipse Fluorescence spectrophotometer (Santa Clara, CA, USA). The sample holder was positioned at a constant height with several angles of incidence of the excitation, which may be varied from 20°–35°. The PL intensities were corrected and normalized with respect to the thickness of the films as previously described in an earlier study.<sup>30</sup>

#### **4.2.5 Film Thickness and Topography:**

A multimode Atomic Force Microscopy (AFM) (supplied by Bruker, Billerica, MA) was utilized for the investigation of the photo-active blend nanostructure and surface topography of the BHJ films in terms of film thickness and morphology. The effects of different morphology on the photovoltaic performance were also compared. All samples were prepared following a similar procedure for device fabrication and the films were coated on pre-cleaned silicon wafers. The samples were also previously vacuum dried inside the glove box overnight. A cross section analysis was used for the active layer thickness determination after scratching the film in a direction that is perpendicular to the scanning axis of the cantilever. The surface topography and the phase images were investigated in tapping mode using J-scanner and Si tips by taking measurements with scales ranging from 5x5 microns to 1x1 micron. The roughness of the films was recorded, as well.

### **4.3 Results and Discussion:**

#### **4.3.1 Solvent and Solvent Additives:**

In this study, the main aim is designing an environmentally friendlier fabrication technique where a novel processing solvent system was introduced and optimized for the best

polymer solar cell performance. To begin with, the usage and optimization of processing solvent systems determined our next steps for the development of a unique eco-friendly polymer solar cell fabrication method. It was critical to determine which solvent system we needed to use in our preliminary experiments. Thus, at first, we evaluated the performance of the previously reported chlorinated solvent system ortho-dichlorobenzene (*o*-DCB) and the processing additives 1-chloronaphthalene (CN) and 1,8-Diiodooctane (DIO) to dissolve the blend of donor polymer PTNT and PC<sub>71</sub>BM acceptor which is very miscible with PTNT.<sup>31</sup> The results were in good agreement in comparison to the earlier work, so we continued to employ the same polymer:acceptor blends to construct the solar cell devices using eco-friendly fabrication systems with non-toxic solvents.

One of the less-toxic non-halogenated solvent we used was *o*-xylene, and it has been well studied in various solar cell studies before as the main processing solvent.<sup>27,32</sup> The non-toxic solvent additives that were initially tested are 1-methoxynaphthalene (MN) and 1-phenylnaphthalene (PN) having a selective solubility in the fabrication of organic solar cells. For the selection of the solvent system, it is significant to consider the ~ 10 nm short exciton diffusion length in BHJ organic solar cells which has been a limitation to be overcome.<sup>33</sup> The introduction of the solvent additives assists to solve this problem as they have the benefit of perfecting the well phase-separated nanomorphology by enabling the efficient charge separation and dissociation from OSCs. The understanding of how these solvents behave depends on their proper selection according to the BHJ blends. In our system, the PTNT:PC<sub>71</sub>BM blend forms extremely phase separated domains of donor polymer and acceptor fullerene constituents where the exciton diffusion is inefficient when processed using spin-coating technique. Some solvent additives can promote this excessive crystallinity in the final molecular orientation which is initially related to the structural properties of donor-acceptor mixture along with the aromaticity nature, miscibility and boiling point of the additives.

<sup>34</sup> On the other hand, the additives we needed to focus on this study were the ones for a blend of semi-crystalline donor polymer and a fullerene. The use of solvent additive in this system improves the vertical phase separation and induces the aggregation as the solvent evaporates to form a final solid thin film as depicted in Figure 4.2.

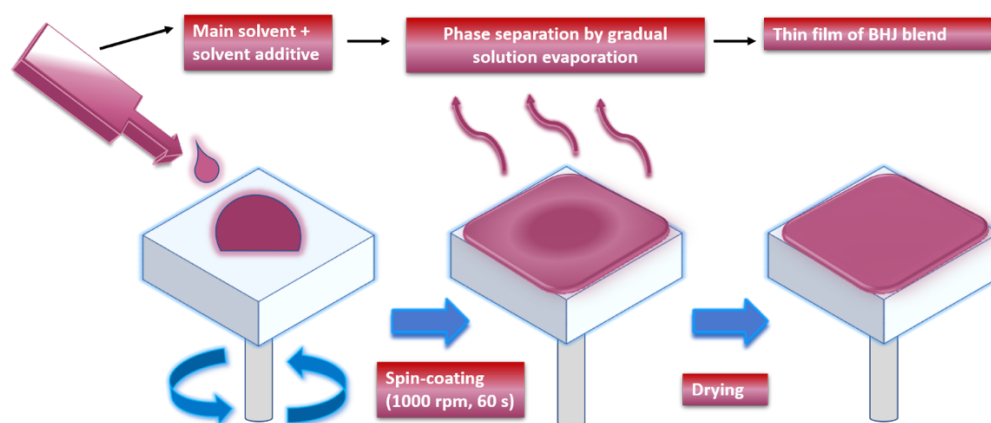


**Figure 4.2:** Illustration of the steps in the spin-coating of BHJ thin films processed by the solvent additive system.

As a result, the gradual solvent removal is successfully completed through different drying kinetics of the thin film formation. Accordingly, the morphology is optimized as such the interfacial area between the donor and the acceptor is decreased with the use of a high boiling point solvent additive as illustrated below in Figure 4.3. Ultimately, an increased charge mobility and solar cell efficiency are achieved by efficient exciton diffusion.

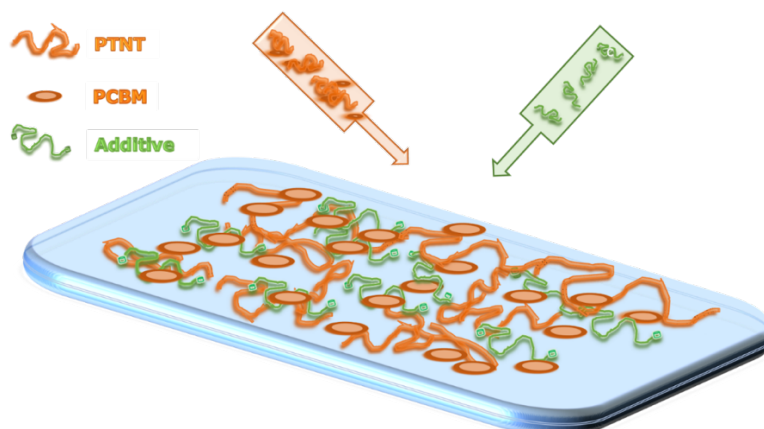


**Figure 4.3:** Representation of the effect of solvent additives (DIO) on PSCs.

Before investigating the effect of these solvent additives on the solar cell performance and device stability; they were researched for their various physical properties and most importantly their eco-friendliness to replace the previously studied toxic DIO additive and to discover more effective and non-toxic additives. These crucial specifications are the definitive standards to categorize the additives as explained in Table 4.1 and Table 4.2 according to Lange's Handbook of Chemistry (1999) and Chemwatch MSDS data available, in which we report the physical properties such as boiling point and vapor pressure and the degree of toxicity, respectively.

**Table 4.1:** Various physical properties of solvents and solvent additives used in this study.

Solvent	Molecular formula	Normal Boiling point (°C)	Vapor pressure (kPa at 25 °C)
<i>o</i> -Xylene	C <sub>8</sub> H <sub>10</sub>	144	0.881
1-Methoxynaphthalene (MN)	C <sub>11</sub> H <sub>10</sub> O	270	0.002
1-Phenylnaphthalene (PN)	C <sub>16</sub> H <sub>12</sub>	324	0.0003
1-Chloronaphthalene (CN)	C <sub>10</sub> H <sub>7</sub> Cl	259	0.003
1,8-Diiodooctane (DIO)	C <sub>8</sub> H <sub>16</sub> I <sub>2</sub>	333	0.00004

As reported, the boiling points of additives are much higher than the main solvent *o*-xylene. Another important category for distinguishing additives is their selective solubility towards PC<sub>71</sub>BM. The fact that high boiling point solvent additives such as DIO dissolving the acceptor fullerene in a greater extent induces self-assembled polymer chain formation during drying. Eventually, these different phases that are formed gradually promote the mechanism of nano-crystalline well phase separated morphology.

In this study, it is also imperative to identify the hazardous effects of these solvents on both environment and health or to propose their green alternatives. The Chemwatch hazard ratings and statements are also used to eliminate unconventional solvent systems and to replace the toxic solvents with the ideal less-toxic counterparts as reported in Table 4.2.

**Table 4.2:** Hazard identification and classifications of the solvents.

Solvent	Flammability	Toxicity	Body Contact	Reactivity	Chronic	Hazard Alert Code
<i>o</i> -xylene	2	2	2	1	0	2
1-methoxynaphthalene (MN)	1	1	1	1	2	2
1-phenylnaphthalene (PN)	1	2	1	1	0	2
1-chloronaphthalene (CN)	1	2	2	1	0	2
1,8-diiodooctane (DIO)	1	2	2	1	0	2

(0= Minimum 1=Low 2=Moderate 3=High 4=Extreme)

As shown in Table 2, processing additives are given in order of **CN (2) > DIO (2) > PN (2) > MN (1)** according to their overall hazard ratings. The green solvent additives 1-methoxynaphthalene (MN) and 1-phenylnaphthalene (PN) are also reported to be slightly different from each other in terms of toxicity based on the current Chemwatch MSDS safety data, hence becoming the best candidates for device fabrication.

It is worth noting that in this study, MN was found to be a very good novel green solvent additive which has not been reported to the date before. Indeed, it was also shown to be suitable for large scale industrial device fabrication purposes facilitating less solution wastage using printing techniques for future OPV experiments.

In particular, the main solvent, *o*-xylene, despite being the most hazardous solvent in this study, has a low toxicity data (2), as well. The outstanding potential of xylenes enabled an extensive OPV research area where they are employed in dissolving numerous different BHJ blends.<sup>35-36</sup> Certainly, the best green solvent alternative of all is water and it can only be used in the case of solar cells fabricated by polymer nanoparticles (PNPs). Yet, in an earlier aqueous PNP solar cell study, it was reported that the performance of devices using PTNT:PC<sub>61</sub>BM nanoparticles dispersed in water is very poor.

### 4.3.2 Photovoltaic Properties:

The photovoltaic technology of harvesting solar energy for the production of electricity has been one of the rapidly developing research areas and its characterization parameters and techniques for solar cells have also been evolving.<sup>24, 37</sup> In this study, the solar cell architecture selected was inverted (ITO-glass/ZnO/PTNT:PC<sub>71</sub>BM/MoO<sub>3</sub>/Ag) as shown in Figure 4.4.

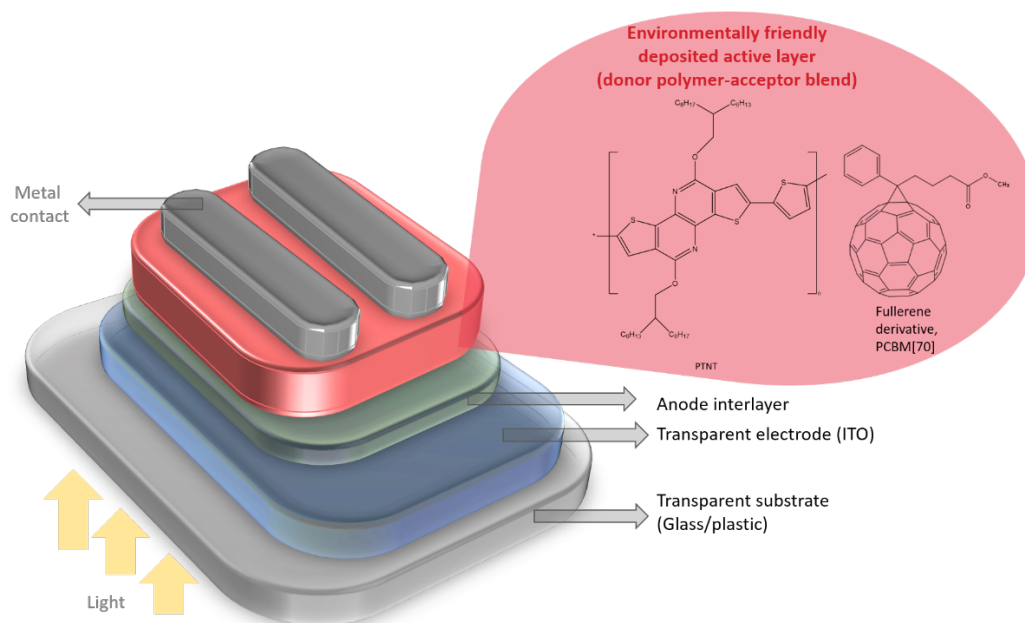


**Figure 4.4:** Polymer solar cell architecture used in this study.

The main motive for such design is to prevent poor device stability. Because, the low work function electrodes that are used in conventional structure (e.g., Ca, Al) can be easily oxidized when exposed to the air and moisture and result in degradation. Moreover, the acidic PEDOT:PSS layer is in contact with the ITO anode in conventional architecture that also degrades the solar cell device. On the other hand, in inverted devices, the charge transport is in reverse direction enabling much higher stability and greater cell efficiency.

The interface layer for the extraction of electrons needs to have materials with a lower LUMO energy level than that of the acceptor material in BHJ layer.

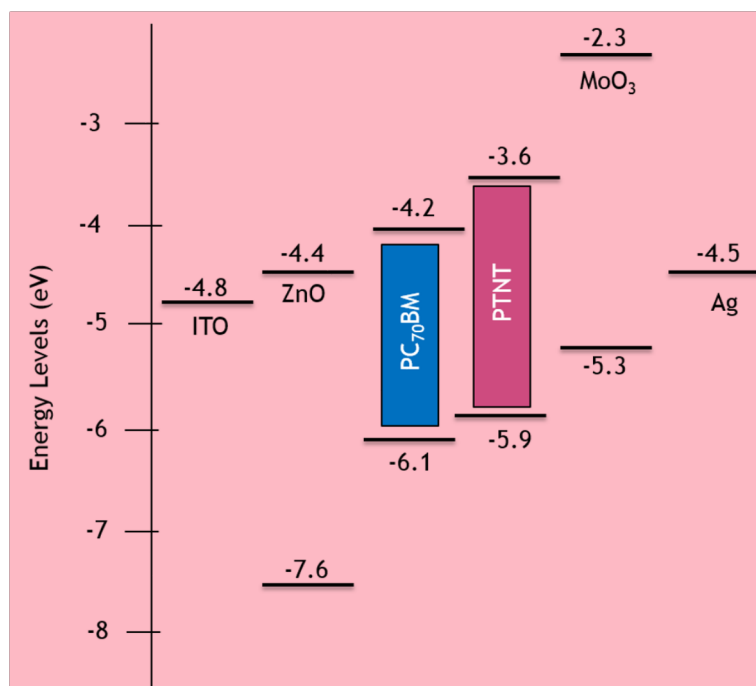


**Figure 4.5:** Energy level diagram of the constructed polymer solar cell.

As illustrated in Figure 4.5, ZnO is also assigned as a hole blocking interfacial layer having a lower HOMO energy level than that of the donor polymer. Thus, ZnO layer is called as cathode buffer layer (CBL). It is also needed to have low cost, stability, good electron transport ability and efficient transparency for photon absorption. Therefore, among the several semiconducting metal oxides, ZnO has been most extensively studied matching the required criteria. The technique used in the current study for the formation of ZnO layer is the low-cost sol-gel method where the post-heat treatment of coated layer is critical for realizing crystalline ZnO as mentioned before.<sup>29</sup> The molybdenum trioxide (MoO<sub>3</sub>) layer in inverted device structure acts as a hole selective interface layer and it is a much better alternative than PEDOT:PSS. The holes that are collected from the high work function electrode needs to be transported through a very thin MoOx layer which also prevents oxidation of the top metal electrode, diffusion of metal ions and oxygen into active layer, hence increasing device lifetime and stability.<sup>38</sup> Its HOMO level (-5.3 eV) is also very close to that of donor polymer (-5.0 eV) which is also beneficial for effectively extracting holes from the active layer as characterized

by ultraviolet photoelectron spectroscopy studies in a previous study.<sup>39</sup> Finally, the metal electrode is replaced in this inverted solar cell study with a high work function air stable metal as Silver (Ag).

It must be also noted that, the organic/electrode interface in the inverted device configuration has a significant influence on device performance. It has been helpful to use MoO<sub>3</sub> as it also has a LUMO level that is much higher than that of PC<sub>71</sub>BM avoiding charge recombination. Furthermore, MoO<sub>3</sub> interface layer is supposed to be pre-annealed to maintain its well attachment to the organic phase. The thickness of MoO<sub>3</sub> layer is also critical in preventing charge leakage.<sup>40</sup> Most importantly, for the formation of BHJ photo-active layer, a non-halogenated solvent system was used and optimized for the best device efficiency as aimed initially. The main solvent *o*-xylene not only dissolves PTNT and PC<sub>71</sub>BM effectively but also it has a much lower toxicity compared to common halogenated solvents. First of all, prior to using solvent additives for improving thin film morphology, another surface energy treatment, annealing, was also tested. Indeed, annealing of the organic active layer before the electrode deposition gives an idea regarding the thermally changed structure of the deposited material for the best stability, phase separation and formation of a proper film, as well as, assisting to the solidifying of the layers and the removal of the remaining solvent. Though, the preliminary annealing experiments did not improve the device efficiency in this study.

The solvent additives that are used to improve the microstructure of the PTNT:PC<sub>71</sub>BM active layer were first optimized using both halogenated additives DIO and CN which are among the most studied additives.<sup>14-15</sup> and non-halogenated ones such as PN was studied for the morphology enhancement of OSCs, as well.<sup>41</sup> The device efficiencies were greatly improved using solvent additive treatment and interestingly the best devices were achieved using non-harmful green solvent systems. Finally, the optimization for the thickness of the active layer is completed using the constant donor-acceptor ratio and concentration for a

systematic device fabrication study. The experiment results to explore the optimum donor-acceptor ratio and film thickness are investigated below in Figure 4.6 :

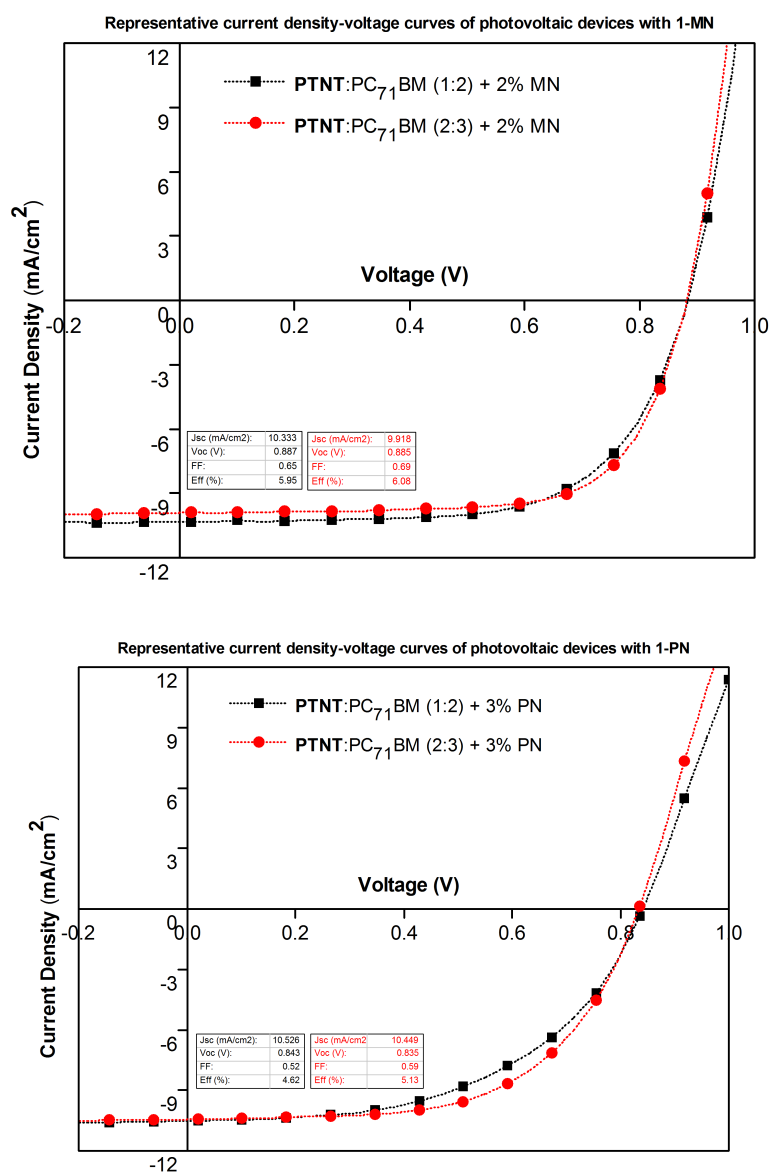


**Figure 4.6:** J-V characteristics of devices optimized using MN and PN additives in different donor-acceptor ratios.

As observed in Figure 4.6, a slightly better performance was accomplished using a 2:3 (w/w%) donor:acceptor ratio in the preparation of BHJ blends.

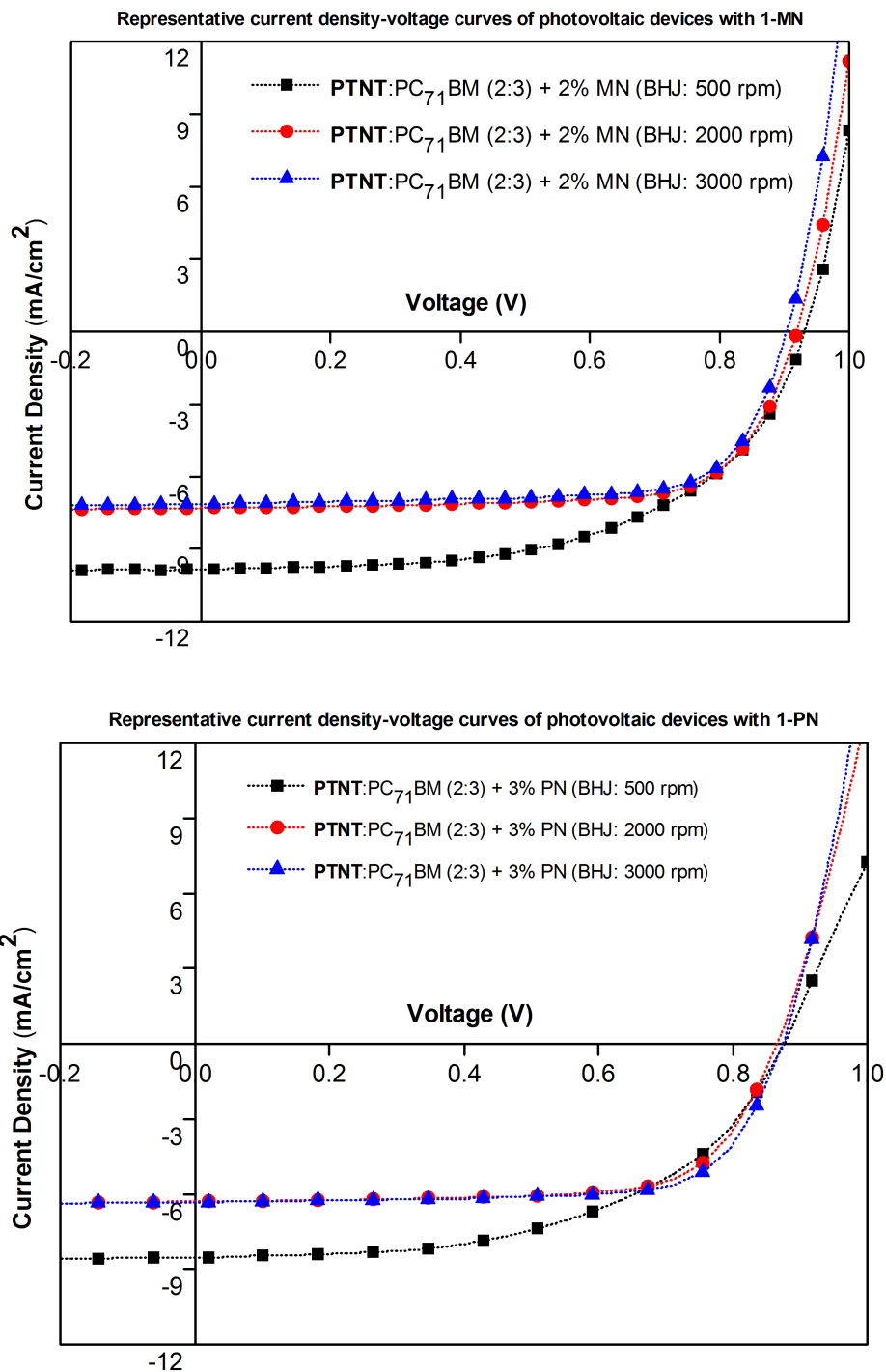


**Figure 4.7:** J-V characteristics of devices optimized using MN and PN additives in different film thicknesses.

In addition, the spin-coating speed was also optimized for the best device performance by eliminating 500 rpm, 2000 rpm and 3000 rpm spin-coating speeds for the non-toxic additive processed devices as given in Figure 4.7. After determining the optimal device fabrication parameters with an eco-friendly approach, several solar cell devices were fabricated without

any surface energy treatment and later using different solvent additives which are both non-halogenated and halogenated. Due to the extreme phase segregated morphology of PTNT:PC<sub>71</sub>BM (2:3 w/w%) BHJ thin film processed from *o*-xylene, the devices without any solvent additive treatment showed a very poor performance as a further motivation and distinct difference to progress to optimize the morphology using additives. On the basis of the current density-voltage measurements, the devices had an average PCE of 1.4%, J<sub>SC</sub> of 2.5 mAcm<sup>-2</sup>, Voc of 0.87 V and FF of 62%. A ratio of 1:2 PTNT:PC<sub>71</sub>BM (wt/wt%) blend showed even lower PCE as stated before in Figure 4.6. However, later, owing to the use of effective solvent additives, the active layer was successfully optimized forming a good phase separation between donor and acceptor moieties of the homogeneous BHJ blend film. The photovoltaic parameters from the solvent additive study were summarised in Table 4.3.

**Table 4.3:** Summary of the photovoltaic performance properties of optimized PTNT:PC<sub>71</sub>BM (2:3) solar cells with mean values and standard deviation from six devices.

Device structure	Solvent + (v/v%) additive	Jsc [mA cm <sup>-2</sup> ]	Voc [V]	FF [%]	PCE [%]	
					Mean	Max
ITO/ZnO/BHJ/MoOx/Ag						
	<i>o</i> -xylene	2.5 ± 0.1	0.877 ± 0.016	62 ± 1	1.4 ± 0.1	1.5
	<i>o</i> -xylene + 2% MN	9.9 ± 0.2	0.879 ± 0.007	69 ± 1	6.0 ± 0.1	6.2
PTNT:PC <sub>71</sub> BM (2:3) 1000 rpm	<i>o</i> -xylene + 3% PN	10.4 ± 0.4	0.837 ± 0.003	59 ± 1	5.2 ± 0.2	5.4
	<i>o</i> -xylene + 3% DIO	8.6 ± 0.6	0.873 ± 0.002	65 ± 1	4.9 ± 0.4	5.2
	<i>o</i> -xylene + 2% CN	6.5 ± 0.2	0.917 ± 0.008	63 ± 1	3.7 ± 0.1	3.9

The non-toxic PN and MN solvent additives showed the best performance having a higher boiling point similar to DIO. However, the slightly lower device efficiency using PN additive could be attributed to the fact that PN has also the biggest potential to remain in the active layer as reported in another OPV study.<sup>42</sup> With the addition of 2% MN solvent additive to the main solvent *o*-xylene, a maximum PCE of 6.2% was achieved and to the best of our knowledge, this was the best device performance reported using high band gap semi-crystalline

PTNT polymer with a novel eco-friendly device fabrication. The J-V and EQE graphs for the representative photovoltaic devices are given below in Figure 4.8a and Figure 4.8b.

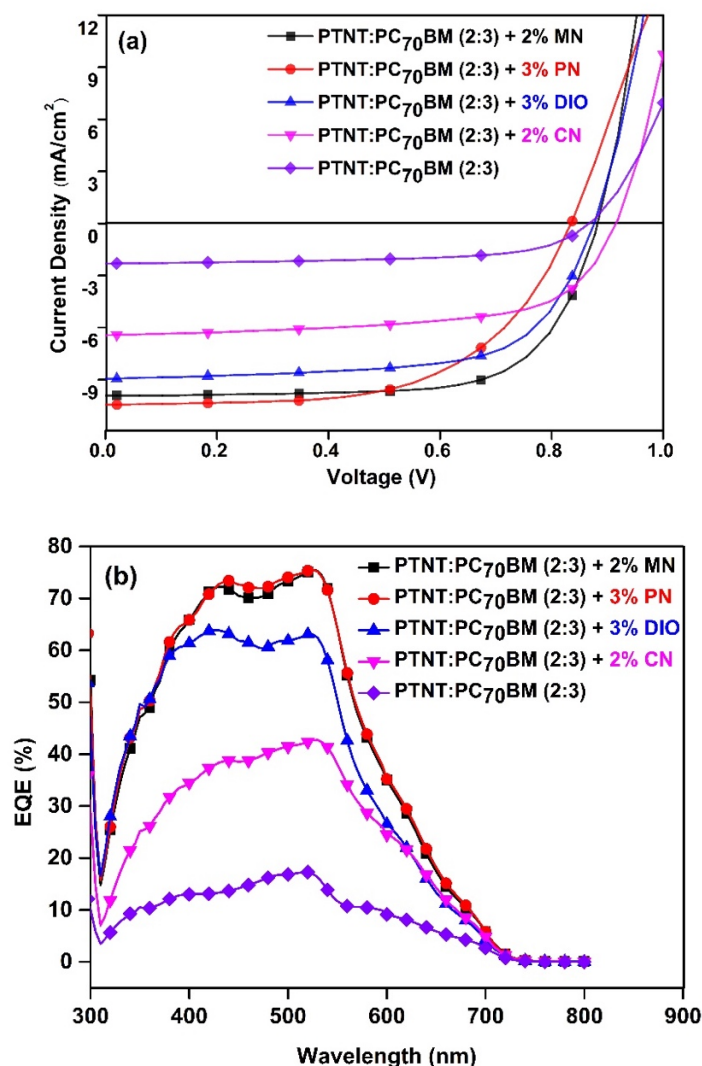


**Figure 4.8:** Photovoltaic devices with and without solvent additives: (a) Representative current density-voltage curves; (b) EQE versus wavelength.

Additionally, the final device efficiency was higher than a previous study having the same BHJ blend using halogenated and toxic *o*-DCB solvent and DIO additive mixture.<sup>18</sup> The addition of 3% PN non-harmful additive gave a reasonably better efficiency, as well. It has an average PCE of 5.2%. The halogenated toxic additives 3% DIO and 2% CN used for comparison were resulted in poorer performance, having an average PCE of 4.9% and 3.7%, respectively.

In Figure 4.8b, the external quantum efficiency (EQE) values are plotted against the wavelength which corresponds to the absorption properties of the individual BHJ films. The EQE was remarkably enhanced, and the calculated theoretical integrated currents are in well agreement with the measured currents as indicated below in Table 4.4:

**Table 4.4:** The integrated currents from EQE (IPCE) compared to the  $J_{sc}$  from I-V measurement of corresponding devices.

Solvent system	Integrated $J_{sc}$ from IPCE (mA/cm <sup>2</sup> )	$J_{sc}$ (mA/cm <sup>2</sup> )
o-xylene	2.2	2.3
o-xylene + 2% MN	9.7	9.9
o-xylene + 3% PN	9.9	10.4
o-xylene + 3% DIO	8.2	8.9
o-xylene + 2% CN	5.9	6.4

The advantages of using MN and PN solvent additives can be significantly realized in conjunction with the EQE efficiency data where the response reaching more than 70% between 400 to 550 nm wavelength range which agrees with the higher  $J_{sc}$  obtained (Figure 4.8a and Table 4.3). Whereas, usage of toxic solvent additives (DIO and CN) gave a much-reduced response while the device without solvent additive was lower considering the response.

### 4.3.3 Photoluminescence (PL):

Another way to understand how the morphology of BHJ blend film changes upon solvent additive treatment is by investigating the PL emission for the degree of exciton quenching. The PL measurements of the thin films of BHJ blends are given in Figure 4.9:

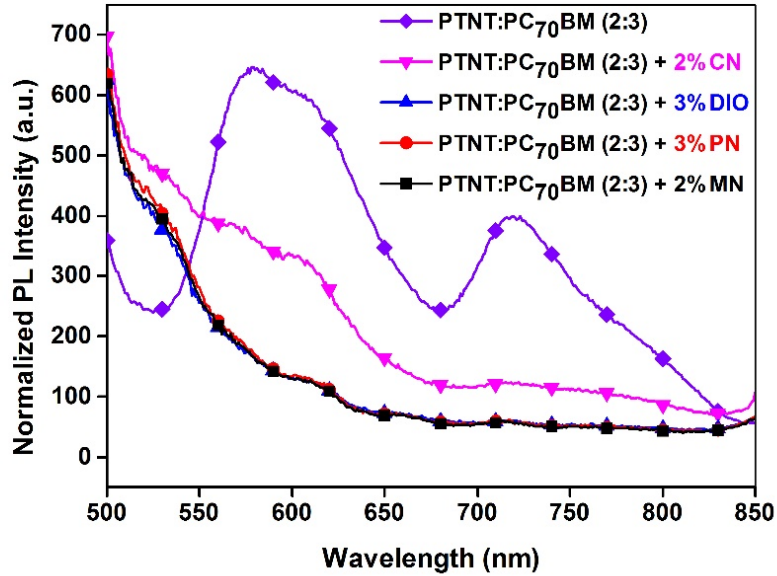


**Figure 4.9:** Normalized PL emission spectra of active layers from PTNT:PC<sub>71</sub>BM blends using different solvent additives (corrected and normalized to film thickness).

The PL emissions from the thin films are distinguishably different from the blend without processed by an additive and from the additive treated thin films. The degree of exciton quenching is the highest when the non-toxic additive was used suggesting good phase separation and better device performance. The quenched blends are consistent with the increased charge mobility, as well. Still, the thin film processed from halogenated CN additive gave a strong emission around 600 nm which explains the low device efficiency and poorer morphology. The normalized PL emissions were corrected with respect to the film thicknesses.

#### 4.3.4 Surface Topography:

Atomic Force Microscopy (AFM) was used for the investigation of the surface treatment effects using solvent additives in order to comprehend the morphology. The topography of the BHJ blend films were thoroughly analysed and the images are given in Figure 4.10. As clearly can be seen, the blend without any treatments does not have a well-

phase separated nanostructure. The bigger domains of donor and acceptor species cause a poor exciton diffusion and a less transparent film. Hence, as also confirmed with AFM, the photovoltaic device efficiency was the lowest without using additives. It is significant to note that additives are divided in regard to diverging effects on thin film blend morphology, either enabling a homogeneously well mixed nanostructure with good phase separation or preventing extremely insulated domains as mentioned before.<sup>43-44</sup>

In this study, the latter is effective as the donor and acceptor phases were very separated in the absence of an additive. So, the inter-mixing and its extent were analysed and the non-halogenated MN additive treated BHJ film gave the most homogeneous film suggesting good charge transport as well as a low roughness value as given in Table 4.5.

In spite of its ability to visualize the film topography, the inner morphology of BHJ blend films are not necessarily the same as AFM is a surface method.<sup>45</sup>

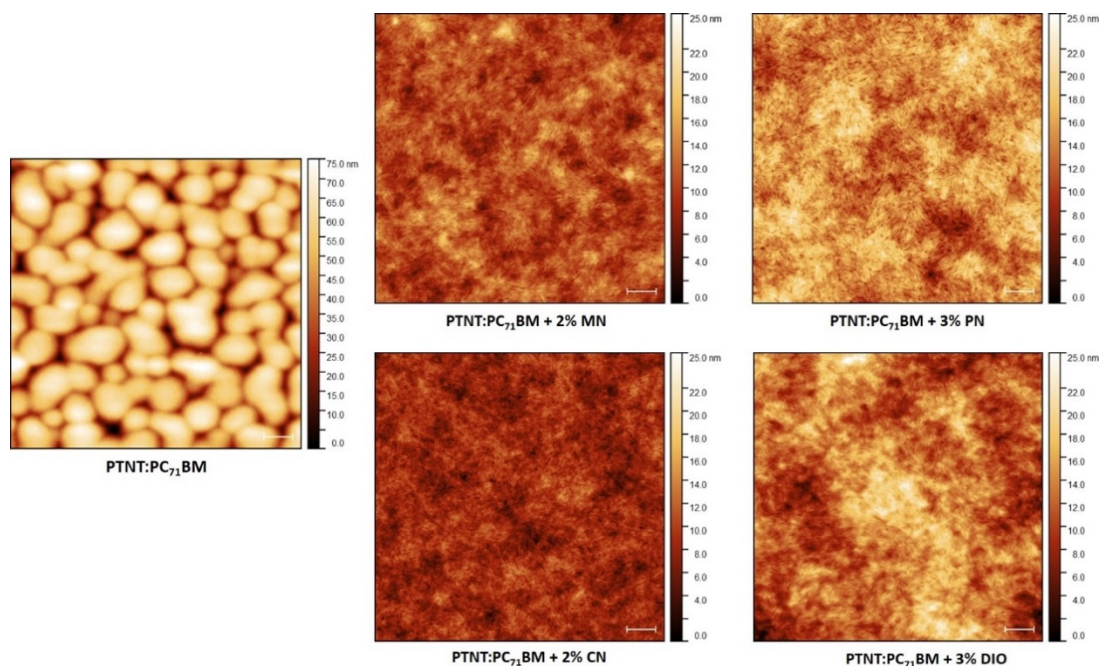


**Figure 4.10:** AFM images (5  $\mu\text{m}$  x 5  $\mu\text{m}$ ) showing the surface topography of PTNT:PC<sub>71</sub>BM (2:3) blend from *o*-xylene with different solvent additives at RT. The scale bar is 500 nm.

**Table 4.5:** Root mean square (rms) value of BHJ films treated by various solvent additives.

	<b>Without additive</b>	<b>2% MN</b>	<b>3% PN</b>	<b>2% CN</b>	<b>3% DIO</b>
rms (nm)	12.9	2.03	2.66	1.81	3.20

The best performing additive MN also had a lower roughness value compared to the device processed with PN (2.66 nm > 2.03 nm) which has a slightly lower power conversion efficiency (5.2% < 6.0%). The AFM images were also scanned for a cross-section analysis in order to predict the BHJ film thicknesses using different additives.

#### 4.4 Conclusion:

In this study, the main goal was to finely optimize the photo-active layer of a BHJ film of an inverted solar cell by following environmentally friendly device fabrication techniques. The most efficient technique in order to successfully achieve a BHJ blend film from a semi-crystalline large bandgap polymer and fullerene acceptor was found to be processed by a solvent additive for the well intermixing and optimized morphology. The previous studies with the same blend only used halogenated solvent additives and achieved a lower device performance.

Nevertheless, by employing solvent additive treatment and thereby optimizing the non-toxic solvent systems, the preparation of the eco-friendly polymer solar cells was completed and a high PCE efficiency of 6% was accomplished using a complete non-halogenated novel solvent system of *o*-xylene + green solvent additive. The green device fabrication was also accompanied by the investigation of nanoscale BHJ blend morphology using photoluminescence and AFM topography analysis. The corresponding exciton quenching degrees with different additives was effective in understanding the active layer properties including thickness and phase separation.

The best performing solar cell device was confirmed to have a stable morphology with consistent photovoltaic properties. The correlated AFM images of the uniform BHJ blends using eco-friendly materials were compared. The usage of non-toxic solvents was also found to be very useful in the fabrication of efficient flexible solar cells and their upscaling for future research.

## 4.5 Contributions:

*Dr. Desta Gedefaw: Synthesized and characterized the polymer and assisted with data interpretation.*

*Prof. Mats Andersson: Conceived the idea, assisted with the interpretation of the data and experiment design.*

## 4.6 References:

1. Liu, Q., Jiang, Y., Jin, K., Qin, J., Xu, J., Li, W., et al. (2020) "18% efficiency organic solar cells." *Sci. Bull.* 65, 272–275.
2. Almeida, M. A. P., Recent Advances in Solar Cells. In *Solar Cells*, 2020; pp 79-122.
3. Di Carlo Rasi, D.; Janssen, R. A. J., 2019 "Advances in Solution-Processed Multijunction Organic Solar Cells" *Adv Mater*, 31 (10), e1806499.
4. Zhang, C.; Heumueller, T.; Gruber, W.; Almora, O.; Du, X.; Ying, L.; Chen, J.; Unruh, T.; Cao, Y.; Li, N.; Brabec, C. J., 2019 "Comprehensive Investigation and Analysis of Bulk-Heterojunction Microstructure of High-Performance PCE11:PCBM Solar Cells" *ACS Appl Mater Interfaces*, 11 (20), 18555-18563.
5. Zhang, Y.; Sajjad, M. T.; Blaszczyk, O.; Parnell, A. J.; Ruseckas, A.; Serrano, L. A.; Cooke, G.; Samuel, I. D. W., 2019 "Large Crystalline Domains and an Enhanced Exciton Diffusion Length Enable Efficient Organic Solar Cells" *Chemistry of Materials*, 31 (17), 6548-6557.
6. Tamai, Y.; Ohkita, H.; Benten, H.; Ito, S., 2015 "Exciton Diffusion in Conjugated Polymers: From Fundamental Understanding to Improvement in Photovoltaic Conversion Efficiency" *J Phys Chem Lett*, 6 (17), 3417-28.
7. Schaffer, C. J.; Schlipf, J.; Dwi Indari, E.; Su, B.; Bernstorff, S.; Muller-Buschbaum, P., 2015 "Effect of Blend Composition and Additives on the Morphology of PCPDTBT:PC71BM Thin Films for Organic Photovoltaics" *ACS Appl Mater Interfaces*, 7 (38), 21347-55.
8. Park, C.-D.; Fleetham, T.; Li, J., 2015 "Development of non-halogenated binary solvent systems for high performance bulk-heterojunction organic solar cells" *Organic Electronics*, 16, 95-100.
9. Park, C.-D.; Fleetham, T. A.; Li, J.; Vogt, B. D., 2011 "High performance bulk-heterojunction organic solar cells fabricated with non-halogenated solvent processing" *Organic Electronics*, 12 (9), 1465-1470.
10. Ma, Z.; Zhao, B.; Gong, Y.; Deng, J.; Tan, Z. a., 2019 "Green-solvent-processable strategies for achieving large-scale manufacture of organic photovoltaics" *Journal of Materials Chemistry A*, 7 (40), 22826-22847.
11. Subianto, S.; Dutta, N.; Andersson, M.; Choudhury, N. R., 2016 "Bulk heterojunction organic photovoltaics from water-processable nanomaterials and their facile fabrication approaches" *Adv Colloid Interface Sci*, 235, 56-69.
12. D'Olieslaeger, L.; Pfanmüller, M.; Fron, E.; Cardinaletti, I.; Van Der Auweraer, M.; Van Tendeloo, G.; Bals, S.; Maes, W.; Vanderzande, D.; Manca, J.; Ethirajan, A., 2017 "Tuning of PCDTBT:PC<sub>71</sub>BM blend nanoparticles for eco-friendly processing of polymer solar cells" *Solar Energy Materials and Solar Cells*, 159, 179-188.

13. Huang, F.; Wu, H.; Cao, Y., 2010 "Water/alcohol soluble conjugated polymers as highly efficient electron transporting/injection layer in optoelectronic devices" *Chem Soc Rev*, 39 (7), 2500-21.
14. Li, Q.; Wang, L. M.; Liu, S.; Zhan, X.; Zhu, T.; Cao, Z.; Lai, H.; Zhao, J.; Cai, Y.; Xie, W.; Huang, F., 2019 "Impact of Donor-Acceptor Interaction and Solvent Additive on the Vertical Composition Distribution of Bulk Heterojunction Polymer Solar Cells" *ACS Appl Mater Interfaces*, 11 (49), 45979-45990.
15. Wang, L.; Zhao, S.; Xu, Z.; Zhao, J.; Huang, D.; Zhao, L., 2016 "Integrated Effects of Two Additives on the Enhanced Performance of PTB7:PC71BM Polymer Solar Cells" *Materials (Basel)*, 9 (3).
16. Wienhold, K. S.; Korstgens, V.; Grott, S.; Jiang, X.; Schwartzkopf, M.; Roth, S. V.; Muller-Buschbaum, P., 2019 "Effect of Solvent Additives on the Morphology and Device Performance of Printed Nonfullerene Acceptor Based Organic Solar Cells" *ACS Appl Mater Interfaces*, 11 (45), 42313-42321.
17. Chen, J.; Bi, Z.; Xu, X.; Zhang, Q.; Yang, S.; Guo, S.; Yan, H.; You, W.; Ma, W., 2019 "Fine Optimization of Morphology Evolution Kinetics with Binary Additives for Efficient Non-Fullerene Organic Solar Cells" *Adv Sci (Weinh)*, 6 (6), 1801560.
18. Kroon, R.; Diaz de Zerio Mendaza, A.; Himmelberger, S.; Bergqvist, J.; Backe, O.; Faria, G. C.; Gao, F.; Obaid, A.; Zhuang, W.; Gedefaw, D.; Olsson, E.; Inganas, O.; Salleo, A.; Muller, C.; Andersson, M. R., 2014 "A new tetracyclic lactam building block for thick, broad-bandgap photovoltaics" *J Am Chem Soc.*, 136 (33), 11578-81.
19. Yu, J. E.; Jeon, S. J.; Choi, J. Y.; Han, Y. W.; Ko, E. J.; Moon, D. K., A, 2019 "3-Fluoro-4-hexylthiophene-Based Wide Bandgap Donor Polymer for 10.9% Efficiency Eco-Friendly Nonfullerene Organic Solar Cells" *Small*, 15 (9), e1805321.
20. Roehling, J. D.; Baran, D.; Sit, J.; Kassar, T.; Ameri, T.; Unruh, T.; Brabec, C. J.; Moule, A. J., 2016 "Nanoscale Morphology of PTB7 Based Organic Photovoltaics as a Function of Fullerene Size" *Sci Rep*, 6, 30915.
21. Gaspar, H.; Figueira, F.; Pereira, L.; Mendes, A.; Viana, J. C.; Bernardo, G., 2018 "Recent Developments in the Optimization of the Bulk Heterojunction Morphology of Polymer: Fullerene Solar Cells" *Materials (Basel)*, 11 (12).
22. Krishnan Jagadamma, L.; Sajjad, M. T.; Savikhin, V.; Toney, M. F.; Samuel, I. D. W., 2017 "Correlating photovoltaic properties of a PTB7-Th:PC<sub>71</sub>BM blend to photophysics and microstructure as a function of thermal annealing" *Journal of Materials Chemistry A*, 5 (28), 14646-14657.
23. Huang, Z.; Fregoso, E. C.; Dimitrov, S.; Tuladhar, P. S.; Soon, Y. W.; Bronstein, H.; Meager, I.; Zhang, W.; McCulloch, I.; Durrant, J. R., 2014 "Optimisation of diketopyrrolopyrrole:fullerene solar cell performance through control of polymer molecular weight and thermal annealing" *J. Mater. Chem. A.*, 2 (45), 19282-19289.

24. Dang, M. T.; Wuest, J. D., 2013 "Using volatile additives to alter the morphology and performance of active layers in thin-film molecular photovoltaic devices incorporating bulk heterojunctions" *Chem Soc Rev*, 42 (23), 9105-26.
25. Chauhan, A. K.; Gusain, A.; Jha, P.; Veerender, P.; Koiry, S. P.; Sridevi, C.; Aswal, D. K.; Gupta, S. K.; Taguchi, D.; Manaka, T.; Iwamoto, M., 2016 "Interfacial charge trapping in the polymer solar cells and its elimination by solvent annealing" *AIP Advances*, 6 (9).
26. Song, X.; Gasparini, N.; Baran, D., 2018 "The Influence of Solvent Additive on Polymer Solar Cells Employing Fullerene and Non-Fullerene Acceptors" *Advanced Electronic Materials*, 4 (10).
27. Zhao, J.; Zhao, S.; Xu, Z.; Song, D.; Qiao, B.; Huang, D.; Zhu, Y.; Li, Y.; Li, Z.; Qin, Z., 2018 "Highly Efficient and Operational Stability Polymer Solar Cells Employing Nonhalogenated Solvents and Additives" *ACS Appl Mater Interfaces*, 10 (28), 24075-24081.
28. Inaba, S.; Arai, R.; Mihai, G.; Lazar, O.; Moise, C.; Enachescu, M.; Takeoka, Y.; Vohra, V., 2019 "Eco-Friendly Push-Coated Polymer Solar Cells with No Active Material Wastes Yield Power Conversion Efficiencies over 5.5. *ACS Appl Mater Interfaces*" 11 (11), 10785-10793.
29. Sun, Y.; Seo, J. H.; Takacs, C. J.; Seifert, J.; Heeger, A. J., 2011 "Inverted polymer solar cells integrated with a low-temperature-annealed sol-gel-derived ZnO Film as an electron transport layer" *Adv Mater*, 23 (14), 1679-83.
30. Holmes, N. P.; Ulum, S.; Sista, P.; Burke, K. B.; Wilson, M. G.; Stefan, M. C.; Zhou, X.; Dastoor, P. C.; Belcher, W. J., 2014 "The effect of polymer molecular weight on P3HT:PCBM nanoparticulate organic photovoltaic device performance" *Solar Energy Materials and Solar Cells*, 128, 369-377.
31. Hedley, G. J.; Ward, A. J.; Alekseev, A.; Howells, C. T.; Martins, E. R.; Serrano, L. A.; Cooke, G.; Ruseckas, A.; Samuel, I. D., 2013 "Determining the optimum morphology in high-performance polymer-fullerene organic photovoltaic cells" *Nat Commun*, 4, 2867.
32. La Notte, L.; Polino, G.; Ciceroni, C.; Brunetti, F.; Brown, T. M.; Di Carlo, A.; Reale, A., 2014 "Spray-Coated Polymer Solar Cells based on Low-Band-Gap Donors Processed with ortho-Xylene" *Energy Technology*, 2 (9-10), 786-791.
33. Menke, S. M.; Holmes, R. J., 2014 "Exciton diffusion in organic photovoltaic cells" *Energy Environ. Sci.*, 7 (2), 499-512.
34. Manley, E. F.; Strzalka, J.; Fauvell, T. J.; Jackson, N. E.; Leonardi, M. J.; Eastham, N. D.; Marks, T. J.; Chen, L. X., 2017 "In Situ GIWAXS Analysis of Solvent and Additive Effects on PTB7 Thin Film Microstructure Evolution during Spin Coating" *Adv Mater*, 29 (43).
35. Dong, X.; Deng, Y.; Tian, H.; Xie, Z.; Geng, Y.; Wang, F., 2015 "Isoindigo-based low bandgap conjugated polymer for o-xylene processed efficient polymer solar cells with thick active layers" *J. Mater. Chem. A*, 3 (39), 19928-19935.

36. Sprau, C.; Buss, F.; Wagner, M.; Landerer, D.; Koppitz, M.; Schulz, A.; Bahro, D.; Schabel, W.; Scharfer, P.; Colsmann, A., 2015 "Highly efficient polymer solar cells cast from non-halogenated xylene/anisaldehyde solution" *Energy Environ. Sci.*, 8 (9), 2744-2752.
37. Jeong, S.; Woo, S.-H.; Lyu, H.-K.; Kim, C.; Kim, W. H.; Han, Y. S., 2014 "Improved Photovoltaic Properties of Polymer Solar Cells with a Phenyl Compound as an Additive" *Journal of Nanoscience and Nanotechnology*, 14 (8), 5988-5992.
38. Chambon, S.; Derue, L.; Lahaye, M.; Pavageau, B.; Hirsch, L.; Wantz, G., 2012 "MoO<sub>3</sub> Thickness, Thermal Annealing and Solvent Annealing Effects on Inverted and Direct Polymer Photovoltaic Solar Cells" *Materials*, 5 (12), 2521-2536.
39. Ahmad, V.; Shukla, A.; Sobus, J.; Sharma, A.; Gedefaw, D.; Andersson, G. G.; Andersson, M. R.; Lo, S.-C.; Namdas, E. B., 2018 "High-Speed OLEDs and Area-Emitting Light-Emitting Transistors from a Tetracyclic Lactim Semiconducting Polymer" *Advanced Optical Materials*, 6 (21).
40. Hermerschmidt, F.; Savva, A.; Georgiou, E.; Tuladhar, S. M.; Durrant, J. R.; McCulloch, I.; Bradley, D. D. C.; Brabec, C. J.; Nelson, J.; Choulis, S. A., 2017 "Influence of the Hole Transporting Layer on the Thermal Stability of Inverted Organic Photovoltaics Using Accelerated-Heat Lifetime Protocols" *ACS Appl Mater Interfaces*, 9 (16), 14136-14144.
41. Zhao, W.; Zhang, S.; Zhang, Y.; Li, S.; Liu, X.; He, C.; Zheng, Z.; Hou, J., 2018 "Environmentally Friendly Solvent-Processed Organic Solar Cells that are Highly Efficient and Adaptable for the Blade-Coating Method" *Adv Mater*, 30 (4).
42. Zhao, J.; Li, Y.; Yang, G.; Jiang, K.; Lin, H.; Ade, H.; Ma, W.; Yan, H., 2016 "Efficient organic solar cells processed from hydrocarbon solvents" *Nature Energy*, 1 (2).
43. McDowell, C.; Abdelsamie, M.; Toney, M. F.; Bazan, G. C., "Solvent Additives: Key Morphology-Directing Agents for Solution-Processed Organic Solar Cells" *Adv Mater*, e1707114.
44. Kim, M.; Lee, J.; Jo, S. B.; Sin, D. H.; Ko, H.; Lee, H.; Lee, S. G.; Cho, K., 2016 "Critical factors governing vertical phase separation in polymer-PCBM blend films for organic solar cells" *Journal of Materials Chemistry A*, 4 (40), 15522-15535.
45. Kumar, M.; Dubey, A.; Reza, K. M.; Adhikari, N.; Qiao, Q.; BommiSETTY, V., 2015 "Origin of photogenerated carrier recombination at the metal-active layer interface in polymer solar cells" *Phys Chem Chem Phys*, 17 (41), 27690-7.

## CHAPTER 5

# Printing eco-friendly polymer solar cells, the effect of molecular weight on efficiency, and morphology characterization

Printing of polymer solar cells using PTNT:PC<sub>71</sub>BM for best efficiency and optimum morphology was achieved and printing conditions were improved for similar polymer donor and acceptor pairs. Record PCE efficiency of 4.6% was reached with PTNT:PC<sub>71</sub>BM donor-acceptor BHJ system with mini-roll coating on PET-ITO flexible substrates. Eco-friendly solvent systems and drying techniques were also investigated, and morphology investigation was carried out for different solvent additives.

## 5.1 Introduction:

The majority of energy sources are non-renewable, and it instigates a major climate change and energy demand challenge. Recent advancements on renewable energy technologies find the best and most abundant solution is still solar energy. More advancements are now being done on improving the existing solar energy devices. The organic photovoltaic solar (OPV) devices come as very promising solutions compared to the silicon based solar cells as they are cost-effective, easily installable, more environmentally friendly and flexible. While silicon based solar cells have been widely used and a good renewable energy resource, they are heavier and more expensive to manufacture and install, also they have high energy payback times 1.6-4.1years (EPBT).<sup>1</sup> During their processing, high temperatures are required and material usage is high. They also have negative effects on environment and hence requires more sustainable alternatives in certain applications. Whereas, OPVs have very low energy payback times (0.2-2 years)<sup>2</sup>, uses photoactive layer that consists of organic materials that are thin and lightweight. They also have potential to be used in many more applications as they can be flexible. In OPVs, the organic thin layer absorbs the photons from sunlight and directly converts them to electricity. Hence, this photoactive layer needs to be very carefully and methodically coated onto glass or plastic substrates using techniques resulting in a favorable morphology in the final device. In this thesis, so far, we presented spin-coating techniques for the glass-ITO based OPV devices, here in this chapter, the printing techniques are explained and examined using a mini-roll coater and a known donor polymer and fullerene acceptor system that forms the photoactive layer. Also, the environmentally friendly solution processing was systematically researched, and printed devices were characterized for the best efficiency and eco-friendliness. The waste of organic ink during the printing of the active layer is

significantly reduced using printing techniques compared to spin-coating. Also, large scale printed solar cells can be done much easier and cost effectively.

The active layer formed by mini-roll coater was done in ambient air similar to large scale printing and most importantly can be done using non-harmful solvents that were discovered in the previous research in this thesis. During mini-roll coating process, conjugated polymers can be used as donors; and fullerenes, non-fullerene small molecules and polymers can be used as acceptors.<sup>3</sup> We used PTNT polymer as donor and experimented on both fullerene and NF acceptors. The solar cell device architecture was kept as inverted as in spin-coating. Other structures can also be implemented for printing solar cells such as conventional and single layer devices. Still, it is critical to be aware of the importance of bulk heterojunction layer in this architecture. The single layered and bi-layered active layers are less effective and show poor performance as discussed in Chapter 1. The ideal morphology in BHJ architecture is achieved by the optimum phase separation of the donor and acceptor materials. These provide good electron and hole separation and good domain size with suitable morphology. The coating of this BHJ active layer is via mini-roll coating and provides different morphology and device characteristics as observed with many other studies using the same device fabrication except the coating method. Therefore, we need to compare the spin coating and printing methods through mini-roll coating and show why we need to further investigate the eco-friendly OPV devices discussed in previous chapters using more scalable MRC fabrication system. In the meantime, spin-coating still provides a small scale and simple device performance data and helps us improve the formula of larger scale devices.

As the printing provides a more controllable, fast, minimum ink wastage and scalable fabrication (small to large scale) of OPV devices, in this final research topic, we need to also examine the compartments of fabrication using roll-to-roll systems such as flexible conductive substrates (ITO-PET, ITO-PEN), the meniscus properties where the thickness of active layer

and the width of solar cell strip is controlled adjusting the distance properties, tubing for each layer, ink flow rates, drum speeds, and the other parameters that change the controlled environment. These properties and parameters of printing via mini-roll coater are given in Methodology section and also will be discussed for their positive and negative effects of printed OPV device performance.

The reservoir of a mini-roll coater keeps the active layer and pumps it with a known flow rate as the drum speed is constant. As more experiments are done using same ink, the instrument parameter can be helpful in calculating theoretically the thickness of printed thin film and how to perfectly form it evenly with good morphology. The coated printed film layer was deposited with metal electrode for the complete device fabrication. These can be done using different materials and methods such as Ag NW coating<sup>4</sup>, metal deposition using a head on slot-die coater<sup>5</sup>, or deposition using a thermal deposition under vacuum.

The strips of the complete device later cut into desired size and examined for the stability. The degradation of printed solar devices contains differences than that of rigid devices as they are more prone to mechanical stress with ITO layer and also the active layer, moisture and O<sub>2</sub> exposure with the permeability of plastic substrate and the thermal and irradiation degradation. The thermal resistance of substrates is also limiting in this sense. The metal oxidation also differs in the printed device case as the encapsulation of devices require more gentle fabrication and a thinner encapsulation cover.<sup>6,7</sup>

These degradation and stability of OPVs can also stem from different type of interface layer fabrication such as ZnO and MoOx.<sup>8</sup> The ZnO NP fabrication and its effect on the stability of device performance while testing is also discussed in this chapter. The irradiance degradation can also be resolved using more stable UV- blocker or additive materials.

The device performance and the morphology of printed active layers also need to be consistent where the topography of devices differ from that of glass-based devices. Therefore, thicker

active layers, and donor-acceptor pairs that can perform good also with thick active layers are selected for the optimum morphology match.

The ITO coated PET needs to have an optimum conductivity and transparency.<sup>9</sup> The synthesized ZnO NPs and the active layer are printed via mini-roll coater and the MoO<sub>x</sub> and metal electrode deposited using thermal vacuum deposition. This thesis also focused on discovering the eco-friendly solvent to process the active layer ink using main and additive solvents for best efficiency as the coating is done in air and a candidate for larger scale roll to roll printing.

Later, a customized head is used in the testing of flexible printed OPV devices for photovoltaic performance. It is important to minimize the mechanical stress on the testing as well as the exposure to air. The printed OPV devices that were reported in literature are described differently as they can just use plastic substrates and not the exact printing methods or they use doctor blading coating method.<sup>10-13</sup> In this thesis, therefore we will mostly focus on the ones that use similar mini-roll coating printing and deposition methods that can be done in air providing upscalability towards large-scale printed solar cells. This limitation will assist us in comparing the coating adjustments, theoretical parameters from flow rates, substrate or drum speeds of roll-to-roll coaters and the designs of complete devices. The strip of dry and wet active layer also needs to be processed the same in each experiment so as to eliminate further parameters which have similar or opposite effects that can collide. The changing controllable parameters that need to be adjusted at first are; material composition, ink concentration, drum speed and the distance of meniscus and drum. Later, flow rate can be adjusted by keeping the drum speed the same. The thicknesses still can vary as the interactions of the ink and substrate and other coated interfacial layers. The thicknesses later can also be characterized via AFM or Profilometry. AFM can also provide surface topography, roughness and the homogeneous mixing of donor acceptor species. In the end, the complete best devices

are ready for further larger scale device testing and degradation research. Also, other environmental and instrumental effects can be analysed on device performance via strip quality, regular defects, and the burn in voltage issues.

## **5.2 Methodology:**

The methods used in this chapter varies in solution coating, solvent processing and final product's ability to be closer to ideal fabrication as it is more scalable.

The flexible substrate used, and the overall environmental impact also makes printing process more sustainable, and recyclable compared to the spin-coating method of fabricating PSCs.

All preliminary tests of organic solar cell production are currently still tested on glass-ITO substrates using spin-coating and thermal evaporation of electrodes. This technique is still fast and gives results to determine the main elements and techniques to achieve high efficiency, it also allows production in an inert atmosphere with less exposure to degrading effects, human and environmental errors.

Whereas there are many disadvantageous conditions we cannot avoid using spin-coating such as using minimum amount of material for only one changing parameter at a time, in other words, longer duration of optimization of experiments. Although it is useful to analyse which materials to use, the devices fabricated uses more solution to be coated with a homogeneous film and the surface's pattern is difficult to pattern reducing reproducibility and scalability. The rigid glass substrate only allows small area of solar device area with more ink used and less homogeneous coverage within the entire area of the substrate creating more difference for each cell on each sample.

The roll-to-roll coating of thin films can also be seen in Figure 5.1 where the sheets and strips of R2R coated solar cells fabricated in a systematic process using much less material and time per device fabrication.

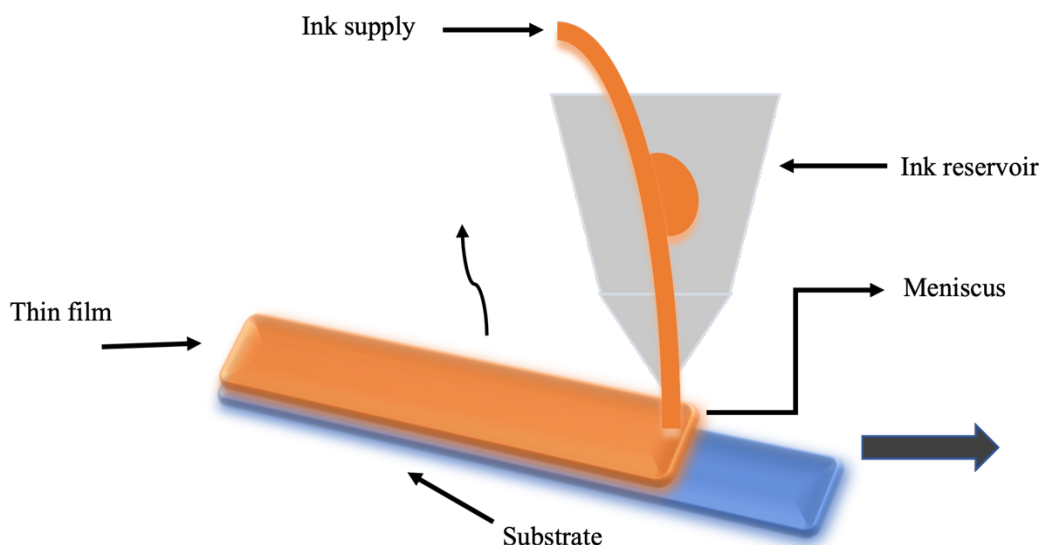


**Figure 5.1:** Slot-die coating (R2R coating).

There are different methods for printing solar cells besides slot-die coating and the reasons of our preference in our thesis is to have access to a Mini-roll coater which uses slot-die coating principles. For large scale manufacturing of organic solar cells, this method will provide the necessary parameters to upscale and optimize the PSC. The roll-to-roll manufacturing can be integrated after combining the results of slot-die coating and integration of continuous production system. Thus, the parameters determined are critical such as flexible substrate type, coating speed, solvent processing, ink composition and ink flow rate, and continuous manufacturing speeds for each coated layer including drying temperatures and times. Later, they will be used for large area continuous production for commercialization.

The structure that is better to employ is also inverted PSC in printed devices. While PET-ITO (polyethylene terephthalate - indium tin oxide) used as the plastic substrate coated with conductive transparent ITO electrode. As it is costly, ITO free printed device studies are being done as well, and their processing can be compared for future research.<sup>14</sup> Here in this thesis, inverted PET-ITO used in mini-roll compact slot-die coater for fabrication of flexible PSCs.

PEDOT:PSS can also be used in this structure as anode in combination with other metal electrodes however its light transmission is very low. Also, as ITO is brittle, the mechanical stress and bending on flexible printed solar cells can be damaging. These challenges are yet to be overcome and analysed. The best approach for us to alleviate these could be careful fabrication and proper coating strategies to have the best adhesion and stability for each layer. ZnO NPs layer and the post-annealing treatments can also be helpful. The image of the slot-die coater used in our experiments is given below in Figure 5.2, it is a practical and compact coater and can be used for initial roll-to-roll printing experiments. The efforts to optimize its components and the solar cell's fabrication parameters are very significant and will be focused here. The lightweight flexible substrates compared to rigid glass ones are the first layers to be prepared for the printing.



**Figure 5.2:** Mini-roll coater (FOM Technologies).

In printing solar cells, as stated, adhesion of each layer is essential and requires the repeatability of processing of adjacent layers and post-treatment of these coated layers.<sup>15</sup> This also means the degradation pathways are also different, there are more effects to consider than moisture and oxidation. The worldwide research priority has been so far given to polymer solar cell efficiency, however as it will be explained in the discussion, we prioritize eco-friendliness and the repeatability of a scalable printed polymer solar cell.

The device architecture is given in Figure 5.3, where flexible commercially available PET substrates coated with transparent ITO electrodes were used (~50 ohm/square) which have higher sheet resistance compared to glass counterparts. The laboratory scale sizes of strips of ZnO NP thin film layer and active layer then slot-die coated in air. Lastly, metal electrodes are deposited. This type of deposition can also be done using custom made flexographic printing which is compatible with slot-die coating system. It could be a back silver electrode where the silver patterns were done using a laser engraved rubber sleeve that's integrated onto a metal cylinder to exchange the printing pattern. A silver paste can be transferred to the roll as such with a paint roller. In this study, we only used thermal metal deposition under vacuum as the devices were still to be scalable and gave good results using Al metal.

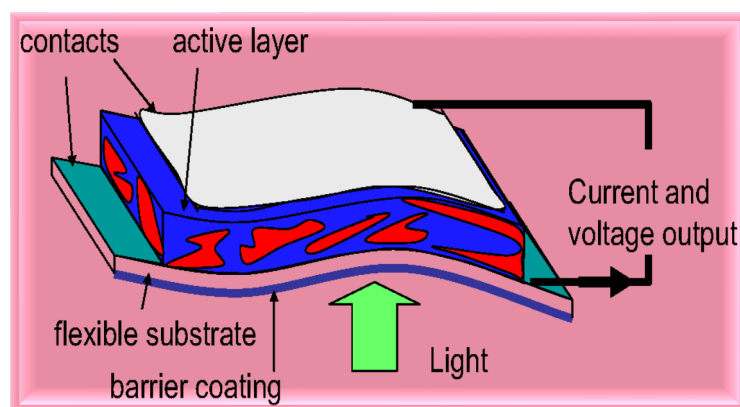
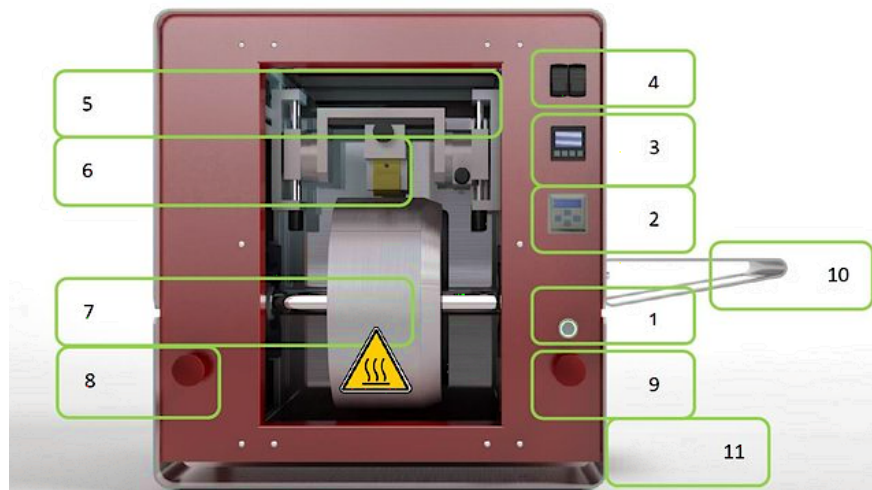


**Figure 5.3:** Flexible PSC device architecture.

The compact mini roll coater thus allows us to test different materials with solution processing, film forming, the compatibility of layers and materials, also the stability of final device architecture. The minimal material consumption facilitates the repeated optimizations and further scalable routine for larger scale coatings.

### 5.2.1 Mini roll coater (MRC) - components and operation:

MRC is a roll-to-roll compatible slot die coating compact machine. It has a 30 cm diameter roll in which the flexible ITO-PET substrates can be fed.



No	Function
1	Reset emergency stop button
2	Rotation speed and direction setting control
3	Temperature setting control
4	Left-on/off temperature switch, and Right-on/off cylinder rotation switch
5	2-axis adjustable mechanism. In relation to the cylinder, the mechanism is regulating coating head height and horizontal position
6	Slot-die head
7	Roll with temperature control
8,9	Emergency shut off left and right side
10	Shelf for pump – with an electrical outlet to be used for the pump
11	On the right side - main on/off switch and fuse box.

**Figure 5.4:** Mini roll coater (MRC) FOM Technologies and the main control units. <sup>16</sup>

A uniform solution is used with much less consumption (less than 50 $\mu$ L) from a meniscus head with 13 mm in width. This coating head is comprised of a meniscus guide, coating head, the ink inlet and the milled groove for the ink's passage. As seen in Figure 5.5, the coating head have tiny amount of dead ink volume (less than 50  $\mu$ L) which allows us to use minimal amount of necessary ink solution for coating, hence a very practical and early implementation method to test different systems with roll coating. The device processing, material interaction, thin film morphology properties and device architecture properties can all be tested with this system in an initial stage to be upscaled for industrial manufacturing and commercialization.

After each layer printing, it is very important to clean and dry properly all slot-die coating parts, like the head, tubing, the drum. The slot-die head needs to be dismantled for this cleaning process as each piece are shown in Figure 5.5. Then, the 2 stainless steel parts are got together using 4 screws. In between, there is also a stainless-steel sheet separator (0.25 mm thick). The slot-die coating head has a 50 mm deep groove where the ink solution is distributed through the slot and forms a stripe of film determined by the width of the meniscus.<sup>17</sup> The height/distance between the meniscus and the rotating cylinder drum is also critical as it determines the optimum film and if not stabilized can cause damage to the meniscus and detrimental defects to the thin film coated. A coated sheet of our fabricated devices and individual samples are also given in Figure 5.7 and 5.8.

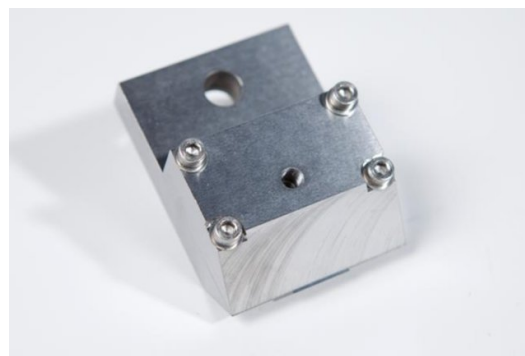
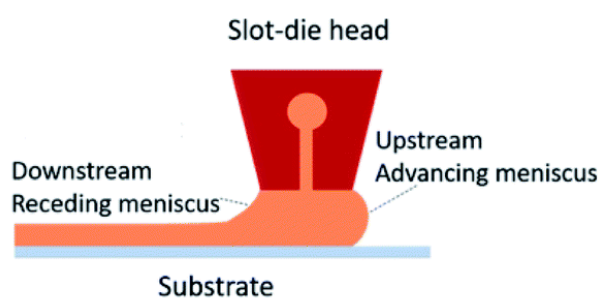


**Figure 5.5:** Schematic diagram of the meniscus formed during the slot-die coating process and MRC slot-die coating head (13 mm).<sup>18</sup>

“This image has been removed due to copyright restriction. Available online from <https://doi.org/10.1016/j.mtcomm.2019.100808>”

**Figure 5.6:** MRC Programmable syringe pump and process of film coating.<sup>19</sup>

In Figure 5.6, the syringe pump system and schematic of process of the delivery of ink to the head from a syringe pump are given. The wet film thickness between the coating head and the substrate can be adjusted via this process and the pump also enables the control of ink

flow rate. This parameter together with drum speed, and ink concentration plays a significant role in determining the thickness in printed thin film layers. The dry and wet thicknesses also vary as the heated drum rolls with varying or constant speeds for individual layers. All these parameters allow us the ideal optimization for best performance devices.

### **5.2.2 ZnO NP and BHJ Preparation:**

Printing techniques for OPV production also allows the printing of ZnO layer, without touching the substrates or disrupting any experimental conditions which differs from ITO-glass based devices where there is more chance of having defects due to multiple steps of different layers of coated films. Here, the layer-by-layer slot-die coating enables us a ZnO nanoparticle NP formed layer with a thin thickness and consistent morphology. As mentioned before, it acts as interphase layer in PSC and as it is based as nanocrystalline ink, the scalable fabrication makes printing method more advantageous in this step, as well. Since it is a semiconductor with remarkable properties, ZnO nanoparticles (NPs) can easily be integrated into printed electronics. Due to its good electron mobility and transparency, it acts as ETL in in PSCs and ZnO NP layer can be achieved with various ways from spin coating, inkjet printing, slot-die coating, thermal evaporation etc. making its deposition an entire research topic for printed organic photovoltaics.<sup>20,21</sup> In this thesis, the slot-die coating is done The ZnO NP layer (35 nm) was deposited with a  $0.1 \text{ mL min}^{-1}$  flowrate, a drum speed of  $1.0 \text{ m min}^{-1}$  and drum temperature of  $70 \text{ }^\circ\text{C}$  to achieve a strip width of around 13 mm (same as meniscus width). The photoactive layer consisting of PTNT polymer as donor and  $\text{PC}_{71}\text{BM}$  fullerene as acceptor formed a BHJ and it is also printed via slot-die coating on top of the ZnO NP layer. The thicknesses were initially adjusted via theoretical predictions and later tested via AFM. (Avg 150-200 nm). The final complete slot-die coated strips were individually cut into the sizes that

will fit to the patterned metal deposition mask. These will also allow the defined solar cell active area which is the same as the glass-ITO ones;  $0.1 \text{ cm}^2$ . The device geometry is summarized as; PET/ITO/ZnO NP/PTNT:PC<sub>71</sub>BM/MoO<sub>x</sub>/Al.

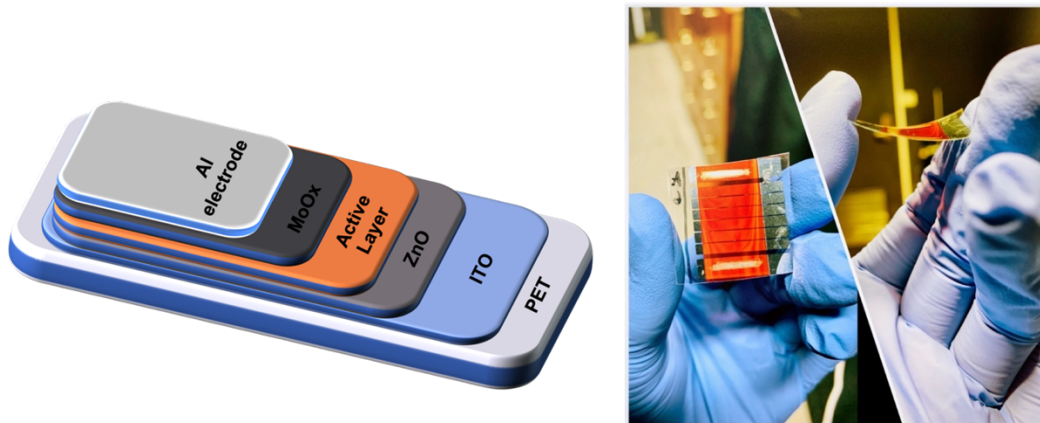


**Figure 5.7:** Printed PTNT:PC<sub>71</sub>BM device geometry schematic and complete device photo.

This easily forms a continuous process as we get more hands-on experience with the mini roll coater with average 3 hours of fabrication duration in total.

MoO<sub>x</sub> (12 nm) and Al electrode (80 nm) were deposited same as spin-coated devices using a thermal deposition under vacuum (Angstrom Engineering – Covap thermal deposition system). As the substrates are plastic, the encapsulation was omitted in this study, and some of the devices were tested couple of times to observe the effect of degradation and loss of device performance due to ambient air. The device characterization was done using Oriel solar simulator with 150 W Xeon lamp (Newport) for J-V curve determination under  $1000 \text{ W/m}^2$  illumination at AM 1.5 (air mass) standard. The simulator is calibrated with a silicon reference cell with known certification. A customized testing sample holder was also used to stabilize each device sample to test under the same conditions.

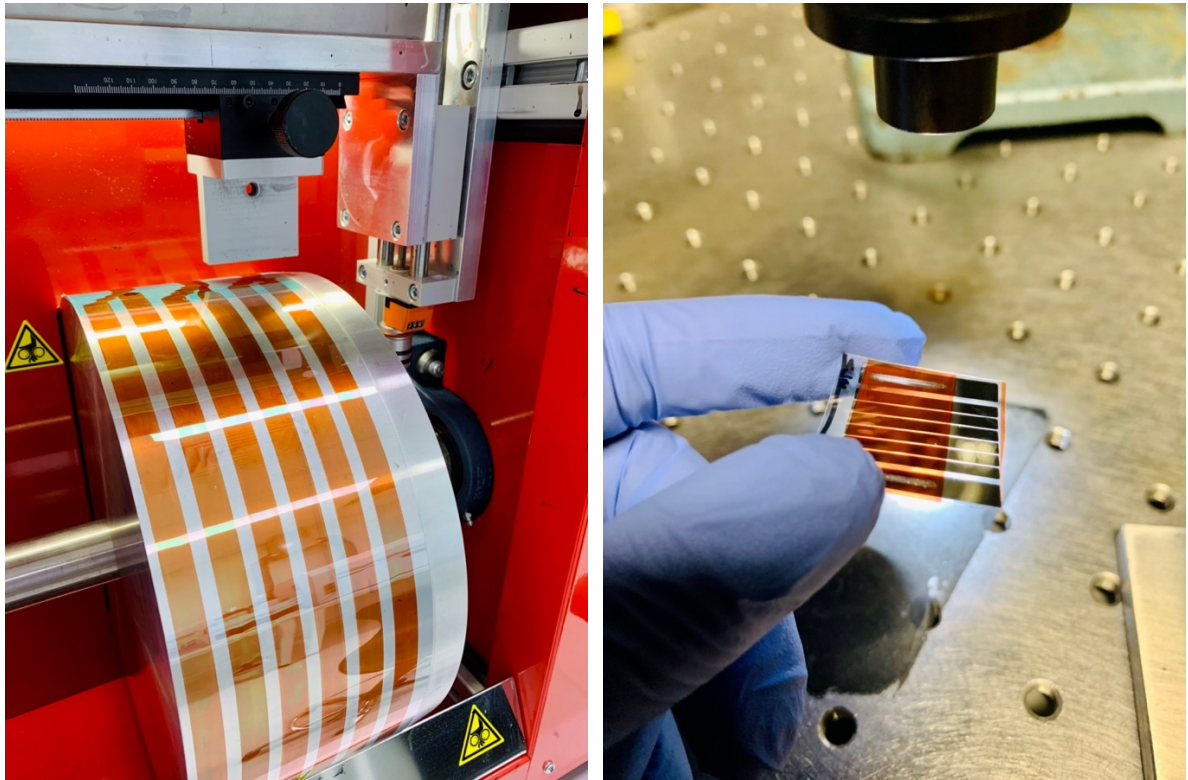


**Figure 5.8:** Strips of slot-die coated thin films and the complete device solar simulation characterization under light.

### **5.3 Slot-die Coating Defects, Adjustments and Printed OPV Degradation:**

To this point, the benefits and superiority of slot-die coating method has been investigated, yet as it requires a different understanding of deposition kinetics and solution interactions, the slot-die coated PSCs will also have different factors for defects, poor device performance and thin film nanoscale morphology issues, as well as instrument-based problems.

The beginning of coating starts from the meniscus of slot-die head and as it leaves the coating window, any defects or incorrect adjustments can cause poor strips of coatings. The ink's properties and the substrate characteristics can also play a role in this interaction.

Moreover, the external factors such as viscosity, adhesion, and substrate movements can also result in defects. <sup>22</sup> During the thesis experiments, these defects were observed, and

the conditions and properties were improved to eliminate them for the best device efficiency and stability. Below, several slot-die coating defects were summarized.

### 5.3.1 Chatter Defects:

This defect occurs across the whole width of coated strip, sometimes appearing with consistent intervals sometimes with just few lines as illustrated in Figure 5.9.

They can be seen via thickness variation of the coating compared to the rest of the coated strip, noticeable defects occurring suddenly, and with spaced interval of defects.

The reasons could be due the change in pressure or flow are of ink pumped to the system, defects in the drum roller, or the pressure changes in the upstream vacuum box.

In our experiments, the reasons were found as the varying distance of the stage to the position of substrate, it needs control with both hands and defects can occur with non-continuous roll-to-roll process. If the lines, chatters are very regular, this is most likely due to the stepping motor;

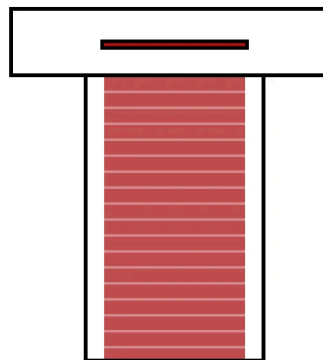


**Figure 5.9:** Appearance of chatter defects during slot-die coating. <sup>23</sup>

### 5.3.2 Ribbing Defects:

These defects occur along the length of the coated strip unlike the horizontal chatter. They are seen as consistent and multiple lines across the width of coating, where the thickness differs, single line or multiple defects can occur as depicted in Figure 5.10.

They can be due to the high shear forces in which the substrate speeds fast, or similarly due to the low pressure at the slot-die exit with low viscosities, and if there is a wide gap between the substrate and slot-die head, these defects are unavoidable. In order to improve the homogeneous film formation and eliminate the defects, the substrate speed can be reduced in order to reduce the shear force, the solution flow rate can be increased to increase the flow pressure or to catch up to the shear force, and finally the distance of slot-die head and substrate can be decreased. Furthermore, increasing the viscosity of solution, adding a vacuum box, or increasing the pressure at the exit can be useful. If there are specific localized defects, this could be due to the defects in the coater, like the slot-die head damage, aggregation of material in meniscus or the mishandling/installation of slot-die head. The drum and the substrate also need to be properly cleaned prior to any coating and be checked for any damages.

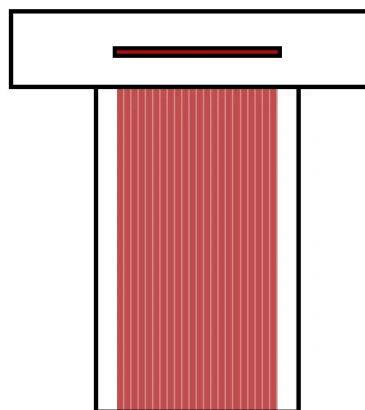


**Figure 5.10:** Appearance of ribbing defects during slot-die coating. <sup>23</sup>

### 5.3.3 Neck-in Defects:

These defects occur at the edges of the coated strip and creates a very poor coating, and the thickened edges can be observed as the wet ink dries along the width of film at a different time as given in Figure 5.11. The reasons could be due to the change in flow dynamics, the mismatch of flow rate and the substrate/drum speed which result in hastening of shear and fluid forces in a incompatible manner. The shear forces are also causing the coating to be accumulated at the centre of strip resulting in higher flow rates at the edges.

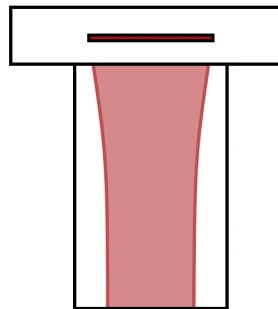


**Figure 5.11:** Appearance of neck-in defects during slot-die coating. <sup>23</sup>

Overcoming these negative effects, can be with the following solutions; the reduction of gap height between slot-die lip as in Figure 5.11 (when slot coating transitions to curtain coating) and the substrate, lowering of speed of coating web with smaller shim thickness which provides together the better compatibility between substrate and solution, finally for solutions with high viscosities and high surface tensions that cause neck-in defects inevitably, surfactant additives can be useful as they reduce the interactions between solvent molecules.

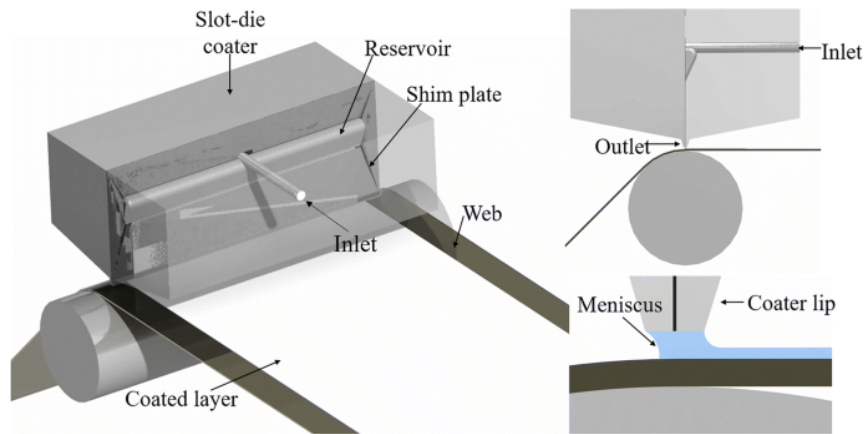


**Figure 5.12:** Slot-die head adjustable components for defect free coating process.

### 5.3.4 Edge Defects:

These defects occur due to the variations in the edge thicknesses of the coated films, mostly resulting in thicker edges as given in Figure 5.13. They can appear along the length of the coating on and off as the position of coating changes. The causes could be the pauses and other human or machine errors where interruptions are very challenging to eliminate and causes unstable coating process. In some cases, when it is first observed, the retraction of the solution can work as it worked in our experiments as well. The fast retraction will stop the flow of solution to the slot-die head and this can help in adjusting the substrate/drum speed.

Decreasing the surface tension to increases the viscosities can reduce the edge thickening defects too. The understanding of other effects resulting edge effects are very complex therefore, it is recommended to carefully analyse what is the problem and with an experienced user introduce or omit certain components. Furthermore, surface treatment such as UV ozone in specific locations can reduce the surface energy and increase the wetting for better coated edges. This could work for small scale devices. In large roll-to-roll sheet processes, even though the intervention is positive it could disrupt the continuous process and can result in contamination.

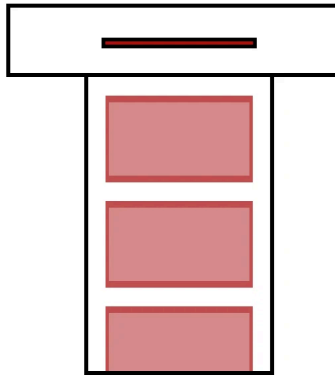


**Figure 5.13:** Appearance of edge defects during slot-die coating. <sup>23</sup>

### **5.3.5 Streak Defects:**

These slot-die coating defects are very common and also observed in our experiments. The depiction of the defects is given in Figure 5.14. The streaks can occur due to the aggregation of materials and thickness variations due to the contamination. Dust or dirt particles are unfortunately causing streaks to be present on the slot-die feed, substrate, and slot-die head at the lip. The slot-die head is not being properly cleaned and dried or the damages done, can also be the reasons of streak defects. If there are permanent streaks regardless of the ink composition and coating parameter variations, it is most likely due to the damage in the slot-die head. Fortunately, we only observed temporary streak formations and carefully cleaned the substrates and the other components of the slot-die coater to eliminate the problem. Moreover, any aggregates in solutions can also be trapped in the slot-die coating system and cause defects. If the streaks are minimal and only occur rarely, increasing the flow rate or increasing the slot-die head channel width can be also useful where reformulating the ink to decrease the aggregations is not preferable.

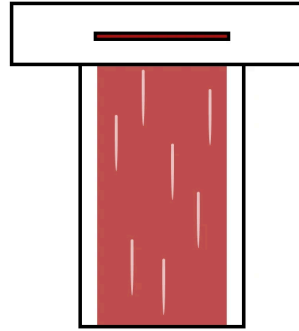


**Figure 5.14:** Appearance of streak defects during slot-die coating.<sup>23</sup>

### 5.3.6 Bubble Defects:

Lastly, bubble defects can occur during slot-die coating at any time. The defects are round and their sizes can vary, they may not contain any coated material which is detrimental to the final thin film morphology, an appearance of the bubble defects is given in Figure 5.15. The main reasons are the air entrapment in the ink solution that is fed from the syringe pumping system, or air entrapment from the fluid delivery (tubing system) or the air destabilisation of the upstream and downstream, meniscus. Low surface tensions can also cause the bubble formations, particularly when surfactants used to achieve this low surface tension. Similarly, with high viscosity solutions, the bubbles stay and more present.

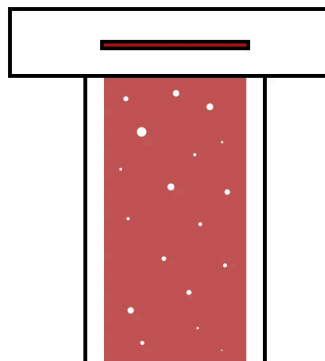


**Figure 5.15:** Appearance of bubble defects during slot-die coating.<sup>23</sup>

In order to remove these trapped air bubbles, the solutions can be degassed before feeding into the ink/fluid delivery system, all airtight systems where connectors and adaptors present can be checked and sealed properly, a PTFE tape can be used for this purpose.

The gap height-to-thickness ratio can be reduced by moving the slot-die coating lip to the substrate where the formation of bubbles can be eliminated by increasing the flow rate of solution. In summary, all these defects and adjustments to properly achieve a homogeneous nanoscale thin film requires good planning and many optimizations to achieve the highest and most stable device performance as it was also done in this study. The processes we conducted for printing PSCs began from designing the slot-die set-up for inverted PSC fabrication, carefully handling each slot-die coater components, maintenance of drum speed and ink delivery system, and the carefully tailored experiment conditions where parameters were only changed one at a time.

## **5.4 Discussion and Results:**

### **5.4.1 Effect of Molecular Weight of PTNT polymer on photovoltaic properties for selection of printed PSCs:**

Different solvent additives and molecular weight of PTNT batch of polymers in PSC fabrication was analysed and optimized prior to the printing of PTNT studies.

In Chapter 4, the PTNT batch used has a Molecular Weight of  $M_n=55.7$  kg/mol and  $M_w=163.2$  kg/mol relative to polystyrene standards. However, as we used the polymer for optimization of eco-friendly solvent processing, the printing of polymer solar cells needed more of PTNT polymer. Several batches of PTNT were synthesized and tested for molecular weight and solvent additive effect. In the end, a final new batch was selected for the printing

experiments which has a molecular weight of  $M_n=23.9$  kg/mol and  $M_w=86.5$  kg/mol relative to polystyrene standards (MJ-A159).

Moreover, prior to the molecular weight studies, MJ-A159 PTNT batch was experimented simultaneously against previous PTNT that was used in Chapter 4 experiments for their performance comparison. MJ-A159 PTNT batch was found to have slightly lower efficiency than the old PTNT batch.

Both MN and MLN additives and several concentration and spin-speeds were also experimented with the remaining PTNT and the new MJ-A159 batch (40 mg & 30 mg in total) and found that MN additive performs better than MLN in this new batch. Later more systematic experiments were also done using different batches of PTNT as explained below.

#### **5.4.2 Device Fabrication:**

The device architecture of inverted BHJ solar cells with PTNT is: ITO/ZnO/PTNT:PC<sub>71</sub>BM (2:3) (25mg/mL)/MoOx/Ag.

The fabrication was done mostly using host solvent o-xylene and 1% MN/ 2% MN / 1%MLN additives. These additives were available during this stage of thesis research and later more additives were experimented for the best polymer batch for the printing solar cells stage.

3 batches of PTNT and their best device performance are summarized below:

1. **MJ-A159 (P1):** Mn=23992, PD=3.607.

BHJ Layer: PTNT:PC<sub>71</sub>BM (1:2) 30 mg/mL in **o-xylene + 1% MN** (Spin speed: 1000 rpm, 60 sn + 3000 rpm, 30s, vacuum dried.)

The films formed with MJ-A159 among the 3 batches of polymers (3 batches of devices are done and best performing is selected).

**Table 5.1:** Photovoltaic properties for **MJ-A159 (P1)** PTNT:PC<sub>71</sub>BM (1:2) 30 mg/mL in **o-xylene + 1% MN**.

Device: <b>MJ-A159 (P1)</b> <b>o-xylene + 1% MN</b>	Jsc (mA/cm <sup>2</sup> )	Voc (V)	FF (%)	Eff (%)
PCE Max	3.936	0.873	52	1.8
Avg	3.774	0.877	52	1.74
Std Dev	0.13477	0.00515	1.5	0.04183

2. **MJ-B55 (P2):** Mn=16550, PD=3.331.

BHJ Layer: PTNT:PC<sub>71</sub>BM (1:2) 30 mg/mL in **o-xylene + 1% MN** (Spin speed: 2000 rpm, 60 sn + 3000 rpm, 30s, vacuum dried.)

The devices with MJ-B55 were also done in 3 batches, and most of them formed less homogeneous films and caused varying photovoltaic data as seen from the standard deviations. The most stable one was given below where the efficiency is still lower than that of with MJ-A159.

**Table 5.2:** Photovoltaic properties for **MJ-B55 (P2)** PTNT:PC<sub>71</sub>BM (1:2) 30 mg/mL in **o-xylene + 1% MN**.

Device: <b>MJ-B55 (P2)</b> <b>o-xylene + 1% MN</b>	Jsc (mA/cm <sup>2</sup> )	Voc (V)	FF (%)	Eff (%)
PCE Max	2.84	0.828	60	1.41
Avg	2.85	0.809	54	1.25
Std Dev	0.799	0.03861	0.9	0.23889

3. **MJ-B67 (P3):** Mn=16577 PD= 3.312.

BHJ Layer: PTNT:PC<sub>71</sub>BM (1:2) 30 mg/mL, **o-xylene + 1% MN** (Spin speed: 1500 rpm, 60 sn + 3000 rpm, 30s, vacuum dried.) Slightly opaque film formed, and the aggregated films increased the efficiency slightly when illuminated.

**Table 5.3:** Photovoltaic properties for **MJ-B67 (P3)** PTNT:PC<sub>71</sub>BM (1:2) 30 mg/mL in **o-xylene + 1% MN**.

Device: <b>MJ-B67 (P3):</b> <b>o-xylene + 1% MN</b>	Jsc (mA/cm <sup>2</sup> )	Voc (V)	FF (%)	Eff (%)
PCE Max	2.474	0.865	65	1.4
Avg	2.478	0.864	63	1.34
Std Dev	0.03800	0.00395	1	0.03948

After eliminating one batch of PTNT, we decided to optimize the film thickness (keeping concentration constant as 25mg/mL) and experimented on spin-speeds and solvent additive selections via MJ-A159 and MJ-B55 batches of PTNT.

**Table 5.4:** Photovoltaic properties summarized for 3 batches of PTNT.

BHJ System	1% MN
<b>P1 (MJ-A159)</b> <b>PTNT:PC<sub>71</sub>BM (1:2)</b> <b>(30 mg/mL)</b>	Jsc (mA/cm <sup>2</sup> ): 3.774 Voc (V): 0.877 FF: 52 <b>η (%): 1.74</b>
<b>P2 (MJ-B55)</b> <b>PTNT:PC<sub>71</sub>BM (1:2)</b> <b>(30 mg/mL)</b>	Jsc (mA/cm <sup>2</sup> ): 2.850 Voc (V): 0.809 FF: 54 <b>η (%): 1.25</b>
<b>P3 (MJ-B67)</b> <b>PTNT:PC<sub>71</sub>BM (1:2)</b> <b>(30 mg/mL)</b>	Jsc (mA/cm <sup>2</sup> ): 2.478 Voc (V): 0.864 FF: 63 <b>η (%): 1.34</b>

Below are also the photovoltaic properties of the best performing devices among different spin-speed coatings; MJ-A159 still performed the best with all different additives using 2 (v/v)% concentration even though had lower efficiency than expected (this could be due to the ITO substrates we used in this particular sets of experiments, so still comparable in this set of devices).

Annealing of devices were also done and found to be less efficient similar as in Chapter 4, so not included in the optimization experiments.

**1. MJ-A159 (P1):** Mn=23992, PD=3.607.

BHJ Layer: PTNT:PC<sub>71</sub>BM (2:3) 25 mg/mL in **o-xylene** + **2% MN** (Spin speed: 1000 rpm, 60 sn + 3000 rpm, 30s, vacuum dried.) The film formed was homogeneous and had only slight defects.

**Table 5.5:** Photovoltaic properties for **MJ-A159 (P1)** PTNT:PC<sub>71</sub>BM (2:3) 25 mg/mL in **o-xylene** + **2% MN**.

Device: <b>MJ-A159 (P1)</b> <b>o-xylene + 2% MN</b>	Jsc (mA/cm <sup>2</sup> )	Voc (V)	FF (%)	Eff (%)
PCE Max	6.297	0.886	60	3.37
Avg	6.205	0.884	60	3.31
Std Dev	0.07380	0.00544	1	0.005050

**2. MJ-A159 (P1):** Mn=23992, PD=3.607.

BHJ Layer: PTNT:PC<sub>71</sub>BM (2:3) 25 mg/mL, **o-xylene + 2% MLN** (Spin speed: 1500 rpm, 60 sn + 3000 rpm, 30s, vacuum dried.)

**Table 5.6:** Photovoltaic properties for **MJ-A159 (P1)** PTNT:PC<sub>71</sub>BM (2:3) 25 mg/mL in **o-xylene** + **2% MLN**.

Device: <b>MJ-A159 (P1)</b> <b>o-xylene + 2% MLN</b>	Jsc (mA/cm <sup>2</sup> )	Voc (V)	FF (%)	Eff (%)
PCE Max	5.89	0.872	56	2.85
Avg	5.430	0.864	56	2.60
Std Dev	0.27233	0.00518	1.5	0.17509

**3. MJ-A159 (P1):** Mn=23992, PD=3.607.

BHJ Layer: PTNT:PC<sub>71</sub>BM (2:3) 25 mg/mL, **o-xylene + 3% DIO** (Spin speed: 1000 rpm, 60 sn + 3000 rpm, 30s, vacuum dried.)

**Table 5.7:** Photovoltaic properties for **MJ-A159 (P1)** PTNT:PC<sub>71</sub>BM (2:3) 25 mg/mL in **o-xylene** + **3% DIO**.

Device: <b>MJ-A159 (P1)</b> <b>o-xylene + 3% DIO</b>	Jsc (mA/cm <sup>2</sup> )	Voc (V)	FF (%)	Eff (%)
PCE Max	9.386	0.872	67	5.46
Avg	8.600	0.876	70	5.23
Std Dev	0.60478	0.00299	2.0	0.19570

**4. MJ-B55 (P2):** Mn=16550 PD=3.331.

BHJ Layer: PTNT:PC<sub>71</sub>BM (2:3) 25 mg/mL, **o-xylene + 2% MN** (Spin speed: 1000 rpm, 60 sn + 3000 rpm, 30s, vacuum dried.)

**Table 5.8:** Photovoltaic properties for **MJ-B55 (P2)** PTNT:PC<sub>71</sub>BM (2:3) 25 mg/mL in **o-xylene + 2% MN**.

Device: <b>MJ-B55 (P2)</b> <b>o-xylene + 2% MN</b>	Jsc (mA/cm <sup>2</sup> )	Voc (V)	FF (%)	Eff (%)
PCE Max	4.309	0.817	66	2.34
Avg	4.222	0.814	66	2.28
Std Dev	0.07147	0.00684	0.5	0.05177

**5. MJ-B55 (P2):** Mn=16550 PD=3.331.

BHJ Layer: PTNT:PC<sub>71</sub>BM (2:3) 25 mg/mL, **o-xylene + 2% MLN** (Spin speed: 1500 rpm, 60 sn + 3000 rpm, 30s, vacuum dried.)

**Table 5.9:** Photovoltaic properties for **MJ-B55 (P2)** PTNT:PC<sub>71</sub>BM (2:3) 25 mg/mL in **o-xylene + 2% MLN**.

Device: <b>MJ-B55 (P2)</b> <b>o-xylene + 2% MLN</b>	Jsc (mA/cm <sup>2</sup> )	Voc (V)	FF (%)	Eff (%)
PCE Max	2.591	0.88	66	1.51
Avg	2.578	0.871	61	1.36
Std Dev	0.02795	0.00763	0.7	0.16990

**6. MJ-B55 (P2):** Mn=16550 PD=3.331.

BHJ Layer: PTNT:PC<sub>71</sub>BM (2:3) 25 mg/mL, **o-xylene + 3% DIO** (Spin speed: 1000 rpm, 60 sn + 3000 rpm, 30s, vacuum dried.)

**Table 5.10:** Photovoltaic properties for **MJ-B55 (P2)** PTNT:PC<sub>71</sub>BM (2:3) 25 mg/mL in **o-xylene + 3% DIO**.

Device: <b>MJ-B55 (P2)</b> <b>o-xylene + 3% DIO</b>	Jsc (mA/cm <sup>2</sup> )	Voc (V)	FF (%)	Eff (%)
PCE Max	5.311	0.873	70	3.24
Avg	5.277	0.865	68	3.10
Std Dev	0.08924	0.00555	2.7	0.13081

**Table 5.11:** Photovoltaic properties summarized for 2 batches of PTNT with MN, MLN and DIO additives compared (MJ-A159 vs MJ-B55).

BHJ System	2% MLN	2%MN	3% DIO
<b>P1 (MJ-A159)</b> <b>PTNT:PC<sub>71</sub>BM (2:3)</b> <b>(25 mg/mL)</b>	Jsc (mA/cm <sup>2</sup> ): 5.430 Voc (V): 0.864 FF: 56 <b>η (%): 2.60</b>	Jsc (mA/cm <sup>2</sup> ): 6.205 Voc (V): 0.884 FF: 60 <b>η (%): 3.31</b>	Jsc (mA/cm <sup>2</sup> ): 8.600 Voc (V): 0.876 FF: 70 <b>η (%): 5.23</b>
<b>P2 (MJ-B55)</b> <b>PTNT:PC<sub>71</sub>BM (2:3)</b> <b>(25 mg/mL)</b>	Jsc (mA/cm <sup>2</sup> ): 2.578 Voc (V): 0.871 FF: 61 <b>η (%): 1.36</b>	Jsc (mA/cm <sup>2</sup> ): 4.222 Voc (V): 0.814 FF: 66 <b>η (%): 2.28</b>	Jsc (mA/cm <sup>2</sup> ): 5.277 Voc (V): 0.865 FF: 68 <b>η (%): 3.10</b>

**P1 (MJ-A159)** PTNT polymer batch gave the highest power conversion efficiency in these preliminary experiments. Although the results vary with previous PTNT experiments discussed in the thesis, the different batches of PTNT with different molecular weights were experimented by carefully keeping their fabrication conditions the same so that we can eliminate the parameters changing other than molecular weight.

In the next step, the photovoltaic properties were analysed with several experiments using P1 and eco-friendly solvent systems. Also, as a reference DIO additive was again compared.

The optimum spin coating conditions for P1 was selected as: 1000 rpm for 60 sec + 3000 rpm for 30 sec, 85°C stirred overnight.

As in Chapter 4, MN additive was found to perform the best, the same percentage (2%) of additive was experimented. After several preliminary optimization experiments with different solvents, and solvent additive ratios, below polymer + solvent additive combinations gave best efficiencies as:

P1 + 2% MN: Best device  $PCE_{avg}$ = 3.3%

P1 + 2% MLN: Best device  $PCE_{avg}$ = 2.6%

P1 + 3% DIO: Best device  $PCE_{avg}$ = 5.2%

Using P1 (PTNT with optimum molecular weight + solubility)

This device efficiency difference presents a good example of an effective solar cell performance with enhanced miscibility of the BHJ constituents due to higher BP and more electron rich unity of MN additive. They ease charge generation. It was also discussed in Chapter 4 how it forms a homogeneous film and separates phases with the best effect on morphological changes using AFM. It has been shown before how topography analysis is crucial before device fabrication while using different surface treatments such as solvent additives.

The 1-MLN additive mostly gives non-transparent films that hinder the photon absorbance and decrease the device performance. It could be attributed to an excess phase segregation.

DIO additive gives a good efficiency of 5% which is higher than earlier device performances, it is interesting to see how Mwt differences changes the response to additives. Although it gives high efficiency, as it is very toxic additive, the printing experiments will not be making use of DIO with PTNT polymer.

Moreover, the enhancement of photovoltaic performance with increasing Mwt can be attributed to the enhanced light absorption and increased charge carrier mobility of PTNT

polymer with high MW, and a proper phase separation in BHJ composite of PTNT:PC<sub>71</sub>BM interpenetrating network. All these results demonstrate that the Mwt of donor polymer plays an important role in the performance of BHJ PSCs. The solvent additives also demonstrate different morphology changing effects altering the phase separation with different Mwt donor polymers.

The crystallization properties and film morphology need to be compared with AFM technique in order to see the nanoscale images of the less-transparent films we have using low Mwt donor polymers and how different ratios of additives affect the film quality.

In conclusion, preparation of environmentally friendly polymer solar cell devices was achieved using different molecular weight batches of PTNT donor polymer and PC<sub>71</sub>BM fullerene acceptor, and their characterization was done successfully revealing their photovoltaic performances and molecular weight effect. Using the optimum batch P1, previously tested solvent systems were experimented again in order to see performance differences and select the best for printing of PTNT experiments. The environmental effects and other fabrication parameters were minimized for this optimization. Still, as these results were with ITO-glass substrates and small-scale devices, the printing section of the thesis will also make use of different additive and other parameter combinations to find the highest performing flexible PTNT device with the large-scale printing potential.

Also, PC<sub>61</sub>BM fullerene will be compared during printing of OPVs (slot-die coating of these cells).

## **5.5 Photovoltaic Properties of PTNT:PC<sub>71</sub>BM and PTNT:ITIC (MJ-A159 batch) devices using different solvent additives:**

In chapter 4, PTNT devices using eco-friendly solvent systems were investigated. The same recipe was tested with more additives later prior to the printing experiments with new batches of PTNT donor polymer.

As mentioned above, new batches of PTNT polymers were synthesized and investigated for their OPV performance to determine the best one to use in printed PSCs. A molecular weight comparison study was conducted initially, among them MJ-A159 batch of PTNT polymer gave the highest efficiency ( $M_n=23.9$  kg/mol,  $M_w=86.5$  kg/mol relative to polystyrene standards),  $PD=3.607$ . This batch had a lower molecular weight than that of PTNT polymer used for Chapter 4 ( $M_n= 55.7$  kg/mol,  $M_w= 163.2$  kg/mol) studies, still high enough to be comparable.

The new batch was tested (after initial preliminary experiments given above) first on ITO-glass devices prior to ITO-PET printed PSC devices with both fullerene and non-fullerene acceptors. Below is the device fabrication for each solvent system and material composition.

The first set of device architectures that were experimented are;

- ITO/ZnO//PTNT:ITIC/MoO<sub>x</sub>/Ag (25 mg/mL) (2:3) in o-xylene + 3% DIO; 85°C over a day + as-cast after drying under vacuum overnight using MJ-A159 batch.
- ITO/ZnO/PTNT:PC<sub>71</sub>BM/MoO<sub>x</sub>/Ag (25 mg/mL) (2:3) in o-xylene + 2% MN, 2% AA, 2% MLN additives, the solution was mixed at 85°C over a day + as-cast after drying under vacuum overnight using MJ-A159 batch.

1. BHJ Layer: PTNT:ITIC (2:3) (25 mg/mL) in o-xylene + 3% DIO (Spin speed: 2000 rpm, 60 s + 3000 rpm, 30 s, vacuum dried.)

The films with 1000 rpm and 1500 rpm (60s) spin-coating were very cloudy. The 2000 rpm spin-speed gave a good film and a stable device.

**Table 5.12:** Photovoltaic properties for PTNT:ITIC (2:3) (25 mg/mL) in o-xylene + 3% DIO.

<b>Device:</b> <b>o-xylene + 3% DIO</b>	Jsc (mA/cm <sup>2</sup> )	Voc (V)	FF (%)	Eff (%)
PCE Max	7.541	1.028	0.45	3.46
Avg	7.277	1.028	0.44	3.31
Std Dev	0.20698	0.00835	0.00516	0.10875

2. BHJ Layer: PTNT:PC<sub>71</sub>BM 25 mg/mL, o-xylene + 2% MN (Spin speed: 1000 rpm, 60 sn + 3000 rpm, 30s, vacuum dried.) The films were good and stable.

**Table 5.13:** Photovoltaic properties for PTNT:PC<sub>71</sub>BM 25 mg/mL, o-xylene + 2% MN.

<b>Device:</b> <b>o-xylene + 2% MN</b>	Jsc (mA/cm <sup>2</sup> )	Voc (V)	FF (%)	Eff (%)
PCE Max	7.838	0.868	0.7	4.75
Avg	7.735	0.868	0.69	4.62
Std Dev	0.20606	0.00492	0.01225	0.21557

3. BHJ Layer: PTNT:PC<sub>71</sub>BM 25 mg/mL, o-xylene + 2% AA (Spin speed: 1000 rpm, 60 sn + 3000 rpm, 30s, vacuum dried.) The films were good, looked thicker than MN and MLN films. Stable device. No opacity was observed unlike the experiment 3 years ago using o-DCB + 3% AA.

**Table 5.14:** Photovoltaic properties for PTNT:PC<sub>71</sub>BM 25 mg/mL, o-xylene + 2% AA.

<b>Device:</b> <b>o-xylene + 2% AA</b>	Jsc (mA/cm <sup>2</sup> )	Voc (V)	FF (%)	Eff (%)
PCE Max	8.982	0.908	0.7	5.72
Avg	8.643	0.910	0.69	5.42
Std Dev	0.27560	0.00133	0.01211	0.26271

4. BHJ Layer: PTNT:PC<sub>71</sub>BM 25 mg/mL, o-xylene + 2% MLN (Spin speed: 1000 rpm, 60 sn + 3000 rpm, 30s, vacuum dried.) The films looked okay.

**Table 5.15:** Photovoltaic properties for PTNT:PC<sub>71</sub>BM 25 mg/mL, o-xylene + 2% MLN.

<b>Device: o-xylene + 2% MLN</b>	Jsc (mA/cm <sup>2</sup> )	Voc (V)	FF (%)	Eff (%)
PCE Max	3.099	0.699	0.54	1.16
Avg	2.146	0.700	0.65	0.96
Std Dev	0.47319	0.00551	0.05428	0.10784

Later, the same polymer batch (MJA159) (PTNT:PC<sub>71</sub>BM (2:3)) was also tested using o-DCB + 2% AA as it was conducted in our first trial of experiments. (Spin speed: 1000 rpm, 60s + 3000 rpm, 30s, vacuum dried.)

To accurately compare, the same fabrication conditions were kept and o-xylene + 2% AA devices were also tested again. (PTNT:PC<sub>71</sub>BM (2:3)) (Spin speed: 1000 rpm, 60s + 3000 rpm, 30s, vacuum dried.)

The results were very consistent and showed us how stable devices were formed using o-xylene + AA system in PTNT: PC<sub>71</sub>BM devices.

Moreover, with same fabrication conditions, a mixture of fullerene and non-fullerene devices were also experimented. PTNT:ITIC:PC<sub>71</sub>BM devices versus PTNT:ITIC devices as reference were fabricated. These 2 systems were tested using o-xylene + 3% DIO solvent systems. Several spin speeds were also used to find the ideal thickness.

5. BHJ Layer: PTNT:PC<sub>71</sub>BM 25 mg/mL, o-xylene + 2% AA (Spin speed: 1000 rpm, 60 sn + 3000 rpm, 30s, vacuum dried.) (Repeated experiment using AA additive to compare with others under exact same conditions)

**Table 5.16:** Photovoltaic properties for PTNT:PC<sub>71</sub>BM 25 mg/mL, o-xylene + 2% AA.

<b>Device: o-xylene + 2% AA</b>	Jsc (mA/cm <sup>2</sup> )	Voc (V)	FF (%)	Eff (%)
PCE Max	8.384	0.922	74	5.69
Avg	7.926	0.919	75	5.42
Std Dev	0.33247	0.00379	0.00548	0.22500

The devices with o-DCB (o-DCB + 2% AA) having still slightly cloudy/opaque films as it was before in our initial preliminary experiment, we managed get a moderate efficiency (~4.65 %). Still as the device has poor morphology and low transparency, this solvent system is still unfavourable, and not environmentally friendly.

6. The mixed fullerene/NF acceptor system, BHJ Layer: PTNT:ITIC:PC<sub>71</sub>BM (1:0.3:1.2) (25 mg/mL) in o-xylene + 3% DIO (Spin speed: 1000 rpm, 60 s + 3000 rpm, 30s, vacuum dried.)

**Table 5.17:** Photovoltaic properties for PTNT:ITIC:PC<sub>71</sub>BM (1:0.3:1.2) (25 mg/mL) in o-xylene + 3% DIO.

<b>Device: o-xylene + 3% DIO</b>	Jsc (mA/cm <sup>2</sup> )	Voc (V)	FF (%)	Eff (%)
PCE Max	8.486	0.881	0.65	4.88
Avg	8.167	0.874	0.65	4.62
Std Dev	0.26094	0.00615	0.00516	0.20331

Below is the photovoltaic properties of PTNT:ITIC devices (2250 rpm, 60 s) fabricated against the mixed acceptor system to see the difference. This was also done to discover the potential of using optimum and/or cost-effective acceptor systems for printed devices. Devices with thin layer of BHJ showed increasing efficiency. Whereas when PC<sub>71</sub>BM used thicker devices performed slightly better. Another outcome is with the introduction of ITIC only, the Voc is high, however device shows very poor efficiency overall due to poor morphology and coating defects. Although there are various effects for this difference, we may conclude it still

had a positive effect on improved charge transfer leading to reduced non-radiative recombination losses and thereby increase in Voc.

7. BHI Layer: PTNT:ITIC (2:3) (25 mg/mL) in o-xylene + 3% DIO (Spin speed: 2250 rpm, 60 s + 3000 rpm, 30s, vacuum dried.)

**Table 5.18:** Photovoltaic properties for PTNT:ITIC (2:3) (25 mg/mL) in o-xylene + 3% DIO.

Device: o-xylene + 3% DIO	Jsc (mA/cm <sup>2</sup> )	Voc (V)	FF (%)	Eff (%)
PCE Max	7.298	1.016	38	2.85
Avg	6.837	1.012	38	2.67
Std Dev	0.32099	0.00764	0.00816	0.11606

**Table 5.19:** Photovoltaic properties summarized for PTNT with MLN, MN, DIO and AA additives compared (MJ-A159)

BHI System	2% MLN	2%MN	3% DIO	2%AA
MJ-A159 PTNT:PC <sub>71</sub> BM (2:3) Tested for AA additive against MLN & MN (25 mg/mL)	Jsc (mA/cm <sup>2</sup> ): 2.146 Voc (V): 0.700 FF: 65 <b>η (%) : 0.96</b>	Jsc (mA/cm <sup>2</sup> ): 7.735 Voc (V): 0.868 FF: 69 <b>η (%) : 4.62</b>		Jsc (mA/cm <sup>2</sup> ): 8.643 Voc (V): 0.910 FF: 69 <b>η (%) : 5.42</b>
MJ-A159 PTNT:PC <sub>71</sub> BM (2:3) Tested for AA additive for best efficiency (25 mg/mL)				Jsc (mA/cm <sup>2</sup> ): 7.926 Voc (V): 0.919 FF: 75 <b>η (%) : 5.42</b>
MJ-A159 PTNT:ITIC (2:3) (25 mg/mL)			Jsc (mA/cm <sup>2</sup> ): 7.277 Voc (V): 1.028 FF: 44 <b>η (%) : 3.31</b>	
MJ-A159 PTNT:ITIC (2:3) Tested against mixed fullerene (25 mg/mL)			Jsc (mA/cm <sup>2</sup> ): 6.837 Voc (V): 1.012 FF: 38 <b>η (%) : 2.67</b>	
MJ-A159 PTNT:ITIC: PC <sub>71</sub> BM (1:0.3:1.2) (25 mg/mL)			Jsc (mA/cm <sup>2</sup> ): 8.167 Voc (V): 0.874 FF: 65 <b>η (%) : 4.62</b>	

## **5.6 Printed Device Performances for PTNT:PC<sub>71</sub>BM(2:3) processed from non-toxic solvent systems:**

The final experiments of this thesis are printing eco-friendly solar cells using a slot-die coater as a mini roll coater technique. For the printing of solar cells, the PTNT polymer was used as a donor and PC<sub>61</sub>BM and PC<sub>71</sub>BM were used as fullerene acceptors; and the solvent systems were chosen as o-xylene + MN & o-xylene + PN & o-xylene + AA as mostly optimized earlier in spin-coated polymer solar cells. These solvent systems gave mostly similar device performance trends and for the best device performance, the device efficiency was higher even though the molecular weight (Mwt) of the solar cell's donor polymer (PTNT) was lower than that of the previous experiments.

In the printing of polymer solar cells, the aim is to discover eco-friendly polymer-acceptor systems for large-area flexible OPVs as they will be candidates for upscaling and later future clean energy resources. The ideal systems need to provide a thermally stable architecture, higher active layer thickness, good mechanical properties for flexibility, and high efficiency. In this thesis, we also focused another very important property which is eco-friendliness of flexible polymer solar cells. Therefore, there are several changes to overcome and many device parameters to optimize for the ideal printed device. The device architecture is the same as ITO-glass inverted PTNT PSC devices except the ZnO NP interface layer formation and the substrate which is ITO-PET (~50 ohms/sq) in printed PSCs.

The mini-roll coater instrument setup was used for printing of solar cells which is a very practical and cost-effective printing technique. The image of the instrument with some of the devices constructed is given in Figure 5.16.



**Figure 5.16:** FOM Mini-roll coater used for printing of polymer solar cells.

The simple device structure is: PET(flexible plastic substrate)/ITO/ZnO NP/BHJ layer/MoOx/Al (Metal electrode). The BHJ active layers tested were PTNT:PC<sub>71</sub>BM and PTNT:PC<sub>61</sub>BM where P1 batch is used as discussed in the preliminary Mwt experiments. Since later in the thesis research, AA solvent additive is also tested and found to be a good candidate for PTNT, it was tested here along with MN, 1-MLN and other additives. The optimization experiments with ITO-glass PTNT devices using AA additive later conducted after P1 optimization and given as summarized in the beginning of this chapter. As a result of these experiments, it was found that AA additive shows much higher performance than MN additive with the P1 PTNT batch, and this is a good indication of how further experiments with same polymer-acceptor and solvent systems can give higher performances and should be tested for the best result.

After printing in air using MRC, the metal electrode evaporation is carried out in the glove box as usual, and device active area was set the same as 0.1 cm<sup>2</sup> by cutting the strips of printed active layers carefully as shown in Figure 5.17 and 5.18.

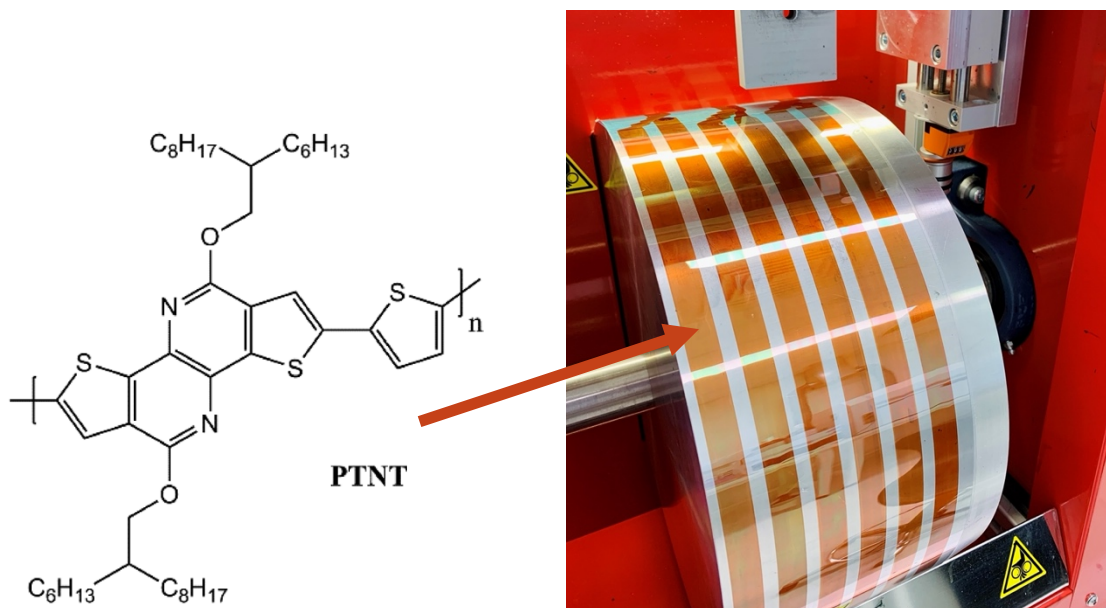


**Figure 5.17:** PTNT structure and the printed strips of photoactive layer using MRC.

### 5.6.1 PTNT Printed Device Photovoltaic Properties:

The ideal recipe was found to be:

PET(flexible plastic substrate)/ITO/PTNT:PC<sub>71</sub>BM/MoO<sub>x</sub>/Al (25 mg/mL)(2:3) processed from *o*-xylene and 2% AA solvent additive, stirred at 85°C overnight and vacuum dried at 10<sup>-7</sup>mbar for 1 hour after drying in big antechamber overnight. The ink is 1 mL in total.

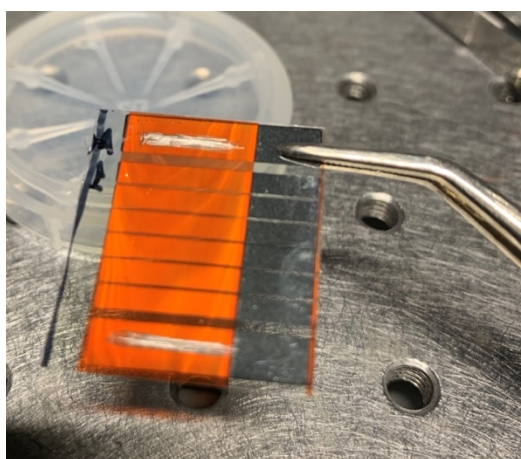


**Figure 5.18:** Printed complete polymer solar cell device.

Below is the complete device data for the best performing printed cell using P1 with and without vacuum drying:

**Table 5.20:** Photovoltaic properties summarized for PTNT:PC<sub>71</sub>BM processed from o-xylene and 2% AA additive solvent system in vacuum dried conditions.

<b>Device: o-xylene + 2% AA vacuum dried</b>	Jsc (mA/cm <sup>2</sup> )	Voc (V)	FF (%)	Eff (%)
PCE Max	8.984	0.899	56	4.56
Avg	8.695	0.904	55	4.27
Std Dev	0.32231	0.00669	1.2	0.1675

As Chapter 3 of the thesis gave insight about how it is important to effectively dry the active layer and remove remaining solvent additives, during printing experiments the same vacuum drying technique was tested, and results compared.

The same experiment was also done without vacuum and the results are below:

**Table 5.21:** Photovoltaic properties summarized for PTNT:PC<sub>71</sub>BM processed from o-xylene and 2% AA additive solvent system without vacuum drying.

<b>Device: o-xylene + 2% AA without vacuum drying</b>	Jsc (mA/cm <sup>2</sup> )	Voc (V)	FF (%)	Eff (%)
PCE Max	8.052	0.900	54	3.89
Avg	8.149	0.892	52	3.77
Std Dev	0.26879	0.00784	1.7	0.112

The average maximum efficiencies of vacuum dried and without vacuum devices were 4.56% and 3.84%, respectively. By this discovery, the eco-friendly fabrication of printed polymer solar cells was found to be best performing via effective drying, in other words,

effective morphology optimization. AFM images were also analysed for this purpose and for comparing other additive and printing conditions.

A lower concentration of AA additive was also experimented using MRC printing; the device architecture is: PET(flexible plastic substrate)/ ITO/PTNT:PC<sub>71</sub>BM/MoO<sub>x</sub>/Al (25 mg/mL) (2:3) in o-xylene + 0.5% AA , 85°C overnight + vacuum dried at 10<sup>-7</sup>mbar for 1 hour. Ink: 1 mL in total.

The maximum and average PCE is found to be very low with low percentage of AA;  $\eta$ : 0.60 % and 0.55, respectively.

**Table 5.22:** Photovoltaic properties summarized for PTNT:PC<sub>71</sub>BM processed from o-xylene and 0.5% AA additive solvent system with vacuum drying.

<b>Device: o-xylene + 0.5% AA vacuum dried</b>	Jsc (mA/cm <sup>2</sup> )	Voc (V)	FF (%)	Eff (%)
PCE Max	1.779	0.818	42	0.60
Avg	1.840	0.785	39	0.55
Std Dev	0.06307	0.042305	2.5	0.0402

Other solvent additives such as MN were also tested against AA additive simultaneously as it was found to be good in previous experiments.

The 2 printed batches of PTNT:PC<sub>71</sub>BM (2:3) o-xylene + 2%AA and 2% MN with vacuum drying were given below:

**Table 5.23:** Photovoltaic properties summarized for PTNT:PC<sub>71</sub>BM processed from o-xylene and 2% AA additive solvent system with vacuum drying (in the same experiment batch to compare the results to 2% MN additive performance).

<b>Device: o-xylene + 2% AA vacuum dried</b>	Jsc (mA/cm <sup>2</sup> )	Voc (V)	FF (%)	Eff (%)
PCE Max	8.267	0.910	55	4.15
Avg	7.614	0.902	55	3.78
Std Dev	0.35092	0.008311	2.7	0.2805

**Table 5.24:** Photovoltaic properties summarized for PTNT:PC<sub>71</sub>BM processed from o-xylene and 2% MN additive solvent system with vacuum drying (in the same experiment batch to compare the results to 2% AA additive performance).

<b>Device: o-xylene + 2% MN vacuum dried</b>	Jsc (mA/cm <sup>2</sup> )	Voc (V)	FF (%)	Eff (%)
PCE Max	3.387	0.947	56	1.78
Avg	3.309	0.946	54	1.69
Std Dev	0.16153	0.004412	2.1	0.1187

Later, printed devices processed with AA and MN additives were annealed and tested for their performance. Similar to the rigid spin coated devices, the efficiencies got lower, and the annealing again found to be not compatible as a surface treatment for this polymer-acceptor system. Yet, as shown above vacuum drying at 10<sup>-7</sup> mbar enhanced the performances.

Below is the device data for printed annealed devices:

**Table 5.25:** Photovoltaic properties summarized for PTNT:PC<sub>71</sub>BM processed from o-xylene and 2% AA additive solvent system with annealing (in the same experiment batch to compare the results to annealed 2% MN additive performance).

<b>Device: o-xylene + 2% AA annealed</b>	Jsc (mA/cm <sup>2</sup> )	Voc (V)	FF (%)	Eff (%)
PCE Max	6.534	0.902	58	3.41
Avg	6.308	0.893	55	3.12
Std Dev	0.452793	0.0163463	3.2	0.38363

**Table 5.26:** Photovoltaic properties summarized for PTNT:PC<sub>71</sub>BM processed from o-xylene and 2% MN additive solvent system with annealing (in the same experiment batch to compare the results to annealed 2% AA additive performance).

<b>Device: o-xylene + 2% MN annealed</b>	Jsc (mA/cm <sup>2</sup> )	Voc (V)	FF (%)	Eff (%)
PCE Max	3.351	0.945	51	1.62
Avg	3.248	0.920	47	1.42
Std Dev	0.103447	0.015082	2.7	0.11652

After testing the annealed devices, other comparison batches were conducted with printing techniques while again using 2% AA devices as reference in the same batch. This was done to ensure the correct comparison as printing and other experimental conditions slightly be different in each batch of device fabrication. For instance, in this batch 2% AA devices gave lower efficiencies, which might be attributed to the quality of printed active layer strips. The defects that can be possible for these results were given in methodology section of this chapter. As we compared this batch again to the 4% AA batch, results still made a comparable study for our printed device performance outcomes.

Below are the printed devices processed o-xylene and 4% AA and 2%AA solvent additives:

**Table 5.27:** Photovoltaic properties summarized for PTNT:PC<sub>71</sub>BM processed from o-xylene and 2% AA additive solvent system with annealing (in the same experiment batch to compare the results to annealed 4% AA additive performance).

<b>Device: o-xylene + 2% AA vacuum dried</b>	Jsc (mA/cm <sup>2</sup> )	Voc (V)	FF (%)	Eff (%)
PCE Max	7.157	0.821	56	3.26
Avg	6.665	0.837	51	2.82
Std Dev	0.66029	0.0163422	3.3	0.39342

**Table 5.28:** Photovoltaic properties summarized for PTNT:PC<sub>71</sub>BM processed from o-xylene and 4% AA additive solvent system with annealing (in the same experiment batch to compare the results to annealed 2% AA additive performance).

<b>Device: o-xylene + 4% AA vacuum dried</b>	Jsc (mA/cm <sup>2</sup> )	Voc (V)	FF (%)	Eff (%)
PCE Max	6.533	0.858	49	2.72
Avg	6.547	0.834	47	2.53
Std Dev	0.26941	0.0162286	1.4	0.11427

For the next step, we decided to examine the effect of mini-roll coater slot-die head as we noticed the effect of height/the meniscus distance to the mini-roll coater drum can change the printed strip qualities, active layer film thickness, and eventually result in a lower device performance even though the printed device recipe is the same where the same main solvent o-xylene and the same percentage of solvent additive like AA were used.

The device photovoltaic properties were given below for the lower head devices:

**Table 5.29:** Photovoltaic properties summarized for PTNT:PC<sub>71</sub>BM processed from o-xylene and 2% AA additive solvent system with vacuum drying (lower slot-die head).

<b>Device: o-xylene + 2% AA vacuum dried lower slot-die head</b>	Jsc (mA/cm <sup>2</sup> )	Voc (V)	FF (%)	Eff (%)
PCE Max	5.912	0.899	48	2.55
Avg	5.757	0.858	46	2.26
Std Dev	0.306245	0.0582492	1.7	0.19023

The device efficiency decreased with lowering the head suggesting that chatter defects could be the underlying reason as briefly mentioned in the methodology section of this chapter. PC<sub>61</sub>BM fullerene was also used against PC<sub>71</sub>BM in printed PSC device using o-xylene and 2% AA system, we increased the concentration of the total ink to 30 mg/mL to reach a similar estimate of film thickness. The device data of both fullerene systems were given in Table 5.30 and 5.31.

**Table 5.30:** Photovoltaic properties summarized for PTNT:PC<sub>71</sub>BM (25mg/mL) processed from o-xylene and 2% AA additive solvent system with vacuum drying (in the same experiment batch to compare the results to PC<sub>61</sub>BM performance).

<b>Device: o-xylene + 2% AA vacuum dried (compared to PC<sub>61</sub>BM)</b>	Jsc (mA/cm <sup>2</sup> )	Voc (V)	FF (%)	Eff (%)
PCE Max	8.464	0.868	54	3.98
Avg	7.912	0.857	51	3.48
Std Dev	0.730126	0.0309144	3.2	0.32

**Table 5.31:** Photovoltaic properties summarized for PTNT:PC<sub>61</sub>BM (30mg/mL) processed from o-xylene and 2% AA additive solvent system with vacuum drying (in the same experiment batch to compare the results to PC<sub>71</sub>BM performance).

<b>Device: o-xylene + 2% AA vacuum dried (PC<sub>61</sub>BM)</b>	Jsc (mA/cm <sup>2</sup> )	Voc (V)	FF (%)	Eff (%)
PCE Max	4.014	0.886	51	1.82
Avg	4.027	0.859	46	1.60
Std Dev	0.094127	0.0225455	4.1	0.21

Finally, using PC<sub>71</sub>BM as fullerene, 0.5% MN additive was also experimented against 2% AA device in the same batch. The device data of both experiments were given below:

**Table 5.32:** Photovoltaic properties summarized for PTNT:PC<sub>71</sub>BM processed from o-xylene and 2% AA additive solvent system with vacuum drying (in the same experiment batch to compare the results to 0.5% MN additive).

<b>Device: o-xylene + 2% AA vacuum dried</b>	Jsc (mA/cm <sup>2</sup> )	Voc (V)	FF (%)	Eff (%)
PCE Max	6.612	0.884	57	3.34
Avg	6.075	0.872	54	2.85
Std Dev	0.379834	0.0076594	2.3	0.28294

The comparison batch of 0.5% MN data was given below, the devices showed very poor performance.

**Table 5.33:** Photovoltaic properties summarized for PTNT:PC<sub>71</sub>BM processed from *o*-xylene and 0.5% MN additive solvent system with vacuum drying (in the same experiment batch to compare the results to 2% AA additive).

<b>Device: o-xylene + 0.5% MN vacuum dried</b>	J <sub>sc</sub> (mA/cm <sup>2</sup> )	V <sub>oc</sub> (V)	FF (%)	Eff (%)
PCE Max	1.315	0.749	34	0.34
Avg	1.316	0.659	33	0.28
Std Dev	0.031735	0.1139017	2.1	0.06218

### 5.6.2 PTNT Printed Device Morphology Studies:

The morphology studies via AFM are also summarized below in Table 5.34. As the roughness gives the optimum film and the homogenous morphology, they were compared for the devices completed, and the additive ratios were compared:

**Table 5.34:** Roughness measurements of printed devices using different solvent additives and ratios (*o*-xy + 2% AA).

Sample : PTNT:PC <sub>60</sub> BM (1:2) ( <i>o</i> -xy + 2%AA)				
Scale	1 um x 1 um		5 um x 5 um	
Scan	R <sub>q</sub> (nm)	R <sub>a</sub> (nm)	R <sub>q</sub> (nm)	R <sub>a</sub> (nm)
1	3.29	2.62	4.33	3.41
2	3.41	2.58	4.14	3.31
3	2.81	2.32	4.3	3.29
4	2.75	2.24	3.87	3.08
5	3.41	2.73	4.03	3.2
<b>Average</b>	<b>3.13</b>	<b>2.50</b>	<b>4.13</b>	<b>3.26</b>
STDev	0.33	0.21	0.19	0.12

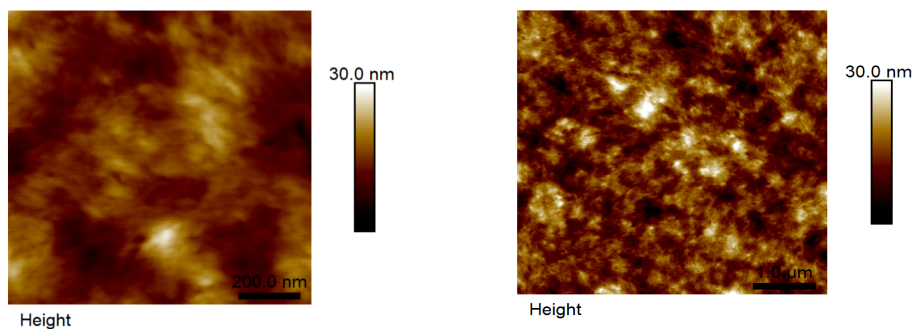


**Figure 5.19:** AFM Topography height images of printed solar cell device (*o*-xy + 2% AA).

The best phase separation and the optimum roughness data were achieved using 2% AA as also seen in the device characterization in Figure 5.19. The phases are well mixed, and the images obtained were the most consistent with multiple height images taken in different scales. The 1um and 200 nm scales were given above.

**Table 5.35:** Roughness measurements of printed devices using different solvent additives and ratios (*o*-xy + 2% MN).

Sample	2% MN			
Scale	1x1 um		5x5 um	
Scan	Rq	ra	Rq	ra
1	14.9	12.6	20.7	16.9
2	14.4	12.1	18	14.5
3	11.4	9.41	18.9	15.2
4	11.5	8.92	20	16
5	9.31	7.67	18.5	14.8
<b>Average</b>	<b>12.3</b>	<b>10.1</b>	<b>19.2</b>	<b>15.5</b>
<i>STDev</i>	2.3	2.1	1.1	1.0

The 2% MN devices had good morphology property in spin coated devices hance gave high PSC efficiencies, however in printed devices, this additive ratio resulted in less efficient devices compared to the 2% AA devices as seen in AFM characterization in Figure 5.20. The phase separation was not efficient, the lower MN ratio was also tested to understand the effect.

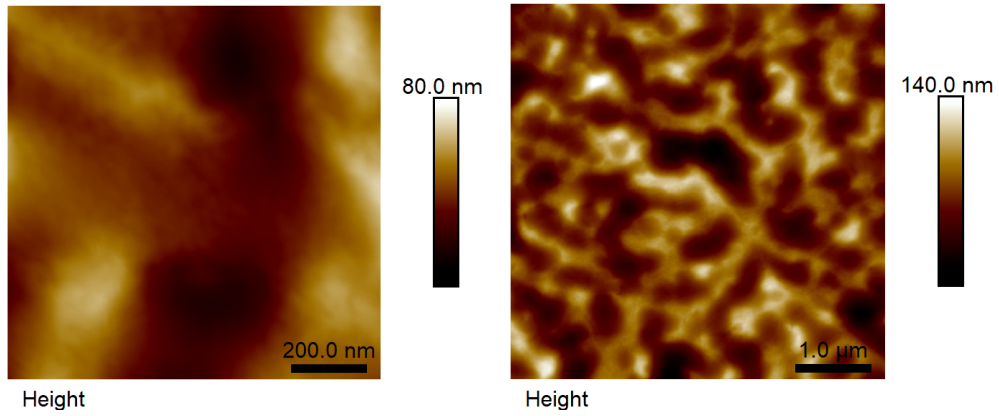


**Figure 5.20:** AFM height images of printed solar cell device (*o*-xy + 2% MN).

**Table 5.36:** Roughness measurements of printed devices using different solvent additives and ratios (*o*-xy + 0.5% MN).

Sample	0.5% MN			
	1x1 μm		5x5 μm	
Scan	Rq	ra	Rq	ra
1	2.46	1.96	3.71	2.97
2	2.72	2.16	3.44	2.77
3	3.07	2.4	3.53	2.78
4	3.54	2.81	3.94	3.14
5	2.61	2.15	3.89	3.13
Average	<b>2.88</b>	<b>2.30</b>	<b>3.70</b>	<b>2.96</b>
STDev	0.43	0.33	0.22	0.18

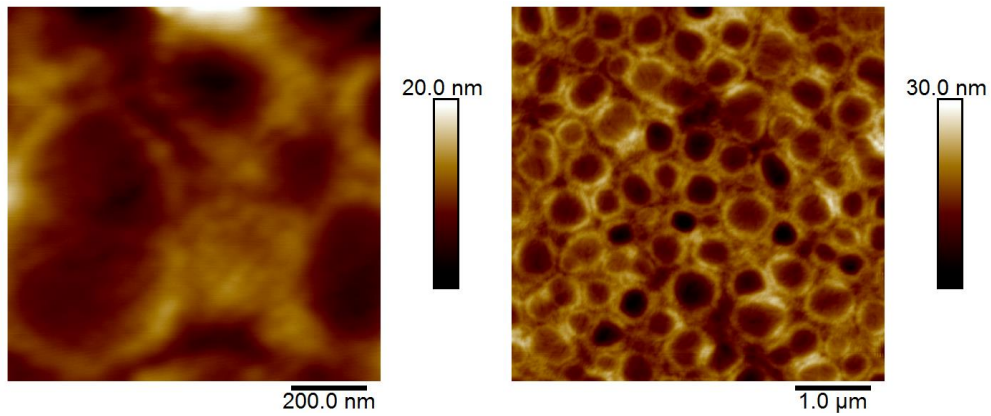


**Figure 5.21:** AFM height images of printed solar cell device (*o*-xy + 0.5% MN).

The 0.5% MN printed devices gave the poorest performance in devices, and it agrees with the morphology characterization where the phase segregation is observed very excessive, and the exciton dissociation distance, thus, the charge transfer is not achievable as supported by AFM studies in Figure 5.21.

**Table 5.37:** Roughness measurements of printed devices using different solvent additives and ratios (*o*-xy + 4%AA).

Sample	4% AA			
	1x1 um		5x5 um	
Scale				
Scan	Rq	ra	Rq	ra
1	1.01	0.728	2.26	0.975
2	0.925	0.731	1.8	1.11
3	0.879	0.692	2.23	1.22
4	0.938	0.734	1.63	1.09
5	0.884	0.696	3.49	1.67
<b>Average</b>	<b>0.9</b>	<b>0.7</b>	<b>2.3</b>	<b>1.2</b>
<i>STDev</i>	<i>0.1</i>	<i>0.0</i>	<i>0.7</i>	<i>0.3</i>

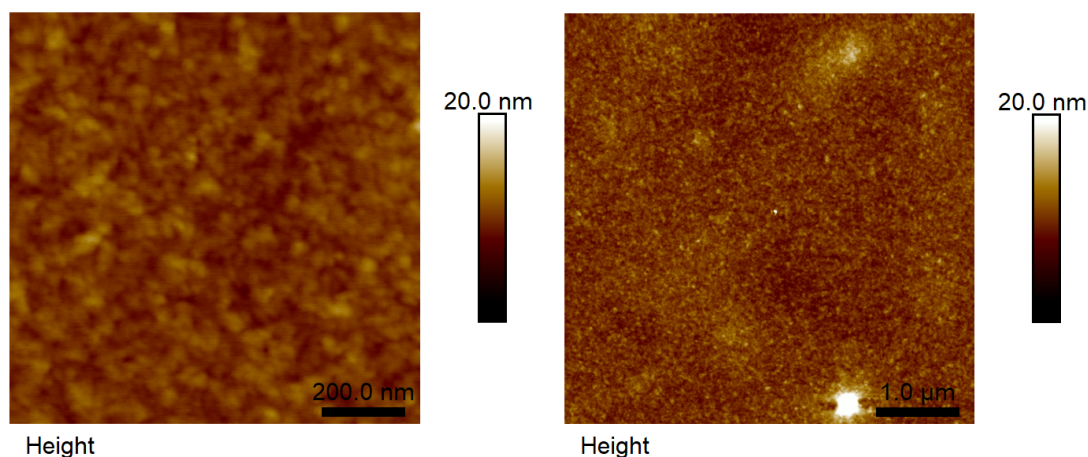


**Figure 5.22:** AFM height images of printed solar cell device (*o*-xy + 4% AA).

The 4% AA devices and printed thin films were difficult to dry due to the higher percentage of solvent additive which has a high boiling point compared to the *o*-xylene and thus the AFM measurements were also done in a more delicate manner, and after a thorough

drying process. Still, the phases were too much mixed and the devices performed poorly as given previously in device characterization in Figure 5.22.

Different topography and roughness properties with varying drum speeds were also examined for topography difference purposes and to examine if they could be effective. The differences in flow rates do not cause distinct variances as seen in the roughness and height images obtained in Figure 5.23 and Figure 5.24, whereas more dramatic modifications in flow rate and drum speeds will result in great change as can be predicted with this trend.

**Table 5.38:** Roughness measurements of printed devices using different coating speeds (Fast Print).

<b>PTNT:PC<sub>61</sub>BM (Fast print)</b>				
Scale	1 um x 1 um		5 um x 5 um	
Scan	Rq (nm)	Ra (nm)	Rq (nm)	Ra (nm)
1	2.56	1.99	3.86	3.06
2	2.58	2.06	3.68	2.93
3	2.62	2.12	3.93	3.12
4	2.70	2.19	3.96	3.16
5	2.39	1.89	3.53	2.82
<b>Average</b>	<b>2.57</b>	<b>2.05</b>	<b>3.79</b>	<b>3.02</b>
STDev	<i>0.11</i>	<i>0.12</i>	<i>0.18</i>	<i>0.14</i>

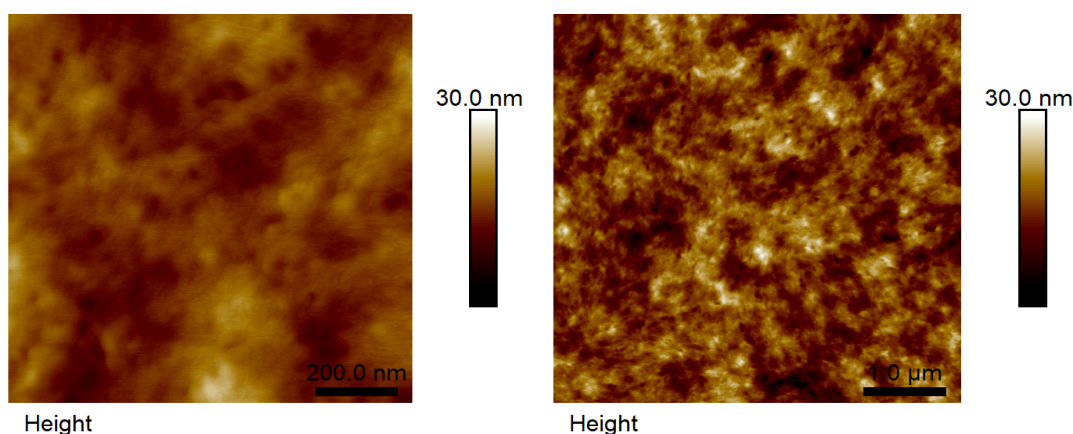


**Figure 5.23:** AFM height images of printed solar cell device (Fast print)

The effect of this test reveals how the drying kinetics and crystallization process of BHJ polymer-acceptor blend ink differ compared to spin-coating technique. The outcome of slight

variation in differing speeds can show us that our system could be a good candidate for a more controlled processing and upscaling of printed polymer solar cells.

**Table 5.39:** Roughness measurements of printed devices using different coating speeds (Slow Print).

<b>PTNT:PC<sub>61</sub>BM (Slow print)</b>				
Scale	1 $\mu\text{m}$ x 1 $\mu\text{m}$		5 $\mu\text{m}$ x 5 $\mu\text{m}$	
Scan	Rq (nm)	Ra (nm)	Rq (nm)	Ra (nm)
1	3.29	2.62	4.33	3.41
2	3.41	2.58	4.14	3.31
3	2.81	2.32	4.30	3.29
4	2.75	2.24	3.87	3.08
5	3.41	2.73	4.03	3.20
<b>Average</b>	<b>3.13</b>	<b>2.50</b>	<b>4.13</b>	<b>3.26</b>
STDev	0.33	0.21	0.19	0.12

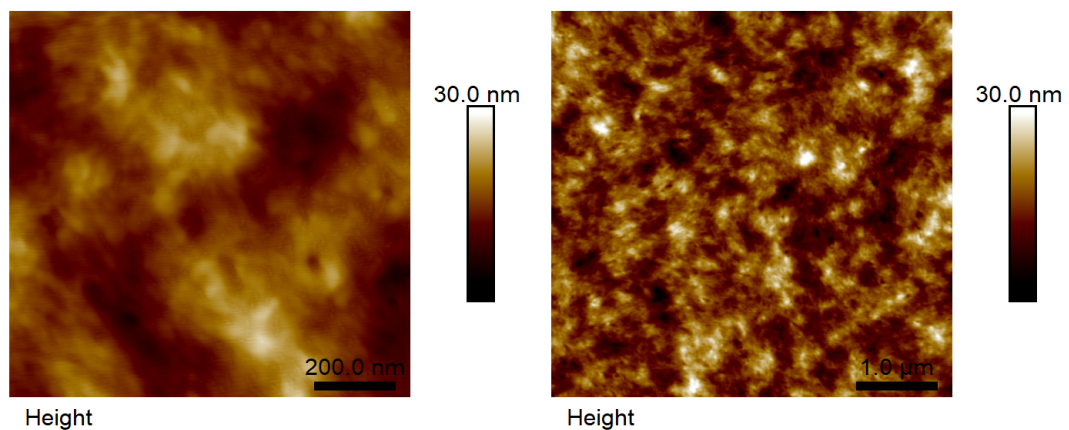


**Figure 5.24:** AFM height images of printed solar cell device (Slow print)

As stated, we achieved only a slight difference which is aimed in printing PSCs to an extent with acceptable different speeds for different industrial and lab scale usages. The mini-roll coater therefore was a successful tool for us to thoroughly examine the effects of ink composition, solvent systems, drying times and further surface treatment such as annealing and vacuum drying as tested in devices printed. In summary, the device characterisations were all

aggregable with the morphology characterizations conducted and gave as insight into how to effectively use the MRC for printing polymer solar cells.

## 5.7 Conclusion:

Many pre-liminary experiments carried out for this chapter in which molecular weight effect of polymers used in their solar cell performance were also investigated before printing of the devices as given in the discussion. Also, different additives were tested for the best device with both rigid and flexible devices. A thorough and systematic elimination were done for the device fabrication steps. The mini-roll coater had also some challenges, and these were improved with different trial of parameters both for during sample preparation stage and MRC instrument setting steps. The best performing eco-friendly printed solar cells were observed for their stability and optimum morphology using AFM topography and thickness analysis. The best performing eco-friendly device gave a max power conversion efficiency of 5.7% and the printed device using the same ink (PTNT:PC<sub>71</sub>BM) and processing solvents (o-xylene + 2% AA) gave an efficiency of max 4.6%. Experiments with other eco-friendly solvent systems were also studied with both spin-coating and mini-roll coating techniques. In summary, our study presented a complete valuable understanding of the active layer optimization and eco-friendliness of the polymer solar cells for future large area flexible organic electronics and their stability and applicability for state-of-the-art technologies.

## **5.8 Contributions:**

***Bradley Kirk:** Has assisted in the fabrication of printed polymer solar cells and AFM measurements and data analysis.*

***Dr. Martyn Jevric:** Assisted with the synthesis of PTNT polymers.*

***Prof. Mats R. Andersson:** Contributed to the methodology of molecular weight study and the printing strategy of PTNT:fullerene PSCs.*

## 5.9 References:

1. Louwen, A., van Sark, W. G. J. H. M., Schropp, R. E. I., Turkenburg, W. C., and Faaij, A. P. C. (2015) "Life-cycle greenhouse gas emissions and energy payback time of current and prospective silicon heterojunction solar cell designs" *Progress in Photovoltaics: Research and Applications*, 23(10), 1406-1428.
2. Lizin, S., Van Passel, S., De Schepper, E., Maes, W., Lutsen, L., Manca, J., and Vanderzande, D. (2013) "Life cycle analyses of organic photovoltaics: a review" *Energy & Environmental Science*, 6(11), 3136-3149.
3. Andersson, L. M. (2015) "Fully Slot-Die-Coated All-Organic Solar Cells" *Energy Technology*, 3(4), 437-442.
4. Chaturvedi, N., Gasparini, N., Corzo, D., Bertrandie, J., Wehbe, N., Troughton, J., and Baran, D. (2021). "All Slot-Die Coated Non-Fullerene Organic Solar Cells with PCE 11%" *Advanced Functional Materials*, 31(14), 2009996.
5. Sears, K. K., Fievez, M., Gao, M., Weerasinghe, H. C., Easton, C. D., and Vak, D. (2017) "ITO-Free Flexible Perovskite Solar Cells Based on Roll-to-Roll, Slot-Die Coated Silver Nanowire Electrodes" *Solar RRL*, 1(8), 1700059.
6. Lee, C.-Y., Tsao, C.-S., Lin, H.-K., Cha, H.-C., Chung, T.-Y., Sung, Y.-M., and Huang, Y.-C. (2021) "Encapsulation improvement and stability of ambient roll-to-roll slot-die-coated organic photovoltaic modules" *Solar Energy*, 213, 136-144.
7. Arredondo, B., del Pozo, G., Hernández-Balaguera, E., Martín, D. M., López González, M. d. C., Romero, B., Madsen, M. (2020) "Identification of Degradation Mechanisms in Slot-Die-Coated Nonfullerene ITO-Free Organic Solar Cells Using Different Illumination Spectra" *ACS Applied Energy Materials*, 3(7), 6476-6485.
8. Lin, Z., Guan, W., Cai, W., Wang, L., Wang, X., He, Z., & Hou, L. (2021) "Effect of anode interfacial modification on the performance of laminated flexible ITO-free organic solar cells" *Energy Science and Engineering*, 9(4), 502-508.
9. Boehme, M., and Charton, C. (2005) "Properties of ITO on PET film in dependence on the coating conditions and thermal processing" *Surface and Coatings Technology*, 200(1), 932-935.
10. Zhao, K., Hu, H., Spada, E., Jagadamma, L. K., Yan, B., Abdelsamie, M., Amassian, A. (2016) "Highly efficient polymer solar cells with printed photoactive layer: rational process transfer from spin-coating" *Journal of Materials Chemistry A*, 4(41), 16036-16046.
11. Bihar, E., Corzo, D., Hidalgo, T. C., Rosas-Villalva, D., Salama, K. N., Inal, S., & Baran, D. (2020) "Fully Inkjet-Printed, Ultrathin and Conformable Organic Photovoltaics as Power

- Source Based on Cross-Linked PEDOT:PSS Electrodes” *Advanced Materials Technologies*, 5(8), 2000226.
12. Lin, Y., Dong, S., Li, Z., Zheng, W., Yang, J., Liu, A., Hou, L. (2018) “Energy-effectively printed all-polymer solar cells exceeding 8.61% efficiency” *Nano Energy*, 46, 428-435.
  13. Jeong, S., Park, B., Hong, S., Kim, S., Kim, J., Kwon, S., Lee, K. (2020) “Large-Area Nonfullerene Organic Solar Cell Modules Fabricated by a Temperature-Independent Printing Method” *ACS Applied Materials & Interfaces*, 12(37), 41877-41885.
  14. Fan, X., Nie, W., Tsai, H., Wang, N., Huang, H., Cheng, Y., Xia, Y. (2019) “PEDOT:PSS for Flexible and Stretchable Electronics: Modifications, Strategies, and Applications” *Advanced Science*, 6(19), 1900813.
  15. Andersen, T. R., Almyahi, F., Cooling, N. A., Elkington, D., Wiggins, L., Fahy, A., Dastoor, P. C. (2016) “Comparison of inorganic electron transport layers in fully roll-to-roll coated/printed organic photovoltaics in normal geometry” *Journal of Materials Chemistry A*, 4(41), 15986-15996.
  16. Sadula, A. (2018). *Investigating Emerging Thin Film Photovoltaic Technologies*.
  17. Gusain, A., Thankappan, A., & Thomas, S. (2020) “Roll-to-roll printing of polymer and perovskite solar cells: compatible materials and processes” *Journal of Materials Science*, 55(28), 13490-13542.
  18. Dai, X.Z., Deng, Y.H., Brackle, C. H. V., and Huang, J. S. (2019) “Meniscus fabrication of halide perovskite thin films at high throughput for large area and low-cost solar panels” *International Journal of Extreme Manufacturing*, 1(2), 022004.
  19. Patidar, R., Burkitt, D., Hooper, K., Richards, D., and Watson, T. (2020) “Slot-die coating of perovskite solar cells: An overview” *Materials Today Communications*, 22, 100808.
  20. Liu, C., Xiao, C., and Li, W. (2021) “Zinc oxide nanoparticles as electron transporting interlayer in organic solar cells” *Journal of Materials Chemistry C*, 9(40), 14093-14114.
  21. Kwon, H.-C., Jeong, W., Lee, Y.-S., Jang, J.-H., Jeong, H.-S., Kim, S., Kang, H. (2022) “Overcoming the Low-Surface-Energy-Induced Wettability Problem of Flexible and Transparent Electrodes for Large-Area Organic Photovoltaic Modules over 500 cm<sup>2</sup>” *Advanced Energy Materials*, 12(21), 2200023.
  22. Hong, S., Lee, J., Kang, H., and Lee, K. (2013) “Slot-die coating parameters of the low-viscosity bulk-heterojunction materials used for polymer solar cells” *Solar Energy Materials and Solar Cells*, 112, 27-35.
  23. Slot-Die Defects, retrieved from <https://www.ossila.com/pages/slot-die-coating-theory>, April 9, 2022.

# CHAPTER 6 – SUMMARY

## 6.1 General summary and conclusions:

The main aim of this thesis has been to optimize eco-friendly polymer solar cells (PSCs) by carefully forming and modifying the photo-active layers for the best device performance. Throughout the experiments that were carried out in different sections, as the first step, the preliminary ones were always carried out for the selection of non-halogenated solvent system that will work efficiently with bulk heterojunction layer (BHJ) materials. These solvent systems have provided the importance of morphology treatment and tailoring the structure of PSCs in terms of their applicability on similar donor-acceptor blends, solvent systems and printed equivalent devices. The active layers that were processed by non-toxic solvents for the first study of this thesis constituted of a semi-crystalline polymer PTNT and a fullerene acceptor PC<sub>71</sub>BM. The performance of the BHJ layer processed from eco-friendly non-halogenated solvent systems were found to be as high as the ones processed from toxic solvent systems and in some cases much higher. These new systems were helpful for the next studies using different polymer-acceptor systems and also using different active layer coating techniques.

In Chapter 4, the best solvent system that showed the highest efficiency was found to be non-toxic o-xylene (main solvent) and MN (solvent additive) for PTNT:PC<sub>71</sub>BM inverted polymer solar cells. The power conversion efficiency (PCE) was around 6% and using Atomic Force Microscopy (AFM), the additive's effect on nano-scale morphology was investigated. This best performing active layer was more homogeneous and assisted for better charge transport agreeing with device photovoltaic characteristics. The photophysical properties were also shown for understanding the active layer preparation and effects of additive treatments. The fact that different green solvent additives had different performance for the solar cells need more testing and reasoning for the following steps in the thesis. The lower vapor pressure of

these solvents along with their different solubilities are behind mechanisms of the active layer process. The inverted structure of these cells gave also more stable devices. Finally, the IPCE measurements gave the EQE efficiencies and helped to see the absorption properties of these active layers and the theoretical integrated currents. The best EQE was reached to more than 70% between 400 to 550 nm.

In Chapter 3, we had 3 different aims, the first one was to eliminate the effect of toxic solvent additive (DIO) in the performance polymer: non-fullerene PSCs (PTB7-Th:ITIC) and find an eco-friendly high performing alternative solvent system for the same BHJ blends. The second aim was to prove the negative effects of halogenated solvent additive DIO and to prove its difficult removal from active layer during spin-coating and slot-die coating and after the complete device fabrication. The best performing system that was reached and showed better solar cell efficiency was using o-xylene (main solvent) and AA (non-toxic solvent additive). The best PCE was higher than 8% and the stability of devices were superior. The existing literature presents that the BHJ layer of this system was processed most commonly with CB (main solvent) and DIO (toxic solvent additive) and similar previous studies suspected the existence of the additive in the active layer after drying and accordingly its effect on faster degradation of PSC devices.

X-ray Photoelectron Spectroscopy (XPS) and Neutral Impact Collision Ion Scattering Spectroscopy (NICISS) were used for the determination of DIO additive in the polymer solar cell active layers and how the different drying techniques helped to remove the solvent additive from the thin layer film. The challenging conditions of these instruments where they use high vacuum chambers are overcome using fast irradiation of the samples, step by step measurement of samples with minimum exposure to air and moisture, and also sample chamber cooling techniques which is novel and very advantageous for air sensitive ultra-thin solvent processed polymer films. The DIO concentration was 0.6% (v/v) in the total BHJ blend compared to CB

main solvent and this challenge also made it difficult to be certain for the determination of additive in the film with these techniques whereas a higher concentration proves it is still present in the film even under ultra-high vacuum. The thermal analysis (DMA and STA) was also carried out in the beginning where DIO was found to be staying in the film of active layers.

The alternative eco-friendly solvent additive AA was also tested using a fullerene acceptor for the photovoltaic properties and compared to the literature findings where they used annealing morphology treatment, the efficiencies of solar cells fabricated were higher without more treatments.

These findings have become the basic approach for the final experiments of this thesis in Chapter 5 which is printing eco-friendly solar cells using a mini roll coater technique. For the printing of solar cells, the PTNT polymer was used as a donor and PC<sub>61</sub>BM and PC<sub>71</sub>BM were used as fullerene acceptors; and the solvent systems were chosen as o-xylene and MN & o-xylene and PN & o-xylene and AA as mostly optimized earlier in spin-coated polymer solar cells. These solvent systems gave mostly similar device performance trends and for the best device performance, the device efficiency was higher even though the molecular weight (Mwt) of the solar cell's donor polymer (PTNT) was lower than that of the previous experiments. Many pre-liminary experiments carried out for this chapter in which the Mwt effect in solar cell performance were also investigated before printing of the devices. Also, different additives were tested for the best device. The mini-roll coater had also its challenges, and these were improved with different trial of parameters both for during sample preparation stage and instrument setting steps.

The best performing eco-friendly printed solar cells were tested for their stability, finally. In summary, this thesis presented a complete valuable understanding of the active layer optimization and eco-friendliness of the polymer solar cells for future flexible organic electronics and their stability and applicability for state-of-the-art technologies.

## 6.2 Future Work:

In future, this thesis will be starting point for several important research topics as it investigates many materials and processes for polymer solar cell fabrication, and also it uses different types of instruments for material and device characterization.

During our research we realized that in the literature, the interactions of materials used in organic solar cells needs to be further investigated as everything is nano-scale, even the smallest change has a profound effect. The criterion for high quality research will take the existing results such as the best performing devices and how they can be improved by eliminating the difficulties we faced or enhancing the experimental conditions.

In particular, the use of additives has its own sets of challenges as they have various effects in many different photo-active layers used in PSCs. For instance, we already have done several preliminary research studies for the degradation of polymer solar cells using DIO additive for photostability aspect. These studies, however, need to be done more meticulously in the future. Other techniques could be paired with future photostability experiments in order to reach definitive outcomes. PTB7-Th polymer is very sensitive to photo-degradation. When it is used with ITIC and DIO, the photostability increases and also decreases depending on the system. These opposite effects need further research with long duration experiments as the focus is on stability rather than device performance. We have done photobleaching preliminary experiments with PTB7-Th, DIO, and ITIC with certain amount of exposure to UV, yet it was hard to interpret the data with a certain conclusion; a more systematic future approach will benefit from this preliminary research. The correlation of how DIO affects the PTB7-Th:ITIC device stability via its inefficient removal versus a device with another popular NF acceptor is a great future research. The high-performance polymer donors such as PM6, PM7, and D18 can also be paired with the popular NF acceptors for the stability studies using solvent processing optimization discussed in this thesis.

XPS and NISS studies for systems with high performing donor and acceptor materials for polymer solar cells are also good for future research using our approach with the analysis of effect of solvent additives and other chemical analysis. This type of future work will help us investigate the actual surface chemistry of these active layers and the arrangement of materials in different conditions. The active layer forming materials when processed with solvent additives can experience a migration of certain materials in different speeds to the surface or bulk. Hence, our study is very significant in suggesting the reasons for such surface science research is necessary and important, and how the different drying techniques we used in this thesis can be repeated to investigate these migration movements in the nano-scale. So far, both in literature and in our preliminary research, surface analysis for the arrangement and movement of elements in photo-active layer of PSCs are hard to interpret for a systematic outcome.

More XRD experiments were also carried out as preliminary research during this thesis for Chapter 3, and future further tests could be beneficial to discuss the chemical structures affected in presence of certain materials such as DIO solvent additive, and how the conditions like temperature and solvent amount are crucial for the crystal formations. These parameters could be improved easily in future with enhanced instrumentation and laboratory conditions.

NMR experiments were also studied briefly for the interaction of ITIC and DIO. The low amount of DIO from our device fabrication experiments also was used in NMR along with other concentrations, also other conditions such as exposure to UV light was combined to NMR studies to be able to detect the changes. However, this study needs large number of experiments and a good interpretation of NMR data for a conclusive and insightful chemical structure change study.

For the polymer solar cells fabricated using PTNT donor and eco-friendly solvent processing, many future studies can also be initiated from our research. Printed PTNT devices

were fabricated in ambient air with mini-roll coater without encapsulation in our research, yet in future, encapsulation techniques for devices with plastic substrates can be investigated and tested over a long term to be able to use these in larger sizes and for commercial use. Moreover, other printing techniques can also be used for our system for a comparison in larger scale and/or with different interface layers and metal electrodes.

Besides high performing polymer and acceptors, for the newly synthesized materials as donor and acceptor pairs, contact angle studies can also be introduced as potential future research in order to test the miscibility of the individual components in the photoactive layer. This active layer study will be a good basis for device fabrication optimizations.

# Appendix

## A.1 J-V graph of PTB7-Th devices:

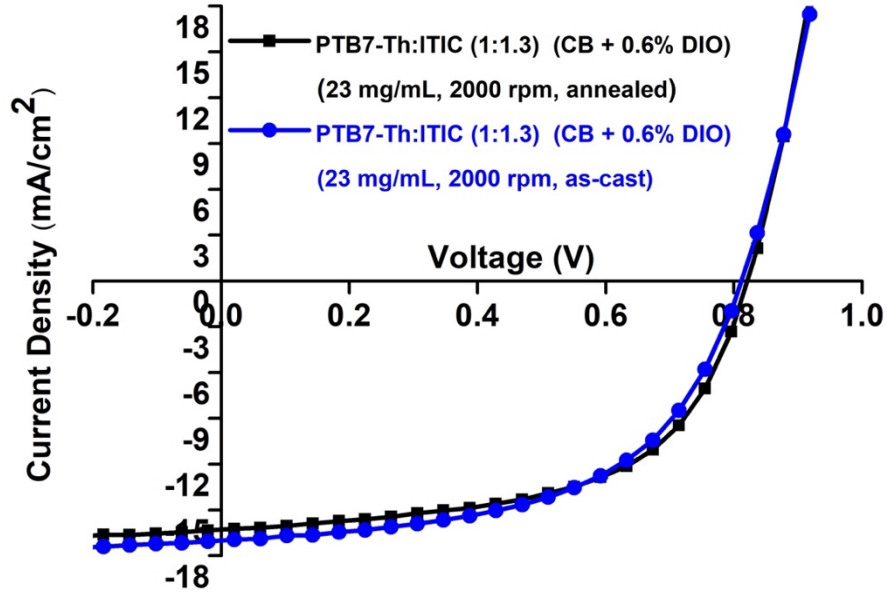


Figure A.1: J-V graph of devices annealed vs as-cast.

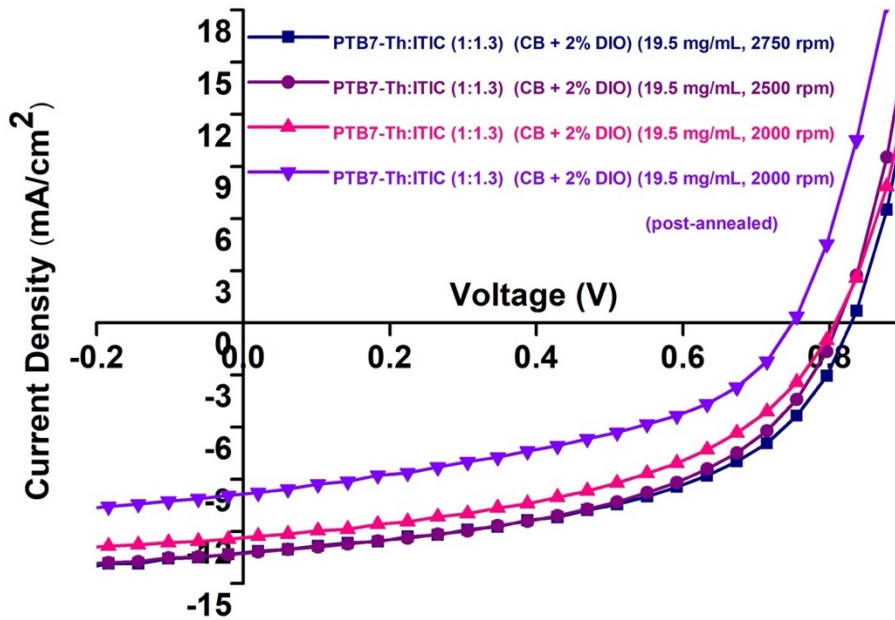


Figure A.2: J-V graphs of devices -thickness optimization.

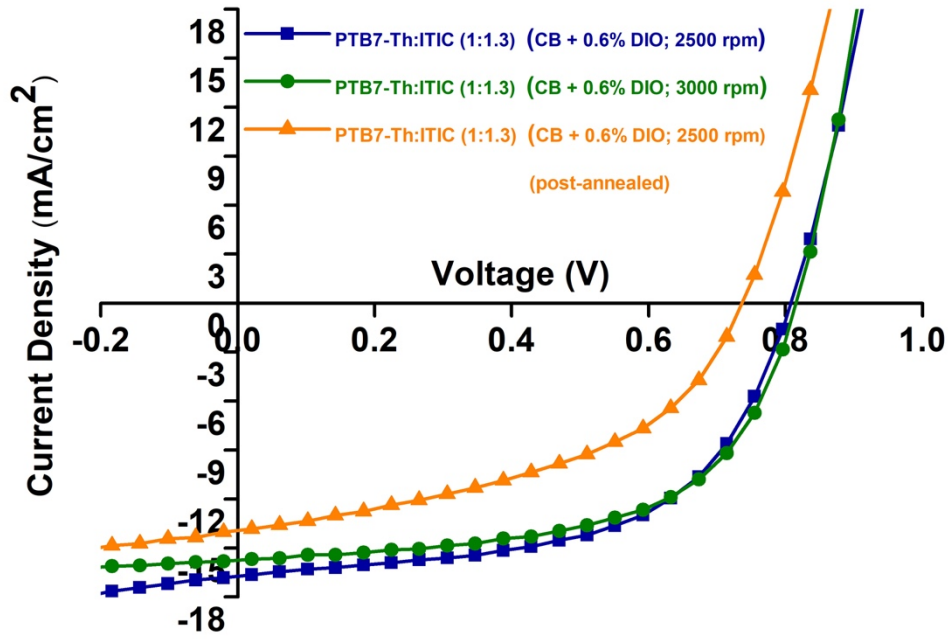


Figure A.3: J-V graphs of devices – DIO concentration optimization.

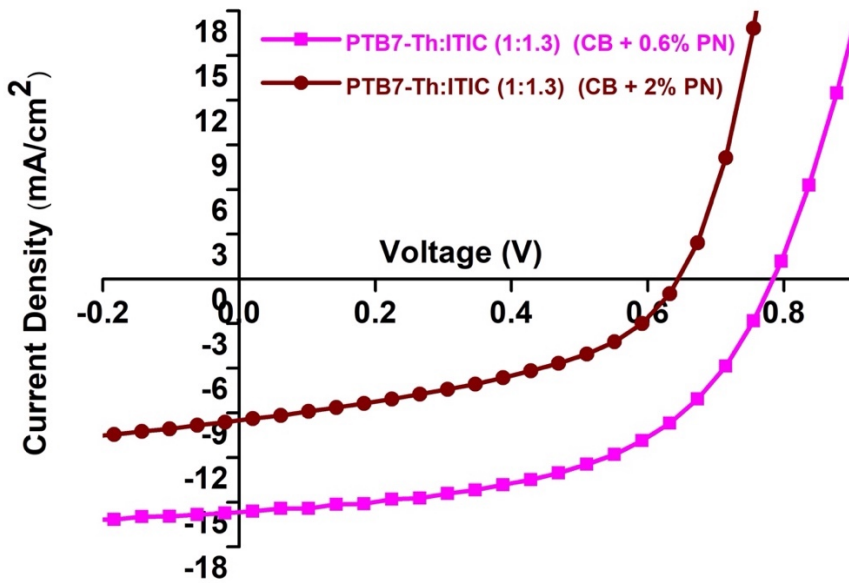


Figure A.4: J-V graphs of devices – PN performance and concentration optimization.

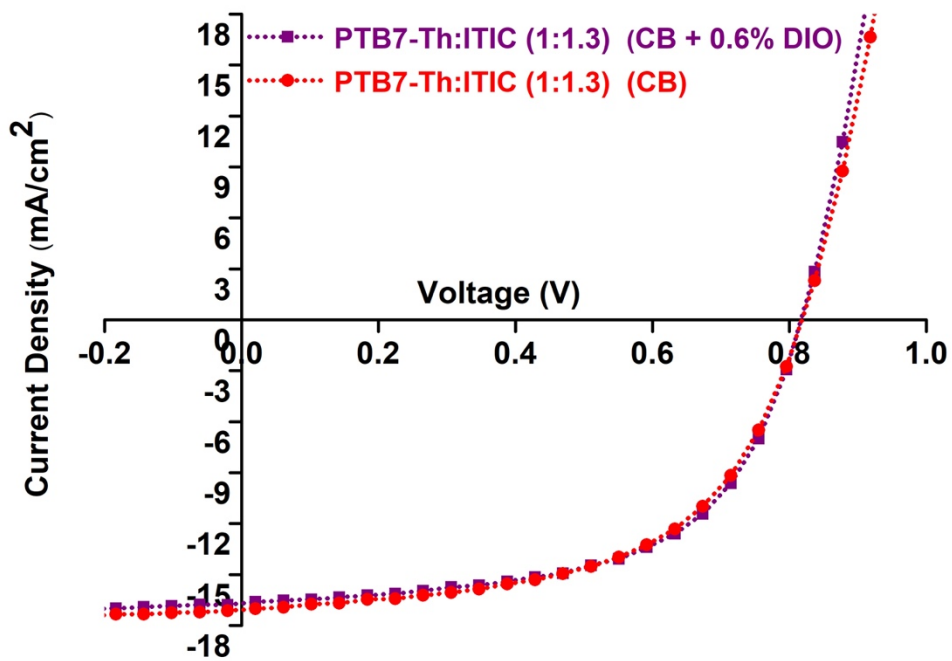


Figure A.5: J-V graphs of devices - DIO performance after drying under high vacuum overnight.

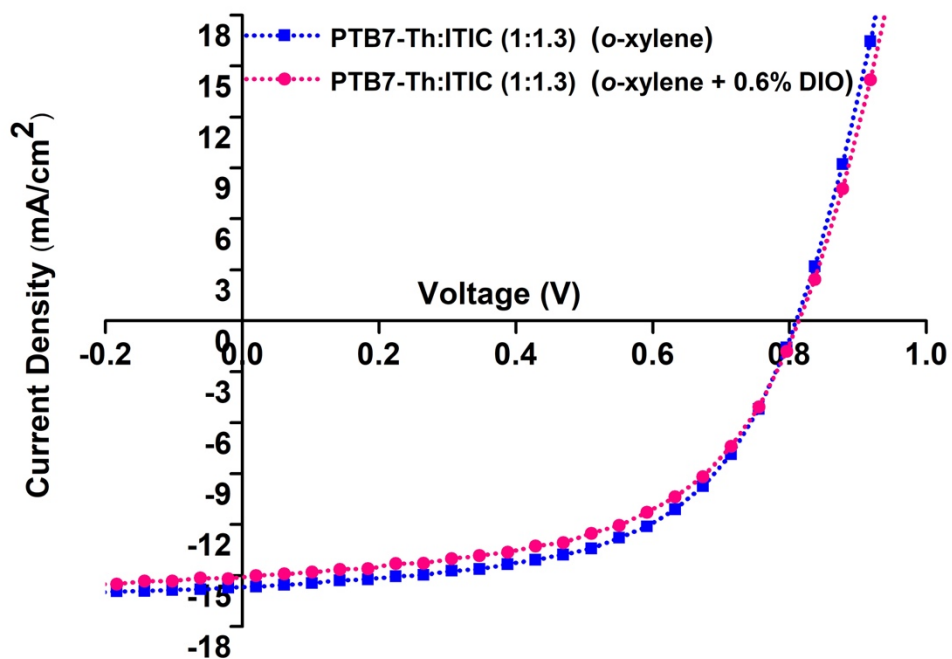


Figure A.6: J-V graphs of devices – DIO comparison using eco-friendly main solvent o-xylene.

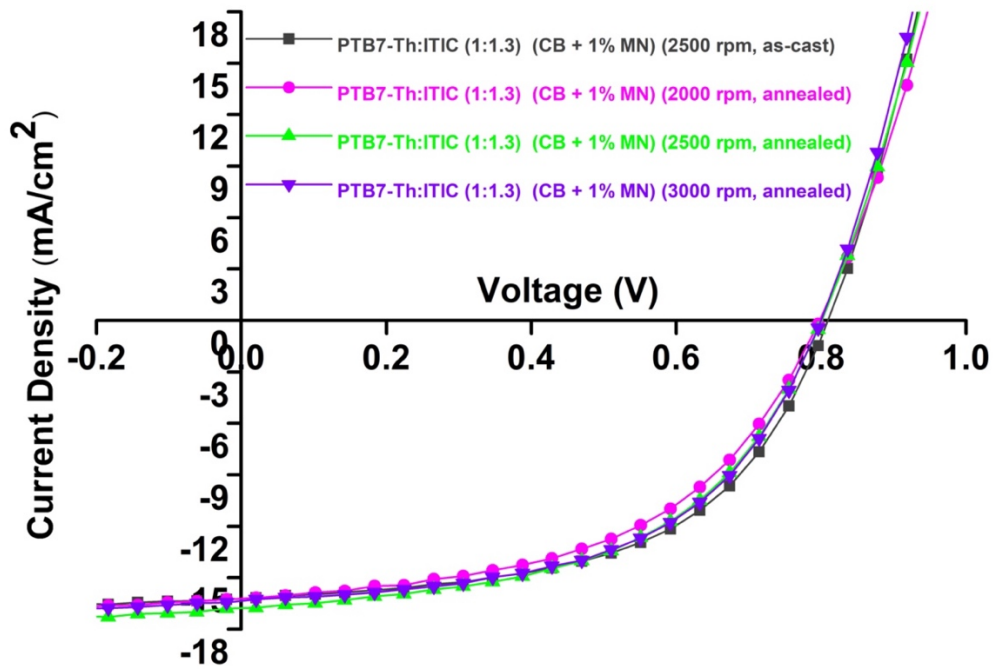


Figure A.7: J-V graphs of devices – MN additive comparison using CB main solvent.

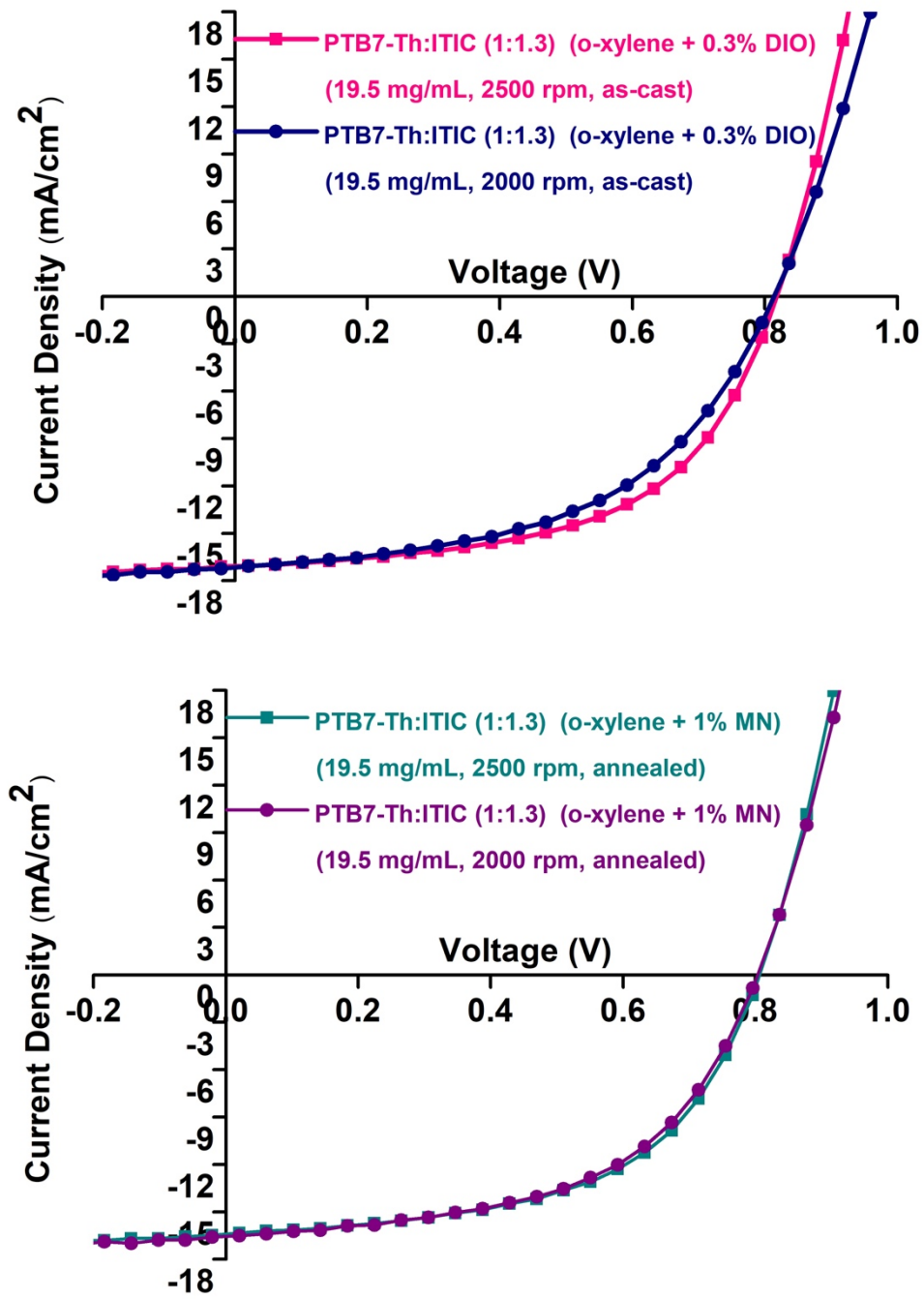


Figure A.8: J-V graphs of devices 0.3% DIO and MN additive comparison using o-xylene.

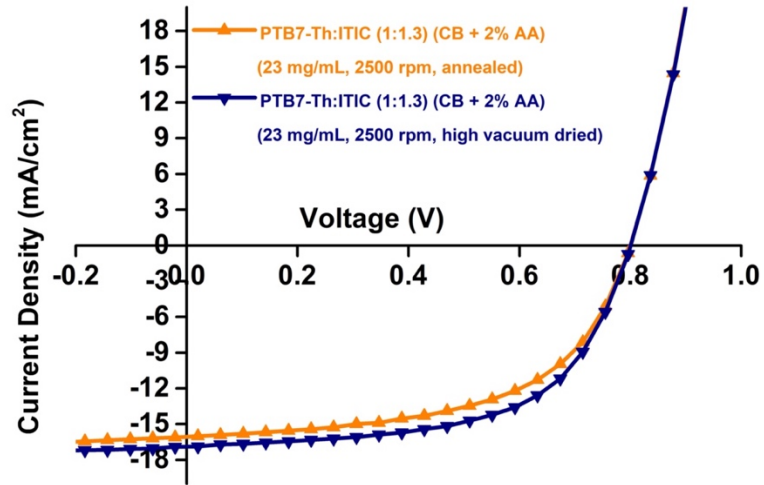


Figure A.9: J-V graphs of devices – CB main solvent + 2% AA additive comparison.

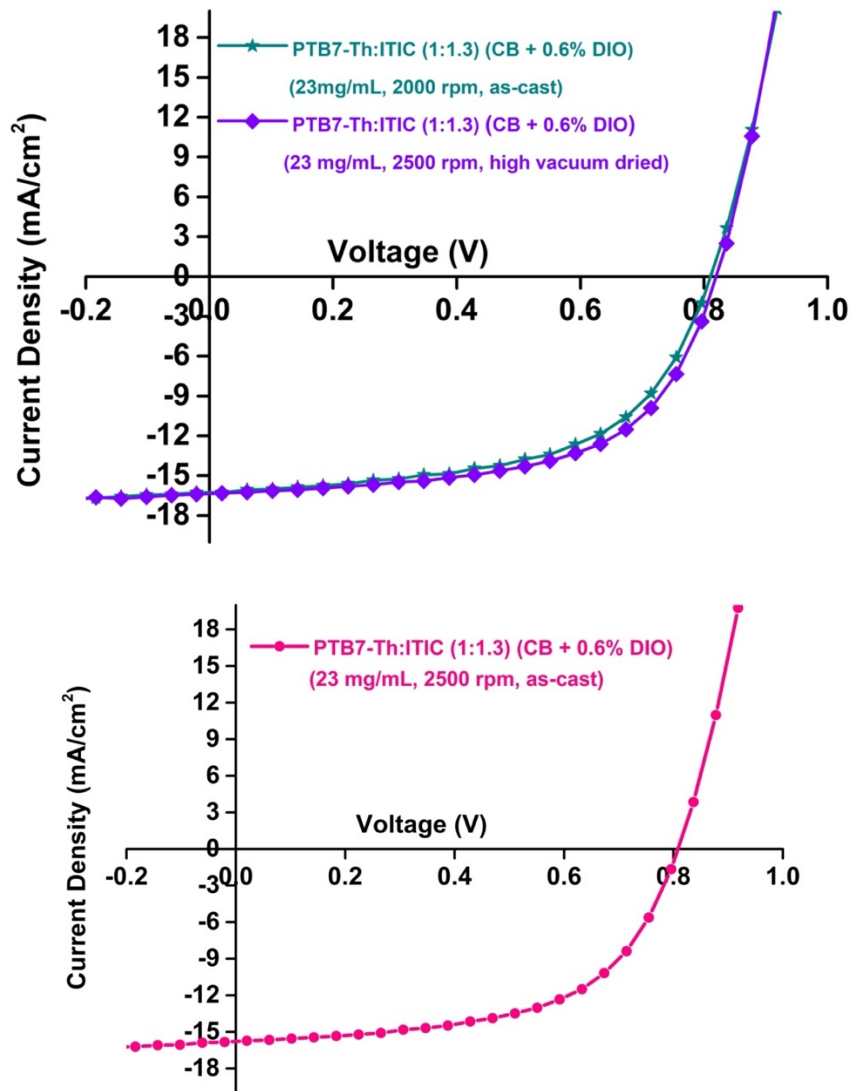


Figure A.10: J-V graphs of devices – CB main solvent + 2% AA high vacuum drying treatment comparison.

## B.1 STA of PTB7-Th blends:

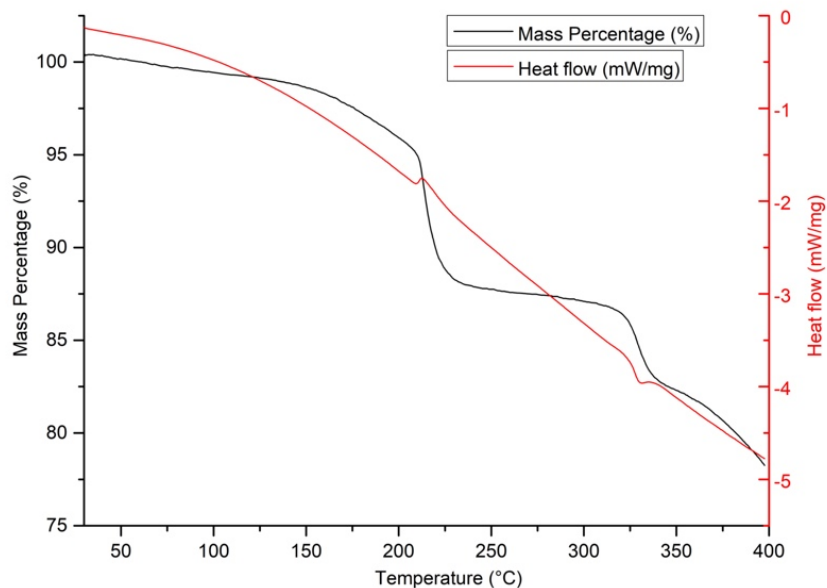


Figure B.1: STA of PTB7-Th: ITIC (1:1.3) CB + 0.6% DIO – 130 °C annealed.

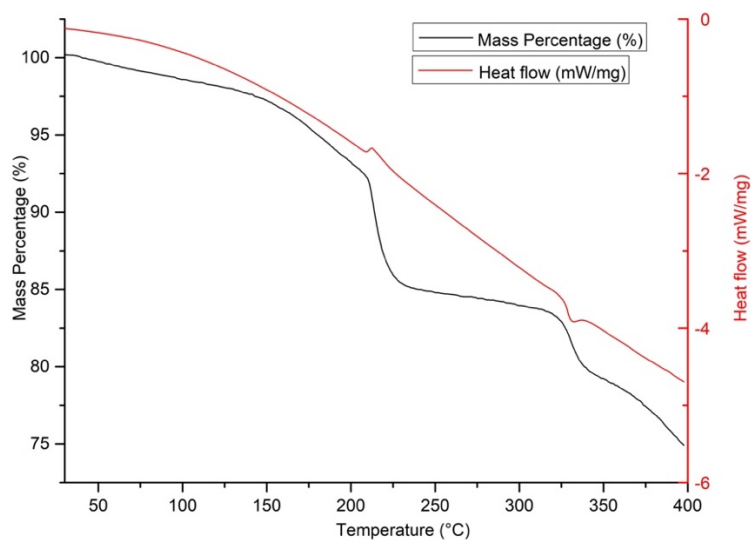
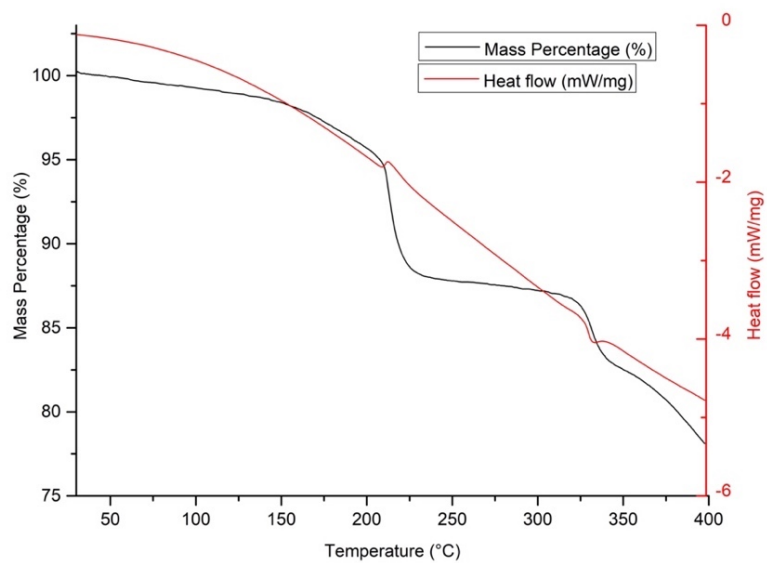


Figure B.2: STA of PTB7-Th: ITIC (1:1.3) CB + 0.6% DIO – vacuum oven dried.



**Figure B.3:** STA of PTB7-Th: ITIC (1:1.3) CB + 0.6% DIO – high vacuum dried.

## C.1 DMA of PTB7-Th blends

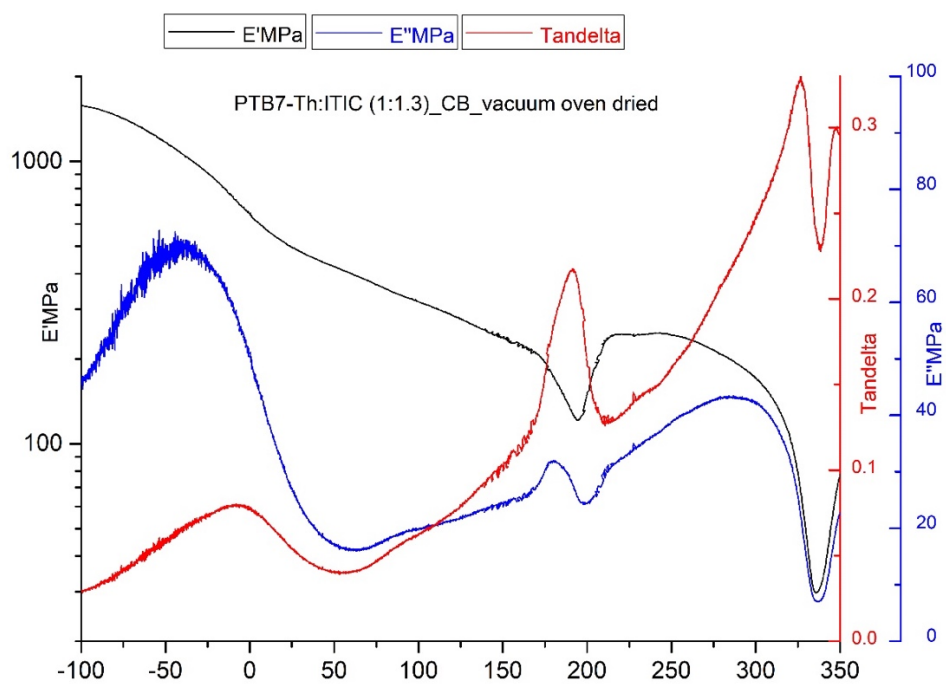


Figure C.1: DMA of PTB7-Th: ITIC (1:1.3) CB vacuum oven dried.

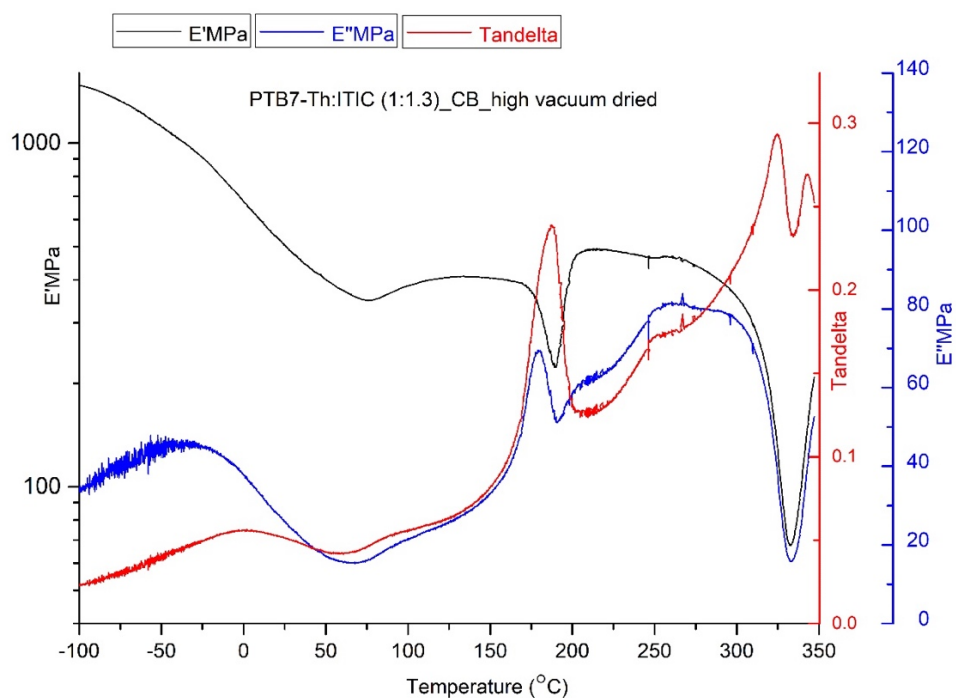
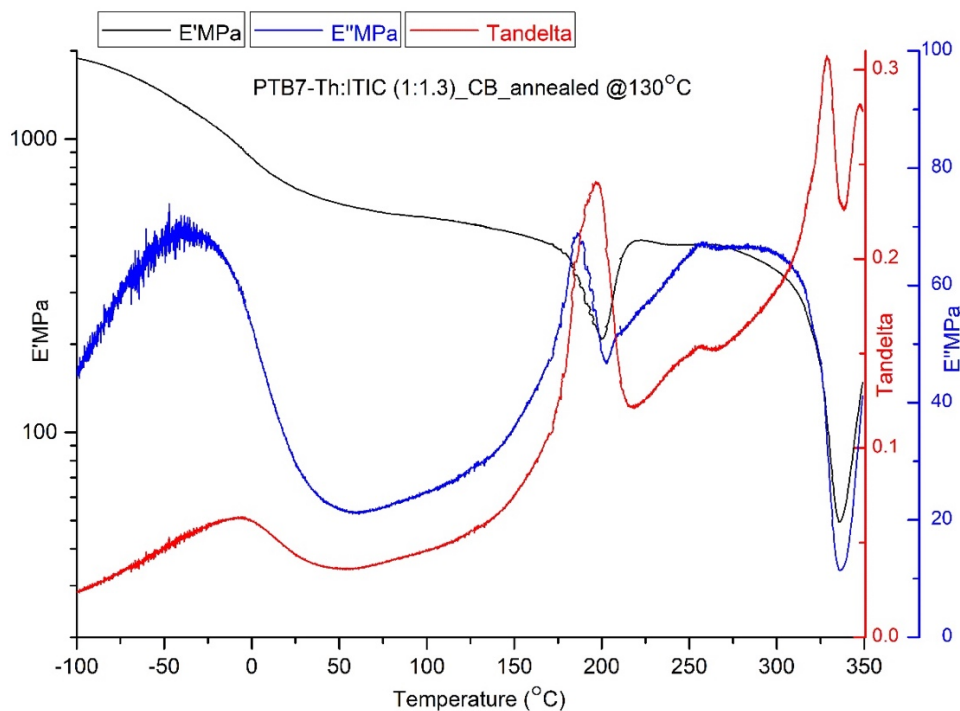
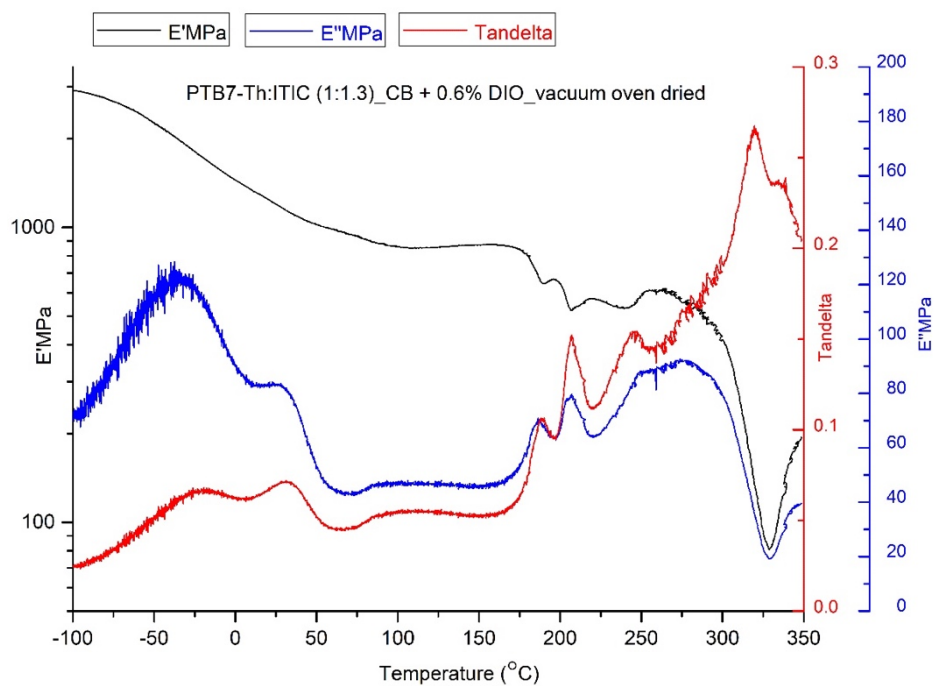


Figure C.2: DMA of PTB7-Th: ITIC (1:1.3) CB high vacuum dried.



**Figure C.3:** DMA of PTB7-Th: ITIC (1:1.3) CB annealed.



**Figure C.4:** DMA of PTB7-Th: ITIC (1:1.3) CB +0.6% DIO vacuum oven dried.

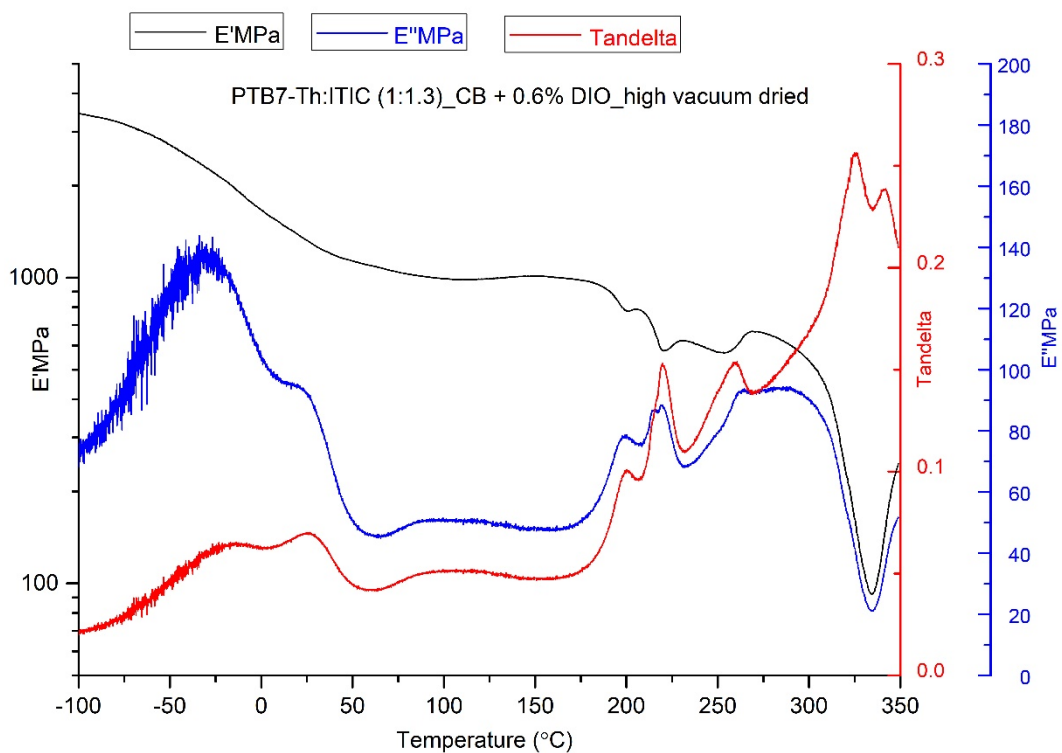


**Figure C.5:** DMA of PTB7-Th: ITIC (1:1.3) CB +0.6% DIO high vacuum dried.

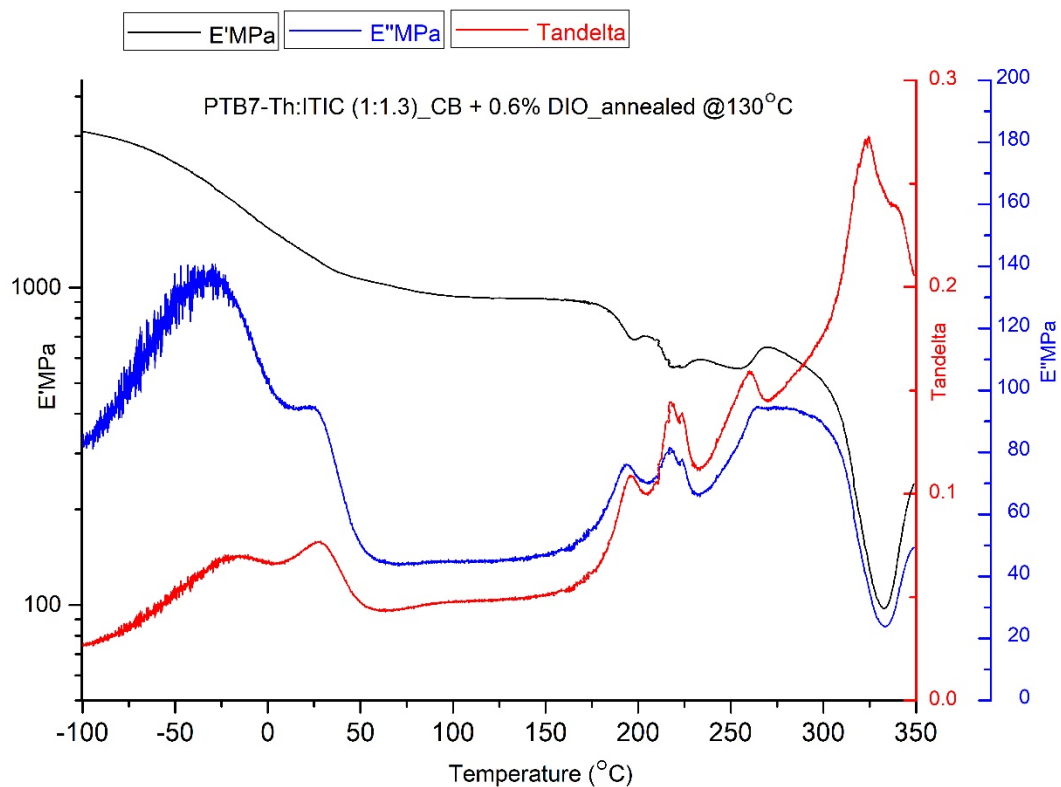


**Figure C.6:** DMA of PTB7-Th: ITIC (1:1.3) CB +0.6% DIO annealed.

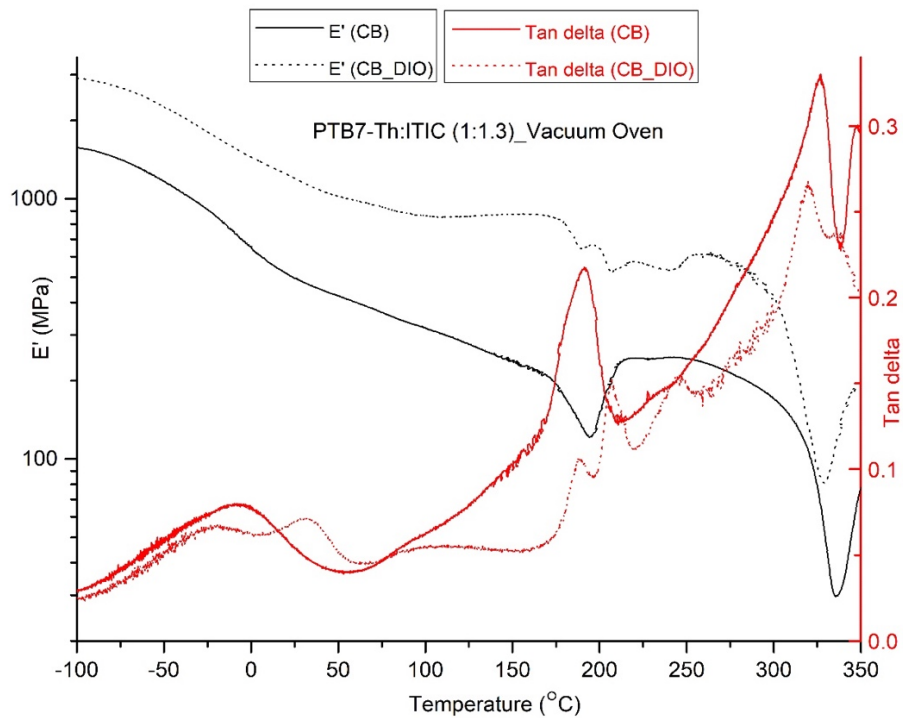


**Figure C.7:** DMA Comparison for CB and CB+DIO samples-vacuum oven.

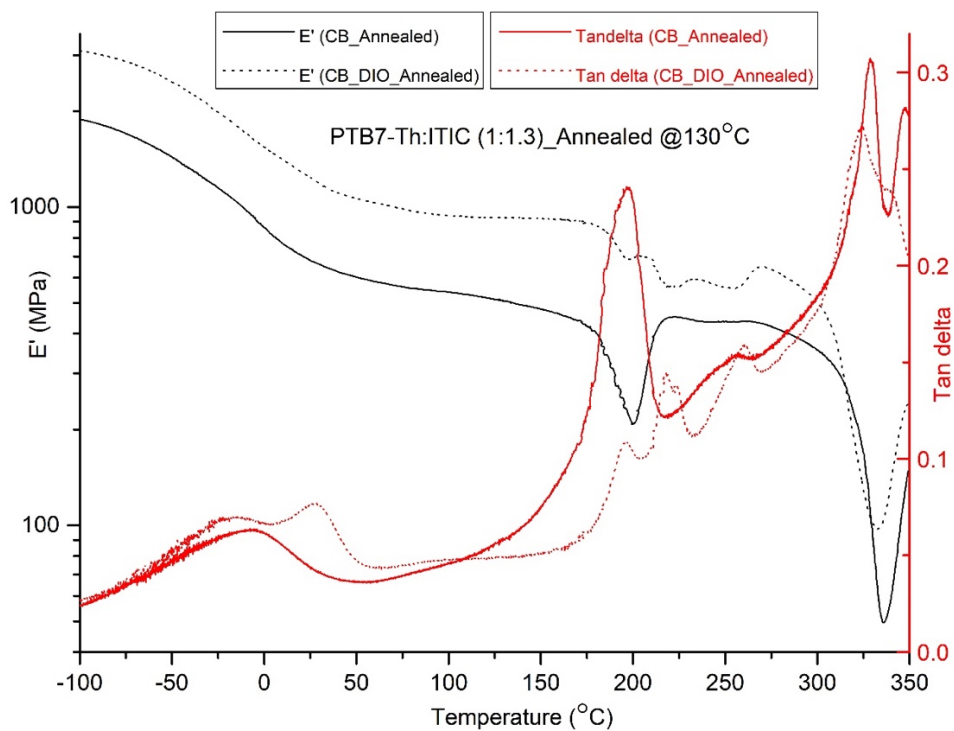


**Figure C.8:** DMA Comparison for CB and CB+DIO samples - annealed.